

## Towards computer assisted cardiac medicine

**Citation for published version (APA):**

Barbarotta, L. (2021). *Towards computer assisted cardiac medicine: sensitivity analysis and data assimilation in models of left ventricular mechanics*. [Phd Thesis 1 (Research TU/e / Graduation TU/e), Biomedical Engineering]. Technische Universiteit Eindhoven.

**Document status and date:**

Published: 13/01/2021

**Document Version:**

Publisher's PDF, also known as Version of Record (includes final page, issue and volume numbers)

**Please check the document version of this publication:**

- A submitted manuscript is the version of the article upon submission and before peer-review. There can be important differences between the submitted version and the official published version of record. People interested in the research are advised to contact the author for the final version of the publication, or visit the DOI to the publisher's website.
- The final author version and the galley proof are versions of the publication after peer review.
- The final published version features the final layout of the paper including the volume, issue and page numbers.

[Link to publication](#)

**General rights**

Copyright and moral rights for the publications made accessible in the public portal are retained by the authors and/or other copyright owners and it is a condition of accessing publications that users recognise and abide by the legal requirements associated with these rights.

- Users may download and print one copy of any publication from the public portal for the purpose of private study or research.
- You may not further distribute the material or use it for any profit-making activity or commercial gain
- You may freely distribute the URL identifying the publication in the public portal.

If the publication is distributed under the terms of Article 25fa of the Dutch Copyright Act, indicated by the "Taverne" license above, please follow below link for the End User Agreement:

[www.tue.nl/taverne](http://www.tue.nl/taverne)

**Take down policy**

If you believe that this document breaches copyright please contact us at:

[openaccess@tue.nl](mailto:openaccess@tue.nl)

providing details and we will investigate your claim.

Towards computer assisted  
cardiac medicine: sensitivity  
analysis and data assimilation in  
models of left ventricular  
mechanics

A catalogue is available from the Eindhoven University of Technology Library.

ISBN: 978-90-386-5187-3

Copyright © 2020 by Luca Barbarotta

All rights reserved. No part of this publication may be reproduced, stored in a retrieval system, or transmitted in any form or by any means, electronic, mechanical, photocopying, recording, or otherwise, without the prior written permission of the author.

Cover Design: Nicola Masotti

Printed by: Ridderprint | [www.ridderprint.nl](http://www.ridderprint.nl)

This work was supported by the European Commission within the Horizon 2020 Framework through the MSCA-ITN-ETN European Training Networks (project number 642458).

# Towards computer assisted cardiac medicine: sensitivity analysis and data assimilation in models of left ventricular mechanics

PROEFSCHRIFT

ter verkrijging van de graad van doctor  
aan de Technische Universiteit Eindhoven,  
op gezag van de rector magnificus prof.dr.ir. F.P.T. Baaijens,  
voor een commissie aangewezen door het College voor Promoties,  
in het openbaar te verdedigen  
op woensdag 13 januari 2021 om 11:00 uur

door

Luca Barbarotta

geboren te Busto Arsizio, Italië

Dit proefschrift is goedgekeurd door de promotoren en de samenstelling van de promotiecommissie is als volgt:

voorzitter: prof.dr. M. Merkx  
1e promotor: prof.dr.ir. F.N. van de Vosse  
copromotor: dr.ir. P.H.M. Bovendeerd  
leden: dr. M. Sermesant (Inria Epione - Université Côte d'Azur)  
prof.dr. L. Dekker (Catharina Ziekenhuis Eindhoven)  
prof.dr. L.R. Hellevik  
(Norwegian University of Science and Technology)  
prof.dr.ir. N.A.W. van Riel  
adviseur: dr.ir. W. Huberts

Het onderzoek of ontwerp dat in dit proefschrift wordt beschreven is uitgevoerd in overeenstemming met de TU/e Gedragscode Wetenschapsbeoefening.

# Contents

<b>1</b>	<b>Introduction</b>	<b>9</b>
1.1	General introduction . . . . .	10
1.2	Cardiac anatomy and function . . . . .	13
1.3	Computer models of the heart . . . . .	14
1.4	Sensitivity analysis and uncertainty quantification . . . . .	17
1.5	Data assimilation methodologies . . . . .	18
1.6	Aims and outline of the thesis . . . . .	19
	References . . . . .	29
<b>2</b>	<b>A Computer Model of the Mechanics of the LV and its Numerical Verification</b>	<b>31</b>
2.1	Introduction . . . . .	33
2.2	Models and methods . . . . .	34
2.2.1	Mathematical models . . . . .	34
2.2.2	Circulation . . . . .	43
2.2.3	Numerical approximation . . . . .	45
2.2.4	Simulations performed . . . . .	53
2.3	Results . . . . .	57
2.3.1	Convergence of strains over p-refinement . . . . .	58
2.3.2	Convergence of strains over h-refinement . . . . .	60
2.3.3	Comparison against Sepran implementation . . . . .	61
2.3.4	Active stress time integration scheme . . . . .	62
2.4	Discussion . . . . .	70
2.5	Conclusion . . . . .	74
	Appendices . . . . .	75
2.A	Detached circulation simulation . . . . .	75
2.B	Inflation of a thick-walled sphere . . . . .	76
	References . . . . .	81

<b>3</b>	<b>In Silico Assessment of Sensitivity of LV Wall Strains to Geometry</b>	<b>83</b>
3.1	Introduction . . . . .	85
3.2	Material and methods . . . . .	86
3.2.1	Geometry . . . . .	86
3.2.2	Material properties . . . . .	87
3.2.3	Computation of left ventricular wall mechanics . . . . .	88
3.2.4	Computation of the unloaded configuration . . . . .	89
3.2.5	Finite element implementation . . . . .	90
3.2.6	Sensitivity analysis approach . . . . .	91
3.3	Results . . . . .	98
3.4	Discussion . . . . .	102
3.4.1	Methods . . . . .	102
3.4.2	Results . . . . .	104
3.4.3	Limitations . . . . .	108
3.5	Conclusions . . . . .	108
	References . . . . .	113
<b>4</b>	<b>In Silico Assessment of Sensitivity of LV Wall Strains to Fiber Orientation</b>	<b>115</b>
4.1	Introduction . . . . .	117
4.2	Material and methods . . . . .	120
4.2.1	Material properties . . . . .	120
4.2.2	Geometry and fiber orientation . . . . .	121
4.2.3	Fiber parameter ranges . . . . .	122
4.2.4	Computation of left ventricular wall mechanics . . . . .	123
4.2.5	Computation of the unloaded configuration . . . . .	124
4.2.6	Finite element implementation . . . . .	125
4.2.7	Sensitivity analysis approach . . . . .	125
4.3	Results . . . . .	131
4.3.1	Complete analysis . . . . .	131
4.3.2	Single-parameter and double-parameter analyses . . . . .	138
4.4	Discussion . . . . .	141
4.4.1	Methods . . . . .	141
4.4.2	Results . . . . .	142
4.4.3	Limitations . . . . .	146
4.5	Conclusions . . . . .	148
	References . . . . .	153

<b>5</b>	<b>Parameter Estimation in a Rule-Based Fiber Orientation model from End Systolic Strains Using the Reduced Order Unscented Kalman Filter</b>	<b>157</b>
5.1	Introduction . . . . .	159
5.2	Methods . . . . .	161
5.2.1	Reduced order unscented Kalman filter . . . . .	161
5.2.2	Simulation settings . . . . .	165
5.3	Results . . . . .	167
5.3.1	Experiment 1: estimation without model error from ground truth . . . . .	167
5.3.2	Experiment 2: estimation without model error . . . . .	169
5.3.3	Experiment 3: estimation with model error . . . . .	171
5.4	Discussion . . . . .	173
5.4.1	Choices . . . . .	174
5.4.2	Results . . . . .	175
5.5	Limitations . . . . .	177
5.6	Conclusion . . . . .	178
	References . . . . .	183
<b>6</b>	<b>General Discussion</b>	<b>185</b>
6.1	Summary of contributions . . . . .	186
6.2	Study limitations . . . . .	188
6.3	Future perspectives . . . . .	190
6.3.1	Model extension . . . . .	190
6.3.2	Prioritize model parameters in pathological cases . . . . .	190
6.3.3	Combining data assimilation and meta-modeling for (al-most) real time computations . . . . .	191
6.4	General conclusions . . . . .	192
	References . . . . .	194
	<b>Summary</b>	<b>197</b>
	<b>Publications</b>	<b>199</b>
	<b>Acknowledgements</b>	<b>201</b>
	<b>Curriculum Vitae</b>	<b>205</b>





# **Chapter 1**

## **Introduction**

## 1.1 General introduction

According to the European Cardiovascular Disease Statistics report of 2017<sup>1</sup>, each year cardiovascular diseases (CVD) cause almost 4 million deaths in Europe. CVD account for 45% of all deaths in Europe and are the main cause of death in most European countries. Moreover, the cost related to CVD affects the EU economy with a burden of 210 billion euros a year, which constitutes an issue for the future sustainability of European healthcare systems. It is therefore important to try to reduce the impact of CVD on people's health and on the sustainability of the healthcare systems.

Technology is one of the pillars that support the sustainability of healthcare systems. Technology can contribute by either improving treatment quality or by decreasing its costs providing, for instance, early and improved diagnosis. An example of technology that contributes by early detecting a pathology is provided by Bonomi et al [7], where a wrist-wearable device is used to detect atrial fibrillation. This technology offers the opportunity to have a distributed controlling system that does not require hospitalization and might contribute to early detection without an increase in the costs. Therefore, it might contribute directly to the patient value [60], that can be expressed as the ratio between the benefit for the patient in terms of health and the cost for the health system. Technology can also contribute through the use of computer models. Computer models of the heart might be used to achieve improved decision making and prognosis. Their use might support the evidence-based medicine approach by enlarging the set of data at cardiologists disposal with personalized model-interpreted patient data. Ideally, in the personalized medicine framework, computer models might help detect potential non-responders to specific therapies and in simulating the outcome of a treatment. Several computer models were developed in the last years and different applications were addressed [61, 9, 52, 71], making these models a promising tool for the future. Nowadays, computer models are commonly used in an inverse analysis framework to extract quantitative biomarkers or interpret the severity of pathology from noisy measurements, typically coming from non-invasive imaging methodologies such as Computed Tomography scan (CT), Magnetic Resonance Imaging (MRI), and Echocardiography. Sermesant et al [70] proposed a methodology to estimate patient-specific myocardial conductivity and contractility from MRI images, invasive left ventricular endocardial electrophysiological mapping and pressure recording. They applied this methodology to simulate different pacing scenarios for two Heart Failure (HF) pa-

---

<sup>1</sup><http://www.ehnheart.org/cvd-statistics.html>

tients. Marchesseau et al [45], applied a methodology based on the Reduced Order Unscented Kalman Filter (ROUKF) to estimate local contractility in the 14 AHA regions of the Left Ventricle (LV) using measurements of regional volumes computed from cine-MRI in three HF patients. Finsberg et al [19], estimated the mechanical activation in seven healthy subjects and seven patients affected by Left Bundle Branch Block (LBBB) using strain and volume measurements from 4D Echocardiography. One of the limiting factors that prevents the application of those models inside the clinics is the lack of systematic validation and the lack of the estimation of the uncertainty affecting model predictions. This issue can be addressed by combining computer models with what is often addressed as Verification, Validation and Uncertainty Quantification (VVUQ) [55]. Verification addresses the question concerning the correctness and the accuracy of the solution of the mathematical problem. Validation assesses the suitability of the mathematical model to model the process observed in the real-world. Uncertainty Quantification allows estimating the probability distribution of the error propagated from the model input to the output through the prediction, thus providing some sort of confidence interval around the prediction.

Most of those computer models are 3D models that typically require a finite element discretization technique. Those models require information about the geometry, the orientation of the fibers constituting the myocardium, boundary conditions, and material properties determining the electro-mechanical response of the tissue such as material stiffness, contractility and moment of activation. While geometry (and potentially also fiber orientation) can be estimated using imaging techniques, material properties have to be estimated non-invasively. The quality of this estimation depends on the level of accuracy of our information about the geometry and fiber orientation, and consequently the amount of uncertainty affecting them. In modeling the heart, most of the models of mechanics involved in inverse approaches put a lot of emphasis in the determination of a patient-specific geometry, while fiber orientation is generally modeled using generic models or ex-vivo measurements adapted to the patient anatomy. This fact might be explained by the relative ease of generating a patient-specific geometry non-invasively using most of the common imaging techniques, although time and human interaction are typically required. Instead, in-vivo assessment of patient-specific fiber orientation via Diffusion Tensor MRI (DT-MRI) is still a challenging task. Advancements in this process have been proposed by Toussaint et al [77]. Their methodology allows reconstructing a patient-specific 3D fiber field by non-invasively acquiring 7 – 10 short-section slices of the patient heart using DT-MRI. Despite the good results in terms of acceleration, there is still an average

error of about  $10^\circ$  and the acquisition process still takes too long (70–100 minutes) to let the use of DT-MRI become a standard clinical examination. A few studies investigated the importance of fiber orientation in the determination of cardiac function [9, 21, 59]. Several sensitivity analyses addressed the role of fiber orientation within models of cardiac mechanics [27, 79, 50, 9, 21, 59]. Nonetheless, those studies present some limitations. Specifically, they are mostly qualitative, since they lack a certain robust sensitivity analysis structure with statistical indices for a quantitative assessment of the quantities of interest. The choice of the parameter ranges is somewhat arbitrary and often unphysiological. They focus on global quantities of interest (single scalar values) to assess the sensitivity of a complex, largely spatially varying 3D vector field as that of myofibers.

This thesis aims to contribute to the development of patient-specific computer models of the LV. The personalized computer model can potentially be applied to simulate different intervention scenarios or to better select groups of patients that would benefit from therapy. Some examples of these applications are reported in Smith et al [73]. In particular, patient-specific models can be applied in the planning of Cardiac Resynchronization Therapies, to reduce dyssynchrony in Heart Failure (HF) patients; in the planning of RadioFrequency Ablation (RFA) therapies, by testing several ablation strategies; in the application of a Left Ventricular Assist Device (LVAD), by improving the patient selection and by identifying situations where the LVAD can induce a myocardial remodeling that promotes recovery from HF. To obtain a patient-specific model from clinical data, often, a geometry is reconstructed from medical images and tissue properties and micro-structure are either inversely estimated or directly included from measurements. In this regard, we investigate the role of geometry and fiber orientation within a model of the mechanics of the LV. To accomplish this task, we apply a global sensitivity analysis methodology based on the elementary effects method [47, 10, 68] to assess the sensitivity of end-systolic strains to geometry and fiber orientation. End-systolic strains were chosen because they can be measured non-invasively in-vivo in clinical practice and can be interpreted by a computer model to provide a direct relation with tissue properties. The ultimate goal is to quantify the effects of different descriptions of geometry and fiber orientation on computed end-systolic strains. These results would also provide precious information on how strain observation should be included to improve the outcome of inverse analysis by highlighting important relations between parameters and strain components.

In this chapter, we briefly describe the anatomy of the heart and its functioning. We give an overview of different modeling choices for the heart and we

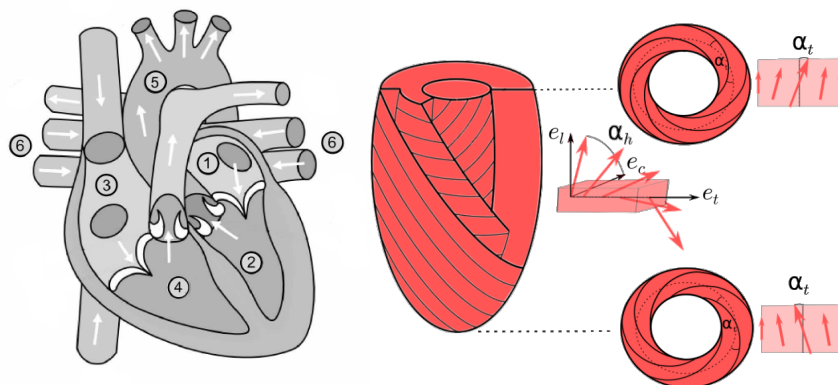


**Figure 1.1:** Representation of the anatomy of the heart and the fiber orientation of the left ventricle. On the left, the heart with labels indicating: (1) the left atrium, (2) the left ventricle, (3) the right atrium, (4) the right ventricle, (5) the aorta, and (6) the pulmonary veins. On the right, an idealized left ventricle with the representation of fiber orientation. The helix angle,  $\alpha_h$ , lies in the circumferential-longitudinal plane and is null when the fiber is oriented circumferentially. Similarly, the transverse angle,  $\alpha_t$ , lies in the circumferential-transverse plane and is null when the fiber is oriented circumferentially.

present our model of the left ventricle. We discuss available sensitivity analysis and uncertainty quantification methods. We provide some background information about currently used data assimilation and parameter estimation techniques and we conclude this chapter with the aims and the outline of the thesis.

## 1.2 Cardiac anatomy and function

The heart is a four chamber hollow organ that pumps blood in our circulatory system thanks to the contractile capabilities of its constituting muscle called myocardium. The four chambers are divided into two atria and two ventricles. Anatomically, the atria and the ventricles are separated by the basal plane. A common way to address this structure is to separate the left heart, Left Ventricle (LV) and the Left Atrium (LA), from the right heart, Right Ventricle (RV) and Right Atrium (RA). The right heart collects the low saturated blood from the circulation and pumps it to the lungs, while the left heart collects the oxygenated blood from the pulmonary veins and pumps it throughout the body via the circulatory system. The pumping action of the heart is determined by the contraction of the myofibers constituting the myocardium. This contraction is induced by an electrical stimulus generated by dedicated

pacemaker cells situated in the sinoatrial node. The signal first activates the atria and then is delayed about 100 ms in the atrioventricular node. Then, the signal is rapidly conducted by specialized fibers, the Purkinje fibers. In the septum, the Purkinje fibers are arranged in two bundle branches: the Right Bundle Branch (RBB) the Left Bundle Branch (LBB). Towards the apex, in the sub-endocardium, these branches bifurcate into many branches. From these branches, the electrical signal starts propagating within the myocardium, mostly from endocardium to epicardium. The delay between the activation of the atria and that of the ventricles allows time for the blood to fill the ventricles. The contraction of the ventricles determines the increase of cavity pressures and allows ejection.

The myocardium is constituted by myofibers embedded in an extracellular matrix of collagen. Myofibers are made by several myofibrils which contain the contractile unit, the sarcomere. Myofibers are similarly distributed among mammals [25, 24, 75, 69] following a right-handed helical path in the sub-endocardium, being circumferential at mid-wall, and following a left-handed helical path in the sub-epicardium. Different histological and DT-MRI measurements highlighted the presence of two angles for the description of fiber orientation: the helix angle, describing the apex-to-base component of the fiber vector; and the transverse angle, describing its endocardium-to-epicardium component. The helix angle largely varies transmurally. A common transmural range of about  $120^\circ$  with negative angles at the epicardium and positive angles at the endocardium is reported. The transverse angle has smaller values than the helix angle, generally having a modulus smaller than  $10^\circ$  [74, 69], and varies both longitudinally and transmurally.

Fiber orientation plays an important role in the determination of the mechanics of the LV. This is because of the strong anisotropy dictated by the presence of the myofibers. Already in the passive state, the myocardium is stiffer along the fiber than perpendicular to the fiber. During myocardial contraction, the build-up of active stress increases further the level of anisotropy. This anisotropy strongly affects the distribution of stress and strains within the myocardium.

### **1.3 Computer models of the heart**

The function of the heart is the result of complex multi-scale and multi-physics coupled phenomena [61]. The electromechanics of the heart describes the way the electrical signal distributes within the myocardium and how the muscle generates stress. The deformation of the myocardium depends on the elec-

trical activation, its ability to generate stress, the concentration of oxygen and metabolites, and the interaction with the blood coming from the circulation. Describing all those phenomena in detail in one single model would greatly increase the complexity and the computational time, let alone the number of parameters and the related uncertainty. Therefore, often phenomenological models are employed as a trade-off between accuracy and computational costs. Within models of electrophysiology, a model for the generation of the Action Potential (AP) and a model for its propagation are required. Different models for the generation of AP have been proposed [28, 5, 44]. The propagation of the AP within the myocardium can be modeled using the bidomain model [22] or the monodomain model, derived from the bidomain model by assuming that the extracellular conductivity tensor is proportional to the intracellular one [34]. Due to the small width of the propagation front and the steep temporal upstroke of the AP, very fine spatial and temporal resolutions are required for solving the bidomain model. An alternative approach consists in computing the spatial distribution of the electrical activation time of the myocardium using the Eikonal equation [20]. This approach is computationally less demanding, not requiring to compute the spatial distribution of action potential at every time step, has been thoroughly investigated [36, 37, 38, 39] and has been applied to simulate different pacing configurations in heart failure patients [70].

Regarding the mechanics, the configuration is computed stemming from the equilibrium between external forces, induced by the cavity pressure and interactions with neighboring tissues, and the myocardial stresses, arising from passive and active deformations. The mechanics is typically described using the Finite Elasticity theory, where the myocardium is modeled as a hyperelastic material with exponential behavior.

Considering that the myocardium is constituted by myofibers that are stiffer than the extracellular matrix, its material law must take into account the anisotropy. To describe the anisotropy within the myocardium two pieces of information are required: the direction of the fibers and their tissue properties. Model parameters describing tissue properties have been generally determined in such a way to represent measurements on explanted hearts in different experiments [16, 30, 15, 72]. More recently, other studies focused on the inverse estimation of those parameters [1, 23, 80, 2] based on observation of either strains, cavity pressure-volume loops, or displacement. Fiber orientation can be described using rule-based models embedding the most important features observed in histological measurements [25, 24, 75] and DT-MRI acquisitions [43, 69]. Generally, rule-based fiber models include only the transmural variability of the helix angle, rarely include the transverse angle,



and neglect circumferential heterogeneity and fiber dispersion. One of the most detailed rule-based fiber models presented in literature is the one presented by Bovendeerd et al [9], which includes transmurally and longitudinally varying helix and transverse angles. Over the years, different atlases of fibers were proposed. In these atlases, fibers were reconstructed from ex-vivo DT-MRI measurements on canine LV [57] or from ex-vivo DT-MRI measurements on human hearts [43]. To include circumferential variability and model spatial fiber dispersion, in some studies fibers from an atlas are mapped and re-oriented to match a patient-specific geometry [40]. Despite the personalized geometry and the geometry-specific re-orientation of fibers, this solution does not lead to a personalized fiber model. This approach only relates a single physiological fiber field to the patient-specific geometry without including the natural variability between individuals or potential variations in fiber orientation induced by pathologies. No patient-specific models with in-vivo fiber information have been proposed yet.

The presence of myofibers inside the myocardium introduces a strong anisotropy along fiber. This fact led the first models of mechanics to describe the myocardium as a transversely isotropic material. Subsequently, LeGrice et al [42, 41] evidenced an ordered laminar arrangement of myocytes. The presence of this arrangement introduces another direction of anisotropy since the bonding between fibers within the same laminar sheet is tighter than the bonding between adjacent laminar sheets. For this reason, the myocardium is often modeled as an orthotropic material [29, 18, 61, 63]. As a consequence, the description of the myocardium as an orthotropic material requires the description of sheet direction, which is much less regular and homogeneous than fiber direction [43], and the definition of more stiffness parameters. Usyk et al [78] showed that the importance of modeling the myocardium as orthotropic is unclear. Consequently, transversely isotropic material laws are still used in models of cardiac mechanics [35, 14, 19, 8, 26, 6, 13, 45, 70].

The mechanical activation of the myocardium can be described using two approaches: the active stress and the active strain. The former is the most used approach [8, 65, 56, 49, 48, 9] and relies on the addition of an active stress term to the passive stress tensor. The active strain approach [64, 51, 58] introduces a multiplicative splitting of the deformation gradient that allows prescribing the active deformation that a myocyte undergoes. This splitting allows to easily prescribe incompressible active deformations which improve numerical properties of the problem. However, since the overall deformation stems from the combination between active (constitutively given) and passive (unknown) deformations, modeling physiological contractions that lead to physiological strain distributions is more difficult.

## 1.4 Sensitivity analysis and uncertainty quantification

Within the framework of Uncertainty Quantification (UQ), forward uncertainty propagation and parameter Sensitivity Analysis (SA) are possible. Forward uncertainty propagation aims at estimating the probability distribution of some Quantity Of Interest (QOI) given that input parameters are stochastic variables. SA aims at quantifying how a perturbation of an input parameter affects the QOI of a model and allows to prioritize the parameters by their influence. It typically involves the computation of derivative-based indices to assess the sensitivity of QOIs to input parameters.

Within SA, two methods can be distinguished: local and global methods. Local SA methods estimate sensitivity indices by perturbing parameters around a single point in the input parameter space. This approach is informative only when the underlying model is linear, as the results can be extended from the sampling point to the whole parameter space. Nonetheless, for its simplicity, it is often used in qualitative SA. When more quantitative information is required, methods based on the exploration of the full input parameter space must be used. In this case, we talk about global SA. An example of global SA method is the Elementary Effect Method (EEM) [67]. This method was first presented by Morris [47] as a screening method and later improved by Campolongo et al [10]. It is a non-intrusive method that has been applied in the cardiovascular field [31, 17]. Hurtado et al [31] applied the EEM to assess the sensitivity of QOI such as action potential duration and maximum intracellular calcium concentration to variations in different maximal conductances using two electromechanical models. Among global SA methods, variance-based methods are considered the gold standard in sensitivity analysis. However, because of the large number of model evaluations required, most often meta-modeling is needed to reduce the high computational cost. Meta-modeling is often used to replicate a scalar QOI as predicted by the original model. The EEM and other variance-based methods can be combined to reduce even further the computation burden. An example of this combination is provided by Donders et al [17]. Donders et al [17] used the EEM to select non-influential parameters in a pulse wave propagation model, consisting of serially connected one-dimensional elements and zero-dimensional Windkessel models, before applying the variance-based Saltelli's method [66] combined with a Generalized Polynomial Chaos (GPC) expansion [76] as meta-model to estimate the sensitivity indices.

In the field of cardiac mechanics, most of the sensitivity studies that address the role of geometry and fiber orientation are qualitative local approaches [21, 14, 27, 79, 50]. Few sensitivity studies addressed the output of the mechanics

model using a structured sensitivity analysis approach such as the stochastic collocation method combined with a GPC meta-model [62, 11, 54]. The only study addressing strains is the one from Campos et al [11]. They investigated the sensitivity of fiber strain averaged in a single region of the AHA segments [53] to the local variation of the LV wall thickness. However, the sensitivity of fiber strain computed in this way might be underestimated, since the strain error related with the uncertainty in the fiber direction is neglected, and the results cannot be easily related with experimental data, since typically fiber orientation is unknown.

### **1.5 Data assimilation methodologies**

The ultimate goal of computer models in the cardiovascular field is the application in the clinic as a supportive tool to clinicians. The most used method to connect computer models with clinical measurements is Data Assimilation (DA). DA aims at improving model prediction by combining the model with observations of reality. DA is often used to determine system properties when incomplete information is available. That is the case in clinical practice, where measurements may be noisy, and spatially and temporally scattered. Two main approaches exist: the variational approach, which relies on the minimization of the error between observations and predictions; and the sequential approach, which is based on statistical estimation theory and aims at minimizing the variability of model error. For particular choices of the error functions the two approaches are equivalent. However, in the variational case, it is not convenient to set the problem in the same way as in the sequential case because it would require to store in memory large dense matrices. To avoid this issue, a combination of a descent method and an adjoint-based approach to compute the gradient of the error is used to minimize directly the error function. The adjoint problem can be derived from the original problem and its computational cost is usually of the same order. This method allows achieving high-resolution parameter estimations, for which the size of the estimated parameter is of the order of that of the unknown of the problem. Examples of this method can be found in [19, 2, 3, 4]. Being framed within the theory of optimization, issues related to lack of convexity and nonlinearity are nontrivial to treat.

The Kalman Filter (KF) [33] is one of the most famous sequential approaches. The goal of the KF is to compute an optimal estimate of the system state given a set of observations. It is called a sequential approach because, as soon as new observations become available, the estimation can be easily updated without

the need for recomputing everything. The KF is optimal under the hypotheses of Gaussianity of the stochastic variables and the linearity of the observation operator. Two main issues prevent the application of the KF to the problem of mechanics of the heart: the inherent nonlinearity of the problem, and the size of the problem. The nonlinearity breaks one of the assumptions of the optimality of the KF. In a discretized finite element problem, the state estimated by the KF is the displacement and the associated covariance matrix is a square matrix of the same size of the displacement. Due to the typical size of those problems, the treatment of such a large dense covariance matrix makes the computational effort required by the KF unbearable. To overcome these limitations, Moireau et al [46] proposed the Reduced Order Unscented Kalman Filter (ROUKF) that exploits the Unscented Transform (UT) [32] to treat the nonlinearity. The UT relies on the choice of specific points (so-called sigma-points) to propagate the mean and covariance of a random variable through a nonlinear operator. The ROUKF allows rewriting the filter using a factorized matrix of reduced rank that is typically much smaller than the state size. In this way, the method does not require the computation of the inverse of large dense matrices and the factorization can be chosen to be restricted to the estimation of the parameter section of the extended state (state and parameters). The resulting method can thus be used on problems with parameters of size much smaller than the state, it is not intrusive, and it does not require the computation of tangent or adjoint problems. The method has been applied in the context of cardiac mechanics to estimate passive stiffness parameters of the myocardium [80] using synthetic data, to estimate regional contractility values [12] using synthetic and animal data, and to estimate regional contractility in healthy volunteers and pathological cases [45].

## 1.6 Aims and outline of the thesis

This thesis aims to contribute to the development of patient-specific computer models of the LV. More specifically, we use a model of the mechanics of the left ventricle proposed by Bovendeerd et al [9] to investigate the sensitivity of end-systolic cardiac strains to settings of geometry and fiber orientation and we make a first step towards data assimilation. The outline of the thesis is as follows. In **chapter 2**, we present a new implementation of the model of the mechanics of the left ventricle proposed by Bovendeerd et al [9] using the FEniCS library. The implementation includes a model of the isolated LV mechanics coupled with a 0D closed-loop circulation model [9]. The mechanics is framed within the context of finite elasticity and the myocardium is modeled as a hy-

perelastic, transversely isotropic, active stress material. A detailed rule-based fiber orientation model is used to prescribe the direction of anisotropy of the myocardium. This model includes longitudinally and transmurally varying helix and transverse angles. The mechanical activation of the myocardium is assumed to occur homogeneously since physiological asynchrony of electrical activation in physiological conditions does not affect significantly the mechanical activation [36]. The new implementation is validated in a theoretical case, is investigated numerically, and compared with its previous implementation.

In **chapter 3** and **chapter 4** we perform sensitivity analyses of end-systolic strains to geometry and fiber orientation. In our analysis, we include complex 3D data as input and we assess their influence on 3D strain distributions. We adopt the EEM since it seems more adequate to compute sensitivity indices of 3D strains without the need for using meta-modeling. In **chapter 3**, we investigate the sensitivity of end-systolic Green-Lagrange strains to variations in the anatomical description of the left ventricle using our model of the mechanics of the left ventricle. The variations in the anatomical description of the left ventricle are defined in terms of deviation from an average geometry using six shape modes defined in [37]. The elementary effects method is used to compute sensitivity indices to evaluate the sensitivity in the physiological case.

In **chapter 4**, a similar analysis is performed for the study of the sensitivity of end-systolic strains to variation in the parameters describing the orientation of fiber within the left ventricular myocardium. In this chapter, the results of the two sensitivity analysis are compared.

Considering the results of our analyses from **chapter 3** and **chapter 4**, in **chapter 5** we present our preliminary results on the application of a methodology based on the ROUKF to estimate patient-specific fiber orientation from observation of end-systolic strains.

In **chapter 6**, we conclude the thesis with a general discussion of overall results achieved by this research putting the results into perspectives.

---

## Bibliography

- [1] L. Asner, M. Hadjicharalambous, R. Chabiniok, D. Peresutti, E. Sammut, J. Wong, G. Carr-White, P. Chowienczyk, J. Lee, A. King, et al. Estimation of passive and active properties in the human heart using 3d tagged mri. *Biomechanics and modeling in mechanobiology*, 15(5):1121–1139, 2016.
- [2] G. Balaban, M. S. Alnæs, J. Sundnes, and M. E. Rognes. Adjoint multi-start-based estimation of cardiac hyperelastic material parameters using shear data. *Biomechanics and modeling in mechanobiology*, 15(6):1509–1521, 2016.
- [3] G. Balaban, H. Finsberg, S. Funke, T. F. Håland, E. Hopp, J. Sundnes, S. T. Wall, and M. E. Rognes. In vivo estimation of elastic heterogeneity in an infarcted human heart. *Biomechanics and Modeling in Mechanobiology*, 17(5):1317–1329, 2018.
- [4] G. Balaban, H. Finsberg, H. H. Odland, M. E. Rognes, S. Ross, J. Sundnes, and S. Wall. High-resolution data assimilation of cardiac mechanics applied to a dyssynchronous ventricle. *International journal for numerical methods in biomedical engineering*, 33(11):e2863, 2017.
- [5] G. W. Beeler and H. Reuter. Reconstruction of the action potential of ventricular myocardial fibres. *The Journal of physiology*, 268(1):177–210, 1977.
- [6] J. Bestel, F. Clément, and M. Sorine. A biomechanical model of muscle contraction. In *International Conference on Medical Image Computing and Computer-Assisted Intervention*, pages 1159–1161. Springer, 2001.
- [7] A. G. Bonomi, F. Schipper, L. M. Eerikäinen, J. Margarito, R. M. Aarts, S. Babaeizadeh, H. M. de Morree, and L. Dekker. Atrial fibrillation detection using photo-plethysmography and acceleration data at the wrist. In *2016 Computing in Cardiology Conference (CinC)*, pages 277–280. IEEE, 2016.
- [8] P. Bovendeerd, T. Arts, J. Huyghe, D. Van Campen, and R. Reneman. Dependence of local left ventricular wall mechanics on myocardial fiber orientation: a model study. *Journal of biomechanics*, 25(10):1129–1140, 1992.
- [9] P. Bovendeerd, W. Kroon, and T. Delhaas. Determinants of left ventricular shear strain. *American Journal of Physiology. Heart and Circulatory Physiology*, 297(3):H1058–68, 2009.

- [10] F. Campolongo, J. Cariboni, and A. Saltelli. An effective screening design for sensitivity analysis of large models. *Environmental modelling & software*, 22(10):1509–1518, 2007.
- [11] J. O. Campos, J. Sundnes, R. W. dos Santos, and B. M. Rocha. Effects of left ventricle wall thickness uncertainties on cardiac mechanics. *Biomechanics and modeling in mechanobiology*, pages 1–13, 2019.
- [12] R. Chabiniok, P. Moireau, P.-F. Lesault, A. Rahmouni, J.-F. Deux, and D. Chapelle. Estimation of tissue contractility from cardiac cine-mri using a biomechanical heart model. *Biomechanics and modeling in mechanobiology*, 11(5):609–630, 2012.
- [13] D. Chapelle, P. Le Tallec, P. Moireau, and M. Sorine. Energy-preserving muscle tissue model: formulation and compatible discretizations. *International Journal for Multiscale Computational Engineering*, 10(2), 2012.
- [14] H. F. Choi, J. D’hooge, F. E. Rademakers, and P. Claus. Influence of left-ventricular shape on passive filling properties and end-diastolic fiber stress and strain. *Journal of Biomechanics*, 43(9):1745–1753, 2010.
- [15] L. L. Demer and F. Yin. Passive biaxial mechanical properties of isolated canine myocardium. *The Journal of physiology*, 339(1):615–630, 1983.
- [16] S. Dokos, B. H. Smail, A. A. Young, and I. J. LeGrice. Shear properties of passive ventricular myocardium. *American Journal of Physiology-Heart and Circulatory Physiology*, 283(6):H2650–H2659, 2002.
- [17] W. Donders, W. Huberts, F. van de Vosse, and T. Delhaas. Personalization of models with many model parameters: an efficient sensitivity analysis approach. *International journal for numerical methods in biomedical engineering*, 31(10), 2015.
- [18] T. S. Eriksson, A. Prassl, G. Plank, and G. A. Holzapfel. Influence of myocardial fiber/sheet orientations on left ventricular mechanical contraction. *Mathematics and Mechanics of Solids*, 18(6):592–606, 2013.
- [19] H. Finsberg, G. Balaban, S. Ross, T. F. Håland, H. H. Odland, J. Sundnes, and S. Wall. Estimating cardiac contraction through high resolution data assimilation of a personalized mechanical model. *Journal of computational science*, 24:85–90, 2018.
- [20] P. C. Franzone, L. Guerri, and S. Tentoni. Mathematical modeling of the excitation process in myocardial tissue: Influence of fiber rotation

- on wavefront propagation and potential field. *Mathematical biosciences*, 101(2):155–235, 1990.
- [21] L. Geerts, R. Kerckhoffs, P. Bovendeerd, and T. Arts. Towards patient specific models of cardiac mechanics: a sensitivity study. In *International Workshop on Functional Imaging and Modeling of the Heart*, pages 81–90. Springer, 2003.
- [22] D. B. Geselowitz and W. Miller. A bidomain model for anisotropic cardiac muscle. *Annals of biomedical engineering*, 11(3-4):191–206, 1983.
- [23] S. Gjerald, J. Hake, S. Pezzuto, J. Sundnes, and S. T. Wall. Patient-specific parameter estimation for a transversely isotropic active strain model of left ventricular mechanics. In *International Workshop on Statistical Atlases and Computational Models of the Heart*, pages 93–104. Springer, 2014.
- [24] R. Greenbaum, S. Y. Ho, D. Gibson, A. Becker, and R. Anderson. Left ventricular fibre architecture in man. *Heart*, 45(3):248–263, 1981.
- [25] A. Grimm, K. Katele, H.-L. Lin, and J. Fletcher. Fiber bundle direction in the mammalian heart. *Basic research in cardiology*, 71(4):381–388, 1976.
- [26] J. M. Guccione, A. D. McCulloch, and L. K. Waldman. Passive Material Properties of Intact Ventricular Myocardium Determined From a Cylindrical Model. *Journal of Biomechanical Engineering*, 113(1):42–55, 02 1991.
- [27] A. Hassaballah, M. Hassan, A. Mardi, and M. Hamdi. Modeling the effects of myocardial fiber architecture and material properties on the left ventricle mechanics during rapid filling phase. *Applied Mathematics & Information Sciences*, 9(1):161, 2015.
- [28] A. L. Hodgkin and A. F. Huxley. A quantitative description of membrane current and its application to conduction and excitation in nerve. *The Journal of physiology*, 117(4):500–544, 1952.
- [29] G. A. Holzapfel and R. W. Ogden. Constitutive modelling of passive myocardium: a structurally based framework for material characterization. *Philosophical Transactions of the Royal Society A: Mathematical, Physical and Engineering Sciences*, 367(1902):3445–3475, 2009.



- [30] J. D. Humphrey and F. C. P. Yin. Biaxial Mechanical Behavior of Excised Epicardium. *Journal of Biomechanical Engineering*, 110(4):349–351, 11 1988.
- [31] D. E. Hurtado, S. Castro, and P. Madrid. Uncertainty quantification of 2 models of cardiac electromechanics. *International Journal for Numerical Methods in Biomedical Engineering*, 33(12):e2894, 2017. e2894 cnm.2894.
- [32] S. J. Julier and J. K. Uhlmann. New extension of the kalman filter to non-linear systems. In *Signal processing, sensor fusion, and target recognition VI*, volume 3068, pages 182–193. International Society for Optics and Photonics, 1997.
- [33] R. E. Kalman. A New Approach to Linear Filtering and Prediction Problems. *Journal of Basic Engineering*, 82(1):35–45, 03 1960.
- [34] J. P. Keener and J. Sneyd. *Mathematical Physiology: Systems Physiology*. II. Springer, 2009.
- [35] R. H. Keldermann, M. P. Nash, H. Gelderblom, V. Y. Wang, and A. V. Panfilov. Electromechanical wavebreak in a model of the human left ventricle. *American Journal of Physiology-Heart and Circulatory Physiology*, 299(1):H134–H143, 2010.
- [36] R. Kerckhoffs, P. Bovendeerd, J. Kotte, F. Prinzen, K. Smits, and T. Arts. Homogeneity of cardiac contraction despite physiological asynchrony of depolarization: a model study. *Annals of biomedical engineering*, 31(5):536–547, 2003.
- [37] R. Kerckhoffs, P. Bovendeerd, F. Prinzen, K. Smits, and T. Arts. Intra- and interventricular asynchrony of electromechanics in the ventricularly paced heart. *Journal of Engineering Mathematics*, 47(3-4):201–216, 2003.
- [38] R. Kerckhoffs, O. P. Faris, P. Bovendeerd, F. W. Prinzen, K. Smits, E. R. McVeigh, and T. Arts. Electromechanics of paced left ventricle simulated by straightforward mathematical model: comparison with experiments. *American Journal of Physiology-Heart and Circulatory Physiology*, 289(5):H1889–H1897, 2005.
- [39] R. C. Kerckhoffs, S. N. Healy, T. P. Usyk, and A. D. McCULLOCH. Computational methods for cardiac electromechanics. *Proceedings of the IEEE*, 94(4):769–783, 2006.

- 
- [40] A. Krishnamurthy, C. T. Villongco, J. Chuang, L. R. Frank, V. Nigam, E. Belezzuoli, P. Stark, D. E. Krummen, S. Narayan, J. H. Omens, et al. Patient-specific models of cardiac biomechanics. *Journal of computational physics*, 244:4–21, 2013.
- [41] I. J. LeGrice, P. J. Hunter, and B. Smaill. Lamina structure of the heart: a mathematical model. *American Journal of Physiology-Heart and Circulatory Physiology*, 272(5):H2466–H2476, 1997.
- [42] I. J. LeGrice, B. Smaill, L. Chai, S. Edgar, J. Gavin, and P. J. Hunter. Lamina structure of the heart: ventricular myocyte arrangement and connective tissue architecture in the dog. *American Journal of Physiology-Heart and Circulatory Physiology*, 269(2):H571–H582, 1995.
- [43] H. Lombaert, J.-M. Peyrat, P. Croisille, S. Rapacchi, L. Fanton, F. Chieriet, P. Clarysse, I. Magnin, H. Delingette, and N. Ayache. Human atlas of the cardiac fiber architecture: study on a healthy population. *IEEE transactions on medical imaging*, 31(7):1436–1447, 2012.
- [44] C.-h. Luo and Y. Rudy. A dynamic model of the cardiac ventricular action potential. i. simulations of ionic currents and concentration changes. *Circulation research*, 74(6):1071–1096, 1994.
- [45] S. Marchesseau, H. Delingette, M. Sermesant, R. Cabrera-Lozoya, C. Tobon-Gomez, P. Moireau, R. F. i Ventura, K. Lekadir, A. Hernandez, M. Garreau, et al. Personalization of a cardiac electromechanical model using reduced order unscented kalman filtering from regional volumes. *Medical image analysis*, 17(7):816–829, 2013.
- [46] P. Moireau and D. Chapelle. Reduced-order unscented kalman filtering with application to parameter identification in large-dimensional systems. *ESAIM: Control, Optimisation and Calculus of Variations*, 17(2):380–405, 2011.
- [47] M. D. Morris. Factorial sampling plans for preliminary computational experiments. *Technometrics*, 33(2):161–174, 1991.
- [48] M. P. Nash and P. J. Hunter. Computational mechanics of the heart. *Journal of elasticity and the physical science of solids*, 61(1-3):113–141, 2000.
- [49] M. P. Nash and A. V. Panfilov. Electromechanical model of excitable tissue to study reentrant cardiac arrhythmias. *Progress in biophysics and molecular biology*, 85(2-3):501–522, 2004.

- [50] A. Nikou, R. C. Gorman, and J. F. Wenk. Sensitivity of left ventricular mechanics to myofiber architecture: A finite element study. *Proceedings of the Institution of Mechanical Engineers, Part H: Journal of Engineering in Medicine*, 230(6):594–598, 2016.
- [51] F. Nobile, A. Quarteroni, and R. Ruiz-Baier. An active strain electromechanical model for cardiac tissue. *International journal for numerical methods in biomedical engineering*, 28(1):52–71, 2012.
- [52] D. Nordsletten, S. Niederer, M. Nash, P. Hunter, and N. Smith. Coupling multi-physics models to cardiac mechanics. *Progress in biophysics and molecular biology*, 104(1-3):77–88, 2011.
- [53] A. H. A. W. G. on Myocardial Segmentation, R. for Cardiac Imaging:, M. D. Cerqueira, N. J. Weissman, V. Dilsizian, A. K. Jacobs, S. Kaul, W. K. Laskey, D. J. Pennell, J. A. Rumberger, T. Ryan, et al. Standardized myocardial segmentation and nomenclature for tomographic imaging of the heart: a statement for healthcare professionals from the cardiac imaging committee of the council on clinical cardiology of the american heart association. *Circulation*, 105(4):539–542, 2002.
- [54] H. Osnes and J. Sundnes. Uncertainty analysis of ventricular mechanics using the probabilistic collocation method. *IEEE Transactions on Biomedical Engineering*, 59(8):2171–2179, 2012.
- [55] P. Pathmanathan and R. A. Gray. Ensuring reliability of safety-critical clinical applications of computational cardiac models. *Frontiers in physiology*, 4:358, 2013.
- [56] P. Pathmanathan and J. P. Whiteley. A numerical method for cardiac mechanoelectric simulations. *Annals of biomedical engineering*, 37(5):860–873, 2009.
- [57] J.-M. Peyrat, M. Sermesant, X. Pennec, H. Delingette, C. Xu, E. R. McVeigh, and N. Ayache. A computational framework for the statistical analysis of cardiac diffusion tensors: application to a small database of canine hearts. *IEEE Transactions on Medical Imaging*, 26(11):1500–1514, 2007.
- [58] S. Pezzuto, D. Ambrosi, and A. Quarteroni. An orthotropic active-strain model for the myocardium mechanics and its numerical approximation. *European Journal of Mechanics-A/Solids*, 48:83–96, 2014.

- 
- [59] M. Pluijmert, T. Delhaas, A. F. de la Parra, W. Kroon, F. W. Prinzen, and P. H. Bovendeerd. Determinants of biventricular cardiac function: a mathematical model study on geometry and myofiber orientation. *Biomechanics and modeling in mechanobiology*, 16(2):721–729, 2017.
- [60] M. E. Porter. What is value in health care? *New England Journal of Medicine*, 363(26):2477–2481, 2010. PMID: 21142528.
- [61] A. Quarteroni, T. Lassila, S. Rossi, and R. Ruiz-Baier. Integrated heart–coupling multiscale and multiphysics models for the simulation of the cardiac function. *Computer Methods in Applied Mechanics and Engineering*, 314:345 – 407, 2017. Special Issue on Biological Systems Dedicated to William S. Klug.
- [62] R. Rodríguez-Cantano, J. Sundnes, and M. E. Rognes. Uncertainty in cardiac myofiber orientation and stiffnesses dominate the variability of left ventricle deformation response. *International journal for numerical methods in biomedical engineering*, 35(5):e3178, 2019.
- [63] S. Rossi, T. Lassila, R. Ruiz-Baier, A. Sequeira, and A. Quarteroni. Thermodynamically consistent orthotropic activation model capturing ventricular systolic wall thickening in cardiac electromechanics. *European Journal of Mechanics-A/Solids*, 48:129–142, 2014.
- [64] S. Rossi, R. Ruiz-Baier, L. F. Pavarino, and A. Quarteroni. Orthotropic active strain models for the numerical simulation of cardiac biomechanics. *International journal for numerical methods in biomedical engineering*, 28(6-7):761–788, 2012.
- [65] J. Sainte-Marie, D. Chapelle, R. Cimirman, and M. Sorine. Modeling and estimation of the cardiac electromechanical activity. *Computers & structures*, 84(28):1743–1759, 2006.
- [66] A. Saltelli. Making best use of model evaluations to compute sensitivity indices. *Computer physics communications*, 145(2):280–297, 2002.
- [67] A. Saltelli, M. Ratto, T. Andres, F. Campolongo, J. Cariboni, D. Gatelli, M. Saisana, and S. Tarantola. *Global sensitivity analysis: the primer*. John Wiley & Sons, 2008.
- [68] A. Saltelli, S. Tarantola, F. Campolongo, and M. Ratto. *Sensitivity analysis in practice: a guide to assessing scientific models*, volume 1. Wiley Online Library, 2004.

- [69] D. F. Scollan, A. Holmes, R. Winslow, and J. Forder. Histological validation of myocardial microstructure obtained from diffusion tensor magnetic resonance imaging. *American Journal of Physiology-Heart and Circulatory Physiology*, 275(6):H2308–H2318, 1998.
- [70] M. Sermesant, R. Chabiniok, P. Chinchapatnam, T. Mansi, F. Billet, P. Moireau, J.-M. Peyrat, K. Wong, J. Relan, K. Rhode, et al. Patient-specific electromechanical models of the heart for the prediction of pacing acute effects in crt: a preliminary clinical validation. *Medical image analysis*, 16(1):201–215, 2012.
- [71] M. Sermesant, H. Delingette, and N. Ayache. An electromechanical model of the heart for image analysis and simulation. *IEEE transactions on medical imaging*, 25(5):612–625, 2006.
- [72] B. Smaill and P. Hunter. Structure and function of the diastolic heart: material properties of passive myocardium. In *Theory of heart*, pages 1–29. Springer, 1991.
- [73] N. Smith, A. de Vecchi, M. McCormick, D. Nordsletten, O. Camara, A. F. Frangi, H. Delingette, M. Sermesant, J. Relan, N. Ayache, et al. euheart: personalized and integrated cardiac care using patient-specific cardiovascular modelling. *Interface focus*, 1(3):349–364, 2011.
- [74] D. Streeter. The cardiovascular system i. In *Handbook of physiology*, pages 61–112. Williams and Wilkins Baltimore, 1979.
- [75] D. D. Streeter Jr, H. M. Spotnitz, D. P. Patel, J. ROSS Jr, and E. H. Sonnenblick. Fiber orientation in the canine left ventricle during diastole and systole. *Circulation research*, 24(3):339–347, 1969.
- [76] B. Sudret. Global sensitivity analysis using polynomial chaos expansions. *Reliability engineering & system safety*, 93(7):964–979, 2008.
- [77] N. Toussaint, C. T. Stoeck, T. Schaeffter, S. Kozerke, M. Sermesant, and P. G. Batchelor. In vivo human cardiac fibre architecture estimation using shape-based diffusion tensor processing. *Medical image analysis*, 17(8):1243–1255, 2013.
- [78] T. Usyk, R. Mazhari, and A. McCulloch. Effect of laminar orthotropic myofiber architecture on regional stress and strain in the canine left ventricle. *Journal of elasticity and the physical science of solids*, 61(1-3):143–164, 2000.

- [79] H. Wang, H. Gao, X. Luo, C. Berry, B. Griffith, R. Ogden, and T. Wang. Structure-based finite strain modelling of the human left ventricle in diastole. *International journal for numerical methods in biomedical engineering*, 29(1):83–103, 2013.
- [80] J. Xi, P. Lamata, J. Lee, P. Moireau, D. Chapelle, and N. Smith. Myocardial transversely isotropic material parameter estimation from in-silico measurements based on a reduced-order unscented kalman filter. *Journal of the mechanical behavior of biomedical materials*, 4(7):1090–1102, 2011.



## **Chapter 2**

# **A Computer Model of the Mechanics of the LV and its Numerical Verification**



### **Abstract**

A new implementation of the models describing the problem of the mechanics of the Left Ventricle coupled with a close-loop circulation model is presented. The new implementation, based on the FEniCS project, has been developed in a modular way in a python package. The high performance is enabled by the C++ back-end implemented in FEniCS together with MPI parallelization by means of distributed linear algebra provided by dedicated external libraries. The new implementation has been tested theoretically, numerically, and against a previous implementation. The results predicted by the new implementation are in good agreement with those predicted by the previous one. Performances are comparable when assuming using the same discretization. However, the new implementation is more robust in the sense that enables simulations whose execution failed with the previous implementation. Moreover, thanks to use high-order schemes used to discretize ODE, the new implementation allows to obtain speedups when using larger time steps while preserving the accuracy of the solution.

The contents of this chapter are partially based on: Barbarotta, L., Rossi, S., Dedè, L. and Quarteroni, A., 2018. A transmurally heterogeneous orthotropic activation model for ventricular contraction and its numerical validation. *International journal for numerical methods in biomedical engineering*, 34(12), p.e3137.

## 2.1 Introduction

The CardioVascular BioMechanics group at the Technical University of Eindhoven has developed during the years a set of models for the modeling of the ventricular mechanics. These models rely on the Finite Element Method (FEM) to discretize the partial differential problem stemming from the momentum balance equation, whose resolution is required to compute the equilibrium configuration of the problem. The myocardium is described within the theory of the finite elasticity and the constitutive law is modeled in terms of a strain energy density function [6]. The activation of the myocardium, that is the ability of myofibers to develop stress upon electrical stimulation, is modeled using an active stress formulation [7]. The FEM discretization requires the definition of a mesh, a partitioning of an approximation of the geometry using simple geometrical elements, that allows the approximation of the integrals required by the approximation of the problem. Two geometries were implemented: one for simulating the left ventricle (LV) only, and one for simulating the BI-Ventricular (BIV) case. Depending on the type of geometry, the mechanics is coupled explicitly with a single closed-loop circulation model for the LV or with a double closed-loop circulation model. Eventually, the active stress generation can be assumed to originate homogeneously throughout the geometry or inhomogeneously according to the solution of the Eikonal equation [17].

All these models were developed on top of the commercial package Sepran [28]. This implementation will be referred in the text as the previous/old implementation or the Sepran implementation. At the beginning of this research, an efficient and modern simulator for the presented problem was considered a cornerstone for the project. However, the development of the underlying library Sepran was discontinued. This would have meant that no more support and no more updates would have been issued during the development of my project. This issue, together with the strong compiler dependency and the lack of support for standard data formats for input/output and visualization, determined the group's choice to derive a new implementation of the models based on a different project.

We decided to base the development of the new implementation on the FEniCS project [19] ([fenicsproject.org](http://fenicsproject.org)). FEniCS is a suite of python packages that allow the definition of partial differential problems that are then solved efficiently using the C++ back-end defined in the Dolfin library. Dolfin is a C++ compiled library whose symbols are exported in python. It interfaces with many linear algebra packages such as PETSc [3], Trilinos [15], and Eigen [12]. PETSc and Trilinos in particular, introduce in the project distributed linear al-

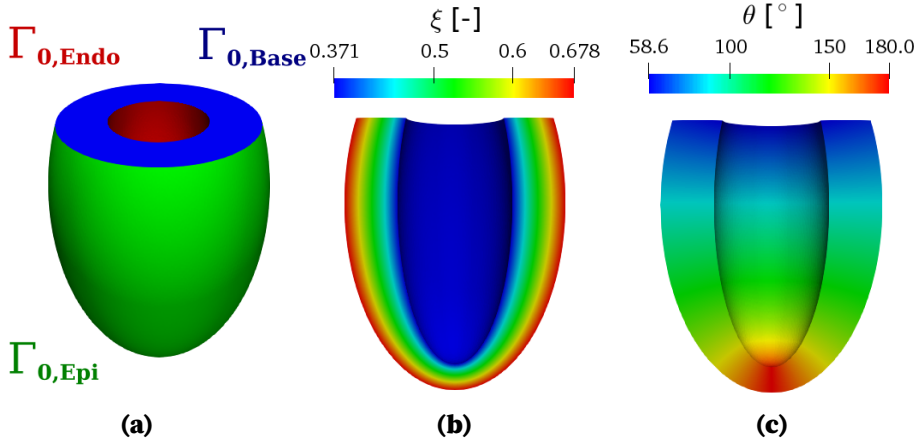


**Figure 2.1:** Representation of geometry and coordinates  $\xi$  and  $\theta$ . On the left, the geometry colored according to the surface labels: red for  $\Gamma_{0,Endo}$ , blue for  $\Gamma_{0,Base}$ , and green for  $\Gamma_{0,Epi}$ ; in the middle and on the right, the spatial distribution of  $\xi$  and  $\theta$ , respectively.

gebra, thus enabling MPI-based parallelization. Moreover, in PETSc and Trilinos many advanced numerical tools are available such as Krylov solvers and algebraic preconditioning techniques. Other important features of the FEniCS project are the possibility of enabling parallel input/output using the HDF5 library [10] and to deal with general scientific formats such as XDMF that can be then visualized using free software like Paraview [2] and VisIt [8]. The existent models were thus newly implemented in a python package named BeatIt ([git@mategit.wfw.wtb.tue.nl:Barbarotta/beatit.git](https://github.com/mategit.wfw.wtb.tue.nl/Barbarotta/beatit.git)).

This chapter is structured as follows. In the first section, the model proposed by Bovendeerd et al [7] is presented and its numerical implementation is detailed. In the second section, the results of different in-silico experiments are compared with the analytical solution and other approximated solutions. In the third section, the results and implementation choices are discussed. Finally, in the last section, the conclusions are presented.

## 2.2 Models and methods

### 2.2.1 Mathematical models

The mathematical model presented in [7] includes the description of the mechanics of the LV coupled with a 0D closed-loop circulation model. The mechanics is framed within the theory of hyper-elasticity and is described by

partial differential equations that enforce conservation of mass and momentum [20]. The myocardium is described as an transversely isotropic nearly-incompressible material [6]. The contraction of the myocardium is modeled in terms of an additive active stress term [17]. The fiber orientation dictates the direction of anisotropy during both passive deformation and active contraction. This orientation is modeled using Legendre polynomials [7]. The partial differential equations are discretized using the Finite Element Method (FEM) and the resulting nonlinear system is solved using the Newton-Raphson method [24, 23].

### LV geometry and fiber orientation

The geometry of an idealized left ventricle can be approximated using a prolate ellipsoidal shape [6]. Such ellipsoid can be describe using the prolate ellipsoidal coordinate system with radial coordinate  $\xi$ , longitudinal coordinate  $\theta$ , and circumferential coordinate  $\phi$ . By fixing a focal length  $f_l$  and the boundaries for  $\xi$  and  $\theta$  the following coordinate system can describe an axisymmetric prolate ellipse

$$\vec{x} = \begin{cases} x = f_l \sinh(\xi) \sin(\theta) \cos(\phi), \\ y = f_l \sinh(\xi) \sin(\theta) \sin(\phi), \\ z = f_l \cosh(\xi) \cos(\theta). \end{cases} \quad (2.2.1)$$

By constraining  $\xi \in [\xi_{endo}, \xi_{epi}]$ ,  $\theta \in [\arccos(z_{base}/\cosh(\xi)), \theta_{apex}]$ , and  $\phi \in [0, 2\pi]$ , an idealized left ventricular geometry can be defined. To achieve a cavity volume of 44 ml and a wall volume of 136 ml, the focal length is set to 43mm,  $\theta_{endo} = 0.371$ ,  $\theta_{epi} = 0.678$ ,  $\theta_{apex} = \pi$ , and the basal plane is defined by the plane  $z_{base} = 24$  mm. The geometry is shown in Figure 2.1a. On this geometry, the circumferential  $\vec{e}_c$ , the longitudinal  $\vec{e}_l$ , and transmural  $\vec{e}_t$  basis vectors can be defined normalizing the derivatives of  $\vec{x}$  with respect to  $\phi$ ,  $\theta$ , and  $\xi$  as follows

$$\vec{e}_c = \frac{\frac{\partial \vec{x}}{\partial \phi}}{\left\| \frac{\partial \vec{x}}{\partial \phi} \right\|_2} = \cos(\phi) \vec{e}_y - \sin(\phi) \vec{e}_x, \quad (2.2.2)$$

$$\begin{aligned} \vec{e}_l = \frac{\frac{\partial \vec{x}}{\partial \theta}}{\left\| \frac{\partial \vec{x}}{\partial \theta} \right\|_2} = & \left( \sinh(\xi) \cos(\theta) \cos(\phi) \vec{e}_x + \sinh(\xi) \cos(\theta) \sin(\phi) \vec{e}_y \right. \\ & \left. - \cosh(\xi) \sin(\theta) \vec{e}_z \right) \left( \sinh^2(\xi) + \sin^2(\theta) \right)^{-\frac{1}{2}}, \end{aligned} \quad (2.2.3)$$

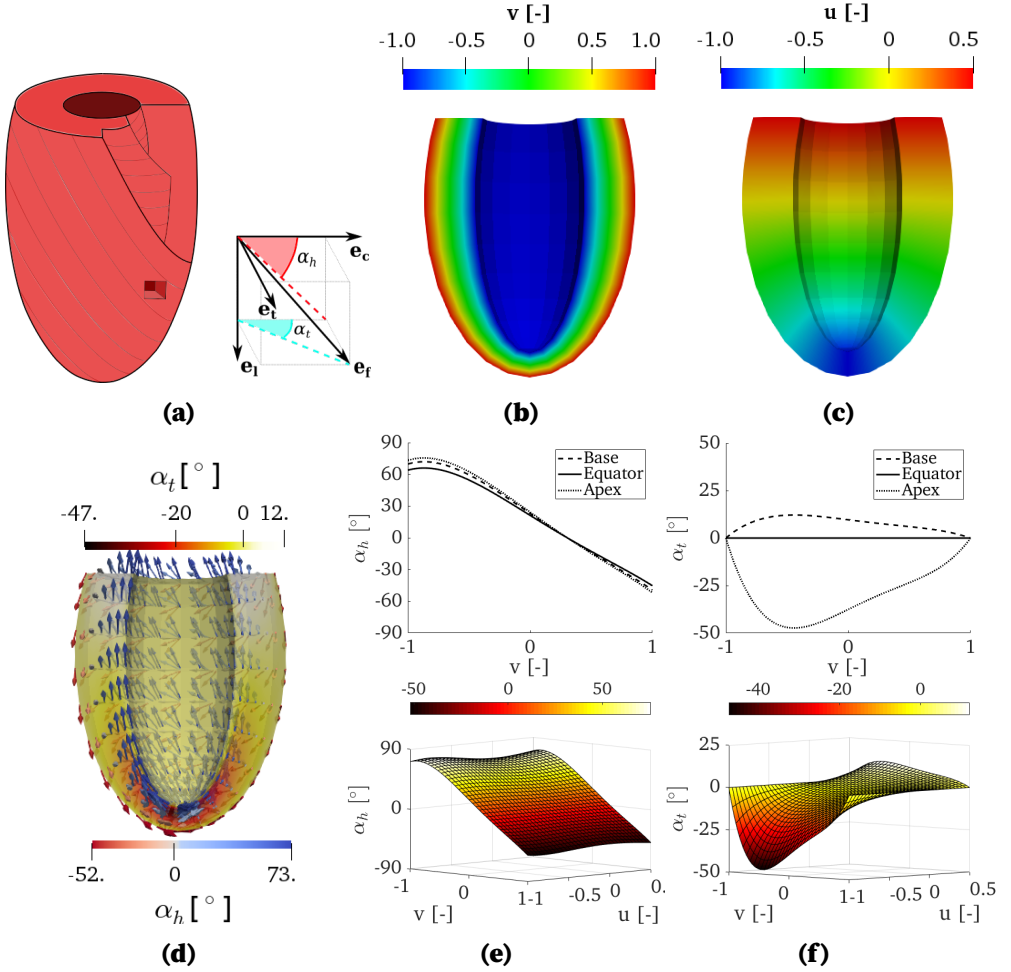


**Figure 2.2:** Representation of the geometry and fiber orientation. The top row shows: on the left, the geometry with a representation of the fiber angles; in the middle and on the right, the spatial distribution of normalized coordinates  $v$  and  $u$ , respectively. The bottom row shows: on the left, a section of the geometry colored using the values of  $\alpha_t$  and the fiber field  $\vec{e}_f$  colored using the values of  $\alpha_h$ ; in the middle, both the transmural and the complete spatial distribution of  $\alpha_h$ ; on the right, the transmural and the complete spatial distribution of  $\alpha_t$ .

$$\vec{e}_t = \frac{\frac{\partial \vec{x}}{\partial \xi}}{\left\| \frac{\partial \vec{x}}{\partial \xi} \right\|_2} = \left( \cosh(\xi) \sin(\theta) \cos(\phi) \vec{e}_x + \cosh(\xi) \sin(\theta) \sin(\phi) \vec{e}_y + \sinh(\xi) \cos(\theta) \vec{e}_z \right) \left( \sinh^2(\xi) + \sin^2(\theta) \right)^{-\frac{1}{2}}. \quad (2.2.4)$$

Figure 2.1b and Figure 2.1c show the spatial distribution of  $\xi$  and  $\theta$ , respectively.

The ellipsoidal coordinates allow to define spatially varying quantities within the geometry. For instance, fiber orientation is provided as a function of the normalized transmural and longitudinal coordinates,  $v$  and  $u$  respectively. These two normalized coordinates  $v$  and  $u$  are computed by integrating numerically the 2-norm of the derivative of the coordinates with respect to  $\xi$  and  $\theta$  respectively, as follows

$$v(\xi, \theta) = (v_{max} - v_{min}) \frac{\int_{\xi_{min}}^{\xi} \sqrt{\sinh^2(\xi') + \sin(\theta)} d\xi'}{\int_{\xi_{min}}^{\xi_{max}} \sqrt{\sinh^2(\xi') + \sin(\theta)} d\xi'} + v_{min}, \quad (2.2.5)$$

$$u(\xi, \theta) = \begin{cases} u_{min} \left( 1 - \frac{\int_{\pi}^{\theta} \sqrt{\sinh^2(\xi) + \sin(\theta')} d\theta'}{\int_{\pi/2}^{\pi} \sqrt{\sinh^2(\xi) + \sin(\theta')} d\theta'} \right), & \text{if } \theta > \frac{\pi}{2}, \\ u_{max} \frac{z}{z_{max}}, & \text{if } \theta \leq \frac{\pi}{2}. \end{cases} \quad (2.2.6)$$

According to [7], we set  $v_{min} = -1$  and  $v_{max} = 1$ , and  $u_{min} = -1$  and  $u_{max} = 0.5$ . Note that the definition of  $u$  requires that  $u$  becomes null at equator.

The orientation of fibers inside the myocardium is described by the helix angle and the transverse angle. The two angles define  $\vec{e}_f$  as the unit vector along the fiber in the following way

$$\vec{e}_f(\alpha_h, \alpha_t) = a(\alpha_h, \alpha_t) \cos(\alpha_t) \vec{e}_c + a(\alpha_h, \alpha_t) \sin(\alpha_t) \vec{e}_t - b(\alpha_h, \alpha_t) \vec{e}_l, \quad (2.2.7)$$

$$a(\alpha_h, \alpha_t) = \sqrt{\frac{1}{1 + \cos^2(\alpha_t) \tan^2(\alpha_h)}}, \quad (2.2.8)$$

$$b(\alpha_h, \alpha_t) = \sqrt{\frac{\cos^2(\alpha_t) \tan^2(\alpha_h)}{1 + \cos^2(\alpha_t) \tan^2(\alpha_h)}}, \quad (2.2.9)$$

where the helix angle defines the component of  $\vec{e}_f$  in the longitudinal-circumferential plane and the transverse angle defines the component in the circumferential-radial plane (Figure 2.2a).  $\alpha_h$  and  $\alpha_t$  are functions of the  $u$  and  $v$ , the normalized longitudinal and transmural coordinates. As in [7], the functional

description of  $\alpha_h$  and  $\alpha_t$  is provided in terms of Legendre polynomials

$$\alpha_h(u, v) = (h_{v0}L_0(v) + h_{v1}L_1(v) + h_{v2}L_2(v) + h_{v3}L_3(v) + h_{v4}L_4(v)) (1 + h_{u2}L_2(u) + h_{u4}L_4(u)), \quad (2.2.10)$$

$$\alpha_t(u, v) = (1 + t_{v1}L_1(v) + t_{v2}L_2(v)) (1 - v^2) (t_{u1}L_1(u) + t_{u3}L_3(u) + t_{u5}L_5(u)), \quad (2.2.11)$$

where  $L_n$  are unnormalized Legendre polynomials of degree  $n$  defined as follows

$$L_0(x) = 1, \quad L_1(x) = x, \quad L_2(x) = \frac{1}{2}(3x^2 - 1), \quad L_3(x) = \frac{1}{2}(5x^3 - 3x), \quad (2.2.12)$$

$$L_4(x) = \frac{1}{8}(353x^4 - 30x^2 + 3), \quad L_5(x) = \frac{1}{8}(63x^5 - 70x^3 + 15x). \quad (2.2.13)$$

The fiber orientation is shown in Figure 2.2 together with the transmural distribution of the helix and transverse angle at different longitudinal locations. The parameters used in the definition of the  $\alpha_h$  and  $\alpha_t$  are reported in Table 2.1.

$h_{ij}$	0	1	2	3	4	5
<b>v</b>	0.362 rad	-1.16 rad	-0.124 rad	0.129 rad	-0.0614 rad	-
<b>u</b>	-	-	0.0984	-	-0.0701	-
$t_{ij}$	0	1	2	3	4	5
<b>v</b>	-	-0.626 rad	0.502 rad	-	-	-
<b>u</b>	-	0.626	-	0.211	-	0.038

**Table 2.1:** Constitutive parameters for the definition of the spatial distribution of fiber orientation [7].

### Hyperelasticity problem

For a deforming body of material, we denote with  $\Omega_0$  and  $\Omega$  the initial and current configurations, respectively. In particular, we take  $\Omega_0$  and  $\Omega$  to be two open sets in  $\mathbf{R}^3$  with Lipschitz boundaries. The deformation is characterized by the motion  $\vec{\phi}: \Omega_0 \rightarrow \Omega$  such that  $\vec{x} = \vec{\phi}(\vec{x}_0)$ , which maps the reference coordinate  $\vec{x}_0 \in \Omega_0$  to the current one  $\vec{x} \in \Omega$ . The vector  $\vec{u} = \vec{x} - \vec{x}_0$  represents the displacement field and relates the position of a particle in the reference

configuration  $\vec{x}_0$  to its position in the current configuration  $\vec{x}$ . We denote the boundaries of  $\Omega_0$  and  $\Omega$  as  $\Gamma_0 = \partial\Omega_0$  and  $\Gamma = \partial\Omega$ , respectively. We also assume that  $\vec{\phi}$  is a diffeomorphism from  $\Omega_0$  to  $\Omega$ , such that the deformation gradient tensor  $\mathbf{F} = \nabla\vec{x} = \mathbf{I} + \nabla\vec{u}$  and the deformation Jacobian determinant  $J = \det(\mathbf{F}) > 0$  are always well defined. We denote with  $\mathbf{H} = J\mathbf{F}^{-T}$  the cofactor of the tensor  $\mathbf{F}$ .

The equations of Lagrangian solid dynamics describe the rate of change of position, density, and momentum of a material body, and can be expressed in an inertial reference frame. In the reference configuration, the equations of static equilibrium are expressed as

$$\rho J = \rho_0 \quad \text{in } \Omega_0, \quad (2.2.14a)$$

$$-\nabla_0 \cdot \mathbf{P} = \rho_0 \vec{b} \quad \text{in } \Omega_0, \quad (2.2.14b)$$

where  $\rho_0$  and  $\rho$  are the reference and current densities,  $\mathbf{P}(\mathbf{F}(\vec{x}_0))$  is the first Piola-Kirchhoff stress tensor,  $\nabla_0 \cdot$  is the divergence operator with respect to the reference coordinates and  $\vec{b}$  represents the external forces acting on the body. In the theory of hyperelasticity,  $\mathbf{P}$  is obtained from a strain energy function  $\mathcal{W}(\mathbf{C})$  as

$$\mathbf{P} = \frac{\partial \mathcal{W}}{\partial \mathbf{C}} \frac{\partial \mathbf{C}}{\partial \mathbf{F}}, \quad \mathbf{C} = \mathbf{F}^T \mathbf{F}, \quad (2.2.15)$$

where  $\mathbf{C}$  is the right Cauchy-Green deformation tensor. According to [6], gravitational and inertial effects are neglected. Equation (2.2.14b) needs to be supplied with appropriate boundary conditions. With this aim, we split the boundary of the left ventricle into three subsets  $\Gamma_{0,Base}$ ,  $\Gamma_{0,Endo}$ , and  $\Gamma_{0,Epi}$ , such that  $\partial\Omega_0 = \Gamma_{0,Base} \cup \Gamma_{0,Endo} \cup \Gamma_{0,Epi}$ . These are shown in Figure 2.1a.  $\Gamma_{0,Base}$  represents the left ventricular basal plane, where we typically impose a Dirichlet condition to block displacement normal to the basal plane to anchor the ventricle and to avoid rigid displacements and rotations. We also prevent the innermost region of the basal ring from moving along the circumferential direction, thus preventing rotation around the long axis.

The surface region  $\Gamma_{0,Endo}$  represents the endocardium, the inner part of the myocardium where the muscle is in contact with blood inside the ventricular cavity. On this portion of the boundary, we set a natural boundary condition to describe the force that the blood exerts on the ventricular wall. We assume that the ventricular pressure in the cavity  $p_v$  is uniformly distributed and that the stress is directed along the normal of the deformed surface. The surface region  $\Gamma_{0,Epi}$  represents the epicardium, the outer part of the myocardium where the muscle is interfaced with the pericardium and the viscous fluids



that reduce frictions between the two tissues. On this surface we set a homogeneous natural boundary condition.

Since the deformed configuration is unknown, we resort to the Piola transformation, which is nonlinear, in order to reformulate the boundary condition in the known reference configuration:

$$\mathbf{P}\vec{N}_0 = -p_v \mathbf{H}\vec{N}_0 \quad \text{on } \Gamma_{0,Endo}. \quad (2.2.16)$$

In summary, the final problem in its strong formulation, endowed with boundary conditions, reads:

$$\left\{ \begin{array}{ll} -\nabla_0 \cdot \mathbf{P}(\vec{u}) = \vec{0} & \text{in } \Omega_0, \quad (2.2.17a) \\ \vec{u} \cdot \vec{N}_0 = \vec{0} & \text{on } \Gamma_{0,Base}, \quad (2.2.17b) \\ u_x = 0 & \text{on } \{\Gamma_{0,Ring} \cap \{x = 0\}\}, \quad (2.2.17c) \\ u_y = 0 & \text{on } \{\Gamma_{0,Ring} \cap \{y = 0\}\}, \quad (2.2.17d) \\ (\mathbf{I} - \vec{N}_0 \otimes \vec{N}_0) \mathbf{P}\vec{N}_0 = \vec{0} & \text{on } \Gamma_{0,Base}, \quad (2.2.17e) \\ \mathbf{P}\vec{N}_0 = -p_v \mathbf{H}\vec{N}_0 & \text{on } \Gamma_{0,Endo}, \quad (2.2.17f) \\ \mathbf{P}\vec{N}_0 = \vec{0} & \text{on } \Gamma_{0,Epi}, \quad (2.2.17g) \end{array} \right.$$

where  $\Gamma_{0,Ring} = \Gamma_{0,Base} \cap \Gamma_{0,Endo}$ . All equations depend on the time  $t > 0$ . Note that we omitted (2.2.14a) in (2.2.17) because incompressibility will be weakly enforced using a nearly incompressible formulation (see section 2.2.1). By introducing the Hilbert space

$$V = \left\{ \vec{v} \in [H^1(\Omega_0)]^3 : \vec{v} \cdot \vec{N}_0 = 0 \text{ on } \Gamma_{0,Base}, v_x = 0 \text{ on } \Gamma_{0,RingX}, \right. \\ \left. v_y = 0 \text{ on } \Gamma_{0,RingY} \right\}, \quad (2.2.18)$$

$$\Gamma_{0,RingX} = \Gamma_{0,Ring} \cap \{\vec{x} \in \Omega_0 : x = [\vec{x}]_1 = 0\}, \quad (2.2.19)$$

$$\Gamma_{0,RingY} = \Gamma_{0,Ring} \cap \{\vec{x} \in \Omega_0 : y = [\vec{x}]_2 = 0\}, \quad (2.2.20)$$

the weak formulation of problem (2.2.17) reads:

$$\text{find } \vec{u} \in V : \int_{\Omega_0} \mathbf{P}(\vec{u}) : \nabla_0 \vec{v} d\vec{V} + \int_{\Gamma_{0,Endo}} p_v J \mathbf{F}^{-T} \vec{N}_0 \cdot \vec{v} d\vec{A} = 0 \quad \forall \vec{v} \in V. \quad (2.2.21)$$

The choice of the functional space is made compatibly with the need to compute gradient of  $\vec{v}$  and  $\vec{u}$  and to preserve square integrability in the sense of Lebesgue.

### Constitutive law for the passive myocardium

We still need to characterize, in problem (2.2.21), the form of the stress tensor. It is common to assume that the myocardial tissue is a hyperelastic material [7, 9, 16, 11] for which the stress tensor can be derived from a pseudo strain-energy function. The myocardium is modeled as a transversely isotropic material and we denote with  $\vec{e}_{f_0}$  the orientation of the cardiac fibers. The strain energy density function is the one proposed by Bovendeerd et al [6] and written in terms of invariants of  $\mathbf{E} = \frac{1}{2}(\mathbf{C} - \mathbf{I})$ , the Green-Lagrange strain tensor, to guarantee frame indifference. By introducing the isotropic invariants

$$\mathcal{I}_1(\mathbf{E}) = \text{tr } \mathbf{E}, \quad \mathcal{I}_2(\mathbf{E}) = \frac{1}{2} \left( \text{tr}(\mathbf{E}^2) - \text{tr}(\mathbf{E})^2 \right), \quad (2.2.22)$$

and the pseudo-invariant

$$\mathcal{I}_{4,f}(\mathbf{E}) = \vec{e}_{f_0} \cdot \mathbf{E} \vec{e}_{f_0}, \quad (2.2.23)$$

the strain energy function reads

$$\mathcal{W} = a_0 (\exp(\mathcal{Q}) - 1), \quad (2.2.24)$$

$$\mathcal{Q} = a_1 \mathcal{I}_1(\mathbf{E})^2 + 2a_1 \mathcal{I}_2(\mathbf{E}) + a_3 \mathcal{I}_{4,f}(\mathbf{E})^2. \quad (2.2.25)$$

### Nearly-incompressible formulation

The constitutive law (2.2.24) is written for an incompressible material. Incompressibility is typically enforced by setting an internal constraint on the constitutive law by means of a Lagrange multiplier, which introduces the pressure field. The introduction of the additional pressure term allows to obtain deformations that preserve the mass. However, this additional term also increases the size of the problem and makes it more difficult to solve computationally. For this reason, a different approach is taken. Incompressibility is weakly enforced using a penalization term, which is added to the strain energy density function. The additional term  $\mathcal{W}_{\text{vol}}$  is the energy term characterizing volume changes  $J = \sqrt{\mathcal{I}_3(\mathbf{C})}$ . It penalizes volume variations by making a deformation more energetically “expensive” when  $J \neq 1$ . Several expressions for  $\mathcal{W}_{\text{vol}}$  are proposed in literature [14]: generally, an optimal choice is to consider a penalty function bounded (from below), convex and whose slope is null in  $J = 1$ . The energy term proposed by Simo et al [27] satisfies the aforementioned prerequisites and read:

$$\mathcal{W}_{\text{vol}}(J) = 4k (J^2 - 1 - 2 \ln J). \quad (2.2.26)$$

The parameter  $k$  in (2.2.26) is called bulk modulus. The bulk modulus is a penalization factor that allows to weakly enforce incompressibility. Ideally incompressibility is enforced for  $k$  approaching infinity. For practical applications, it is sufficient to set a finite value for  $k$  that allows only slight deviation from incompressibility. The final form of the strain energy function and of the first Piola-Kirchhoff stress tensor reads as follows

$$\mathcal{W} = a_0 \left( \exp \left( a_1 \mathcal{I}_1(\mathbf{E})^2 + 2a_1 \mathcal{I}_2(\mathbf{E}) + a_3 \mathcal{I}_{4,f}(\mathbf{E})^2 \right) - 1 \right) + 4k (J^2 - 1 - 2 \ln J). \quad (2.2.27)$$

$$\mathbf{P} = 2a_0 \exp(\mathcal{Q}) \left( (a_1 - a_2) (\mathbf{E} : \mathbf{I}) \mathbf{F} + a_2 \mathbf{F} \mathbf{E} + a_3 (\vec{e}_{f_0}^T \cdot \mathbf{E} \vec{e}_{f_0}) \mathbf{F} \vec{e}_{f_0} \otimes \vec{e}_{f_0} \right) + 8k (J^2 - 1) \mathbf{F}^{-T}. \quad (2.2.28)$$

The parameters involved in the definition of the first Piola-Kirchhoff stress tensor (2.2.28) are shown in Table 2.2

Passive stress model				
$a_0$ [kPa]	$a_1$ [-]	$a_2$ [-]	$a_3$ [-]	$k$ [kPa]
0.4	3	3	3	10

**Table 2.2:** Constitutive parameters of the passive myocardium model [7].

### Active stress formulation

The active term of the first Piola-Kirchhoff stress tensor is modeled through a serial arrangement of an elastic element and a contractile element. The active stress, adopted from [7], acts along fiber direction and is dependent on sarcomere and contractile lengths, time and velocity as follows:

$$\mathbf{P}_a = \frac{l_{s0}}{l_s} f_{\text{iso}}(l_c) f_{\text{twitch}}(t_a, l_s) E_a (l_s - l_c) \mathbf{F} \vec{e}_{f_0} \otimes \vec{e}_{f_0}, \quad (2.2.29)$$

where  $l_s$  is the sarcomere length,  $l_c$  is the contractile length,  $l_{s0}$  is the stress-free sarcomere length,  $t_a$  is the activation time,  $f_{\text{iso}}$  is the length dependent stress term,  $f_{\text{twitch}}$  is the time dependent stress term, and  $E_a$  is the stiffness of the elastic element. The expressions of  $f_{\text{iso}}$  and  $f_{\text{twitch}}$  are

$$f_{\text{iso}}(l_c) = T_0 \tanh^2 [a_l (l_c - l_{c0})] \chi_{[l_{c0}, +\infty)}(l_c), \quad (2.2.30)$$

$$f_{\text{twitch}}(t_a, l_s) = \tanh^2 \left( \frac{t_a}{\tau_r} \right) \chi_{[0, b(l_s - l_d)]}(t_a) \tanh^2 \left( \frac{b(l_s - l_d) - t_a}{\tau_d} \right), \quad (2.2.31)$$

where  $T_0$  is the reference active stress level,  $a_l$  models the steepness of the stress-length curve,  $l_{c0}$  is the contractile element threshold below which the active stress is zero, the rise and decay of  $f_{\text{twitch}}$  is dictated by  $\tau_r$  and  $\tau_d$ ,  $b$  modulates the twitch duration depending on the sarcomere length,  $l_d$  is the sarcomere length corresponding to a twitch duration of zero, and  $\chi_A(x)$  is the indicator function of the variable  $x$  on the set  $A$ . Finally, the time evolution of the contractile length is given by

$$\frac{dl_c}{dt} = [E_a (l_s - l_c) - 1] v_0, \quad (2.2.32)$$

where  $v_0$  is the unloaded shortening velocity.

The constitutive parameter settings of the active stress model are given in Table 2.3.

Active stress model				
$T_0$ [kPa]	$E_a$ [ $\mu\text{m}^{-1}$ ]	$a_l$ [ $\mu\text{m}^{-1}$ ]	$l_{c0}$ [ $\mu\text{m}$ ]	$l_{s0}$ [ $\mu\text{m}$ ]
160	20	2	1.5	1.9
$\tau_r$ [ms]	$\tau_d$ [ms]	$b$ [ms/ $\mu\text{m}$ ]	$l_d$ [ $\mu\text{m}$ ]	
75	150	160	-0.5	

**Table 2.3:** Constitutive parameters of the active stress model [7].

### 2.2.2 Circulation

The LV cavity pressure is determined by the interaction between the blood inside the ventricular chamber and the myocardium. Following [7], to describe the blood distribution within the body a 0D model is used. This model is constituted by two three-elements Wind-Kessel [29] models. The two three-elements Wind-Kessel share the same resistive element and model the systemic and pulmonary circulations, respectively. The model is briefly sketched in Figure 2.3 using the electric equivalence. In fact in this representation, capacitors are used to model the ability of vessels to store blood, resistors are

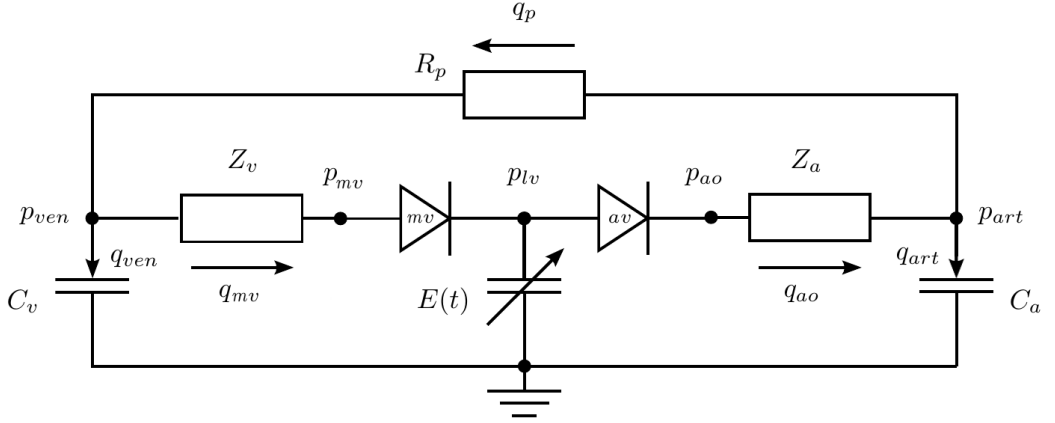


**Figure 2.3:** Representation of the electric-equivalent of the circulation model.

used to model viscous properties of the vessels, and diodes are used to model ideal valves. The governing equations for resistive and compliant elements are

$$\Delta p = Rq, \quad C \frac{dp}{dt} = \frac{dV}{dt} = q, \quad (2.2.33)$$

respectively. Including these equations in the system in Figure 2.3 leads to the system of ordinary differential equations:

$$C(p_{lv}) \left\{ \begin{array}{l} q_p = \frac{p_{art} - p_{ven}}{R_p}, \\ q_{ao} = \frac{p_{ao} - p_{art}}{Z_a} = \chi_{av} \frac{p_{lv} - p_{art}}{Z_a}, \\ q_{mv} = \frac{p_{ven} - p_{mv}}{Z_v} = \chi_{mv} \frac{p_{ven} - p_{mv}}{Z_v}, \\ \frac{dV_{lv}}{dt} = q_{mv} - q_{ao}, \\ \frac{dV_{art}}{dt} = q_{ao} - q_p, \\ V_{ven} = V_{tot} - V_{lv} - V_{art}, \\ C_a \frac{dp_{art}}{dt} = \frac{dV_{art}}{dt}, \\ C_v \frac{dp_{ven}}{dt} = \frac{dV_{ven}}{dt}, \end{array} \right. \quad (2.2.34)$$

where the initial conditions for the two latter differential equations are  $V_{art}^0$  and  $V_{ven}^0$ , which are the volume of blood stored in arteries and veins, respec-

tively, when the transmural pressure is null. Note that  $p_{mv}$  and  $p_{ao}$  are equal to  $p_{lv}$  when the mitral and aortic valves are open, respectively. This behavior is modeled using the indicator functions  $\chi_{mv}$  and  $\chi_{av}$  that return one when the respective valve is open and zero otherwise. Note also that the valves are the only source of nonlinearity inside the circulation model.

The resulting circulation model can be coupled with any sort of model of the LV, provided that this model can estimate the cavity pressure and cavity volume. As an example of this, in Figure 2.3 the LV is represented using a time varying elastance model, which linearly relates cavity pressure and cavity volume by means of a non-linearly varying time-dependent elastance factor  $E(t)$ . The parameters used in the circulation model are taken from [7] and are shown in Table 2.4. The model is initialized by setting  $p_{art} = 11.5$  kPa and  $V_{ven} = V_{tot} - V_c - V_{art}$ , exploiting the balance of circulating blood.

$R_p$	$1.2 \times 10^{-1}$	kPa · ms/mm <sup>3</sup>
$Z_a$	$10^{-2}$	kPa · ms/mm <sup>3</sup>
$Z_v$	$5 \times 10^{-3}$	kPa · ms/mm <sup>3</sup>
$V_{tot}$	$5 \times 10^6$	mm <sup>3</sup>
$V_{art}^0$	$5 \times 10^5$	mm <sup>3</sup>
$V_{ven}^0$	$3 \times 10^6$	mm <sup>3</sup>
$C_a$	$2.5 \times 10^4$	mm <sup>3</sup> /kPa
$C_v$	$6 \times 10^5$	mm <sup>3</sup> /kPa

**Table 2.4:** Parameters of the circulation model.

## 2.2.3 Numerical approximation

### Spatial discretization

We want to solve problem (2.2.21) using the Galerkin method. Given that the space  $V$  is an separable Hilbert space, this method allows to obtain an approximation of the solution of the original infinite dimensional problem by projecting this problem onto a finite dimensional subspace [26]. To create this finite dimensional subspace, the finite element method relies on the introduction of a discretization of the domain by means of a mesh. On this mesh, a set of shape functions defines a basis for the subspace, thus allowing the projection of the problem. The meshing procedure introduces a polygonal approximation  $\bar{\Omega}_{0,h}$  of the geometry  $\bar{\Omega}_0$ . This procedure creates a partitioning  $\mathcal{T}_h$  of the domain  $\bar{\Omega}_{0,h}$  of non-overlapping elements such that the union of all the elements equals the domain:  $\Omega_{0,h} = \cup_{K \in \mathcal{T}_h} K$ . Where the inside of each

element must be non-empty and the intersection of the insides of any pair of elements in  $\mathcal{T}_h$  must be empty. Moreover, if a pair of elements has a non empty intersection, this intersection must be either a whole face or a whole edge or a vertex. The diameter of an element is indicated by  $h_K$ , while the maximum diameter over the mesh is indicated by  $h = \max_{K \in \mathcal{T}_h} h_K$ . We only consider partitioning made by linear tetrahedra. The space of continuous finite elements is then the set of globally continuous functions that are locally polynomials on each element  $K$  of  $\mathcal{T}_h$

$$X_h^r = \{v_h \in C^0(\bar{\Omega}_{0,h}) : v_h|_K \in \mathbb{P}_r \ \forall K \in \mathcal{T}_h\}. \quad (2.2.35)$$

For a variational problem satisfying the hypothesis of Lax-Milgram theorem [22], a convergence result for the finite element method states that, if the exact solution  $\vec{u} \in H^{r+1}(\Omega)$ , then

$$\|\vec{u} - \vec{u}_h\|_{H^1(\Omega)} \leq \frac{M}{\alpha} Ch^r |\vec{u}|_{H^{r+1}(\Omega)}, \quad (2.2.36)$$

where  $\vec{u}_h$  is the approximated solution,  $M$  and  $\alpha$  are the continuity and coercivity constants of the Lax-Milgram theorem, respectively, and  $C$  is a constant independent from  $h$  and  $\vec{u}$ . Note that (2.2.36) relates the accuracy of the approximation to the mesh resolution  $h$ , the degree of the basis functions, and the regularity of the solution. This result also suggests two methods to control the accuracy of the approximation: refining the mesh by decreasing  $h$  ( $h$ -refinement), and by increasing the polynomial order ( $p$ -refinement, as long as the regularity of  $\vec{u}$  allows it). In the following we will consider the effects of global  $h - p$ -refinement.

We project problem (2.2.21) on  $V_h$ , defined as follows

$$V_h = \left\{ \vec{v}_h \in [X_h^r]^3 : \vec{v}_h \cdot \vec{N}_0 = 0 \text{ on } \Gamma_{0,Base} \right\}. \quad (2.2.37)$$

A general function  $\vec{v}_h$  of  $V_h$  can be expressed as a linear combination of basis functions of (2.2.37)

$$\vec{v}_h(\vec{x}_0) = \sum_{i=1}^n v_i \vec{\phi}_i(\vec{x}_0), \quad (2.2.38)$$

where  $\vec{x}_0 \in \Omega_{0,h}$ ,  $n$  is the total number of degrees of freedom introduced by the spatial discretization and  $\vec{\phi}^i$  is the  $i$ -th Lagrangian basis function. In this

context the displacement and the deformation gradient can be defined as

$$\vec{u}_h = \sum_{j=1}^n u_j \vec{\phi}_j(\vec{x}_0), \quad (2.2.39)$$

$$\mathbf{F}_h(\vec{x}_0) = \mathbf{I} + \sum_{j=1}^n u_j \nabla_0 \vec{\phi}_j(\vec{x}_0), \quad (2.2.40)$$

respectively. Note that the order of polynomial interpolation is dictated by the choice of  $r$  in (2.2.37). Then, we define  $J_h = \det(\mathbf{F}_h)$  and  $\mathbf{H}_h = J_h \mathbf{F}_h^{-T}$ .

By introducing Gauss-Jacobi quadrature rules with  $n_q$  and  $n_{qBD}$  nodes over domain and boundaries, whose weights are  $w(\vec{x}_{0,q})$  and  $w_{BD}(\vec{x}_{0,q})$  respectively and by plugging (2.2.39) and (2.2.40) into (2.2.21), we derive the corresponding algebraic formulation for the elastostatic problem. By setting

$$L_i(\vec{u}_h) = \sum_{q=1}^{n_q} w(\vec{x}_{0,q}) \left[ \mathbf{P}(\mathbf{F}_h(\vec{x}_{0,q})) : \nabla_0 \vec{\phi}_i(\vec{x}_{0,q}) \right], \quad (2.2.41)$$

$$B_i^N(\vec{u}_h) = \sum_{q=1}^{n_{qBD}} w_{BD}(\vec{x}_{0,q}) \left[ p_v \mathbf{H}_h(\vec{x}_{0,q}) \vec{N}_0 \cdot \vec{\phi}_i(\vec{x}_{0,q}) \right], \quad (2.2.42)$$

the sum of (2.2.41) and (2.2.42) yields the algebraic nonlinear system

$$\mathcal{M}(\vec{u}_h) = \mathbf{L}(\vec{u}_h) + \mathbf{B}^N(\vec{u}_h) = \vec{0}. \quad (2.2.43)$$

Note that for the sake of brevity in (2.2.41) and (2.2.42) numerical integration is performed in a loop over the mesh elements, while in reality the integration is preformed in the reference element because of its computational efficiency. This is achieved by mapping the reference element to each element and changing the variable under the integral sign, for instance:

$$\int_{K_i} \nabla_{\vec{x}} u(\vec{x}) \cdot \vec{v}(\vec{x}) \, d\vec{x} \stackrel{\vec{x}=\vec{F}_i(\hat{\vec{x}})}{=} \int_{\hat{K}} \mathbf{J}_{G,i}^{-T} \nabla_{\hat{\vec{x}}} u(F_i(\hat{\vec{x}})) \cdot \vec{v}(F_i(\hat{\vec{x}})) \det(\mathbf{J}_{G,i}) \, d\hat{\vec{x}}, \quad (2.2.44)$$

where  $[\mathbf{J}_{G,i}]_{jk} = \partial F_{i,j} / \partial \hat{x}_k$  is the Jacobian matrix of the geometric transformation that maps the reference element to the  $i$ -th element  $K_i$ . In particular, for our affine finite element approach, the expression for  $\mathbf{J}_{G,i}$  can be obtained exploiting the linear Lagrangian basis functions of the reference element [22]

$$x = \sum_{i=1}^4 X_i \hat{\phi}_i(\hat{\vec{x}}), \quad y = \sum_{i=1}^4 Y_i \hat{\phi}_i(\hat{\vec{x}}), \quad z = \sum_{i=1}^4 Z_i \hat{\phi}_i(\hat{\vec{x}}), \quad (2.2.45)$$



where  $X_i, Y_i, Z_i$  are the coordinates of the vertices of the current element. Note that this approach is different with the one implemented in Sepran, since Sepran implements isoparametric finite elements. In fact, in isoparametric finite elements, the basis functions used in (2.2.45) are of the same family and degree of those used for the approximation of the solution.

### Linearization

We solve the nonlinear problem (2.2.43) by the Newton-Raphson method [5, 23]. The method exploits information from the Jacobian  $J$  of  $\mathcal{M}(\vec{u})$  to achieve the solution of the nonlinear problem:

$$\begin{aligned}
 J_{ij}(\vec{u}_h)\delta u_j &= \lim_{\varepsilon \rightarrow 0} \frac{\mathcal{M}_i(\vec{u}_h + \varepsilon \delta \vec{u}_j) - \mathcal{M}_i(\vec{u}_h)}{\varepsilon} \\
 &= \sum_{q=1}^{n_q} w_q \nabla_0 \vec{\phi}_{i,q} : \frac{\partial \mathbf{P}}{\partial \mathbf{F}}(\mathbf{F}_h(\vec{x}_{0,q})) \left[ \delta u_j \nabla_0 \vec{\phi}_{j,q} \right] \\
 &\quad + \sum_{q=1}^{n_{qBD}} w_{BD,q} \vec{\phi}_{i,q} \cdot \left[ p_v \left[ \left( \mathbf{F}_h^{-T}(\vec{x}_{0,q}) : \delta u_j \nabla_0 \vec{\phi}_{j,q} \right) \mathbf{I} \right. \right. \\
 &\quad \left. \left. - \mathbf{F}_h^{-T}(\vec{x}_{0,q}) \left( \delta u_j \nabla_0 \vec{\phi}_{j,q} \right)^T \right] \mathbf{H}_h(\vec{x}_{0,q}) \vec{N}_0 \right], \quad (2.2.46)
 \end{aligned}$$

where we denote with  $\delta \vec{u}_j = \delta u_k \delta_{k,j}$ ,  $w_q = w(\vec{x}_{0,q})$ ,  $w_{BD,q} = w_{BD}(\vec{x}_{0,q})$  and  $\vec{\phi}_{j,q} = \vec{\phi}_j(\vec{x}_{0,q})$ . The fourth order tensor  $\partial \mathbf{P} / \partial \mathbf{F}$  depends only on the constitutive assumptions of the material and it is symbolically derived by FEniCS [19] from the strain energy density function as

$$\frac{\partial \mathbf{P}}{\partial \mathbf{F}} = \frac{\partial^2 \mathcal{W}}{\partial \mathbf{F} \partial \mathbf{F}}. \quad (2.2.47)$$

Given an initial guess  $\vec{u}_h^0$ , the solution of (2.2.43) is achieved as the limit (should it exist) of the sequence  $\{\vec{u}_h^n\}$ , such that

$$\mathbf{J}(\vec{u}_h^n) \delta \vec{u}_h^{n+1} = \mathcal{M}(\vec{u}_h^n) \quad (2.2.48)$$

$$\vec{u}_h^{n+1} = \vec{u}_h^n - \delta \vec{u}_h^{n+1}. \quad (2.2.49)$$

The Dirichlet boundary condition is enforced algebraically by manipulating the rows of the matrix:

$$J_{jDj} = \delta_{jD,j} \quad \text{for } j = 1, \dots, n, \quad (2.2.50)$$

$$\mathcal{M}_{jD} = \delta \vec{u}_{jD}^n \delta_{n,0}, \quad (2.2.51)$$

being  $j_D$  the index identifying a Dirichlet node and  $\delta\bar{u}_{j_D}$  the value of the boundary condition.

### Time discretization and coupling between mechanics and circulation

The natural boundary condition in problem (2.2.21) is dictated by the blood pressure within the LV cavity. Depending on the state of the valves, this pressure is determined by circulation model (2.2.34). When the aortic valve is open,  $p_{lv}$  is equal to  $p_{ao}$  and the blood can flow from the LV through the aorta, injecting blood in the circulatory system and decreasing the LV cavity volume. Conversely when the mitral valve is open,  $p_{lv}$  equals  $p_{mv}$  and the blood enters the LV from the circulatory system, increasing the LV cavity volume. The result is a coupled mechanics-circulation problem. To solve this problem, we first discretize the circulation model. The algebraic-differential system in (2.2.34) is fully discretized by integrating exactly the last two equations and applying two different numerical schemes to the equations governing the balance of flows for the LV and the arterial node. A Forward Euler scheme is introduced for backward compatibility

$$\left\{ \begin{array}{l} q_p^{(n)} = \frac{p_{art}^{(n)} - p_{ven}^{(n)}}{R_p}, \\ q_{ao}^{(n)} = \chi_{av} \frac{p_{lv}^{(n)} - p_{art}^{(n)}}{Z_a}, \\ q_{mv}^{(n)} = \chi_{mv} \frac{p_{ven}^{(n)} - p_{mv}^{(n)}}{Z_v}, \\ V_{lv}^{(n+1)} = V_{lv}^{(n)} + dt \left( q_{mv}^{(n)} - q_{ao}^{(n)} \right), \\ V_{art}^{(n+1)} = V_{art}^{(n)} + dt \left( q_{ao}^{(n)} - q_p^{(n)} \right), \\ V_{ven}^{(n+1)} = V_{tot} - V_{lv}^{(n+1)} - V_{art}^{(n+1)}, \\ p_{art}^{(n+1)} = \frac{V_{art}^{(n+1)} - V_{art}^{(0)}}{C_a}, \\ p_{ven}^{(n+1)} = \frac{V_{ven}^{(n+1)} - V_{ven}^{(0)}}{C_v}, \end{array} \right. \quad (2.2.52)$$

and an implicit second order Crank-Nicholson scheme

$$\mathbf{A}\vec{x}^{(n+1)} = \vec{b}, \quad (2.2.53)$$

where

$$\mathbf{A} = \begin{bmatrix} 1 & 0 & 0 & 0 & 0 & 0 & \frac{-1}{R_p} & \frac{1}{R_p} \\ 0 & 1 & 0 & 0 & 0 & 0 & \frac{\chi_{av}^*}{Z_a} & 0 \\ 0 & 0 & 1 & 0 & 0 & 0 & 0 & \frac{\chi_{mv}^*}{Z_v} \\ 0 & \frac{dt}{2} \chi_{av}^* & -\frac{dt}{2} \chi_{mv}^* & 1 & 0 & 0 & 0 & 0 \\ \frac{dt}{2} & -\frac{dt}{2} \chi_{av}^* & 0 & 0 & 1 & 0 & 0 & 0 \\ 0 & 0 & 0 & 1 & 1 & 1 & 0 & 0 \\ 0 & 0 & 0 & 0 & \frac{-1}{C_a} & 0 & 1 & 0 \\ 0 & 0 & 0 & 0 & 0 & \frac{-1}{C_v} & 0 & 1 \end{bmatrix}, \quad (2.2.54)$$

$$\vec{x} = \begin{bmatrix} q_p \\ q_{ao} \\ q_{mv} \\ V_{lv} \\ V_{art} \\ V_{ven} \\ p_{art} \\ p_{ven} \end{bmatrix}, \quad \vec{b} = \begin{bmatrix} 0 \\ \frac{p_{lv}}{Z_a} \chi_{av} \\ \frac{-p_{lv}}{Z_v} \chi_{mv} \\ V_{lv}^{(n)} + \frac{dt}{2} \left( q_{mv}^{(n)} \chi_{mv}^{(n)} - q_{av}^{(n)} \chi_{av}^{(n)} \right) \\ V_{art}^{(n)} + \frac{dt}{2} \left( q_{ao}^{(n)} \chi_{av}^{(n)} - q_p^{(n)} \right) \\ V_{tot} \\ -V_{art}^0 \\ -V_{ven}^0 \\ -C_v \end{bmatrix}. \quad (2.2.55)$$

Note that the valves, represented by  $\chi_{av}$  and  $\chi_{mv}$ , introduce nonlinearity in the system; therefore in  $\mathbf{A}$ ,  $\chi_{av}^*$  and  $\chi_{mv}^*$  are treated explicitly but will be updated during the iterative scheme that solves the non linearity.

To solve the nonlinearity, we adopted an iterative approach that requires successive resolutions of both problems, coupled by  $p_{lv,k}^{(n)}$  (cavity pressure at time  $n$  at iteration  $k$ ), until the coupling condition is met. This coupling condition makes sure that the distance between the LV cavity volume computed from the circulation,  $V_{lv,k}^{(n+1)}$

$$V_{lv,k}^{(n+1)} = V_{lv}^{(n)} + \frac{dt}{2} \left( q_{mv}^{(n)} - q_{ao}^{(n)} + q_{mv,k}^{(n+1)} \chi_{mv,k-1}^{(n+1)} - q_{ao,k}^{(n+1)} \chi_{av,k-1}^{(n+1)} \right), \quad (2.2.56)$$

and the one computed using the finite element model of the LV mechanics,  $V_{c,k}$ , is smaller than a predefined tolerance. At iteration  $k$ , given a deformation  $\vec{x}_k$  that takes the undeformed configuration  $\Sigma_0$  to  $\Sigma_k$ , the cavity pressure  $V_{c,k}$

can be computed as follows

$$V_{c,k} = \int_{\Sigma_k} \vec{d}v = \int_{\Sigma_k} \frac{1}{3} \nabla \cdot (\vec{x}_k - \vec{x}_{o,base}) \vec{d}v \quad (2.2.57)$$

$$= \frac{1}{3} \int_{\partial\Sigma_k} (\vec{x}_k - \vec{x}_{o,base}) \vec{n} d\vec{a}, \quad (2.2.58)$$

$$= \frac{1}{3} \int_{\partial\Sigma_0} (\vec{x}_k - \vec{x}_{o,base}) J_k \mathbf{F}_k^{-T} \vec{N}_0 d\vec{A}, \quad (2.2.59)$$

$$= -\frac{1}{3} \int_{\Gamma_0, Endo} (\vec{x}_k - \vec{x}_{o,base}) J_k \mathbf{F}_k^{-T} \vec{N}_0 d\vec{A}, \quad (2.2.60)$$

Note that,  $\Sigma_k$  is assumed to have a planar cap at the base.  $\vec{n}$  is the vector normal to  $\partial\Sigma_k$ , and  $x_{o,base}$  is a reference point on the planar cap at the base. In (2.2.60), we exploited the fact that on the planar cap  $\vec{x}_k - \vec{x}_{o,base}$  is orthogonal to the  $\vec{n}$ .

To drive the mechanics towards the desired  $V_c$ , a fixed-point iterative scheme is used to estimate the cavity pressure  $p_{lv,k}^{n+1}$ . The scheme is the following. At the first iteration, the pressure is extrapolated from the previous time steps:  $p_0^{n+1} = 2p^n - p^{n-1}$ , then

$$p_{k+1}^{n+1} = p_k^{n+1} + \frac{1}{C_{lv,k}^{n+1}} (V_{c,k}^{n+1} - V_{lv,k}^{n+1}), \quad (2.2.61)$$

where the LV compliance  $C_{lv,k}$  is modeled as follows

$$C_{lv,k} = \begin{cases} \frac{V_{c,k}^{n+1}}{p_{lv,k}^{n+1}}, & k = 0, \\ \frac{V_{c,k}^{n+1} - V_{c,k-1}^{n+1}}{p_{lv,k}^{n+1} - p_{lv,k-1}^{n+1}}, & k > 0. \end{cases} \quad (2.2.62)$$

### Strains computation

The computation of strains is performed during post processing. There are a few reasons behind this choice. The first one is that a simulation must store a minimum amount of output that allows to repeat the simulation or restart it from the last saved state in order to minimize disk occupancy. In fact, many derived quantities may be required from different analyses. Consequently, these quantities can be obtained by post processing the output of the simulation. The second reason is that the post-processing problem is a much simpler

one and might benefit from using different numerical techniques together with parallel computing.

During the post processing, the state of the simulated problem is loaded in all/a subset of the available time steps and output quantities can be computed. Typically from a mechanical point of view, we are interested in tissue deformation. In this regard, during post processing we are mostly interested in computing strains. When computing strains in-vivo, different reference configurations for the computation of strains are possible. Commonly, either of end diastolic, end-systolic, or begin ejection configurations are used as reference. Given a reference displacement  $\vec{u}_{Ref}$ , the Green-Lagrange strains at time  $t$  can be computed as follows

$$\mathbf{F}_{Ref} = \mathbf{I} + \nabla_0 \vec{u}_{Ref}(\vec{x}), \quad (2.2.63)$$

$$\mathbf{F}(\vec{x}, t) = \mathbf{I} + \nabla_0 \vec{u}(\vec{x}, t), \quad (2.2.64)$$

$$\mathbf{F}^{Ref \rightarrow t}(\vec{x}) = \mathbf{F}(\vec{x}, t) (\mathbf{F}_{Ref})^{-1}, \quad (2.2.65)$$

$$\mathbf{E}^{Ref \rightarrow t}(\vec{x}) = \frac{1}{2} \left[ \left( \mathbf{F}^{Ref \rightarrow t}(\vec{x}) \right)^T \mathbf{F}^{Ref \rightarrow t}(\vec{x}) - \mathbf{I} \right], \quad (2.2.66)$$

$$\vec{e}_i^{Ref}(\vec{x}) = \frac{\mathbf{F}^{Ref}(\vec{x}) \vec{e}_i(\vec{x})}{\|\mathbf{F}^{Ref}(\vec{x}) \vec{e}_i(\vec{x})\|_2}, \quad (2.2.67)$$

$$E_{kl}^{Ref \rightarrow t}(\vec{x}) = \mathbf{E}^{Ref \rightarrow t}(\vec{x}) \vec{e}_k^{Ref}(\vec{x}) \cdot \vec{e}_l^{Ref}(\vec{x}), \quad (2.2.68)$$

where  $\vec{e}_k$  and  $\vec{e}_l$  are normal unit vectors defined on  $\Omega_0$ . Note that if  $\vec{u}_{Ref} = 0$ , strains are computed using the unloaded configuration as reference, since  $\mathbf{F}_{Ref} = \mathbf{I}$ . The strains are computed projecting expression (2.2.68) using the  $L^2(\Omega_0)$  scalar product onto a scalar finite element space of the same degree of the polynomials used in the computation of the displacement. The strain is obtained by solving the following linear system

$$\mathbf{A} \vec{y} = \vec{b}, \quad (2.2.69)$$

$$A_{ij} = \int_{\Omega_0} \phi_i(\vec{x}) \phi_j(\vec{x}) \, d\vec{x}, \quad (2.2.70)$$

$$b = \int_{\Omega_0} E_{kl}^{Ref \rightarrow t}(\vec{x}) \phi_i(\vec{x}) \, d\vec{x}, \quad (2.2.71)$$

where  $\phi_i$  and  $\phi_j$  are the test and trial functions, respectively. The integrals in (2.2.70) and (2.2.71) are computed using Gaussian quadrature with degree of exactness twice as large as the degree of the polynomials used in the discretization of the displacement.

Once computed, strains can be stored as they are in an HDF5 file format, without loss of information. For visualization instead, strains are stored in an

XDMF file that keeps only vertex values. For this reason, during visualization of strains they might look less smooth than they actually are.

## 2.2.4 Simulations performed

To test whether the code implementation was carried out correctly and to understand what level of approximation of the solution is needed, several experiments are performed.

### Cardiac cycle: the effect of spatial discretization

Concerning the anisotropic active stress mechanics, no known analytical solution is available. We assess the accuracy of the solution numerically. According to (2.2.36), the accuracy of the solution can be improved by increasing the order of the basis functions, if the exact solution is regular enough, or by decreasing the size of the mesh elements. We try both strategies making use of anisotropic meshes in order to speed up computations and we compare the results with a very fine isotropic mesh. In this analysis, beside the mesh implemented in Sepran, three anisotropic meshes are considered: a coarse mesh, MC; a medium mesh, MM; and a reference fine mesh, MF. The four meshes are shown in Figure 2.4. Three finite elements spaces are used for the spatial discretization of the problem. These spaces, defined in (2.2.35), share the same family (Lagrangian) and differ by the degree of the polynomials: linear ( $r=1$ ), quadratic ( $r=2$ ), and cubic ( $r=3$ ). We use the combination of the mesh label and the degree of polynomials used in the spatial discretization to label a simulation. For instance, a cardiac cycle performed using the coarse mesh, MC, with cubic basis functions ( $r=3$ ) is labeled as MC3. An overview of the combinations of mesh resolution and finite element spaces used in the following analyses is provided in Table 2.5.

As output of interest we focus on transmural distributions of end-systolic Green-Lagrange strains using the end-diastolic configuration as reference, since we expect that this choice will lead to strains with maximum magnitude. Eventually, we compare the same quantities of interest obtained with the mesh and the finite element space stemming from the previous analyses to the results of the previous implementation.

A cardiac cycle simulation consist in the resolution of the LV mechanics-circulation coupled problem for every time step of the four phases determined by the state of the valves. These four phases are: the passive filling, the isovolumic contraction, the ejection, and the isovolumic relaxation.

analysis	label		
p-refinement	MC1	MC2	MC3
h-refinement	MC2	MM2	MF2

analysis	label	
comparison with Sepran	MM2	Sepran
integration scheme for active stress	FEdt2	RK4dt8

**Table 2.5:** Simulation labels for the four analyses presented: p-refinement, h-refinement, comparison with Sepran, and active stress discretization scheme. Note that the Sepran label denotes a cardiac cycle performed with iso-parametric quadratic finite elements and a mesh with 108 hexahedral elements. For the integration scheme for active stress, scheme FEdt2 denotes the use of the Forward Euler scheme with time step of 2 ms and RK4dt8 denotes the use of the explicit four stages Runge-Kutta scheme with time-step of 8 ms. In these last two cardiac cycles, the combination MC2 is used.

The passive filling is characterized by the open state of the mitral valve and the close state of the aortic valve. During this phase, the small residual active stress of the previous cardiac cycle vanishes completely and the LV is inflated by the blood flowing through the mitral valve. When the active stress level in the myocardium starts rising again, the LV cavity pressure increases determining the closure of the mitral valve when this pressure reaches the atrial pressure. This moment is referred to as the end diastole.

The isovolumic contraction takes place when both aortic and mitral valve are closed and the active stress level is increasing. The contraction of the myocardium determines a rapid increase of cavity pressure, since blood cannot flow.

When the cavity pressure reaches the aortic pressure, the aortic valve opens allowing the blood to flow through the aorta. This moment is referred to as the beginning of ejection. With the aortic valve open, the LV ejects the blood and the cavity pressure increases until the active stress reaches the maximum before starting to decline. The ejection phase ends when the cavity pressure goes below the aortic pressure again. This moment is referred to as end systole or end ejection.

During the isovolumic relaxation, the active stress decreases and both the aortic and the mitral valve are closed, thus preventing the blood from flowing from and to the LV. The decrease of active stress determines a rapid decrease of cavity pressure. When the cavity pressure falls below the atrial pressure, the mitral valve opens and the passive filling starts again.

**Convergence of strains over p-refinement** Starting from a mesh resolution comparable to that employed by Bovendeerd et al [7] (108 hexahedral elements Figure 2.4a), where the previous implementation of the model was used, we performed cardiac cycle simulations using three different spatial discretizations where the displacement field is approximated by linear ( $r = 1$ , (2.2.37)), quadratic ( $r = 2$ ) and cubic ( $r = 3$ ) basis functions. To generate the mesh used in this analysis, mesh MC, we started from the number of hexahedra of the structured mesh of quadratic hexahedra generated by Sepran. We converted a quadratic hexahedron with 6 linear tetrahedra and we slightly increased the number of circumferential elements in order to achieve a better geometrical approximation of the ellipsoidal shape using linear tetrahedra. For this reason the number of tetrahedra is larger than 6 times the number of hexahedra. The mesh generated with this features has 12 elements in the circumferential direction, 5 elements in the longitudinal direction, and 3 elements in the transmural direction. An additional cardiac cycle simulation is performed for reference. This reference simulation involves the use of a fine isotropic mesh with element size of 2 mm, labeled as MF, and the definition of a finite element space with quadratic basis functions ( $r = 2$  in (2.2.37)). The meshes, MC and MF, used in this analysis are shown in Figure 2.4b and Figure 2.4d, respectively. Figure 2.4 also shows the original quadratic mesh used in the previous Sepran implementation.

We assessed the six end-systolic strain components of the Green-Lagrange strain tensor, following (2.2.69) and (2.2.68), in ellipsoidal coordinates using the end-diastolic configuration as reference. Each cardiac cycle simulation consist in 400 time steps which involves the resolution of the coupled circulation-mechanics problem.

The parameters used in all the simulations are the same employed in [7] and are reported in Table 2.1, Table 2.2, Table 2.3, and Table 2.4.

**Convergence of strains over h-refinement** We repeat the cardiac cycle experiment by increasing the number of elements, while keeping the order and family of finite element employed fixed. Three meshes of linear tetrahedra are considered: 2 anisotropic meshes, MC (Figure 2.4b) and MM (Figure 2.4c); and a very fine isotropic mesh, MF (Figure 2.4d). The simulations were performed using the same set of parameters, the same temporal discretization and the end-systolic strains were computed as in the previous experiment.

**Comparison against previous implementation** Two simulations consisting in 15 cardiac cycles are performed using the new BeatIT package and the



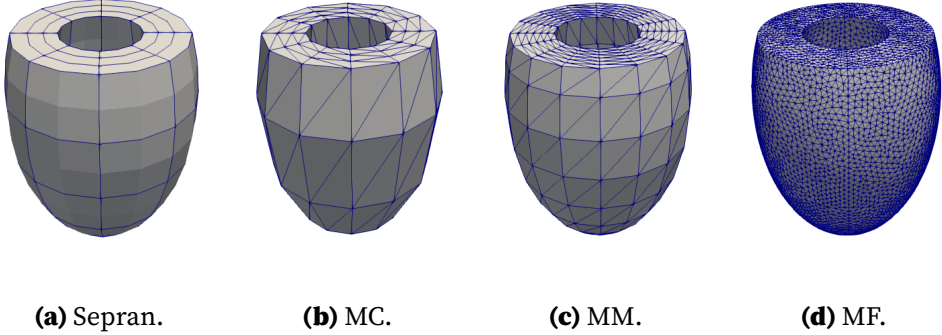


**Figure 2.4:** The meshes used in the verification of the implementation. The first from the left is the mesh of quadratic hexahedra of the previous implementation in Sepran as used in [7] and [17]. The second from the left, MC (972 elements), has 12 circumferential, 5 longitudinal, and 3 transmural elements. The third from the left, MM (5.472 elements) has 16 circumferential, 10 longitudinal, and 6 transmural elements. The last mesh from the left, the reference isotropic mesh MF (68.924 elements), has element size of 2 mm.

previous implementation in Sepran. We considered the last cycle of both simulations as the hemodynamical converged state and we computed end-systolic Green-Lagrange strains using the end-diastolic configuration as reference. The strains are computed using the same approach as before using (2.2.68) and (2.2.69), but along the basis vectors of the cylindrical coordinates:  $\vec{e}_c$  the circumferential direction,  $\vec{e}_z$  the longitudinal direction (constantly along the LV long-axis), and  $\vec{e}_r$  the radial direction. These vectors are defined as follows:

$$r = \sqrt{x^2 + y^2}, \quad \varphi = \begin{cases} \arctan(y/x), & \text{if } x > 0, \\ \pi + \arctan(y/x), & \text{if } x < 0, \\ \frac{y}{|y|} \frac{\pi}{2}, & \text{if } x = 0, \end{cases} \quad (2.2.72)$$

$$\vec{e}_c = \frac{r}{|r|} \begin{bmatrix} -\sin(\varphi) \\ \cos(\varphi) \\ 0 \end{bmatrix}, \quad \vec{e}_z = \begin{bmatrix} 0 \\ 0 \\ 1 \end{bmatrix}, \quad \vec{e}_r = \begin{bmatrix} \sin(\varphi) \\ \cos(\varphi) \\ 0 \end{bmatrix}. \quad (2.2.73)$$

**Cardiac cycle: integration scheme for active stress** To compare the results of the new BeatIT package with the previous Sepran package, we needed to limit differences in the numerical implementation. However, an upgrade in the discretization scheme of (2.2.32) might improve the stability and the accuracy of the computations. In the previous implementation, the ordinary differential equation for the time evolution of the contractile length  $l_c$  used

in the active stress model was discretized using a Forward-Euler scheme. Recalling (2.2.32), the scheme reads

$$l_c^{n+1} = l_c^n + dt [E_a (l_s^{n+1} - l_c^n) - 1] v_0. \quad (2.2.74)$$

This method is linear, single-step, and has linear order of convergence. Moreover, is only conditionally asymptotically stable. In fact, when increasing the time step over 2 ms the simulation fails at the beginning of the isovolumic contraction, which is the beginning of the active stress generation. To overcome this issue, different numerical schemes can be employed. Specifically, a good candidate should be a high order method with a larger region of stability. Explicit Runge-Kutta methods [23] are nonlinear, single step methods whose order of accuracy relates with the number of function evaluations of the scheme. A fourth-order Runge-Kutta method requires the evaluation of the function at four different stages

$$\left\{ \begin{array}{l} K_1 = [E_a (l_s^{n+1} - l_c^n) - 1] v_0, \\ K_2 = \left[ E_a \left( l_s^{n+1} - \left( l_c^n + dt \frac{K_1}{2} \right) \right) - 1 \right] v_0, \\ K_3 = \left[ E_a \left( l_s^{n+1} - \left( l_c^n + dt \frac{K_2}{2} \right) \right) - 1 \right] v_0, \\ K_4 = [E_a (l_s^{n+1} - (l_c^n + dt K_3)) - 1] v_0, \\ l_c^{n+1} = l_c^n + \frac{dt}{6} [K_1 + 2K_2 + 2K_3 + K_4]. \end{array} \right. \quad (2.2.75)$$

Theoretically, the resulting scheme has higher order of accuracy and larger region of stability than the one previously implemented. Potentially, it should allow to solve the problem with a larger time step, still preserving the accuracy. For this reason, a comparison between the two schemes has been carried out. Two cardiac cycle simulations have been performed using mesh MC (Figure 2.4b) and quadratic basis functions. In one simulation, the same scheme of the previous implementation (2.2.74) was adopted using a time step of 2 ms (FEdt2). In another simulation, the Runge-Kutta scheme in (2.2.75) was adopted using a time step of 8 ms (RK4dt8).

## 2.3 Results

The implementation of the models presented in the previous section is tested and validated in several experiments. The results are reported in this section. First, only the circulation is tested and the results are compared with those

obtained from a simulation using the previous implementation. Then, five experiments for the mechanics are presented. In the first experiment, the implementation is validated against the theoretical solution in a simple test case involving only the passive mechanics of an isotropic material. In the second and third experiments, numerical tests to find the optimal values for the mesh resolution and the degree of the polynomial used in the spatial discretization of the problem are carried out. After the comparison of the strains obtained using the old and the new implementations, a new discretization technique for the active stress model is tested against the one implemented in Sepran.

### 2.3.1 Convergence of strains over p-refinement

The number of degrees of freedom for the four considered function spaces are reported in Table 2.6 together with the computational times. The computational times refer to simulations run on a single core on a Intel(R) Core(TM) i7-4710MQ CPU @ 2.50GHz workstation.

Simulation	Quadrature Degree	Dofs	Matrix Assembly	Linear System	Cardiac Cycle
MC1	2	972	0.005 s	0.02 s	1 min 41 s
MC2	2	4.863	0.07 s	0.07 s	5 min 40 s
MC3	4	15.366	0.45 s	0.55 s	35 min 30 s
MF2	2	311.214	5.55 s	48 s	29 h 34 min 16 s

**Table 2.6**

The four simulated cardiac cycles resulted in the pressure volume loops represented in Figure 2.5. Values for the cavity pressure and cavity volume for MC1, MC2, MC3, and MF2 are shown in Table 2.7. Simulation MC1 led to an ejection fraction of 57.4 % larger than those obtained for MC2 and MC3, 52.4 % and 52.0 % respectively. The pressure-volume loops for simulations MC2 and MC3 coincide. The reference simulation, MF2, presents a larger ejection fraction, mostly due to the larger compliance. In this regard, Figure 2.5b shows a detail of the pressure-volume relation during the passive filling. It shows that the compliance of the left ventricular cavity increase with the number of degrees of freedom. Figure 2.5b shows how the geometrical approximation of the domain affects the determination of initial cavity volume, considering that all the meshes are built starting from the same geometry. In fact, the initial cavity volume for MF is exactly 44 mL while for MC is 40.5 mL. This error introduces a shift in the pressure-volume diagram. Moreover, given the same mesh MC, the compliance is affected by the interpolation order. Using

linear interpolation results in a steeper curve while with quadratic and cubic interpolation the two lines have very limited differences. Also mesh resolution affects the computation of cavity volume, since keeping  $r = 2$  and using MC and MF leads to slightly different curves even after compensating for the error on the initial cavity volume.

	MC1	MC2	MC3	MF2
$V_{c,0}$	41.32 mL	40.51 mL	40.51 mL	44.77 mL
$V_{c,ED}$	92.82 mL	99.00 mL	99.80 mL	108.3 mL
$p_{lv,max}$	16.87 kPa	16.21 kPa	16.15 kPa	17.31 kPa

**Table 2.7:** Convergence of strains over p-refinement. Unloaded cavity volume,  $V_{c,0}$ , end-diastolic cavity volume,  $V_{c,ED}$ , and peak cavity pressure,  $p_{lv,max}$ , for simulations MC1, MC2, MC3, and MF2.

The transmural distributions of the six components of the end-systolic Green-Lagrange strain tensor are shown in Figure 2.9. The strain components are interpolated on a transmural line at mid-ventricle ( $z = -15$  mm, 39 mm below the base, having the LV a long-axis of 78 mm, shown in Figure 2.9). The average error with the reference along the line in 1-norm normalized using the infinity-norm (the maximum of the absolute value across the nodes) for each strain component for the three cases is reported in Table 2.8.  $E_{cc}$ ,  $E_{ll}$ , and  $E_{cl}$  in models MC1, MC2 and MC3 with the coarse mesh present little deviations from model MF2 with the fine mesh. For  $E_{tt}$ ,  $E_{ct}$  and  $E_{lt}$ , only MC2 and MC3 achieve a qualitative good prediction. Note in particular that the best prediction is achieved for  $E_{tt}$  with quadratic interpolation. Instead, for  $E_{ct}$  and for  $E_{lt}$ , the improvement in the prediction when using cubic interpolation is mostly due to a better fit in the sub-epicardial region.

	MC1	MC2	MC3
$E_{cc}$	4 %	6 %	13 %
$E_{ll}$	19 %	13 %	21 %
$E_{tt}$	23 %	10 %	14 %
$E_{cl}$	19 %	16 %	20 %
$E_{ct}$	47 %	16 %	9 %
$E_{lt}$	24 %	14 %	8 %

**Table 2.8:** Convergence of strains over p-refinement. Average 1-norm of the error with MF2 along the transmural line normalized with the infinity-norm in MF2:  $\|E_{cc}\|_{\infty} = 0.28$ ,  $\|E_{ll}\|_{\infty} = 0.23$ ,  $\|E_{tt}\|_{\infty} = 0.87$ ,  $\|E_{cl}\|_{\infty} = 0.14$ ,  $\|E_{ct}\|_{\infty} = 0.37$ ,  $\|E_{lt}\|_{\infty} = 0.27$ .

### 2.3.2 Convergence of strains over h-refinement

The number of degrees of freedom for the three considered function spaces are reported in Table 2.9 together with the computational times. The computational times refer to simulations run in serial on a Intel(R) Core(TM) i7-4710MQ CPU @ 2.50GHz workstation. In Figure 2.6 the pressure-volume loops

Simulation	Dofs	Matrix Assembly	Linear System	Cardiac Cycle
MC2 (Figure 2.4b)	4.863	0.07 s	0.07 s	5 min 40 s
MM2 (Figure 2.4c)	24.516	0.4 s	1.2 s	50 min 10 s
MF2 (Figure 2.4d)	311.214	5.55 s	48 s	29 h 34 min 16 s

**Table 2.9:** Problem sizes and computational times using the three listed meshes using quadratic interpolation and quadrature with degree of exactness of 2.

of the three simulation are shown. All the three simulations achieved a similar end-systolic cavity volume of about 46 mL. The main differences are in the three end-diastolic cavity volumes: 99 mL, 105 mL, and 108 mL for MC2, MM2, and MF2, respectively. This difference is larger than the error in the initial cavity volume induced by the discretization with linear tetrahedra. In fact MC2 and MM2 have a reduced cavity volume of 41 mL and 43 mL compared to the exact cavity volume of 44 mL. Values for cavity pressure and cavity volume are shown in Table 2.10. The difference in cavity volumes increases during the passive filling, as an improvement in mesh resolution results in a more compliant LV, as can be observed from Figure 2.6b. From the differences in end-diastolic cavity volume also follow slightly different peak pressures, with the coarsest mesh having the smallest (16.21 kPa) and the finest mesh having the largest peak pressure (17.31 kPa).

	MC2	MM2	MF2
$V_{c,0}$	40.51 mL	43.06 mL	44.77 mL
$V_{c,ED}$	99.00 mL	105.2 mL	108.3 mL
$p_{lv,max}$	16.21 kPa	16.88 kPa	17.31 kPa

**Table 2.10:** Convergence of strains over h-refinement. Unloaded cavity volume,  $V_{c,0}$ , end-diastolic cavity volume,  $V_{c,ED}$ , and peak cavity pressure,  $p_{lv,max}$ , for simulations MC2, MM2, and MF2.

Figure 2.10 shows the six independent components of the end-systolic Green-Lagrange strain tensor. In all three cases, there is an agreement in the transmural trend of the three lines. Among the two anisotropic meshes, the results

in MC2 are the furthest from the reference simulation, MF2. The average error with the MF2 along the line in 1-norm normalized using the infinity-norm for each strain component for the three cases is reported in Table 2.11. The average 1-norm of the difference with MF2 for MC2 is at least twice as large as that obtained using MM2. Moreover, the prediction obtained using MM2 is spatially more consistent with those obtained with MF2. In this respect, as an example, in Figure 2.11 we show the transmural distribution of  $E_{ll}$ ,  $E_{ct}$ , and  $E_{lt}$  near the base ( $z = 20$  mm) and the apex ( $z = -35$  mm). The transmural trend of strains predicted in MM2 matches best those obtained in MF2, while MC2 has the largest offset. In fact, the average 1-norm error with MF2 for MC2 is about twice as large than that of MM2 for all the strain components along all the three lines (see Table 2.10). The only exception is  $E_{tt}$  at the apex, which has similar error for MC2 (29 %) and MM2 (34 %) due to much lower values assumed by  $E_{tt}$  in MF2 at the epicardium (not shown).

	base		mid-ventricle		apex	
	MC2	MM2	MC2	MM2	MC2	MM2
$E_{cc}$	7 %	2 %	6 %	1 %	4 %	1 %
$E_{ll}$	53 %	4 %	13 %	3 %	9 %	1 %
$E_{tt}$	12 %	4 %	10 %	5 %	29 %	34 %
$E_{cl}$	33 %	6 %	16 %	7 %	30 %	13 %
$E_{ct}$	24 %	4 %	16 %	7 %	19 %	11 %
$E_{lt}$	29 %	8 %	14 %	7 %	13 %	8 %

**Table 2.11:** Convergence of strains over h-refinement. Average 1-norm of the error with MF2 along the basal, mid-ventricular, and apical transmural lines normalized with the infinity-norm in MF2:  $\|E_{cc}\|_{\infty} = 0.28$ ,  $\|E_{ll}\|_{\infty} = 0.23$ ,  $\|E_{tt}\|_{\infty} = 0.87$ ,  $\|E_{cl}\|_{\infty} = 0.14$ ,  $\|E_{ct}\|_{\infty} = 0.37$ ,  $\|E_{lt}\|_{\infty} = 0.27$ .

### 2.3.3 Comparison against Sepran implementation

Figure 2.7a shows the pressure-volume diagrams of the last cycle of the two simulations: Sepran and MM2. The sepran and BeatIT implementations yielded end-diastolic cavity volumes of 101 mL and 98 mL, end-systolic cavity volume of 38 mL and 37 mL, and ejection fractions of 62 % and 63 %, respectively. The BeatIT simulation achieved a converged end-diastolic cavity volume of about 98 mL and an end-systolic cavity volume of about 37 mL, leading to an ejection fraction of about 63%. The two main differences reside in the slightly higher peak pressure reached by the BeatIT implementation and the slightly lower passive stiffness during the filling phase of the Sepran implementation

(Figure 2.7b).

In Figure 2.12 are shown the six independent end-systolic Green-Lagrange strain components using the end-diastolic configuration as reference. The strains refer to the last cycle of both simulations where we reached a converged hemodynamic state, thus limiting potential effects of different initialization of the hemodynamics. Visually from Figure 2.12, the best agreement is achieved for  $E_{cc}$ ,  $E_{zz}$ ,  $E_{rr}$ , and  $E_{cz}$ , while  $E_{cr}$ ,  $E_{zr}$  present only a similar transmural distribution but the two lines deviate from each other. For  $E_{zr}$  the main difference occurs in the sub-endocardium, while for  $E_{cr}$  the deviation between the two lines is larger. The average 1-norm of the difference of the two lines is: 0.007 for  $E_{cc}$ , 0.009 for  $E_{zz}$ , 0.062 for  $E_{rr}$ , 0.013 for  $E_{cz}$ , 0.074 for  $E_{cr}$ , 0.063 for  $E_{zr}$ . The same values normalized with the infinity-norm of the respective strain computed in MM2 are: 2.6 % for  $E_{cc}$ , 3.4 % for  $E_{zz}$ , 5.8 % for  $E_{rr}$ , 12 % for  $E_{cz}$ , 26 % for  $E_{cr}$ , 21 % for  $E_{zr}$ .

### 2.3.4 Active stress time integration scheme

The active stress model relies on the solution of an Ordinary Differential Equation (ODE) that describes the time evolution of the length of the contractile element of the fiber model. In Sepran, this ODE is discretized using the first order Forward Euler method. In BeatIT, we discretize the same ODE using a four-stages explicit Runge-Kutta of order 4. The higher order of the Runge-Kutta scheme allows to obtain the same accuracy with a larger discretization step, thus leading to a performance improvement. The results in terms of pressure-volume loop and in terms of end-systolic strains are shown in Figure 2.8 and Figure 2.13, respectively. From Figure 2.8 can be noticed that the two curves overlap for most of the cycle with only a small deviation at begin ejection, when the aortic valve opens. In terms of tissue deformation, instead, no noticeable differences can be seen from Figure 2.13.

The use of the four-stages Runge-Kutta scheme allows a fourfold increase of the time discretization step and preserves the accuracy of the predictions of strains, thus allowing to achieve a speedup of about four times for a cardiac cycle simulation.

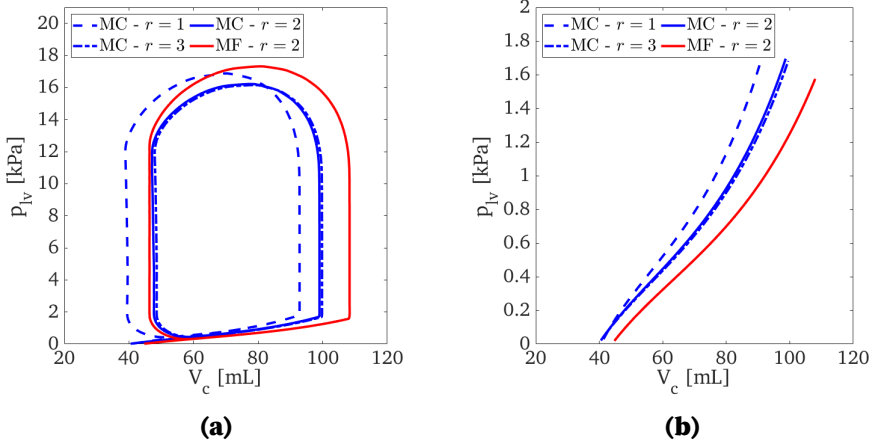


**Figure 2.5:** Convergence of strains over p-refinement. Pressure-volume diagram of the simulated cardiac cycles. On the left is shown pressure-volume loop of the full cardiac cycle while on the right is shown the pressure-volume relation during passive filling. The blue lines represents the simulation on mesh MC (Figure 2.4b) using linear (dashed), quadratic (solid), and cubic (dash-dotted) Lagrangian basis functions. The red line represents the simulation on the isotropic reference mesh (Figure 2.4d).

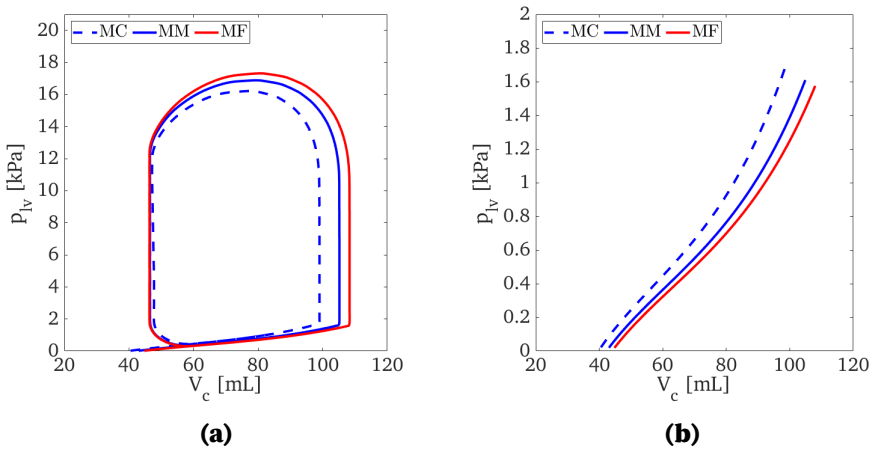


**Figure 2.6:** Convergence of strains over h-refinement. Pressure-volume diagram of the simulated cardiac cycles. On the left is shown pressure-volume loop of the full cardiac cycle while on the right is shown the pressure-volume relation during passive filling. The blue lines represent the simulations on mesh MC (dashed, Figure 2.4b) and MF (solid, Figure 2.4b). The red solid line represents the simulation on the isotropic reference mesh (Figure 2.4d). All the simulations were performed using quadratic interpolation.



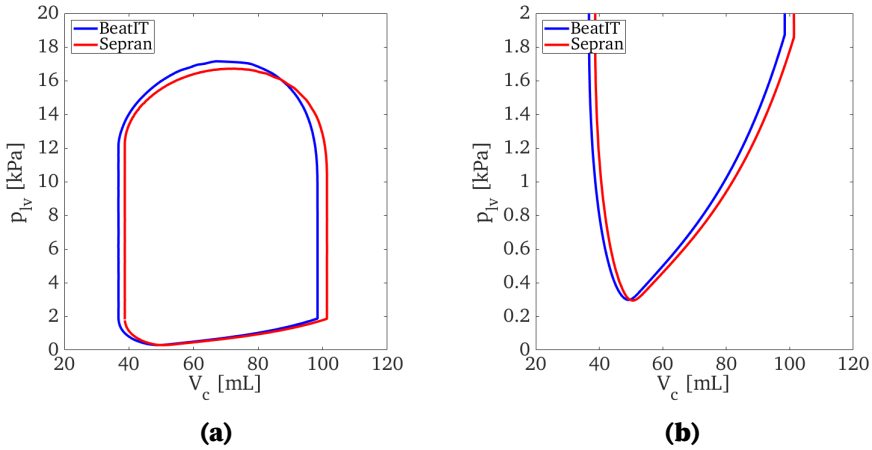


**Figure 2.7:** Comparison against Sepran implementation. Pressure-volume diagram of the simulated cardiac cycles. On the left is shown pressure-volume loop of the full cardiac cycle while on the right is shown the pressure-volume relation during passive filling. The blue line represents the simulation on mesh MM (Figure 2.4c) using affine finite elements with quadratic Lagrangian basis functions on tetrahedra. The red solid line represent the simulation performed in Sepran using the mesh in Figure 2.4a using isoparametric finite elements with quadratic interpolation on hexahedra.

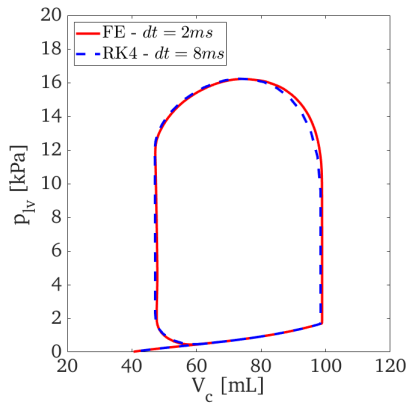


**Figure 2.8:** Active stress time integration scheme. Pressure-volume diagram of the simulated cardiac cycles. The blue dashed line represents the simulation on mesh MC (Figure 2.4c) using quadratic Lagrangian basis functions for the spatial discretization and fourth-order explicit Runge-Kutta discretization for the active stress model (2.2.32) (RK4dt8). The red solid line represents the simulation using the same mesh and same spatial discretization, but different temporal discretization using the Forward-Euler scheme (FE dt2).

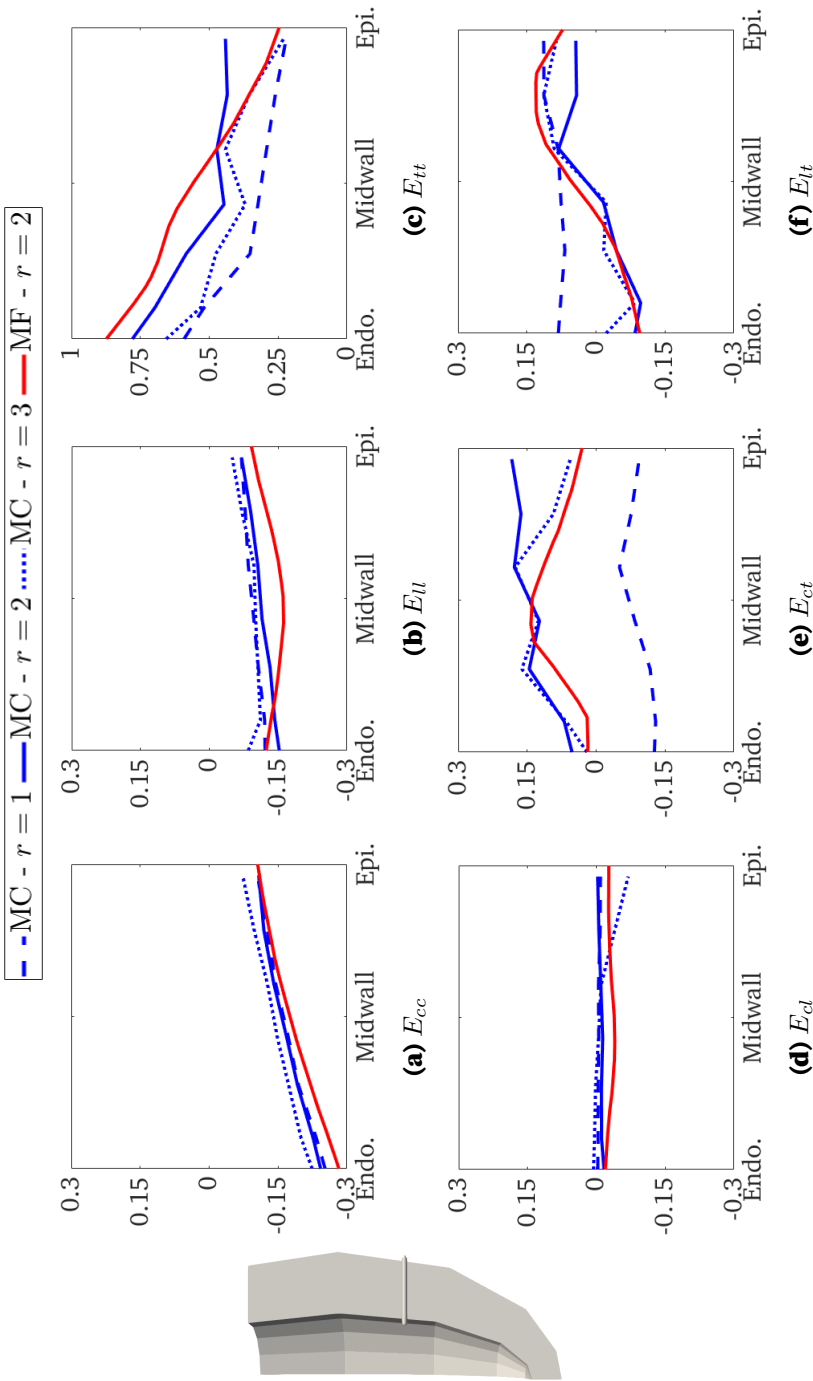


**Figure 2.9:** Convergence of strains over p-refinement. Transmural distribution of the end-systolic Green-Lagrange strain components in ellipsoidal coordinates using the end-diastolic configuration as reference. The blue lines represent the simulation on mesh MC (Figure 2.4b) using linear (dashed), quadratic (solid), and cubic (dash-dotted) Lagrangian basis functions. The red line represents the simulation on the isotropic reference mesh (Figure 2.4d). The strain components are interpolated on a transmural line at mid-ventricle. In the top row there are the three normal strains: the circumferential strain ( $E_{cc}$ ), the longitudinal strain ( $E_{ll}$ ), and the transmural strain ( $E_{tt}$ ). In the bottom row there are the three shear strains: the circumferential-longitudinal strain ( $E_{cl}$ ), the circumferential-transmural strain ( $E_{ct}$ ), the longitudinal-transmural strain ( $E_{lt}$ ).

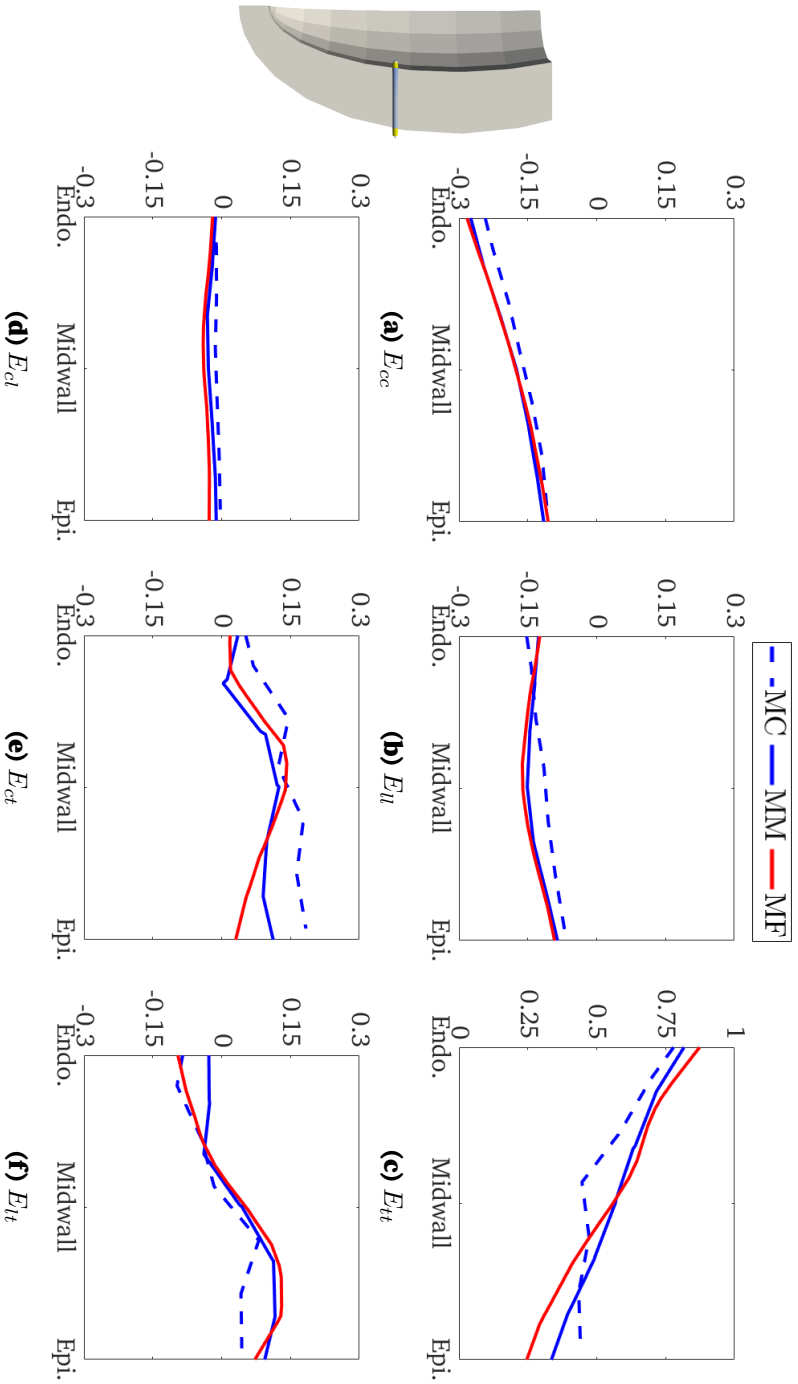


**Figure 2.10:** Convergence of strains over h-refinement. Transmural distribution of the end-systolic Green-Lagrange strain components in ellipsoidal coordinates using the end-diastolic configuration as reference. The strain components are interpolated on a transmural line at mid-ventricle. The blue dashed line represents the simulation on MC (Figure 2.4b), the blue solid line represents the simulation on MM (Figure 2.4c), and the red solid line represents the simulation on MF (Figure 2.4d). In all the simulations quadratic Lagrangian basis functions were used in the discretization. In the top row there are the three normal strains: the circumferential strain ( $E_{cc}$ ), the longitudinal strain ( $E_{ll}$ ), and the transmural strain ( $E_{tt}$ ). In the bottom row there are the three shear strains: the circumferential-longitudinal strain ( $E_{cl}$ ), the circumferential-transmural strain ( $E_{ct}$ ), the longitudinal-transmural strain ( $E_{lt}$ ).

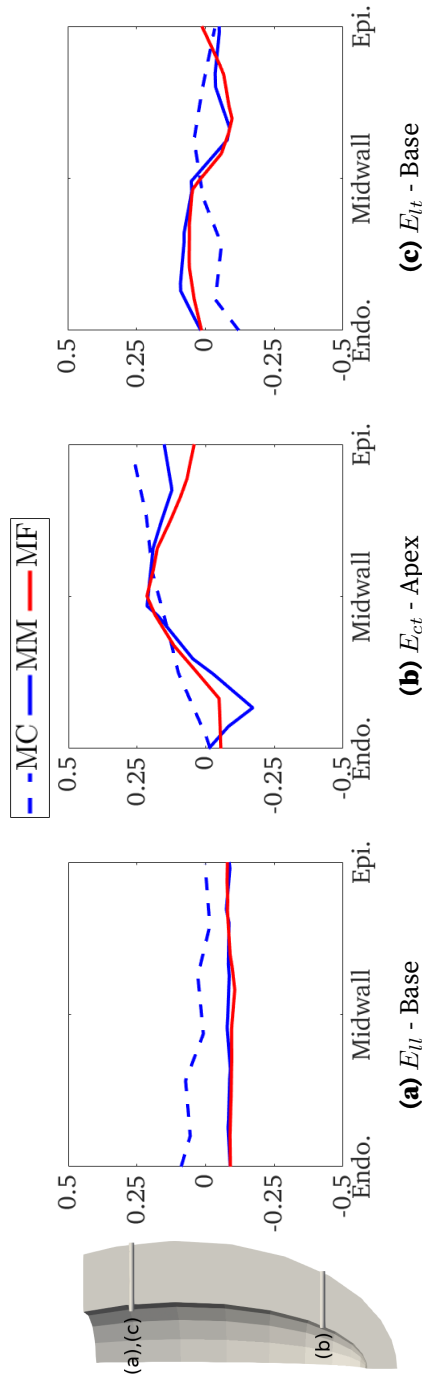


**Figure 2.11:** Convergence of strains over h-refinement. Transmural distribution of the end-systolic Green-Lagrange strain components in ellipsoidal coordinates using the end-diastolic configuration as reference. The blue dashed line represents the simulation on mesh MC (Figure 2.4b), the blue solid line represents the simulation on mesh MM (Figure 2.4c), and the red solid line represents the simulation on the isotropic reference mesh (Figure 2.4d). In all the simulations quadratic Lagrangian basis functions were used in the discretization. On the left there is the longitudinal strain ( $E_{ll}$ ) near the base, in the center the circumferential-transmural shear strain ( $E_{ct}$ ) near the apex, and on the right the longitudinal-transmural shear strain ( $E_{it}$ ) near the base.

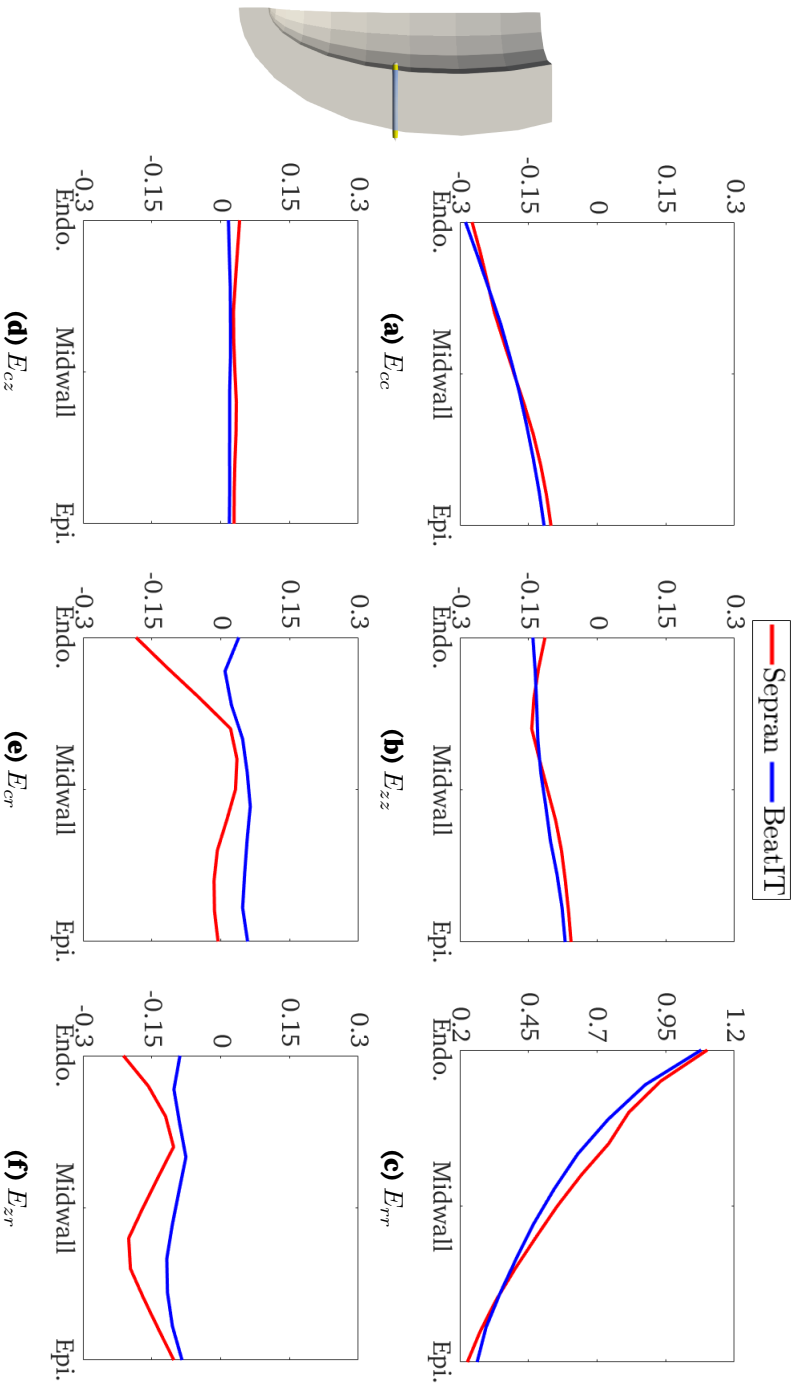


**Figure 2.12:** Comparison against Sepran implementation. Transmurial distribution at mid-ventricle of end-systolic Green-Lagrange strains using as reference the end-diastolic configuration. The results refer to the last simulated cycle where the hemodynamics reached a steady states in both simulations. The blue solid line shows the results performed using the new package BeatIT with mesh MM (Figure 2.4c) and affine finite elements with quadratic Lagrangian basis functions on tetrahedra (MM2), the red line shows the results performed using the previous implementation in Sepran using mesh Figure 2.4a and isoparametric finite elements with quadratic basis functions on hexahedra.

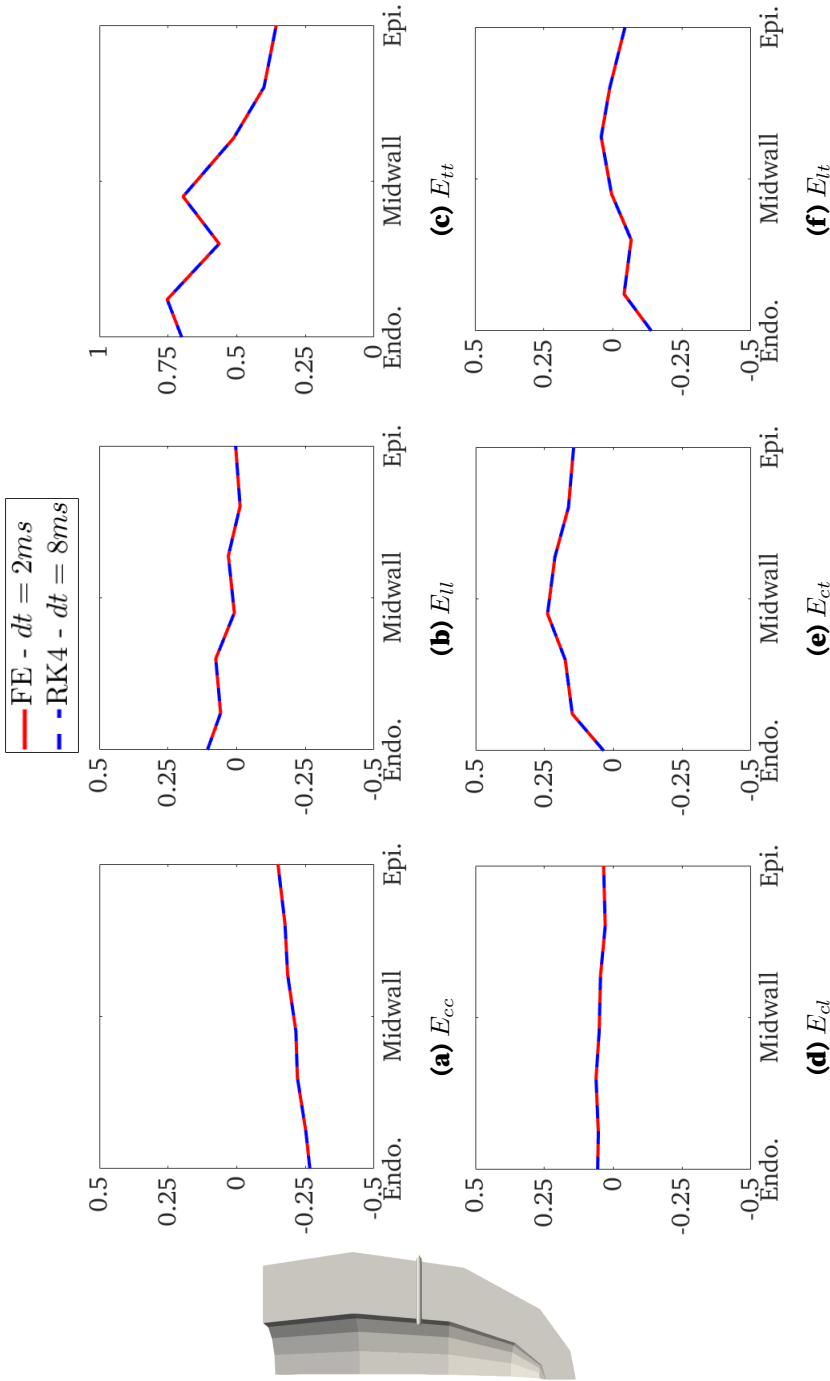


**Figure 2.13:** Active stress time integration scheme. Transmurial distribution of the end-systolic Green-Lagrange strains in ellipsoidal coordinates using the end-diastolic configuration as reference. The blue dashed line represents the simulation on mesh MC (Figure 2.4c) using quadratic Lagrangian basis functions for the spatial discretization and fourth-order explicit Runge-Kutta discretization for the active stress model (2.2.32) (RK4dt8). The red solid line represents the simulation using the same mesh and same spatial discretization, but different temporal discretization using the Forward-Euler scheme (FEdt2).

## 2.4 Discussion

We developed a finite element package using an open source library. The development was relatively quick thanks to the python interface of the FEniCS library. The BeatIT package has been conceived in a modular way so that the coupled solver for the mechanics-circulation problem can be split in two detached solvers or a bi-ventricular solver can be easily created by extending the LV solver. The new package has several numerical tools made available by PETSc [3], ranging from iterative solvers to many type of algebraic preconditioners.

We assessed the outcome of the implementation using the analytical solution available for a simplified test case and results coming from the previous implementation. We also assessed numerically the quality of the prediction of strains by varying the order of the finite element space and the mesh resolution.

We validated the new implementation using an analytical solution for the problem of passive filling of a thick-walled isotropic sphere. The analytical and the numerical solutions are in excellent agreement (see 2.B). This result validates the implementation of the passive isotropic mechanics. Instead, no theoretical validation is possible for the anisotropic active mechanics. In this respect, we resort to numerical assessments and comparison with previous results. The actual phenomenon that we want to simulate includes the coupling of the mechanics with the circulation model. Thanks to the modularity of the BeatIT implementation, the circulation model could be detached from the coupled solver and could be tested aside. The hemodynamics of the circulation model shows an excellent agreement Figure 2.14. In fact, by inserting cavity pressure and cavity volume coming from the mechanics simulated in Sepran and comparing the resulting hemodynamics in the two implementations, no differences emerged.

To assess the quality of predictions and to prove some sort of numerical convergence of the solution, we checked the influence of numerical discretization on transmural distribution of end-systolic Green-Lagrange strains. Since no analytical solution is available for the problem, we generated a numerical solution approaching the limit of our computational capabilities. This approximation relies on quadratic finite elements and the isotropic mesh MF (Figure 2.4d). The goal was to find the optimum balance between the accuracy of the predicted strains and the computational cost of a cardiac cycle. We first analyzed the order of the finite elements basis functions starting from a mesh comparable with that used in Sepran (Figure 2.4a). This analysis showed that quadratic finite elements led to a reduction of 31 % of the largest strain error

with a fourfold increase of the computational cost as compared to linear elements. Increasing further the order of polynomials to three only decreased the strain error of about 7 % for two out of six strain components, with a sevenfold increase of the computational cost. Therefore, we found an optimal balance between geometrical approximation and functional approximation by discretizing the problem using quadratic continuous Lagrangian basis functions (Figure 2.9). This is because, keeping fixed the number of degrees of freedom, in an affine finite element approach the geometrical approximation of curved domains is larger with higher order finite elements. This geometrical approximation error affects the computation of the cavity volume and consequently also the steady state solution of the coupled circulation-mechanics problem. On the other hand, the quality of prediction of strains with linear finite elements is rather poor, especially for  $E_{tt}$ ,  $E_{ct}$ , and  $E_{lt}$  (Figure 2.10).

We then tuned the mesh resolution keeping the same finite element space. Using the resulting quadratic continuous Lagrangian finite elements, we qualitatively checked the transmural distribution of end-systolic strains at base, mid-ventricle, and apex when refining the mesh. We found a deviation between MM2 and MF2 of less than 8 % at basal and mid-ventricular level for all the strain components and a deviation of less than 13 % at apex for five out of six strain components, with the only exception  $E_{tt}$  deviating by 35 %. The deviation between MC2 and MF2 is at least twofold larger than that of MM2 for all the strains and all the three locations except for  $E_{tt}$  at apex which is comparable. The strains obtained using the anisotropic mesh MM are comparable with those predicted using our reference isotropic mesh MF (Figure 2.10), but the computational cost of using mesh MM is much smaller (about 36 times). Beside the results shown in this document, we also tested other meshes in the neighborhood of the resolution of mesh MM and we did not find fundamental variations. We concluded that, even though mesh MM is computationally not the cheapest mesh among those considered, it gives robust estimations in view of the mesh morphing operation that will be considered in the model personalization process.

We compared the end-systolic Green-Lagrange predicted by the BeatIT package with a dataset of strain predicted by Sepran. The dataset included strains in cylindrical coordinates. We found a deviation of less than 6 %, which we consider very good, for the normal strains. While a larger deviation is found for shear strains, with the largest difference for  $E_{cr}$  (26 %). There might be several reasons behind this deviation. We investigated four possible causes. Although the models implemented in BeatIT show numerical convergence, there might be implementation issues that hinder the adherence to the mathematical model. We do not know whether this error resides in the new or in



the old implementation. The only non validated parts are the anisotropic mechanics and the active stress implementations. First, concerning anisotropic mechanics, we compared nodal values of fiber orientation with those generated by previous implementation revealing no meaningful differences (the magnitude of the maximum difference was below 0.01 %). Moreover, fibers are defined differently in the two implementations: in Sepran, the fiber vector is defined at quadrature node; in BeatIT, it is defined at mesh nodes and then interpolated on quadrature nodes. In BeatIT, the two approaches were compared and no meaningful differences emerged (not shown in this document). Second, we realized that the active stress model is rather sensitive to its numerical implementation. For instance, the peak pressure is affected by the mesh resolution and by the choice of finite elements. Although the differences in ejection fraction are quite limited (about 1.5 %), this difference might be induced by a deviation of the spatial distribution of the active stress, thus leading to a difference in the prediction of strains. We could not assess the effects on the active stress generation of mesh refinement in Sepran, since implementation issues prevented the generation of finer meshes, especially in the longitudinal direction. Instead, from the BeatIT side, we assessed numerically the quality of strain predictions and we found good agreement with our reference solution. Third, in the comparison other implementation details might have played a role in determining the differences emerged. In particular, the computation of cavity volume and the computation of strains were carried out differently. In the Sepran package, the cavity was meshed extruding endocardial surface element into tetrahedra having the vertex in the center of the basal plane. In the BeatIT package this method is substituted with formula (2.2.60), which is easier to implement and independent from the problem discretization. The two methods have a different approximation error that might affect the pressure-volume loops. This difference might modify the steady state equilibrium of the circulation-mechanics coupled problem, thus leading to comparison at end-systolic configurations having slightly different cavity pressures. Fourth, in the new implementation strains are computed by projecting the strain expression onto the same finite element space used to compute the displacement field (coherently made scalar). In the previous implementation, the nodal values of the deformation gradient were multiplied accordingly with the nodal values of the basis vectors of the coordinates system to compute the node-wise expression of the strains. In this respect, it is curious that this issue would mainly affect  $E_{cr}$  and  $E_{zr}$ . For the sake of time, we did not investigate further into these differences. Instead, we accepted the new implementation to be a good numerical approximation of the problem. Given the good qualitative agreement between the results obtained with the

two implementations, we consider the new implementation mature enough to be employed in this research project.

Performance-wise, the two implementations are similar. When using the mesh generated in Sepran (Figure 2.4a) and MC2 (Figure 2.4b), both the implementations achieved a cardiac cycle in approximately 5 min, although in the BeatIT simulation the number of degrees of freedom was larger (3213 for Sepran, 4.863 for BeatIT). We could not compare the performances with finer meshes with the previous implementation, because of implementation issues in the Sepran model that prevented the simulation from running.

Performance can be further improved by using the fourth order Runge-Kutta scheme for the discretization of the ordinary differential equation involved in the active stress formulation (2.2.32). This scheme is of fourth order, meaning that with the same time step the approximation error is proportional to the fourth power of the time step, thus leading to a much smaller approximation error as compared to the first order Forward-Euler implemented in Sepran. For this reason and because of the larger stability region of the fourth order Runge-Kutta scheme, increasing the time step of the problem allows to preserve the accuracy of the solution. As opposed to Sepran, where larger time steps led to divergence, this scheme allowed the increase of the time step from 2 ms to 8 ms obtaining the same strain prediction (Figure 2.13), thus impacting the overall simulation time by a factor of 4. A downside of this approach occurs at the aortic valve opening where a small deviation in the pressure volume loop can be noticed (Figure 2.8), due to the larger time step. We only tested the four-stages Runge-Kutta scheme with homogeneous activation. It is still to be proven whether a larger time discretization step could be used when considering asynchronous activation. As a future improvement, an adaptive approach for the selection of the time discretization step should be considered.

The simulation of a cardiac cycle using mesh MM and quadratic Lagrangian basis functions takes approximately 50 min. We tried to improve the performances by using parallel computing. The time employed in the stiffness matrix assembly scaled linearly with the number of cores, but the time required for the resolution of the linear system did not scale as nicely. In fact, the MUMPS direct solver in parallel worsened the performance, most likely due to the communication overhead involved in the multiplicative matrix decomposition performed in parallel. Nonetheless, the MUMPS direct solver resulted to be the fastest solver available in PETSc through from the FEniCS interface. We also tried to use iterative solvers. None of the combinations of available iterative solvers/algebraic preconditioners converged to a solution, with the exception of the combination of a biconjugate gradient stabi-

lized method combined with the Hypr BoomerAMG preconditioner (parallel multi-grid factorization) [18]. This combination applied to the reference problem (isotropic mesh MF with 68.924 elements, 311.214 dofs, quadratic Lagrangian basis functions), where the advantages of using an iterative solver should be more evident, led to the resolution of the linear system in 90 s using 4 core, which is still 50% slower than MUMPS on a single core. To understand this behavior, we estimated the condition number of the stiffness matrix using a singular value decomposition on a coarser isotropic mesh and we realized that the condition number of the matrix is very high, thus affecting the number of iterations needed by an iterative solver to converge. The reasons behind this behavior are beyond the scope of this thesis; however, we name some possible causes to be addressed in the future. The tissue stiffness along fiber direction largely varies in time, due to the activation of myocytes, and in space, due to the spatially varying fiber distribution. This large variability might affect the overall condition number of the stiffness matrix. The combination of strong anisotropy and nearly-incompressibility might as well affect the condition number of the problem [13]. In this regard, the use of an active strain based model [25, 1, 4] might alleviate the issue, since it allows to introduce incompressible active deformations during the activation of myocytes. Lastly, also the choice of the boundary conditions might affect the problem. Especially the stress-free condition at epicardium.

## 2.5 Conclusion

We successfully implemented the new BeatIT package for the finite element approximation of the mechanics of the LV. The package relies on the python interface of the FEniCS library and high performances are granted by its C++ back-end. Thanks to the interface between PETSc and FEniCS, distributed linear algebra is available, thus enabling parallel computing. However, at the current stage of the model parallel computing does not improve performance. In general, the new implementation is more robust with respect to the choice of the compiler and relies on open source compilers. The new implementation is also more robust in the sense that runs simulation that failed in the previous implementations. This robustness allowed to perform several numerical assessments on the implementation. From those assessments, we recommend the use of an anisotropic mesh with 16 circumferential elements, 10 longitudinal elements, and 6 transmural elements and the use of continuous quadratic Lagrangian finite elements for the approximation of the displacement. Using this discretization the computational time for a cardiac cycle is

about 50 min and error in strains is typically below 8 %. The use of the explicit Runge-Kutta scheme for the ODE of the active stress model allows to speed up computations by a factor of 4.

## **Appendix**

### **2.A Detached circulation simulation**

The close loop circulation model presented in 2.2.3 has already been tested using the previous implementation. We need to assess that the results of the new implementation match with the previous one. To do so, we coupled the new implementation of the circulation model with the LV cavity volume and cavity pressure of a reference simulation performed with the previous implementation. In Sepran, we performed several cardiac cycles allowing to achieve an hemodynamical steady state of the solution. From this solution, the LV pressure and the cavity volume were extracted and introduced as input in a simulation of the circulation using the new implementation of the circulation model. We then compared the two results in terms of arterial and venous pressures and arterial, venous, and peripheral flows.

The comparison of aortic and venous pressures, and aortic, venous and peripheral flows are reported in Figure 2.14. The two results match very well with a maximum relative error on both pressures and flows of  $5 \times 10^{-3}$ , mostly due to discrepancies at valves change of state, where the curves tend to be steeper.

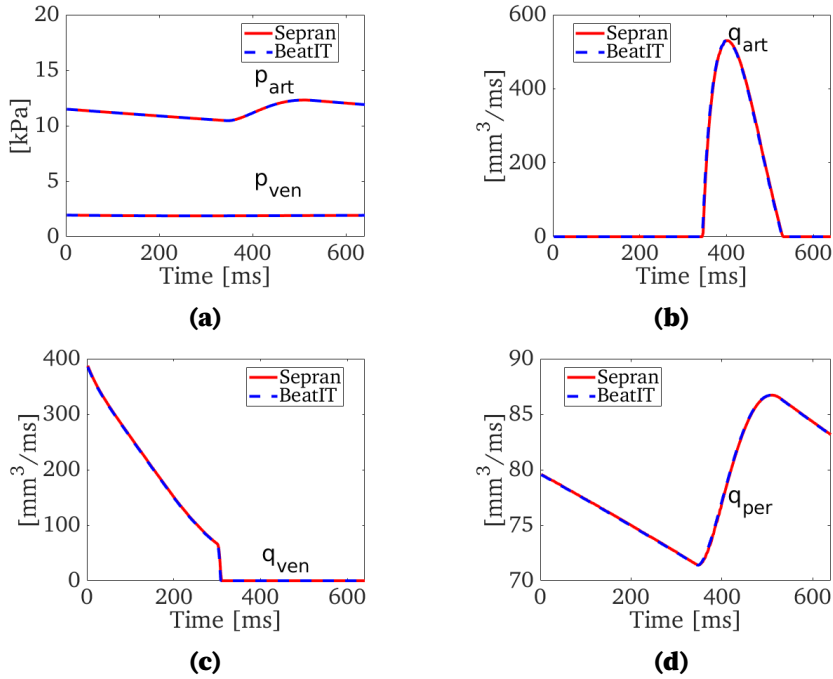


**Figure 2.14:** Comparison of pressures and flows of the circulation model using the new BeatIT implementation and the old Sepran implementation.

## 2.B Inflation of a thick-walled sphere

We assess the correct implementation of the isotropic passive mechanics by testing the result of a simulation performed with the new BeatIT package against the analytical solution of the inflation of a thick-walled sphere. To test our implementation of the mechanics, we check the numerical solution of the inflation of a sphere against the known analytical solution (see 5.2.2 in [21]).

The problem is the following. Given a sphere in spherical polar coordinates:

$$A \leq R \leq B, \quad 0 \leq \Theta \leq \pi, \quad 0 \leq \Phi \leq 2\pi, \quad (2.B.1)$$

under the following deformation

$$r = (R^3 + a^3 - A^3)^{1/3} = Rf(R), \text{ with } f(R) = \left(1 + \frac{a^3 - A^3}{R^3}\right)^{1/3} = \lambda \quad (2.B.2)$$

$$\theta = \Theta, \quad (2.B.3)$$

$$\phi = \Phi, \quad (2.B.4)$$

where  $a$  is the inner radius of the deformed configuration, with deformation gradient

$$\mathbf{F} = (f(R) + Rf'(R)) \vec{e}_r \otimes \vec{E}^R + f(R) (\vec{e}_\theta \otimes \vec{E}^\Theta + \vec{e}_\phi \otimes \vec{E}^\Phi) \quad (2.B.5)$$

$$= \frac{1}{f(R)^2} \vec{e}_r \otimes \vec{E}^R + f(R) (\vec{e}_\theta \otimes \vec{E}^\Theta + \vec{e}_\phi \otimes \vec{E}^\Phi), \quad (2.B.6)$$

$$= \frac{1}{\lambda^2} \vec{e}_r \otimes \vec{E}^R + \lambda (\vec{e}_\theta \otimes \vec{E}^\Theta + \vec{e}_\phi \otimes \vec{E}^\Phi), \quad (2.B.7)$$

where  $\vec{e}_r, \vec{e}_\theta, \vec{e}_\phi$  are the basis vectors of the spheroidal polar coordinates,  $\vec{E}^R, \vec{E}^\Theta, \vec{E}^\Phi$  the dual basis. The deformation is isochoric with principal stretches  $\lambda_1 = f(R)^{-2} = \lambda^{-2}, \lambda_2 = \lambda_3 = f(R) = \lambda$ . Following [21], assuming a stress free boundary condition on the outer surface, the load acting on the inner wall can be obtained

$$p = \int_{\lambda_a}^{\lambda_b} \frac{d\mathcal{W}(\lambda)}{\lambda^3 - 1} d\lambda, \quad (2.B.8)$$

where  $\lambda_a = a/A$  and  $\lambda_b = b/B$  are the radial stretch at the two boundaries, and  $\mathcal{W}(\lambda)$  is the strain energy function defined in (2.2.24) in which  $Q$  and  $\mathbf{E}$  are rewritten in terms of  $\lambda$  (the volumetric energy term in (2.2.26) is null since the deformation is isochoric).

We simulated the inflation of a quarter of sphere with inner radius  $A = 3$  mm and outer radius  $B = 5$  mm. The sphere is modeled as an isotropic material described by the strain energy (2.2.27) with  $a_3 = 0$ . A mesh of linear tetrahedra of about 18.000 nodes approximates the domain on which a finite element space with quadratic basis functions is generated, resulting in  $\sim 50.000$  dofs. The sphere is loaded on the inner surface with pressure increments until reaching 5 kPa and the cavity ( $V_c$ ), and the wall ( $V_w$ ) volumes are computed. From the volume the radial stretches on the surfaces can be computed

$$\lambda_a = \sqrt[3]{\frac{V_c}{\frac{4}{3}\pi A^3}}, \quad \lambda_b = \sqrt[3]{\frac{V_c + V_w}{\frac{4}{3}\pi B^3}}. \quad (2.B.9)$$

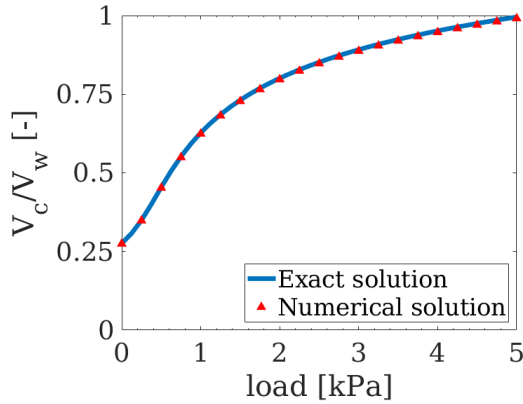


**Figure 2.15:** Volume ratio  $V_c$  over  $V_w$  as function of the load. The blue solid line represents the analytical solution and the red triangles represents the simulated solution.

For a given load,  $\lambda_a$  and  $\lambda_b$  are computed from the simulated  $V_c$  and  $V_w$  and are fed into the integral in (2.B.8), which is solved numerically in Matlab. The stretch/load combination of the analytical and simulated solutions are shown in Figure 2.15. The simulation took 7.5 min on a workstation with Intel core i7-4710MQ running on one core. 40 load increments were set and on average 3 iterations of the Newton-Raphson algorithm were needed to achieve an absolute tolerance of  $5 \times 10^{-7}$  on the residual. Each Newton step required the assembly of a Jacobian matrix (0.82s) and the resolution of a linear system (2.9 s using the LU decomposition implemented in MUMPS [?]).

---

## Bibliography

- [1] D. Ambrosi and S. Pezzuto. Active stress vs. active strain in mechanobiology: Constitutive issues. *Journal of Elasticity*, 107(2):199–212, Apr 2012.
- [2] U. Ayachit. *The paraview guide: a parallel visualization application*. Kitware, Inc., 2015.
- [3] S. Balay, S. Abhyankar, M. F. Adams, J. Brown, P. Brune, K. Buschelman, L. Dalcin, A. Dener, V. Eijkhout, W. D. Gropp, D. Karpeyev, D. Kaushik, M. G. Knepley, D. A. May, L. C. McInnes, R. T. Mills, T. Munson, K. Rupp, P. Sanan, B. F. Smith, S. Zampini, H. Zhang, and H. Zhang. *PETSc users manual*. Technical Report ANL-95/11 - Revision 3.12, Argonne National Laboratory, 2019.
- [4] L. Barbarotta, S. Rossi, L. Dedè, and A. Quarteroni. A transmurally heterogeneous orthotropic activation model for ventricular contraction and its numerical validation. *International journal for numerical methods in biomedical engineering*, 34(12):e3137, 2018.
- [5] A. Ben-Israel. A Newton-Raphson method for the solution of systems of equations. *Journal of Mathematical Analysis and Applications*, 15(2):243 – 252, 1966.
- [6] P. Bovendeerd, T. Arts, J. Huyghe, D. Van Campen, and R. Reneman. Dependence of local left ventricular wall mechanics on myocardial fiber orientation: a model study. *Journal of biomechanics*, 25(10):1129–1140, 1992.
- [7] P. Bovendeerd, W. Kroon, and T. Delhaas. Determinants of left ventricular shear strain. *American Journal of Physiology. Heart and Circulatory Physiology*, 297(3):H1058–68, 2009.
- [8] H. Childs. *Visit: an end-user tool for visualizing and analyzing very large data*. 2012.
- [9] K. D. Costa, J. W. Holmes, and A. D. McCulloch. Modelling cardiac mechanical properties in three dimensions. *Philosophical Transactions of the Royal Society of London A: Mathematical, Physical and Engineering Sciences*, 359(1783):1233–1250, 2001.
- [10] M. Folk, G. Heber, Q. Koziol, E. Pourmal, and D. Robinson. An overview of the hdf5 technology suite and its applications. In *Proceedings of the EDBT/ICDT 2011 Workshop on Array Databases*, pages 36–47, 2011.



- [11] Y. Fung. Mathematical representation of the mechanical properties of the heart muscle. *Journal of Biomechanics*, 3(4):381 – 404, 1970.
- [12] G. Guennebaud, B. Jacob, et al. Eigen. URL: <http://eigen.tuxfamily.org>, 2010.
- [13] V. Gurev, P. Pathmanathan, J.-L. Fattebert, H.-F. Wen, J. Magerlein, R. A. Gray, D. F. Richards, and J. J. Rice. A high-resolution computational model of the deforming human heart. *Biomechanics and modeling in mechanobiology*, 14(4):829–849, 2015.
- [14] S. Hartmann and P. Neff. Polyconvexity of generalized polynomial-type hyperelastic strain energy functions for near-incompressibility. *International Journal of Solids and Structures*, 40(11):2767–2791, 2003.
- [15] M. A. Heroux, R. A. Bartlett, V. E. Howle, R. J. Hoekstra, J. J. Hu, T. G. Kolda, R. B. Lehoucq, K. R. Long, R. P. Pawlowski, E. T. Phipps, et al. An overview of the trinos project. *ACM Transactions on Mathematical Software (TOMS)*, 31(3):397–423, 2005.
- [16] G. Holzapfel and R. Ogden. Constitutive modelling of passive myocardium: a structurally based framework for material characterization. *Philosophical Transactions of the Royal Society A: Mathematical, Physical and Engineering Sciences*, 367(1902):3445–3475, 2009.
- [17] R. Kerckhoffs, P. Bovendeerd, J. Kotte, F. Prinzen, K. Smits, and T. Arts. Homogeneity of cardiac contraction despite physiological asynchrony of depolarization: a model study. *Annals of biomedical engineering*, 31(5):536–547, 2003.
- [18] Lawrence Livermore National Laboratory. hypre: High Performance Preconditioners.
- [19] A. Logg, K.-A. Mardal, and G. Wells. Automated solution of differential equations by the finite element method: The FEniCS book, volume 84. Springer Science & Business Media, 2012.
- [20] R. Ogden. Non-linear elastic deformations. Courier Dover Publications, 1997.
- [21] R. W. Ogden. Non-linear elastic deformations. Courier Corporation, 1997.
- [22] A. Quarteroni. Numerical models for differential problems, volume 2. Springer, 2010.

- [23] A. Quarteroni, R. Sacco, and F. Saleri. Numerical mathematics. Springer Science & Business Media, 2010.
- [24] A. Quarteroni and A. Valli. Numerical approximation of partial differential equations, volume 23. Springer Science & Business Media, 2008.
- [25] S. Rossi, T. Lassila, R. Ruiz-Baier, A. Sequeira, and A. Quarteroni. Thermodynamically consistent orthotropic activation model capturing ventricular systolic wall thickening in cardiac electromechanics. *European Journal of Mechanics-A/Solids*, 48:129–142, 2014.
- [26] S. Salsa. Partial differential equations in action: from modelling to theory, volume 99. Springer, 2016.
- [27] J. Simo and R. Taylor. Quasi-incompressible finite elasticity in principal stretches. continuum basis and numerical algorithms. *Computer Methods in Applied Mechanics and Engineering*, 85(3):273–310, 1991.
- [28] A. van den Berg, G. Segal, and D. A. Yuen. Sepran: A versatile finite-element package for a wide variety of problems in geosciences. *Journal of Earth Science*, 26(1):89–95, 2015.
- [29] N. Westerhof, J. Lankhaar, and B. Westerhof. The arterial windkessel. *Medical & Biological Engineering & Computing*, 47(2):131–141, Feb 2009.



## **Chapter 3**

# **In Silico Assessment of Sensitivity of LV Wall Strains to Geometry**

### **Abstract**

Personalized cardiac medicine aims at assisting clinicians with model based interpretation of the patient's data, observed in the clinic. Since model input data are affected by errors and uncertainty, it is important to assess the sensitivity of model output to its input. In this work we use a Finite Element model of left ventricular (LV) mechanics to assess the sensitivity of LV end systolic wall strains to geometry. Six principal shape modes, extracted from an atlas of LV geometries using principal component analysis, have been used to model the variability of the geometry of a population of 300 asymptomatic volunteers. Green-Lagrange strains during ejection were expressed with respect to the local circumferential (c), longitudinal (l) and transmural (t) direction. We observed that shape mode 1 (related to variation in size within the population) must be personalized for an accurate prediction of the normal strains  $E_{cc}$ ,  $E_{tt}$ , and the shear strain  $E_{ct}$ . For the prediction of  $E_{ll}$ ,  $E_{cl}$ , and  $E_{lt}$  also shape modes 2 and 3 (related to the basal diameter and its orientation in the anteroseptal-inferolateral direction, and the basal orientation in the inferoseptal-anterolateral direction) must be included in the geometry description. Shape modes 4, 5, and 6 can be considered non influential. Finally, no meaningful interaction between the shape modes emerged.

The contents of this chapter are based on: Barbarotta, L. and Bovendeerd, P., 2019, June. A computational approach on sensitivity of left ventricular wall strains to geometry. In International Conference on Functional Imaging and Modeling of the Heart (pp. 240-248). Springer, Cham.

### 3.1 Introduction

Decision making in the clinic relies on the availability of relevant patient data. In diagnosis and treatment of cardiac disease, such data ideally should contain spatial maps of for example contractility, tissue stiffness and electrical activation time. However, direct measurement of such quantities may be impossible, or limited due to the invasiveness of the measurement technique. Therefore, these quantities should be derived from information that can be assessed in the patient. Personalized cardiac medicine aims at assisting clinicians with model based interpretation of the patient's data, observed in the clinic. In the last decades, several attempts were made to try estimating patient specific cardiac tissue properties such as contractility [9, 18, 27, 28, 29]. Recently, a variational approach has been used to perform high resolution data assimilation on strains computed from 4D echocardiographic measurements to estimate tissue properties in-vivo [3, 12]. These studies included in their analyses patient specific left ventricular (LV) [3, 12, 27, 28, 29] or bi-ventricular [9, 18] geometries. The application of this methodology to inversely represents the patient's data inside the model is typically affected by errors and uncertainty. It is therefore important to assess the sensitivity of model output to its input to understand whether a pathology can be observed regardless the uncertainty propagated from the input. Geometry is typically a parameter of mathematical models of the heart and it is possible to reconstruct the patient's geometry non invasively. However, besides being affected by geometrical approximations, such as exclusions of the papillary muscles and trabeculae, patient specific geometries are also affected by measurement and reconstruction errors. Furthermore, the generation of a patient specific mesh, required for a simulation of the cardiac mechanics, is a complex operation which is time consuming and difficult to automatize. Finally, the geometry obtained clinically does not represent the unloaded state of the patient's heart, and additional steps need to be taken to estimate the unloaded geometry, needed in finite element computations. For these reasons it is important to quantify the effects that such assumptions on the description of a personalized geometry introduce. In this work we use simulations of LV mechanics to assess the global sensitivity of 3D end-systolic strain distributions on realistic variations in model geometry based on human data from the Cardiac Atlas Project (CAP, <http://www.cardiacatlas.org> [13]).

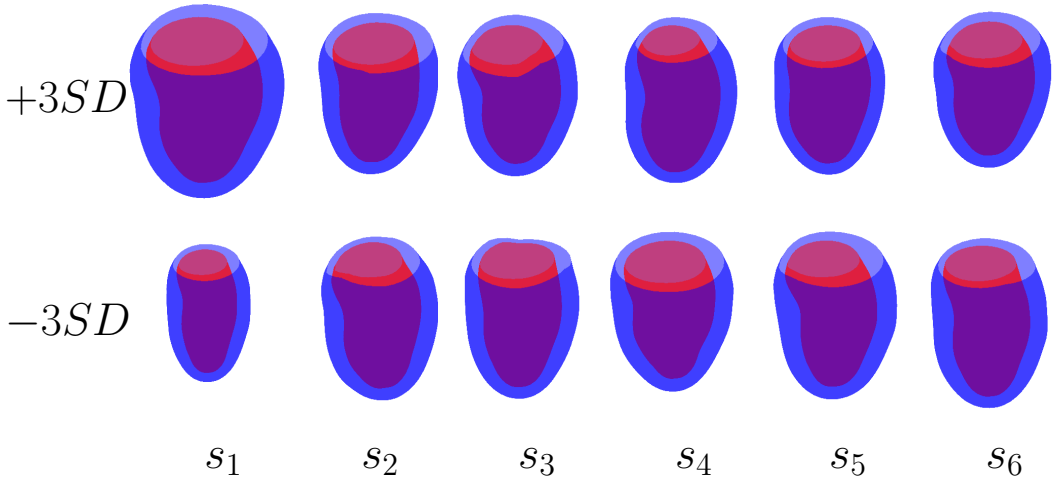


**Figure 3.1:** Surface representation of the shape modes. From left to right, geometric variation due to shape modes  $s_1$  through  $s_6$  is demonstrated by adding them to the average geometry by an amount of  $+3SD$  (top row) and  $-3SD$  (bottom row). We may interpret the shape modes in the following way: mode 1 describes the variation of the size, mode 2 describes how the base diameter varies together with its orientation in the antero-septal-infero-lateral direction, mode 3 describes the basal plane orientation in the infero-septal-antero-lateral direction, mode 4 the conicity, mode 5 describes the asymmetry between the wall thickness at septum and that at the lateral side, and mode 6 describes how the length varies together with its basal plane orientation in the septal-lateral direction.

## 3.2 Material and methods

### 3.2.1 Geometry

We obtained geometric data from the CAP, in particular shape models from 300 asymptomatic volunteers derived from images from the Multi Ethnic Study of Atherosclerosis (MESA) [5]. Zhang et al [30] and Medrano-Gracia et al [20] applied Principal Component Analysis (PCA) to those shape models, to summarize the geometrical complexity using only few shape modes in order to study the shape variation within the human population and the remodeling following a myocardial infarction. From their PCA on a population of asymptomatic volunteers, six end-diastolic shape modes explaining about 80% of the population variability were made freely available by CAP. The data include information about epicardial and endocardial surface meshes. The surfaces of the six shape modes at  $\pm 3SD$  from the average are shown in Figure 3.1. The SD of the shape modes is reported in Table 3.1. Interpretation of the modes is not straightforward, since they are given in terms of non trivial three di-

mensional vector fields. Nonetheless, an interpretation is given in Figure 3.1. We used these data to generate representative geometries, defined by combinations of shape modes. We interpolated the associated end-diastolic surface meshes onto the surfaces of an idealized left ventricular template mesh, after aligning the two basal planes. Then, using the transmural coordinate, numerically integrated from the ellipsoidal coordinates defining the template mesh, the internal nodes of the mesh were moved in order to obtain transmurally even elements. By using this method, we were able to generate high quality meshes for arbitrary end-diastolic configurations. The deformation gradient of the geometric mapping from the template mesh to the deformed mesh was used to reorient the vector fields defined over the template mesh to the end-diastolic configuration. In particular the end-diastolic fiber orientation is obtained as follows

$$\vec{e}_{f,ED} = \frac{\mathbf{F}_{T \rightarrow ED} \vec{e}_{f,T}}{\|\mathbf{F}_{T \rightarrow ED} \vec{e}_{f,T}\|_2}, \quad (3.2.1)$$

where  $\vec{e}_{f,T}$  is the fiber orientation of the template geometry and  $\mathbf{F}_{T \rightarrow ED}$  is the deformation gradient of the geometric mapping. Note that this operation preserve the tangentiality of fibers on the surfaces. An example of mesh and fiber field generated using this technique can be seen in Figure 3.2.

$SD_1$	$SD_2$	$SD_3$	$SD_4$	$SD_5$	$SD_6$
0.7967	0.4597	0.3443	0.3007	0.2512	0.2429

**Table 3.1:** Standard deviations of the shape modes.

### 3.2.2 Material properties

We simulated LV mechanics using the model by Bovendeerd et al [6]. Briefly, the myocardium is described as an hyperelastic fiber-reinforced transversely isotropic active stress material. The Cauchy stress tensor  $\sigma$  thus reads

$$\sigma = \sigma_p + \sigma_a \vec{e}_f \otimes \vec{e}_f. \quad (3.2.2)$$

The active stress  $\sigma_a$  is adopted from Bovendeerd et al [12]. It depends on sarcomere and contractile element lengths, time elapsed since activation (assumed to be simultaneous throughout the ventricle) and sarcomere shortening velocity, and acts along the current fiber direction  $\vec{e}_f$  (see 2.2.1 for details).



The passive stress  $\sigma_p$  is derived from a strain energy density function as follows

$$\sigma_p = \frac{1}{\det(\mathbf{F})} \mathbf{F} \frac{\partial \mathcal{W}}{\partial \mathbf{E}} \mathbf{F}^T, \quad (3.2.3)$$

where  $\mathcal{W}$  is composed of a term  $\mathcal{W}^{shape}$ , describing response to change in shape, and a term  $\mathcal{W}^{volume}$ , representing near incompressibility:

$$\mathcal{W} = \mathcal{W}^{shape} + \mathcal{W}^{volume}, \quad (3.2.4)$$

$$\mathcal{W}^{shape} = a_0 (\exp Q - 1), \quad (3.2.5)$$

$$Q = a_1 \mathcal{I}_1^2 + 2a_2 \mathcal{I}_2 + a_3 \mathcal{I}_{4,f}^2, \quad (3.2.6)$$

$$\mathcal{W}^{volume} = 4k (J^2 - 1 - 2 \ln J), \quad (3.2.7)$$

where  $\mathcal{I}_{\{1,2\}}$  are the invariants of the Green-Lagrange tensor  $\mathbf{E}$ ,  $\mathcal{I}_{4,f}$  is the pseudo-invariant of  $\mathbf{E}$  introducing the anisotropy along myofibers,  $J$  is the determinant of the deformation gradient  $\mathbf{F}$ , and  $a_{\{0,1,2,3\}}$  and  $k$  are a constitutive parameters. Note that  $\mathcal{W}^{volume}$  was modified from Bovendeerd et al [6] according to Simo et al [?] to comply with assumptions of positivity, convexity, and unboundedness at both zero and infinity. The values of the constitutive parameters are given in Table 2.2. The orientation of fibers inside the myocardium is described by the helix angle and the transverse angle, describing the base-to-apex component and the endocardium-to-epicardium component of the fiber vector, respectively. These angles were specified by high order Legendre polynomials of normalized transmural and longitudinal coordinates [6]. In Bovendeerd et al [6] the model has been evaluated against experimental strains measured using MRI tagging on three healthy volunteers.

### 3.2.3 Computation of left ventricular wall mechanics

Left ventricular wall mechanics was computed by solving for equilibrium between forces related to active stress, passive stress and cavity pressure:

$$\left\{ \begin{array}{ll} \text{Div}(\mathbf{P}(\mathbf{F})) = \vec{0} & \text{in } \Omega_0, \\ \mathbf{P}\vec{n}_0 = -pJ\mathbf{F}^{-T}\vec{n}_0 & \text{on } \Gamma_{0,Endo}, \\ \mathbf{P}\vec{n}_0 = \vec{0} & \text{on } \Gamma_{0,Epi}, \\ \vec{u} \cdot \vec{n}_0 = 0 & \text{on } \Gamma_{0,Base}, \\ u_x = 0 & \text{on } \{\Gamma_{0,Base} \cap \Gamma_{0,Endo} \cap \{x = 0\}\}, \\ u_y = 0 & \text{on } \{\Gamma_{0,Base} \cap \Gamma_{0,Endo} \cap \{y = 0\}\}, \end{array} \right. \quad (3.2.8)$$

where  $\mathbf{P}$  is the first Piola-Kirchhoff stress tensor;  $\mathbf{F}$  is the deformation gradient; and  $\partial\Omega_0 = \Gamma_{0,Base} \cup \Gamma_{0,Endo} \cup \Gamma_{0,Epi}$  represents the decomposition of the unloaded boundary in basal, endocardial and epicardial surfaces, respectively; and  $\vec{n}_0$  is the normal vector defined over those surfaces. Note that in (3.2.8)  $\vec{n}_0$  at base is parallel to  $\vec{e}_z$ , and that we suppressed rotations around  $\vec{e}_z$  by blocking circumferential displacements of nodes within the intersection of the endocardial basal ring and those on the  $x$  and  $y$  axes.

We did not couple our LV model to the closed circulation model described in Bovendeerd et al [6]. Instead, we let the heart fill until a fixed preload of 1.5 kPa was reached. From this end-diastolic state, we then simulated the isovolumic contraction phase by initiating active stress development and computing the increase of cavity pressure while keeping cavity volume constant. As soon as cavity pressure reached a preset afterload pressure of 12 kPa, we let the heart eject against this constant pressure until it reached the end-systolic state, defined as the state of minimum cavity volume. From the simulations, end-systolic strains with respect to the end-diastolic configuration were computed using the Green-Lagrange strain tensor along the wall-bound basis vectors in circumferential ( $\vec{e}_c$ ), longitudinal ( $\vec{e}_l$ ), and transmural ( $\vec{e}_t$ ) directions.

### 3.2.4 Computation of the unloaded configuration

To perform a finite element simulation of LV mechanics we need to recover a virtually unloaded configuration from the loaded end-diastolic configuration, provided in the atlas. In order to estimate this unloaded configuration, we deflated the end-diastolic configuration using a standard approach based on the concept of Inverse Design [15]. This method relies on the solution of the momentum balance equation in the deformed configuration  $\Omega$  as follows

$$\begin{cases} \operatorname{div}(\boldsymbol{\sigma}(\mathbf{F})) = \vec{0} & \text{in } \Omega, \\ \boldsymbol{\sigma}\vec{n} \cdot \vec{n} = -p & \text{on } \Gamma_{Endo}, \\ \boldsymbol{\sigma}\vec{n} = \vec{0} & \text{on } \Gamma_{Epi}, \end{cases} \quad (3.2.9)$$

and the same kinematic boundary conditions of (3.2.8). The sought solution is the displacement from  $\Omega$  to the virtually stress free configuration  $\Omega_0$

$$\vec{x}_0(\vec{x}) = \vec{x} - \vec{u}(\vec{x}), \quad (3.2.10)$$

$$\mathbf{F}(\vec{x}_0) = \frac{\partial \vec{x}}{\partial \vec{x}_0}(\vec{x}_0). \quad (3.2.11)$$

Since  $\Omega_0$  and its metric are unknown, the derivatives involved in the definition of  $\mathbf{F}$  cannot be computed. However, the problem can be circumvented by

using the spatial deformation gradient  $\mathbf{f}$ , defined as

$$\begin{aligned}\mathbf{f}(\vec{x}) &= \left( \mathbf{I} - \frac{\partial \vec{u}(\vec{x})}{\partial \vec{x}} \right) \\ &= \left( \mathbf{I} + \frac{\partial \vec{u}(\vec{x}_0)}{\partial \vec{x}_0} \right)^{-1} \Bigg|_{\vec{x}_0 = \vec{x} - \vec{u}} = \mathbf{F}^{-1}(\vec{x}).\end{aligned}\quad (3.2.12)$$

Consequently the Cauchy stress tensor reads

$$\begin{aligned}\boldsymbol{\sigma}(\mathbf{F}) &= \boldsymbol{\sigma}(\mathbf{f}^{-1}) \\ &= \frac{\mathbf{f}^{-1}}{\det(\mathbf{f}^{-1})} \frac{\partial \mathcal{W}}{\partial \mathbf{E}} \Bigg|_{\mathbf{F} = \mathbf{f}^{-1}} \mathbf{f}^{-T},\end{aligned}\quad (3.2.13)$$

where we assumed that no residual active stress  $\sigma_a$  is present during diastole. To solve (3.2.9), an end-diastolic pressure load  $p$  is needed. Since the pressure is unknown, we increment the pressure load until the unloaded configuration reaches an estimated unstressed cavity volume. We assumed that under normal circumstances this volume  $V_{c,0}$  would be equal to  $V_{c,ES}$ , the volume at end ejection. In turn, this volume was estimated from the end-diastolic cavity volume by assuming a physiological ejection fraction (EF) of 60%

$$V_{c,0} \approx V_{c,ES} = (100 - EF) V_{c,ED}. \quad (3.2.14)$$

Note that the solution of (3.2.9) modifies the domain on which the fibers are defined and affects their orientation. Therefore, fiber orientation in the unloaded state  $\vec{e}_{f,0}$  is defined as a function of  $\mathbf{f}$  and  $\vec{e}_{f,ED}$  as follows

$$\vec{e}_{f,0} = \frac{\mathbf{f} \vec{e}_{f,ED}}{\|\mathbf{f} \vec{e}_{f,ED}\|_2}. \quad (3.2.15)$$

### 3.2.5 Finite element implementation

We implemented our Finite Element model in a python package based on the FEniCS library (fenicsproject.org, [1]). The spatial discretization of the problem was studied in order to achieve an accurate prediction of strains at an affordable computational cost. In this respect, we use a sub-parametric finite element approach where the geometry is discretized using linear tetrahedra on top of which the solution is discretized using continuous piece-wise quadratic Lagrangian polynomials. The spatial discretization resulted in 5760 elements and 24519 degrees of freedom. The nonlinear problem was solved using the Newton-Raphson algorithm and the resulting linear systems were solved using the LU decomposition implemented in the MUMPS library [2].

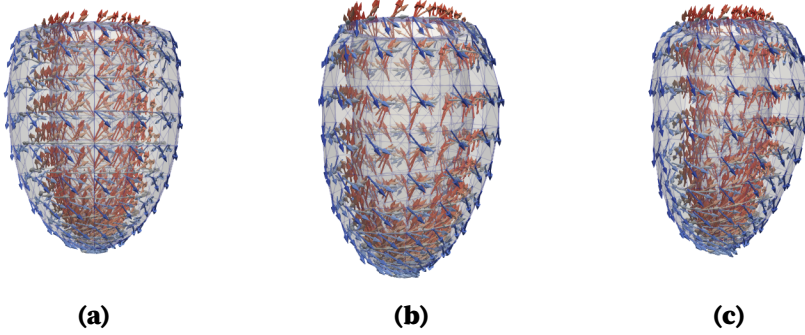


**Figure 3.2:** View of meshes and fibers for the template geometry (left), and the end-diastolic configuration (middle) and the reconstructed unloaded geometry (right) of the average geometry.

### 3.2.6 Sensitivity analysis approach

In our sensitivity study we employ the Elementary Effects method [25]. It is a global sensitivity analysis method that was first presented by Morris [21] as a screening method and later improved by Campolongo et al [7]. It is a non-intrusive method that has been applied in the cardiovascular field [16, 11]. It allows to compute sensitivity indices of the strain distributions without requiring the use of meta-modeling techniques.

For the sensitivity analysis we considered the 6 shape modes  $s_i$  ( $i = 1, \dots, 6$ ). We varied each mode over a range of 1 SD around the mean. We built a structured grid with a  $p$  nodes resolution along each mode direction in the parameter space yielding  $p^6$  shape mode combinations. Using an optimized sampling strategy we generated  $r$  trajectories with a maximum spread [7], visiting a total of  $M$  different shape mode combinations. Each trajectory visits a set of 7 shape mode combination  $(\vec{s}^{j1}, \vec{s}^{j2}, \vec{s}^{j3}, \vec{s}^{j4}, \vec{s}^{j5}, \vec{s}^{j6}, \vec{s}^{j7})$  that allows the computation of an elementary effect along every shape mode direction  $i$  ( $\vec{s}^{ji+1} = \vec{s}^{ji} + \Delta_i \vec{e}_i$ , for  $i = 1, \dots, 6$ ). A shape mode combination  $\vec{s}^j = (s_1^j, \dots, s_6^j)$  univocally determines a geometry as follows

$$\vec{g}^j(\vec{x}) = \vec{g}^{avg}(\vec{x}) + \sum_{i=1}^6 s_i^j \vec{v}_i(\vec{x}), \quad (3.2.16)$$

where the  $\vec{v}_i(\vec{x})$  are the eigenvectors stemming from the PCA, and  $\vec{g}^{avg}(\vec{x})$  is the average geometry of the atlas. As output we considered all six end-systolic Green-Lagrange strain components  $E_{\alpha\beta}$ , referred to the state at end diastole, where  $\alpha$  and  $\beta$  are in  $\{c, l, t\}$ .

Per strain component  $E_{\alpha\beta}$  and per node  $\vec{x}_i$ , we computed the coefficient of variation (CV), defined as the standard deviation of the strain component computed over all the simulated geometries normalized with respect of the norm of the average respective strain.

$$E_{\alpha\beta}^{avg}(\vec{x}_i) = \frac{1}{M} \sum_{j=1}^M E_{\alpha\beta}(\vec{x}_i, \vec{s}^j), \quad (3.2.17)$$

$$CV_{E_{\alpha\beta}}^{avg}(\vec{x}_i) = \frac{\sqrt{\frac{1}{M-1} \sum_{j=1}^M \left( E_{\alpha\beta}(\vec{x}_i, \vec{s}^j) - E_{\alpha\beta}^{avg}(\vec{x}_i) \right)^2}}{\|E_{\alpha\beta}^{avg}(x)\|_{\infty}}, \quad (3.2.18)$$

where  $i = 1, \dots, N$ ,  $N$  is the number of nodes used in the discretization of the finite element LV model, and  $\|E_{\alpha\beta}^{avg}(x)\|_{\infty}$  is the  $\ell^{\infty}$  norm over all the  $N$  LV nodes  $\vec{x}_i$ . To analyze the contribution of each shape mode to the CV, we first assessed the elementary effects  $EE_i$ . For a specific point in the parameter space  $\vec{s} = (s_1, \dots, s_6)$ ,  $EE_{i,\alpha\beta}$  gives an estimation of the effect that a geometric perturbation through a change in a shape mode  $s_i$  by an amount  $\Delta_i$  has on a strain component  $E_{\alpha\beta}$ :

$$EE_{i,\alpha\beta}(\vec{x}_j, \vec{s}) = \frac{E_{\alpha\beta}(\vec{x}_j, \vec{s} + \Delta_i \vec{e}_i) - E_{\alpha\beta}(\vec{x}_j, \vec{s})}{\Delta^*}, \quad (3.2.19)$$

$$\Delta^* = \frac{p}{2(p-1)}, \quad (3.2.20)$$

$$\Delta_i = 2\Delta^* SD_i, \quad (3.2.21)$$

where  $j = 1, \dots, N$ ,  $\vec{e}_i$  is the  $i$ -th vector of the standard orthogonal basis of the six dimensional parameter space,  $p$  is the grid resolution of the parameter space, and the values of the standard deviations  $SD_i$  are given in Table 3.1. The use of two different  $\Delta$  (3.2.20) and (3.2.21) is dictated by the need to guarantee an appropriate adimensional uniform sampling in the image of the assumed probability distribution of each shape mode ( $\Delta^* \in (0, 1)$ ) and to transform this node sampling in the considered range for each shape mode ( $\Delta_i \in [-SD_i, +SD_i]$ ) according to the choice of the probability distribution.

Elementary effects EE were computed for all six end-systolic strain components. By collecting all the elementary effects over the trajectories, three sen-

sitivity indices were computed as follows:

$$\mu_{i,\alpha\beta}(\vec{x}_k) = \frac{1}{r} \sum_{j=1}^r EE_{i,\alpha\beta}^j(\vec{x}_k, \vec{s}^{j_i}), \quad (3.2.22)$$

$$\mu_{i,\alpha\beta}^*(\vec{x}_k) = \frac{1}{r} \sum_{j=1}^r |EE_{i,\alpha\beta}^j(\vec{x}_k, \vec{s}^{j_i})|, \quad (3.2.23)$$

$$\sigma_{i,\alpha\beta}(\vec{x}_k) = \sqrt{\frac{1}{r-1} \sum_{j=1}^r \left( EE_{i,\alpha\beta}^j(\vec{x}_k, \vec{s}^{j_i}) - \mu_{i,\alpha\beta}(\vec{x}_k) \right)^2}, \quad (3.2.24)$$

where  $k = 1, \dots, N$ ,  $r$  is the number of trajectories,  $\mu_i$  gives an overall estimation of the effect of a variation on shape mode  $s_i$ ,  $\mu_i^*$  is used to detect whether variations on  $s_i$  are non influential, and  $\sigma_i$  gives information about how much the effect of a perturbation on  $s_i$  depends on the sampling point in the parameter space, giving an estimation of the ensemble of the shape mode's effects due to interactions and nonlinear behaviors. Note that these quantities are statistics of the elementary effects and therefore are summed over the number of trajectories.

To obtain the average strain variation within the parameter space, we multiplied the indices  $\mu_{i,\alpha\beta}(\vec{x})$  and  $\mu_{i,\alpha\beta}^*(\vec{x})$  by the variation step  $\Delta^*$  and normalized them with the infinity norm of the respective strain computed in the average shape ( $\vec{s} = (0, 0, 0, 0, 0, 0)$ ) as follows:

$$\hat{\mu}_{i,\alpha\beta}(\vec{x}_j) = \frac{\mu_{i,\alpha\beta}(\vec{x}_j) \Delta^*}{\|E_{\alpha\beta}^{ref}(\vec{x})\|_{\infty}}, \quad (3.2.25)$$

$$\hat{\mu}_{i,\alpha\beta}^*(\vec{x}_j) = \frac{\mu_{i,\alpha\beta}^*(\vec{x}_j) \Delta^*}{\|E_{\alpha\beta}^{ref}(\vec{x})\|_{\infty}}, \quad (3.2.26)$$

$$\hat{\sigma}_{i,\alpha\beta}(\vec{x}_j) = \frac{\sigma_{i,\alpha\beta}(\vec{x}_j) \Delta^*}{\|E_{\alpha\beta}^{ref}(\vec{x})\|_{\infty}} \quad (3.2.27)$$

where  $i$  varies between 1 and 6 as the shape modes, and  $j = 1, \dots, N$ .  $\hat{\mu}_{i,\alpha\beta}$ ,  $\hat{\mu}_{i,\alpha\beta}^*$ , and  $\hat{\sigma}_{i,\alpha\beta}$  are computed per node  $\vec{x}_j$ , and thus are scalar fields with spatial variability and are algebraically represented, as all the sensitivity indices, in the average geometry.

To summarize the detailed information in  $\hat{\mu}_{i,\alpha\beta}(\vec{x})$  and  $\hat{\mu}_{i,\alpha\beta}^*(\vec{x})$  we compute the average 1-norm which is the 1-norm re-scaled using the number of nodes

involved in the finite element LV discretization  $N$

$$\hat{\mu}_{i,\alpha\beta}^{avg} = \frac{1}{N} \|\hat{\mu}_{i,\alpha\beta}(\vec{x})\|_1 = \frac{1}{N} \sum_{j=1}^N |\hat{\mu}_{i,\alpha\beta}(x_j)|, \quad (3.2.28)$$

$$\hat{\mu}_{i,\alpha\beta}^{*,avg} = \frac{1}{N} \|\hat{\mu}_{i,\alpha\beta}^*(\vec{x})\|_1 = \frac{1}{N} \sum_{j=1}^N |\hat{\mu}_{i,\alpha\beta}^*(x_j)|, \quad (3.2.29)$$

$$\hat{\sigma}_{i,\alpha\beta}^{avg} = \frac{1}{N} \|\hat{\sigma}_{i,\alpha\beta}^*(\vec{x})\|_1 = \frac{1}{N} \sum_{j=1}^N |\hat{\sigma}_{i,\alpha\beta}^*(x_j)|. \quad (3.2.30)$$

We use  $\hat{\sigma}_{i,\alpha\beta}^{avg}$  to estimate the interactions between the shape modes. To this end, we observed the ratio between the average 1-norm of  $\hat{\mu}_{i,\alpha\beta}^{avg}$  and  $\hat{\sigma}_{i,\alpha\beta}^{avg}$ . We defined three levels of interaction using the reference value  $3/2$ . If  $\hat{\mu}_{i,\alpha\beta}^{avg}$  over  $\hat{\sigma}_{i,\alpha\beta}^{avg}$  exceeds this value the interaction is considered weak, if  $\hat{\mu}_{i,\alpha\beta}^{avg}$  over  $\hat{\sigma}_{i,\alpha\beta}^{avg}$  fall below  $2/3$  the interaction is considered strong. In the remaining case the interaction is considered moderate.

In the current study we choose  $r = 500$  trajectories over a parameter space grid with resolution  $p = 4$  for a total of  $M = 2339$  simulations.

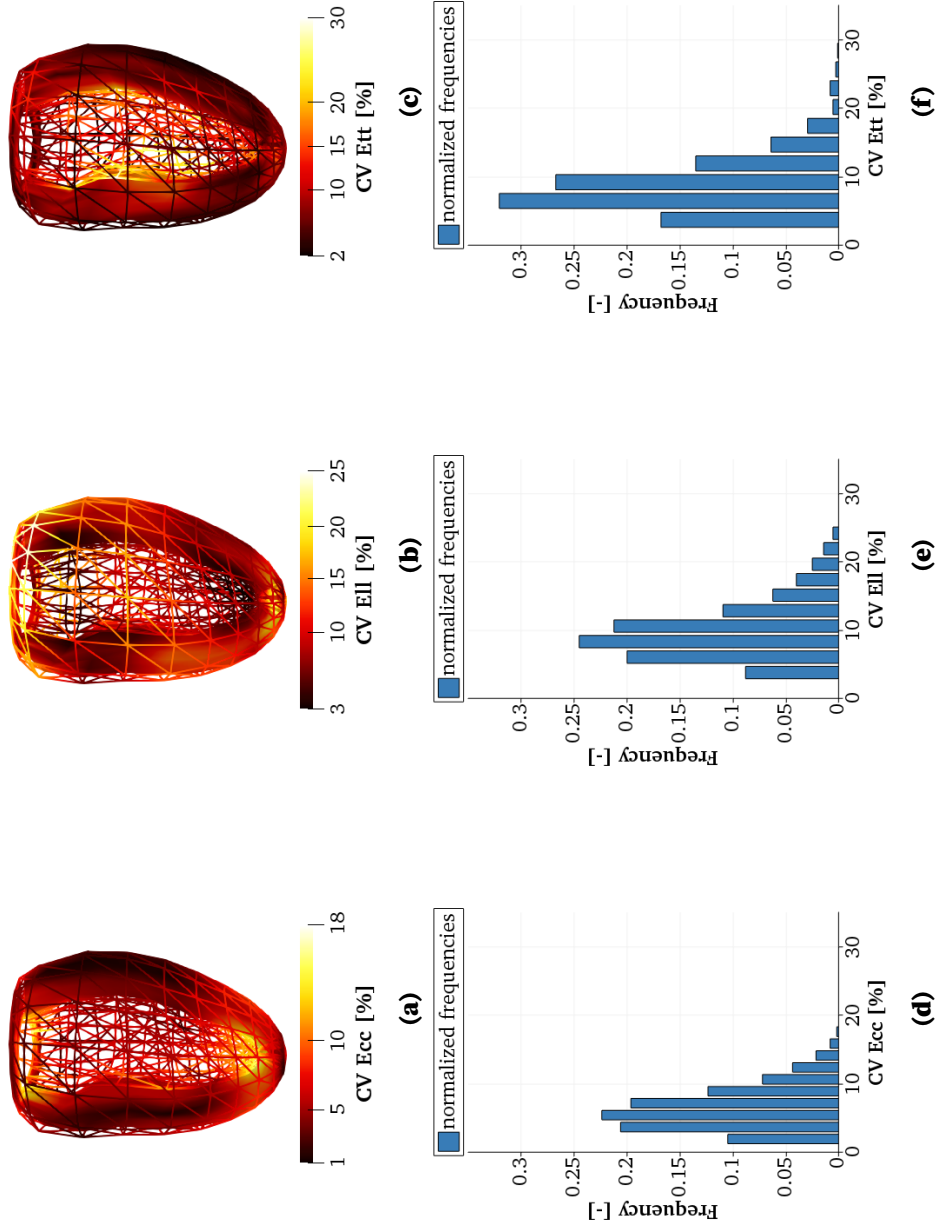


**Figure 3.3:** Per-node coefficient of variation (CV) of normal strains. From left to right CV of circumferential, longitudinal, and transmural strains. The top row shows the spatial distribution presented on the average unloaded geometry, the histograms in the bottom row show the frequency within the geometry.



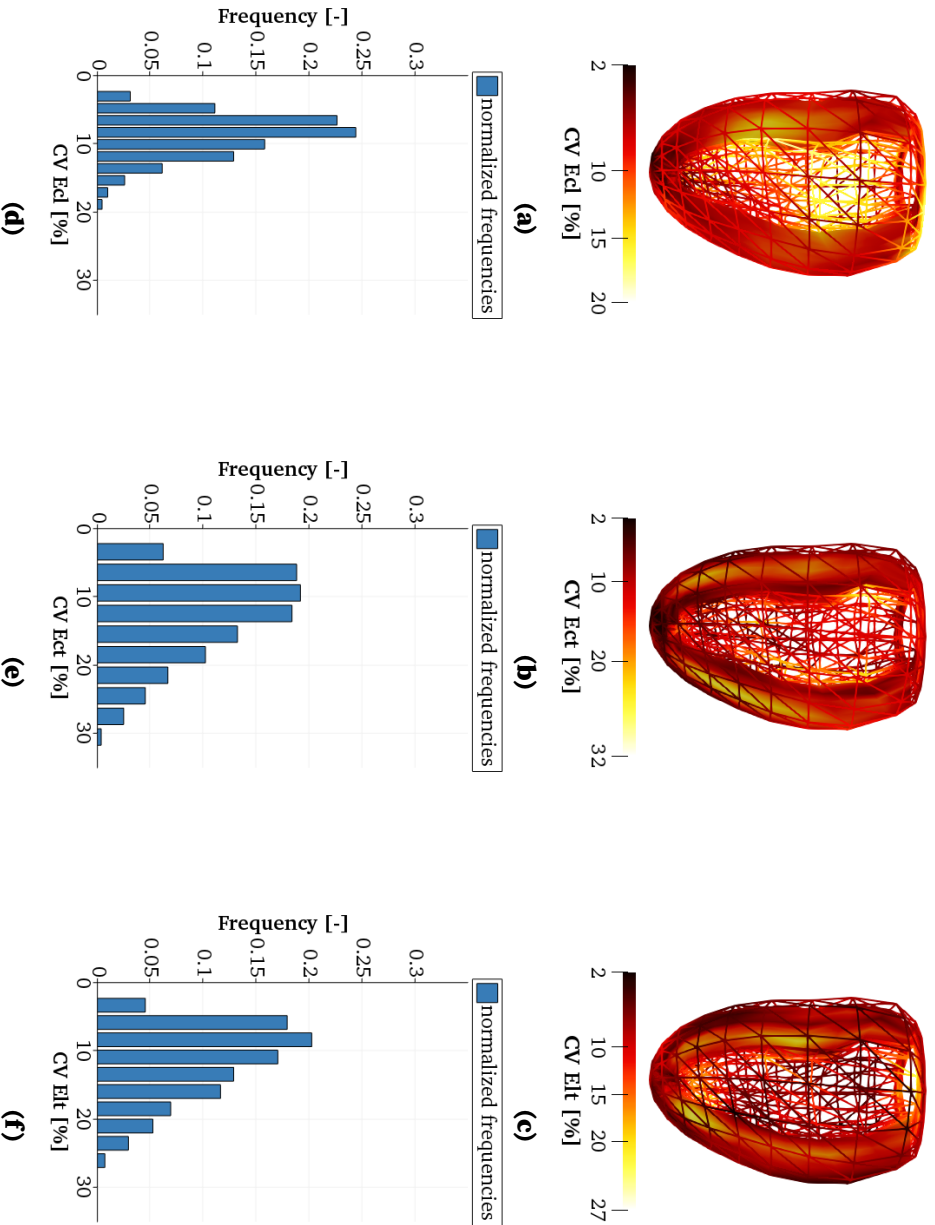


**Figure 3.4:** Per-node CV of shear strains. From left to right CV of circumferential-longitudinal, circumferential-transmural, and longitudinal-transmural shear strains. The top row shows the spatial distribution presented on the average unloaded geometry, the histograms in the bottom row show the frequency within the geometry.

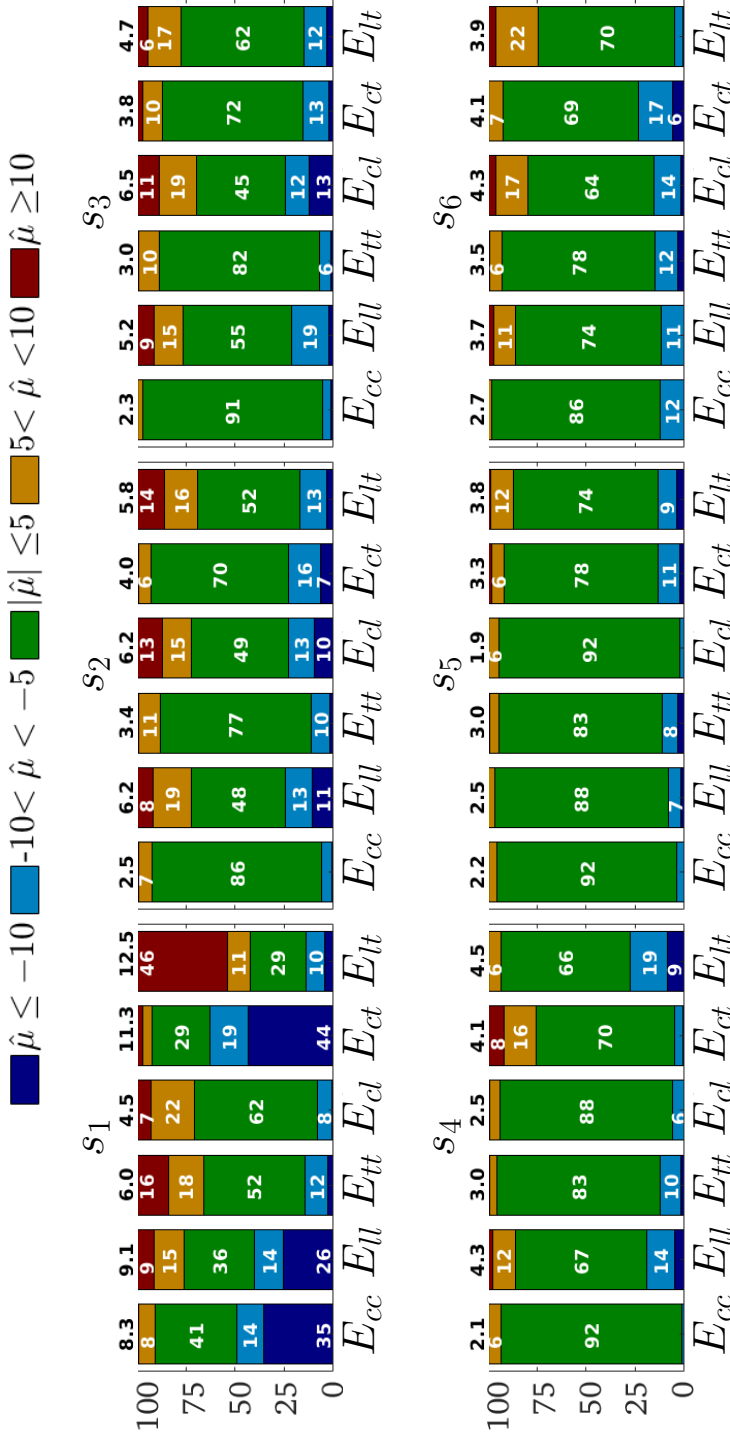


**Figure 3.5:** Bar plots of the spatial distribution of  $\hat{\mu}$  for the six end-systolic strains. Each bar is divided in five. The blue bar represents the fraction of the geometry with  $\hat{\mu}_{i,\alpha\beta}(\vec{x}) < -10$ , the light blue bar the one with  $-10 < \hat{\mu}_{i,\alpha\beta}(\vec{x}) < -5$ , the green bar the portion where  $\hat{\mu}_{i,\alpha\beta}(\vec{x}) < 5$ , the yellow bar represents the fraction of the geometry with  $5 < \hat{\mu}_{i,\alpha\beta}(\vec{x}) < 10$ , and the red one the region with  $\hat{\mu}_{i,\alpha\beta}(\vec{x}) > 5$ . On top of each bar it is written in black the value of  $\hat{\mu}_{i,\alpha\beta}^{avg}$  for the respective mode and strain. The five values written in white on the bars indicates the frequency of  $\hat{\mu}_{i,\alpha\beta}(\vec{x})$  in the respective sub-regions. For the sake of readability we did not indicate the number for bars smaller than 5%.

### 3.3 Results

The unloading procedure resulted in an average unloaded cavity volume  $V_{c,0}$  of about 43mL ( $\pm 8$ mL mainly due to mode 1) and an average cavity pressure of 1.46kPa ( $\pm 0.05$ kPa), both within physiological ranges, with an average ratio of unloaded cavity volume to wall volume  $V_{c,0}/V_w = 0.34$ . The average end-diastolic, the unloaded, and the wall volumes of the geometries for each shape mode are reported in Table 3.2 with their SD.

	$V_{c,ED}$ [mL]	$V_{c,0}$ [mL]	$V_w$ [mL]
shape mode 1	$107.8 \pm 15.4$	$42.8 \pm 6.1$	$125.9 \pm 16.4$
shape mode 2	$106.3 \pm 0.9$	$42.4 \pm 0.4$	$124.6 \pm 0.7$
shape mode 3	$106.0 \pm 0.6$	$42.4 \pm 0.3$	$124.3 \pm 1.0$
shape mode 4	$106.5 \pm 0.2$	$42.6 \pm 0.1$	$125.0 \pm 0.5$
shape mode 5	$106.4 \pm 1.4$	$42.6 \pm 0.6$	$124.9 \pm 3.7$
shape mode 6	$106.2 \pm 0.4$	$42.6 \pm 0.2$	$124.7 \pm 1.9$

**Table 3.2:** Per shape mode average end-diastolic cavity volume  $V_{c,ED}$ , unloaded cavity volume  $V_{c,0}$ , and wall volume  $V_w$  with their standard deviation.

The constant preload-constant afterload experiment resulted in an average stroke volume of about 58mL  $\pm 10$ mL and an ejection fraction of about 53%  $\pm 1\%$ .

Regarding strain distributions, Figure 3.3 shows the spatial distribution and the histogram of the coefficient of variation (CV) of normal strains: the circumferential strain  $E_{cc}$ , the longitudinal strain  $E_{ll}$  the transmural strain  $E_{tt}$ . The norms used in the definition of CV in (3.2.18) were:

$$\|E_{cc}^{avg}\|_{\infty} = 0.31, \quad \|E_{ll}^{avg}\|_{\infty} = 0.22, \quad \|E_{tt}^{avg}\|_{\infty} = 1.2. \quad (3.3.1)$$

The maximum values occur in the basal plane region for  $E_{cc}$  and  $E_{ll}$ , and on the endocardial surface for  $E_{tt}$ , while the minimum values occur on the epicardial surface for  $E_{cc}$  and  $E_{tt}$ , and in the basal and apical region of the endocardial surface for  $E_{ll}$ . The bottom row of Figure 3.3 shows the distribution of the coefficient of variation of normal strains. For  $E_{cc}$ ,  $E_{ll}$ , and  $E_{tt}$  the coefficient of variation ranges are about 1%  $\sim$  18%, 3%  $\sim$  25%, and 2%  $\sim$  30%, respectively, whereas the mean values of  $CV \pm SD$  are 6%  $\pm$  3%, 10%  $\pm$  4%, 9%  $\pm$  4%, respectively.

Figure 3.4 shows the spatial distribution and the histogram of the coefficient of variation for the shear strains: the circumferential-longitudinal shear strain  $E_{cl}$ , the circumferential-transmural shear strain  $E_{ct}$ , the longitudinal-transmu-

ral shear strain  $E_{lt}$ . The norms of the average shear strains were:

$$\|E_{cl}^{avg}\|_{\infty} = 0.14, \quad \|E_{ct}^{avg}\|_{\infty} = 0.37, \quad \|E_{lt}^{avg}\|_{\infty} = 0.36. \quad (3.3.2)$$

The maximum values occur in the equatorial region of the endocardium and on the base for  $E_{cl}$ , on the apical sub-epicardium for  $E_{ct}$ , in the sub-endocardial region between equator and apex for  $E_{lt}$ , while the minimum values occur on the epicardial surface for  $E_{lt}$  and in the apical region for  $E_{cl}$  and  $E_{ct}$ . For the  $E_{cl}$ ,  $E_{ct}$ , and  $E_{lt}$  the coefficient of variation ranges are about 2% – 20%, 2% – 32%, and 2% – 27%, while the mean values of  $CV \pm SD$  are  $9\% \pm 3\%$ ,  $13\% \pm 6\%$ ,  $12\% \pm 5\%$ , respectively.

To explain how the different shape modes contribute to the CV of the strains, in Table 3.3 we report the sensitivity indices  $\hat{\mu}_{i,\alpha\beta}^{*,avg}$  for the six considered strains and the six shape modes. Recalling that  $\hat{\mu}_{i,\alpha\beta}^*$  is an upper bound on  $\hat{\mu}_{i,\alpha\beta}$ , the overall sensitivity,  $\hat{\mu}_{i,\alpha\beta}^{*,avg}$  represents the maximum average normalized effect that a variation of the shape through mode  $s_i$  by an amount  $\Delta_i$  (see (3.2.21) and Table 3.1) has on the strain component  $E_{\alpha\beta}$ . Being a good proxy for the Sobol total effect index  $S_T$  [7],  $\hat{\mu}_{i,\alpha\beta}^*$  can be used to detect non influential parameters. We highlighted values above 5% in pink and those larger than 10% in red. In this respect,  $\hat{\mu}_{4,\alpha\beta}^{*,avg}$ ,  $\hat{\mu}_{5,\alpha\beta}^{*,avg}$ , and  $\hat{\mu}_{6,\alpha\beta}^{*,avg}$  are always smaller than 5%.  $\hat{\mu}_{2,\alpha\beta}^{*,avg}$  and  $\hat{\mu}_{3,\alpha\beta}^{*,avg}$  are between 5% and 10% only for  $E_{ll}$ ,  $E_{cl}$ , and  $E_{lt}$ . Instead, except for  $E_{cl}$ ,  $\hat{\mu}_{1,\alpha\beta}^{*,avg}$  is always larger than 5% with  $\hat{\mu}_{1,ct}^{*,avg}$  and  $\hat{\mu}_{1,lt}^{*,avg}$  larger than 10%.

	$s_1$	$s_2$	$s_3$	$s_4$	$s_5$	$s_6$
$E_{cc}$	8.4	2.7	2.5	2.3	2.4	2.9
$E_{ll}$	9.3	6.4	5.4	4.4	2.7	3.9
$E_{tt}$	6.6	3.9	3.5	3.5	3.5	3.9
$E_{cl}$	4.8	6.3	6.6	2.7	2.2	4.4
$E_{ct}$	11.5	4.4	4.1	4.3	3.6	4.4
$E_{lt}$	12.8	6.2	5.1	4.7	4.1	4.3

**Table 3.3:** Spatially averaged relative sensitivity of strains  $E_{\alpha\beta}$  (rows) to variations in shape mode  $s_i$  (columns), expressed in parameter  $\hat{\mu}_{i,\alpha\beta}^{*,avg}$  [%]. Values above 5% are highlighted in pink. Those above 10% are highlighted in red.

Figure 3.5 shows the distribution of the normalized strain variations  $\hat{\mu}_{i,\alpha\beta}(\vec{x})$  over the LV nodes, for the six strain components. To explain the presentation, we first focus on the effect of mode  $s_1$  on the normal strain  $E_{cc}$ , presented in the upper left bar. The green bar indicates that in 41% of the LV nodes the effect of variation along  $s_1$  on  $E_{cc}$  was below 5% of the value of  $E_{cc}$  in the

central geometry. The dark blue bar indicates that  $E_{cc}$  was reduced by more than 10% of the average value in 35% of the nodes. A dark red bar would indicate the percentage of geometries with an increase of  $E_{cc}$  by more than 10% of the average value. The absence of this part indicates that geometric variations through mode 1 have an asymmetric effect on  $E_{cc}$ , with a tendency to decrease it. The two remaining regions indicate the prevalence of variations in mode 1 that increase (yellow) or decrease (light blue) the average strain in the range of 5% – 10%. Variations through mode  $s_1$  affect  $E_{ll}$  beyond the 10% threshold level in 35% of the cases as well, but the distribution is less asymmetric, with 9% exceeding the +10% level and 26% exceeding the –10% level.  $E_{ct}$  and  $E_{lt}$  are affected in magnitude beyond the 10% threshold in about 47% and 50% of the cases, with a strong tendency for a decrease of  $E_{ct}$  and an increase of  $E_{lt}$ . When comparing between shape modes, mode 1 is found to cause the most prominent changes.

Shape mode 2 affects mainly  $E_{ll}$ ,  $E_{cl}$ , and  $E_{lt}$ , although only about 20% of the values exceed the threshold of 10%.  $E_{ll}$  and  $E_{cl}$  present a rather symmetric distribution of extreme values, while  $E_{lt}$  has a slight tendency to increase with increase of mode 2. The effect of shape mode 3 on the strains is similar to that of shape mode 2. None of shape modes 4, 5, and 6 affects strains more than the 10% threshold value in more than 10% of the values.

Figure 3.6 shows how variation in geometry through mode  $s_1$  affects cardiac strains as a function of location in the LV, represented through the AHA 17 segment representation for both the sub-endocardium and sub-epicardium. We see that increments along shape mode 1 lead to reductions of  $E_{cc}$  in the apical area, reductions of  $E_{ct}$  mainly in the sub-epicardium, and increments of  $E_{lt}$  in the sub-endocardium. Due to increases along shape mode 1  $E_{ll}$  decreases in the apical regions and increases elsewhere in the sub-epicardium, while both  $E_{cl}$  and  $E_{tt}$  mainly increase in the apical regions.

Variation along shape modes 2 and 3 primarily affected strain components  $E_{ll}$ ,  $E_{cl}$  and  $E_{lt}$  (Figure 3.5). The spatial distribution of the change in these strain components is shown in Figure 3.7. An increase along shape mode 2 affects  $E_{ll}$  more at the epicardium than at the endocardium, with a tendency to decrease  $E_{ll}$  at the septal side and increase it at the lateral side. Similarly, increases along shape mode 3 affect  $E_{ll}$  slightly more at the epicardium, with a tendency to increase  $E_{ll}$  in the inferolateral region and decrease it in the antero-septal region. The effects of variations along both shape mode 2 and 3 affect  $E_{cl}$  similarly at the endocardium and epicardium. Increments in shape mode 2 have the tendency to decrease  $E_{cl}$  in the inferior segments and increase it in the anterior ones, while increments in shape mode 3 have the tendency to increase  $E_{cl}$  in the inferolateral segments and decrease it in the

anteroseptal ones. Transmurally, increases in  $E_{lt}$  due to increments in shape mode 2 mainly shows a shift towards positive values in the sub-endocardial inferior region. Going from endocardium to epicardium, increases in  $E_{lt}$  due to increments in shape mode 3 shift from the infero-septal segments at base to the same segments at equator and decreases in  $E_{lt}$  due to increments in shape mode 3 shift from lateral segments at base to antero-lateral segments at equator. In general for  $E_{ll}$  and  $E_{lt}$  the effects of both shape modes 2 and 3 tend to occur in small scattered regions, while for  $E_{cl}$  these regions are less scattered and they have more spatial consistency.

Table 3.4 shows the ratio  $\hat{\mu}_{i,\alpha\beta}^{avg}/\hat{\sigma}_{i,\alpha\beta}^{avg}$  used to estimate the interactions between the shape modes. The reference value  $2/3$  is used to define three intervals for three level of interactions:  $[0, 2/3]$  for the high interaction region,  $(2/3, 3/2]$  for the moderate interaction region, and  $(3/2, +\infty)$  for the low interaction region. For almost all the shape modes and strain components the ratio is close or above 2, thus falling in the low interaction region, meaning that the effect of a perturbation along a shape mode is about twice as strong than effects due to nonlinear behavior or interactions between shape modes. For  $E_{tt}$ , instead, shape modes 2 to 5 fall in the moderate interaction region. However, those shape modes are considered non influential for  $E_{tt}$  (see Table 3.3) and therefore also the magnitude of either interactions or nonlinear effects, being smaller than  $\hat{\mu}_{i,\alpha\beta}^{avg}$ , are considered non influential.

	$s_1$	$s_2$	$s_3$	$s_4$	$s_5$	$s_6$
$E_{cc}$	4.6	1.9	1.8	1.9	2.0	2.5
$E_{ll}$	3.7	3.4	3.0	3.0	1.8	2.3
$E_{tt}$	1.8	1.5	1.3	1.4	1.3	1.6
$E_{cl}$	2.2	3.9	4.2	2.4	1.6	3.6
$E_{ct}$	3.7	1.8	1.8	2.2	1.8	2.1
$E_{lt}$	3.4	2.2	1.9	2.1	1.9	1.8

**Table 3.4:** Nonlinear behavior and interactions between the shape modes, represented through the ratio between  $\hat{\mu}_{i,\alpha\beta}^{avg}$  and  $\hat{\sigma}_{i,\alpha\beta}^{avg}$ . Values falling within the high interaction range  $[0, 2/3)$  are highlighted in red, values within the moderate interaction interval  $[2/3, 3/2)$  are highlighted in pink, and values within the low interaction interval  $[3/2, +\infty)$  are kept in white background.

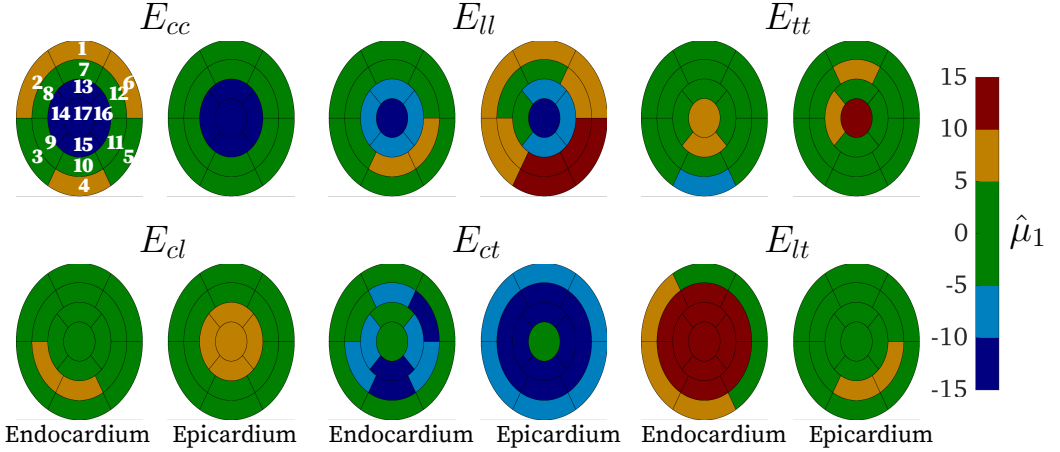


**Figure 3.6:** Effect of variation of shape mode 1 as a function of location in the LV, visualized in an AHA 17 segments representation for the sub-endocardial and the sub-epicardial regions of the LV. The top row shows  $\hat{\mu}_1$  for the normal strains. The bottom row shows  $\hat{\mu}_1$  for the shear strains. The 17 segments are named as follows: 1 basal anterior, 2 basal anteroseptal, 3 basal inferoseptal, 4 basal inferior, 5 basal inferolateral, 6 basal anterolateral, 7 mid anterior, 8 mid anteroseptal, 9 mid inferoseptal, 10 mid inferior, 11 mid inferolateral, 12 mid anterolateral, 13 apical anterior, 14 apical septal, 15 apical inferior, 16 apical lateral, 17 apex.

## 3.4 Discussion

### 3.4.1 Methods

#### Geometry

The geometry of a 3D finite element model is a high resolution parameter that would be unfeasible to treat in a sensitivity study. Therefore, we adopted the Principal Component Analysis, presented by Zhang et al [30] and Medrano-Gracia et al [20], and used the first six shape modes to represent the geometrical feature variation within the population. A disadvantage of our approach is that these modes are not straight forward to interpret, being non trivial three dimensional vector fields. However, they represent a realistic variation of the geometry, and allow us to impose well motivated ranges for variation of the geometry.

To obtain a stress-free configuration, we assumed an ejection fraction  $EF = 60\%$  and that the stress free cavity volume  $V_{c,0}$  is comparable with the end-systolic cavity volume  $V_{c,ES}$ . We then recovered stress free cavity volume using (3.2.14). These assumptions led to physiological values of end-diastolic pressure and to an average ratio  $V_{c,0}/V_w \sim 0.34$  ( $V_w \sim 125\text{mL}$ ,  $V_{c,0} \sim 43\text{mL}$ )

consistent with experimental finding of Nikolić et al [22] ( $V_{c,0}/V_w = 0.29$ ) and McCulloch et al [19] ( $V_{c,0}/V_w = 0.28$ ).

We started from the fiber distribution from [6] and, to preserve the tangentiality of fibers to the surfaces, we re-oriented them using the geometric mapping between the template mesh and the reconstructed end-diastolic configuration. This operation broke the symmetry of the template fiber field and introduced slight and physiological spatial heterogeneity. However, this also introduced slight differences in the fiber orientations of different geometries that might have confounded our results. To this end, further investigations on sensitivity of end-systolic strains to fiber orientation are needed.

### **Fixed preload-fixed afterload experiments**

In this study we evaluate the effect of the amount of detail in the description of the LV geometry on myocardial wall strains. To do so, we employed a finite element simulator of the mechanics of the LV [6]. Simple replacement of the ellipsoidal geometry in the latter model by any of the geometries in the current study, without modifying the circulation model, would have confounded the effects of the geometry with the effect of a possible mismatch between cardiac size and circulation model. To circumvent this problem, we choose to replace the circulation model by pressure boundary conditions of 1.5 kPa at end filling, and 12 kPa during ejection.

### **Sensitivity analysis**

We applied the elementary effects method to compute sensitivity indices of the 3D distribution of end-systolic strains. We decided to observe end-systolic strains referred to the state of end diastole because their measurement is non invasively viable in clinical practice by means of imaging techniques and because more and more inverse approaches to estimate patient's data using computer models rely on strain measurements. Furthermore, at end systole the contraction of myofibers reaches the peak, thus allowing to estimate the pump function of the LV.

Each shape mode has been sampled assuming a uniform distribution. The range of this distribution is within one standard deviation around the mean, with the standard deviation of each mode coming from the principal component analysis. The six shape modes are sorted in descending order with respect to the amount of the overall variance that they describe. Consequently, the first modes were varied more than the last modes. However, this reflects the actual distribution of geometrical features described by the shape modes



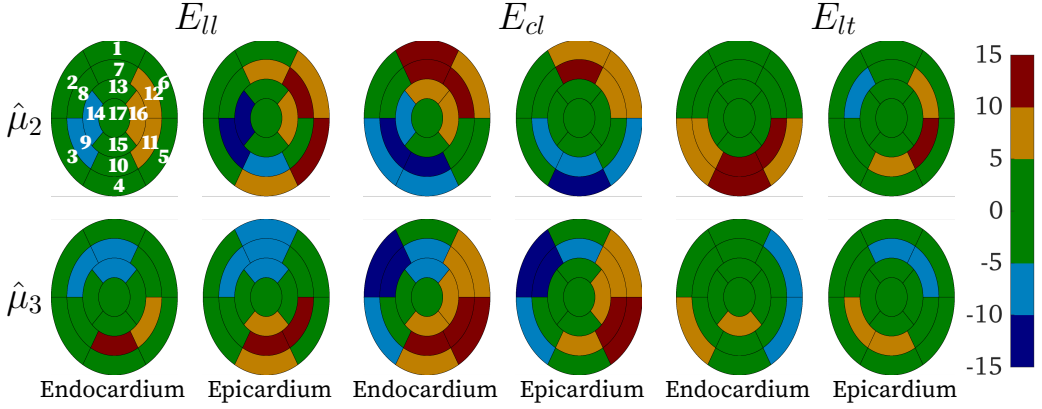


**Figure 3.7:** AHA 17 segments representation for the sub-endocardial and the sub-epicardial regions of the LV. The top row shows  $\hat{\mu}_2$  for  $E_{ll}$ ,  $E_{cl}$ , and  $E_{lt}$ . The bottom row shows  $\hat{\mu}_3$  for the same strains. The 17 segments are named as follows: 1 basal anterior, 2 basal anteroseptal, 3 basal inferoseptal, 4 basal inferior, 5 basal inferolateral, 6 basal anterolateral, 7 mid anterior, 8 mid anteroseptal, 9 mid inferoseptal, 10 mid inferior, 11 mid inferolateral, 12 mid anterolateral, 13 apical anterior, 14 apical septal, 15 apical inferior, 16 apical lateral, 17 apex.

within the human population. Moreover, the magnitude of the difference between geometries induced by each shape mode variation does not always relate with the respective variance. For instance, shape mode 6, which has the smallest variance, introduces differences in geometries larger than shape mode 4 and 5. We scanned the resulting parameter space using 500 trajectories and we computed the three sensitivity indices. We checked the convergence and we found that in the last 50 trajectories the change in the average 1-norm of these indices was two orders of magnitude smaller than the smallest index. The CV of the strain components changed by less than 0.5%.

### 3.4.2 Results

Our results indicate that end-systolic shear strains are more sensitive to geometry than normal strains. The histograms in Figure 3.3 and Figure 3.4 show that the distributions of the coefficients of variation of shear strains  $E_{ct}$  and  $E_{lt}$  present the largest means and standard deviations. The maximum variability for both strains happens between the equatorial and the apical regions, where the CV reaches approximately 30% (Figure 3.4). We cannot exclude that this effect is not only due to the variation in geometry, but also due to a slight variation in fiber orientation. In our model, fiber orientation is defined using normalized coordinates, which are subject to slight errors in the mapping between the template geometry and the unloaded configuration. Considering

that shear strains are more sensitive to fiber orientation than normal strains [? ], this might partly explain the higher sensitivity of shear strains as compared to normal strains.

It is not straightforward to determine a threshold under which a strain variation can be considered non influential. Among others, this threshold value would depend on the methodology of strain measurement, and on the magnitude of the effect that the pathology under investigation has on strains. In particular, the accuracy achieved by a measurement technique is the ultimate limit that allows to distinguish between two strain measurements. Since the accuracy level of the various imaging techniques is unclear, we analyze our results assuming different values of accuracy for the strain measurements. If this accuracy level would be above 15% for every strain component, none of the shape modes would affect the simulated strains in a way that could be discerned by different measurements of the same patient. Therefore, an average geometry could be adopted in this case. If this accuracy level would be about 10%, then Figure 3.5 shows that only shape mode 1 must be considered influential, especially for shear strains  $E_{ct}$  and  $E_{lt}$ . For these strains an increase in shape mode 1 would lead to an observable increase ( $E_{lt}$ ) or decrease ( $E_{ct}$ ) in almost 50% of the geometry. The same holds  $E_{cc}$  and  $E_{ll}$  for which an increase in shape mode 1 exerts an observable decrease in strain in about 30% of the geometry. If the accuracy level would be about 5%, shape mode 1 plays a major role for all the strains with the exception of  $E_{cl}$ , for which shape mode 2 and 3 are more important. The influence of shape mode 1 tends to appear in a more clustered fashion with high spatial coherence, as shown in Figure 3.6. In particular, increments in shape mode 1 greatly contribute in decreasing apical values of  $E_{cc}$  and  $E_{ll}$ , and sub-epicardial values of  $E_{ct}$ , and greatly contribute in increasing sub-endocardial values of  $E_{lt}$ . Instead, the influence of shape modes 2 and 3 mainly affects  $E_{ll}$ ,  $E_{cl}$ , and  $E_{lt}$  and tends to appear in general less strongly than that of shape mode 1, with the only exception of  $E_{cl}$ . As shown in Figure 3.7, the distribution of  $\hat{\mu}_2$  and  $\hat{\mu}_3$  for  $E_{ll}$  and  $E_{lt}$  is more scattered with low spatial coherence, while for  $E_{cl}$  their distribution is more clustered. This means that the way we model the basal diameter, the basal orientation, and the distance between the basal and equatorial plane Figure 3.1 affects the prediction of  $E_{cl}$  as shown in Figure 3.7. From Table 3.3 none of the shape modes present a clear lack of influence, since all values are in the same order of magnitude. However, shape modes 4, 5, and 6 do not affect any of the strain components more than the lowest of the threshold values that we considered in this analysis (5%). In this sense, we consider those three modes non influential.

We used  $\sigma$  to get information about the interaction between shape modes. We

reasoned that  $\mu_i$  measures the effect of an error in setting  $s_i$ , whereas  $\sigma_i$  estimates how  $\mu_i$  changes due to the errors in setting the other parameters. To understand whether  $\sigma_i$  can be considered large, we used the ratio  $\mu_i/\sigma_i$ . This ratio can be seen as a signal to noise ratio: when it is high the error in setting  $s_i$  is stronger than the errors affecting the other parameters interacting with  $s_i$ ; therefore,  $s_i$  must be personalized if considered influential. Conversely when  $\mu_i/\sigma_i$  is low, the interactions dominates the error on  $s_i$  and further investigations are needed to discover which parameters contribute the most to the uncertainty affecting  $s_i$  and possibly personalize them. Finally, when  $\mu_i$  and  $\sigma_i$  are comparable we define the interaction moderate meaning that the error on setting  $s_i$  approximately equals the ones due the error on the other parameters. In this case, if  $\mu_i$  is considered non influential also the interactions are regarded as non significant. If  $\mu_i$  is considered influential more analysis is required to address which parameters interact the most with  $s_i$ . In our analysis, almost all the strain components have a ratio  $\mu_i/\sigma_i$  larger than  $3/2$  for all the shape modes. This means that the shape modes are rather independent and do not interact much. The only exception to this is  $E_{tt}$ , for which we observed a slightly moderate interaction of modes 2 through 5 (Table 3.4); however, due to the non influential nature of those modes (Table 3.3) for the considered strain the relevance of this interaction is limited. The limited interactions found in this study thus did not require further investigations to distinguish between contributions due to non linear behavior and true interactions and suggest that the influential parameters must be prioritized while the non influential ones can be set to generic values without largely affecting the strains. Therefore, if the goal is to accurately observe  $E_{cc}$ ,  $E_{tt}$ , and  $E_{ct}$ , shape mode 1, representing the size variation within the human population, must be included in the personalization of the geometry. To correctly predict  $E_{ll}$ ,  $E_{cl}$ , and  $E_{lt}$ , shape mode 2 and shape mode 3 must be personalized, representing the basal diameter/orientation in the anteroseptal-inferolateral direction and the basal orientation in the inferoseptal-anterolateral direction, respectively.

The data set included in this work has been used elsewhere to understand how pathologies such as myocardial infarction affect the remodeling of the heart [26]. The purpose of those studies was to establish the effectiveness of algorithms that try to categorize the health state of a patient based on the shape of the heart. However, our goal is to contribute to approaches that aim for a physics based interpretation of measured quantities by using data assimilation techniques. In this approach it is important to quantify the sensitivity to input data and to prioritize them. In our study, we quantify the effect of one of these inputs, the geometry, on strains, and sort geometrical features

(the shape modes) by importance. The application of sensitivity analysis techniques to investigate the effect of geometry on output of models of cardiac mechanics is not new. Campos et al [8] applied the probabilistic collocation method to study the effects of wall thickness uncertainty during the passive filling. They included among the quantities of interest end-diastolic Cauchy fiber stress and Green-Lagrange fiber strain averaged in a region of the lateral side of the myocardium. They concluded that stress is the highly influenced by wall thickness and that the effect of uncertainty in wall thickness is comparable with, and in some cases larger than, the one due to uncertainty in the wall stiffness. Choi et al [10] studied the role of geometric features of an ellipsoidally shaped LV, such as sphericity and volume (and indirectly wall thickness), concluding that the transmural distribution of end-diastolic fiber stress and strain are strongly affected by the longitudinal curvature and wall thickness. However, the geometries included in their study do not always reflect the human anatomy and they did not quantify the sensitivity of the quantities of interest. Furthermore, both the studies of Campos and Choi address passive filling only. Geerts et al [14] investigated the role of geometry in an ellipsoidally shaped LV during systole. They found that LV geometry variations considered representative for the biological range changed the equatorial distribution of active myofiber stress and shortening by about 10 to 15%. Pluijmert et al [24] performed a local sensitivity analysis on a biventricular geometry varying both left and right ventricles and also myofiber orientation. They concluded that varying the short- to long-axis ratio by 27% in the LV and the length of the right ventricle by 16% led to changes in the pump work of about 5%. The studies by Geerts et al [14] and Pluijmert et al [24] addressed pump function at tissue and organ level, but they did not focus on changes in strains. That is what we aimed at in our current study, in view of the potential use of strains as an input for a data assimilation procedure. In a preliminary study [4], we presented our methodology for the global sensitivity of end-systolic strains with a brief overview on preliminary results. In this study we better summarized the uncertainty on the spatial distribution of strains using the averaged 1-norm, bar plots and by using the AHA17 representation to identify regions affected the most by shape mode variations. According to our knowledge, this is the first work in which a detailed description of real human LV geometries has been used in a global sensitivity analysis framework to systematically quantify the effect that variations in the geometry description introduce on 3D end-systolic strain fields.

### 3.4.3 Limitations

Limitations of this study are related to the choice of the mathematical model, the availability of data, and the computational cost. Regarding the mathematical model, we assumed the onset of active stress development to be simultaneous throughout the geometry. Even though it has been suggested that pattern of mechanical activation is less inhomogeneous than pattern of electrical depolarization [17], the effect of asynchronous mechanical activation might be investigated. Regarding the availability of data, we note that the shape modes included information about the LV only. For this reason we only use an isolated LV geometry. Although in principle it might be possible to extend our analysis to bi-ventricular geometries, we expect that adding the right ventricle might affect the spatial distribution of LV strains, but not so much the sensitivity indices. Another source of uncertainty concerns the boundary conditions. The uniform pressure boundary condition at the endocardial surface and the stress free conditions at the epicardial surface are commonly used in other models in literature and considered appropriate. Applying realistic boundary conditions at the base, to represent the interactions with the atria and the large arteries is less obvious. At the base we avoided rigid body motions trying not to constrain the basal deformations too much. In fact, we adopted the same boundary conditions applied in [6], that are in line with other models in literature and comply with the findings of a recent study comparing different choices of boundary conditions [23]. Due to the high computational cost related to the sensitivity analysis we performed, we could not refine the grid for the discretization of the shape mode space. This would have required further compromises in the discretization of the finite element solution or the use of meta-modeling techniques. This also motivated our choice for a uniform distribution in the shape mode space; at a higher resolution it would be more natural to better approximate a Gaussian distribution. Consequently, our analysis is affected by a slight over representation of extreme geometries that we tried to contain by limiting the domain to only one standard deviation around the average geometry.

## 3.5 Conclusions

In this work we assessed the sensitivity of LV end-systolic wall strains to LV geometry, varied according to six shape modes reported in literature [30, 20]. We concluded that shape mode 1 (related to LV size) must be personalized for an accurate prediction of  $E_{cc}$ ,  $E_{tt}$ , and  $E_{ct}$ . For an accurate prediction of  $E_{ll}$ ,  $E_{cl}$ , and  $E_{lt}$  also shape modes 2 and 3 (related to the basal diameter and its ori-

entation in the anteroseptal-inferolateral direction, and the basal orientation in the inferoseptal-anterolateral direction) must be included in the personalization of the geometry. Instead, shape modes 4, 5, and 6 can be set to a generic value without largely affecting the prediction of strains. To the best of our knowledge this is the first attempt to apply global sensitivity techniques to quantify the effects that different real human LV geometries have on 3D end-systolic strain fields.

## **Acknowledgement**

This work was supported by the European Commission within the Horizon 2020 Framework through the MSCA-ITN-ETN European Training Networks (project number 642458).

## Bibliography

- [1] M. S. Alnæs, J. Blechta, J. Hake, A. Johansson, B. Kehlet, A. Logg, C. Richardson, J. Ring, M. E. Rognes, and G. N. Wells. The fenics project version 1.5. *Archive of Numerical Software*, 3(100), 2015.
- [2] P. R. Amestoy, A. Guermouche, J.-Y. L'Excellent, and S. Pralet. Hybrid scheduling for the parallel solution of linear systems. *Parallel Computing*, 32(2):136–156, 2006.
- [3] G. Balaban, H. Finsberg, S. Funke, T. F. Håland, E. Hopp, J. Sundnes, S. T. Wall, and M. E. Rognes. In vivo estimation of elastic heterogeneity in an infarcted human heart. *Biomechanics and Modeling in Mechanobiology*, 17(5):1317–1329, 2018.
- [4] L. Barbarotta and P. Bovendeerd. A computational approach on sensitivity of left ventricular wall strains to geometry. In *International Conference on Functional Imaging and Modeling of the Heart*, pages 240–248. Springer, 2019.
- [5] D. E. Bild, D. A. Bluemke, G. L. Burke, R. Detrano, A. V. Diez Roux, A. R. Folsom, P. Greenland, D. R. Jacobs Jr., R. Kronmal, K. Liu, et al. Multi-ethnic study of atherosclerosis: objectives and design. *American journal of epidemiology*, 156(9):871–881, 2002.
- [6] P. H. M. Bovendeerd, W. Kroon, and T. Delhaas. Determinants of left ventricular shear strain. *American Journal of Physiology-Heart and Circulatory Physiology*, 297(3):H1058–H1068, 2009.
- [7] F. Campolongo, J. Cariboni, and A. Saltelli. An effective screening design for sensitivity analysis of large models. *Environmental modelling & software*, 22(10):1509–1518, 2007.
- [8] J. O. Campos, J. Sundnes, R. W. dos Santos, and B. M. Rocha. Effects of left ventricle wall thickness uncertainties on cardiac mechanics. *Biomechanics and modeling in mechanobiology*, pages 1–13, 2019.
- [9] R. Chabiniok, P. Moireau, P. F. Lesault, A. Rahmouni, J. F. Deux, and D. Chapelle. Estimation of tissue contractility from cardiac cine-mri using a biomechanical heart model. *Biomechanics and modeling in mechanobiology*, 11(5):609–630, 2012.

- 
- [10] H. F. Choi, J. D’hooge, F. E. Rademakers, and P. Claus. Influence of left-ventricular shape on passive filling properties and end-diastolic fiber stress and strain. *Journal of Biomechanics*, 43(9):1745–1753, 2010.
- [11] W. Donders, W. Huberts, F. van de Vosse, and T. Delhaas. Personalization of models with many model parameters: an efficient sensitivity analysis approach. *International journal for numerical methods in biomedical engineering*, 31(10), 2015.
- [12] H. Finsberg, G. Balaban, S. Ross, T. F. Håland, H. H. Odland, J. Sundnes, and S. T. Wall. Estimating cardiac contraction through high resolution data assimilation of a personalized mechanical model. *Journal of Computational Science*, 24:85 – 90, 2018.
- [13] C. G. Fonseca, M. Backhaus, D. A. Bluemke, R. D. Britten, J. D. Chung, B. R. Cowan, I. D. Dinov, J. P. Finn, P. J. Hunter, A. H. Kadish, et al. The cardiac atlas project—an imaging database for computational modeling and statistical atlases of the heart. *Bioinformatics*, 27(16):2288–2295, 2011.
- [14] L. Geerts, R. Kerckhoffs, P. Bovendeerd, and T. Arts. Towards patient specific models of cardiac mechanics: A sensitivity study. In I. E. Magnin, J. Montagnat, P. Clarysse, J. Nenonen, and T. Katila, editors, *Functional Imaging and Modeling of the Heart*, pages 81–90, Berlin, Heidelberg, 2003. Springer, Springer Berlin Heidelberg.
- [15] S. Govindjee and P. A. Mihalic. Computational methods for inverse deformations in quasi-incompressible finite elasticity. *International Journal for Numerical Methods in Engineering*, 43(5):821–838, 1998.
- [16] D. E. Hurtado, S. Castro, and P. Madrid. Uncertainty quantification of 2 models of cardiac electromechanics. *International Journal for Numerical Methods in Biomedical Engineering*, 33(12):e2894, 2017. e2894 cnm.2894.
- [17] R. Kerckhoffs, P. Bovendeerd, J. Kotte, F. Prinzen, K. Smits, and T. Arts. Homogeneity of cardiac contraction despite physiological asynchrony of depolarization: a model study. *Annals of biomedical engineering*, 31(5):536–547, 2003.
- [18] S. Marchesseau, H. Delingette, M. Sermesant, R. Cabrera-Lozoya, C. Tobon-Gomez, P. Moireau, R. M. Figueras i Ventura, K. Lekadir, A. Hernandez, M. Garreau, et al. Personalization of a cardiac electromechani-



- cal model using reduced order unscented kalman filtering from regional volumes. *Medical image analysis*, 17(7):816–829, 2013.
- [19] A. D. McCulloch, B. Smaill, and P. Hunter. Regional left ventricular epicardial deformation in the passive dog heart. *Circulation research*, 64(4):721–733, 1989.
- [20] P. Medrano-Gracia, B. R. Cowan, B. Ambale-Venkatesh, D. A. Bluemke, J. Eng, J. P. Finn, C. G. Fonseca, J. A. C. Lima, A. Suinesiaputra, and A. A. Young. Left ventricular shape variation in asymptomatic populations: the multi-ethnic study of atherosclerosis. *Journal of Cardiovascular Magnetic Resonance*, 16(1):56, Jul 2014.
- [21] M. D. Morris. Factorial sampling plans for preliminary computational experiments. *Technometrics*, 33(2):161–174, 1991.
- [22] S. Nikolić, E. L. Yellin, K. Tamura, H. Vetter, T. Tamura, J. S. Meisner, and R. Frater. Passive properties of canine left ventricle: diastolic stiffness and restoring forces. *Circulation Research*, 62(6):1210–1222, 1988.
- [23] M. Peirlinck, K. L. Sack, P. De Backer, P. Morais, P. Segers, T. Franz, and M. De Beule. Kinematic boundary conditions substantially impact in silico ventricular function. *International journal for numerical methods in biomedical engineering*, 35(1):e3151, 2019.
- [24] M. Pluijmert, T. Delhaas, A. F. de la Parra, W. Kroon, F. W. Prinzen, and P. H. M. Bovendeerd. Determinants of biventricular cardiac function: a mathematical model study on geometry and myofiber orientation. *Biomechanics and Modeling in Mechanobiology*, 16(2):721–729, 2017.
- [25] A. Saltelli, M. Ratto, T. Andres, F. Campolongo, J. Cariboni, D. Gatelli, M. Saisana, and S. Tarantola. *Global sensitivity analysis: the primer*. John Wiley & Sons, 2008.
- [26] A. Suinesiaputra, P. Ablin, X. Albà, M. Alessandrini, J. Allen, W. Bai, S. Çimen, P. Claes, B. R. Cowan, J. D’hooge, N. Duchateau, J. Ehrhardt, A. F. Frangi, A. Gooya, V. Grau, K. Lekadir, A. Lu, A. Mukhopadhyay, I. Oksuz, N. Parajuli, X. Pennec, M. Pereañez, C. Pinto, P. Piras, M. Rohé, D. Rueckert, D. Säring, M. Sermesant, K. Siddiqi, M. Tabassian, L. Teresi, S. A. Tsaftaris, M. Wilms, A. A. Young, X. Zhang, and P. Medrano-Gracia. Statistical shape modeling of the left ventricle: Myocardial infarct classification challenge. *IEEE Journal of Biomedical and Health Informatics*, 22(2):503–515, March 2018.

- [27] V. Y. Wang, H. I. Lam, D. B. Ennis, B. R. Cowan, A. A. Young, and M. P. Nash. Modelling passive diastolic mechanics with quantitative mri of cardiac structure and function. *Medical image analysis*, 13(5):773–784, 2009.
- [28] J. Xi, P. Lamata, J. Lee, P. Moireau, D. Chapelle, and N. Smith. Myocardial transversely isotropic material parameter estimation from in-silico measurements based on a reduced-order unscented kalman filter. *Journal of the mechanical behavior of biomedical materials*, 4(7):1090–1102, 2011.
- [29] J. Xi, P. Lamata, S. Niederer, S. Land, W. Shi, X. Zhuang, S. Ourselin, S. G. Duckett, A. K. Shetty, C. A. Rinaldi, et al. The estimation of patient-specific cardiac diastolic functions from clinical measurements. *Medical image analysis*, 17(2):133–146, 2013.
- [30] X. Zhang, B. R. Cowan, D. A. Bluemke, J. P. Finn, C. G. Fonseca, A. H. Kadish, D. C. Lee, J. A. C. Lima, A. Suinesiaputra, A. A. Young, et al. Atlas-based quantification of cardiac remodeling due to myocardial infarction. *PloS one*, 9(10):e110243, 2014.



## **Chapter 4**

# **In Silico Assessment of Sensitivity of LV Wall Strains to Fiber Orientation**

**Abstract**

In this chapter we use a Finite Element model of left ventricular (LV) mechanics to assess the sensitivity of LV end systolic wall strains to fiber orientation. A 5-parameter rule based description of the fiber orientation in terms of helix and transverse angles has been used to describe the spatial variation throughout the LV wall. The five parameters include: the transmural offset  $h_v^0$ , the transmural slope  $h_v^1$ , and the longitudinal slope  $h_u^1$  of the helix angle; and the longitudinal offset  $t_u^0$ , and the longitudinal slope  $t_u^1$  of the transverse angle. The ranges for the five parameters represent the variability within the human population, as inferred from DTI measurements found in literature. End systolic Green-Lagrange strains with respect of the end diastolic state were expressed with respect to the local circumferential (c), longitudinal (l) and transmural (t) direction. The results show that the strain components most affected by fiber orientation are  $E_{ct}$  ( $38 \pm 18\%$ ), and  $E_{cl}$  ( $25 \pm 8\%$ ). The most influential parameters are found to be  $t_u^0$  and  $h_v^0$ .  $t_u^0$  affects all the strain components, but in particular  $E_{ct}$  ( $\sim 35\%$ ), and the  $h_v^0$  affects especially  $E_{cl}$  ( $\sim 18\%$ ). Furthermore,  $t_u^0$  interacts mostly with  $t_u^1$ , and vice-versa.

## 4.1 Introduction

Computer models of the heart are developing towards a stage where they can be used in the context of personalized medicine. These models have been used in recent studies to estimate cardiac (pathological) tissue properties from patients by combining patient measured deformation data and data assimilation techniques. It is expected that the spatio-temporal maps of cardiac deformation constitute a rich source of information for retrieval of spatial maps of tissue properties. Some studies estimated passive material properties of the myocardium [36, 37, 38], while others aimed at estimating contractility and activation time [9, 1, 8, 18]. While data assimilation methods are precious tools that potentially make possible the transition from research models to models that can be used in the clinic, for a reliable clinical use of such methods it is also important to provide interval confidence of the validity of the provided solution. Sensitivity Analysis (SA) and Uncertainty Quantification (UQ) are essential steps in this process, allowing to estimate and weigh uncertainty coming from modeling assumptions, noise, and measurement error propagated from the input.

In models of cardiac mechanics, fiber orientation is both a major source of uncertainty and an important determinant of tissue stress and strain, as shown in [28, 12]; nonetheless, fiber orientation is typically modeled only in terms of a linearly varying helix angle [10, 16, 27, 30]. Streeter et al [33] made one of the first attempts to perform histological measurements on fiber orientation and identified the helix angle, the angle defining the base-to-apex component of the fiber vector (see Figure 4.1), to vary non-linearly in transmural direction, between  $60^\circ$  at endocardium and  $-60^\circ$  at epicardium. In a later study, Streeter et al [32] also identified the transverse angle, describing the endocardium-to-epicardium component of the fiber vector; in the apical part of the left ventricle it was found to be small and negative. These findings were later confirmed in other studies performed using Diffusion Tensor Imaging (DTI) [11]. Lombaert et al [17] built an atlas of myofiber orientation from a population of 10 ex-vivo healthy human hearts and provided an estimation of the distributions of the helix and the transverse angle within the human population. Typically, the measurement error of these angles is about  $10^\circ$  [11]. To create a patient-specific model, ideally fiber orientation should be measured in vivo. The main challenges for in-vivo fiber orientation measurements are the long acquisition time and the movement of the heart. To reduce the long acquisition time of fully 3D in-vivo DTI measurements, DTI acquisitions on several short-axis slices of the ventricles are used in the reconstruction of the 3D fields [34]. Typically, the in-vivo measurement error is higher than

the ex-vivo DTI measurement error. Due to its low magnitude (about  $10^\circ$ ), the transverse angle is more affected by this error.

In view of the limited accuracy with which fiber orientation can be determined, it is important to quantify how the output of computer models of the mechanics of the heart are affected by this uncertainty. Few studies are present in literature in this context. Some of them only qualitatively investigated the sensitivity of cavity volume, and fiber stress and strain during the passive filling to variations of the helix angle [13, 35, 24]. Often non-physiological values for the helix angle were used, such as constant helix angles [13] or spatial distributions of the helix angle with a transmural range much smaller ( $60^\circ$ , [35, 24]) or much larger ( $160^\circ$ , [24]) than the histologically observed range of about  $120^\circ$ . Only in [13, 35, 24] a physiological transverse angle was included, showing no influence on end-diastolic cavity volume.

A more quantitative and complete UQ technique has been employed in Rodriguez-Cantano et al [29] to quantify the sensitivity to both rule-based fiber orientation (using both helix and transverse angles) and random fiber fields. They computed the main and total Sobol indices for four scalar global quantities of interest based on Quasi-Monte Carlo (QMC) simulations, Polynomial Chaos Expansion (PCE), and Karhunen-Loève expansion. However, the observed LV end-diastolic quantities can be easily measured using imaging techniques but provided no insight about how the local mechanics is affected by the uncertainty. Geerts et al [12] compared the sensitivity of fiber stress and strain during the active phase of the cardiac cycle to limited variations in geometry and helix angle using a LV model. Pluijmert et al [28] compared the sensitivity of averaged local and global quantities to variations in the biventricular (BIV) geometry and variation in the fiber orientation according to a remodeling algorithm presented in Kroon et al [15]. In the latter, it is difficult to properly quantify the sensitivity to the specific parameters determining the fiber orientation, such as helix and transverse angle and their spatial distribution. Both studies suggest that fiber orientation plays a major role in the mechanics of the LV during the active phase. However, the variations in fiber orientation included in Geerts et al [12] are somewhat arbitrary and involved only the helix angle, while those included in Pluijmert et al [28] were determined by an algorithm and may not be realistic. Moreover, these studies used a local sensitivity approach in which a quantitative assessment of quantities of interest was achieved over only few parameter combinations.

For this reason, the goal of this study is to quantify the effects that variations in the fiber description within the variability observed in the human population have on end-systolic strain distributions of a computer model of the LV mechanics with a realistic geometry and to assess the sensitivity to the parame-

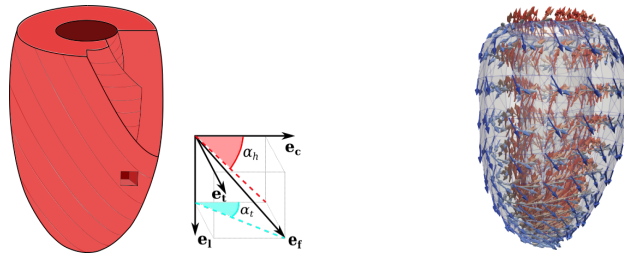


**Figure 4.1:** Representation of the helix and transverse angles definitions (left) and reference fiber field for the unloaded average geometry (right). The helix angle,  $\alpha_h$ , is the angle between the circumferential direction ( $e_c$ ) and the projection of the fiber vector ( $e_f$ ) onto the circumferential-longitudinal plane. The transverse angle,  $\alpha_t$ , is the angle between the circumferential direction and the projection of the fiber vector onto the circumferential-transmural plane.

ters describing the fiber field. Besides quantifying the uncertainty propagated from fiber orientation to the strains, the results of this analysis might give a precious insight to the development of a personalization method to compute fiber orientation [21, 22], highlighting possible relations between strains and fiber parameters. Moreover, to put the results into perspective, we compare the effect that realistic variations on the description of the LV geometry and realistic variations on fiber orientation have on end-systolic strain distributions.



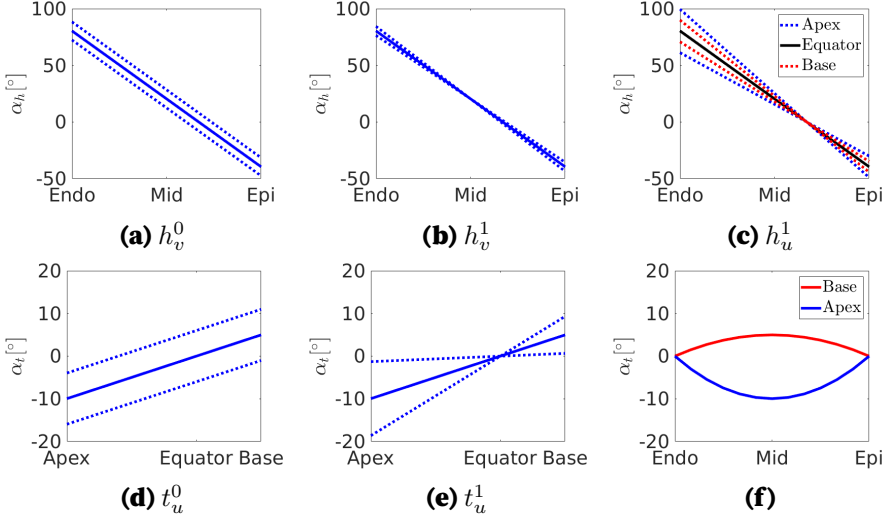


**Figure 4.2:** Representation of the meaning of the parameters involved in the description of the helix and transverse angles. 4.2a and 4.2b show the influence of  $h_v^0$  and  $h_v^1$  on the transmural variation of the helix angle at equator. The solid lines represent their reference values and the dashed lines their two extremes. 4.2c shows how  $h_u^1$  affects the transmural and longitudinal distribution of the helix angle. The black solid line represents the reference extreme values of  $h_u^1$  at the equator, the blue dashed lines represents the extremes of  $h_u^1$  at the apex, and the red dashed lines represents the extremes of  $h_u^1$  at the base. The bottom row shows how the parameters involved in the description of the transverse angle affect its longitudinal distribution. 4.2d and 4.2e show the influence of  $t_u^0$  and  $t_u^1$ , respectively. The solid lines represent their reference values and the dashed lines their two extremes. 4.2f shows the transmural distribution of the transverse angle using reference values for  $t_u^0$  and  $t_u^1$ .

## 4.2 Material and methods

### 4.2.1 Material properties

We simulated LV mechanics using the model by Bovendeerd et al [6]. Briefly, the myocardium is described as an hyperelastic fiber-reinforced transversely isotropic active stress material. The Cauchy stress tensor  $\sigma$  thus reads

$$\sigma = \sigma_p + \sigma_a \vec{e}_f \otimes \vec{e}_f. \quad (4.2.1)$$

The active stress  $\sigma_a$  is adopted from Bovendeerd et al [6]. It depends on sarcomere and contractile element lengths, time elapsed since activation (assumed to be simultaneous throughout the ventricle) and sarcomere shortening velocity, and acts along the current fiber direction  $\vec{e}_f$  (see 2.2.1 for details). The passive stress  $\sigma_p$  is derived from a strain energy density function as fol-

lows

$$\boldsymbol{\sigma}_p = \frac{1}{\det(\mathbf{F})} \mathbf{F} \frac{\partial \mathcal{W}}{\partial \mathbf{E}} \mathbf{F}^T, \quad (4.2.2)$$

where  $\mathcal{W}$  is composed of a term  $\mathcal{W}^{shape}$ , describing response to change in shape, and a term  $\mathcal{W}^{volume}$ , representing near incompressibility:

$$\mathcal{W} = \mathcal{W}^{shape} + \mathcal{W}^{volume}, \quad (4.2.3)$$

$$\mathcal{W}^{shape} = a_0 (\exp Q - 1), \quad (4.2.4)$$

$$Q = a_1 \mathcal{I}_1^2 + 2a_2 \mathcal{I}_2 + a_3 \mathcal{I}_{4,f}^2, \quad (4.2.5)$$

$$\mathcal{W}^{volume} = 4k (J^2 - 1 - 2 \ln J), \quad (4.2.6)$$

where  $\mathcal{I}_{\{1,2\}}$  are the invariants of the Green-Lagrange tensor  $\mathbf{E}$ ,  $\mathcal{I}_{4,f}$  is the pseudo-invariant of  $\mathbf{E}$  introducing the anisotropy along myofibers,  $J$  is the determinant of the deformation gradient  $\mathbf{F}$ , and  $a_{\{0,1,2,3\}}$  and  $k$  are a constitutive parameters. Note that  $\mathcal{W}^{volume}$  was modified from Bovendeerd et al [6] according to Simo et al [?] to comply with assumptions of positivity, convexity, and unboundedness at both zero and infinity.

## 4.2.2 Geometry and fiber orientation

We use a realistic geometry derived from the MESA study [20]. This geometry and its fiber field are obtained using a transformation that deforms a template geometry and its fiber field. The template geometry is an idealized geometry defined by the prolate ellipsoidal coordinate system

$$\begin{cases} x = f_l \sinh(\xi) \sin(\theta) \cos(\phi) \\ y = f_l \sinh(\xi) \sin(\theta) \sin(\phi) \\ z = f_l \cosh(\xi) \cos(\theta) \end{cases} \quad (4.2.7)$$

where  $f_l$  is the focal length set to 43 mm. The endocardial and epicardial surfaces are defined by  $\xi = 0.371$  and  $\xi = 0.678$ , respectively. The base is modeled as a plane orthogonal to the long axis intersecting the geometry at 24 mm. On this geometry, the circumferential  $\vec{e}_c$ , the longitudinal  $\vec{e}_l$ , and transmural  $\vec{e}_t$  basis vectors are defined as in 2.2.1. Geometry and mesh generation, the computation of the normalized transmural ( $v$ ) and longitudinal ( $u$ ) coordinates, and the mapping of scalar and vector fields are performed using the method presented in 3.2.

The orientation of fibers inside the myocardium is described by the helix angle and the transverse angle, where the helix angle defines the component

of the fiber unit vector,  $\vec{e}_f$ , in the longitudinal-circumferential plane and the transverse angle defines the component in the circumferential-transmural plane (Figure 4.1).

The functional description of  $\alpha_h$  and  $\alpha_t$  characterizes the fiber orientation inside the myocardium. To this end, we use five parameters, three for the helix angle and two for the transverse angle

$$\alpha_h(u, v) = (h_v^0 + h_v^1 v) (1 + h_u^1 u), \quad (4.2.8)$$

$$\alpha_t(u, v) = (1 - v^2) (t_u^0 + t_u^1 u). \quad (4.2.9)$$

The five parameters introduce variability in the fiber orientation as follows (see Figure 4.2):  $h_v^0$  describes the transmural offset of the helix angle,  $h_v^1$  describes the transmural slope and defines the transmural range of the helix angle,  $h_u^1$  describes the longitudinal variability of the helix angle,  $t_u^0$  describes the longitudinal offset of the transverse angle ( $t_u^0 = 0$  means that the transverse angle is nil at equator),  $t_u^1$  describes the longitudinal slope of the transverse angle. Note that the transverse angle is assumed to be always null on both the endocardial and epicardial surfaces and that its transmural distribution is assumed to be parabolic. Geometry and fiber orientation are shown in Figure 4.1 and the parameter representations are shown in Figure 4.2.

### 4.2.3 Fiber parameter ranges

The reference values for the five parameters describing the helix and the transverse angles have been obtained performing an analytical projection on our model of the helix angle reported in Bovendeerd et al [6] and the transverse angle reported in Geerts et al [11] using the scalar product defined in  $L^2([-1, 0.5] \times [-1, 1])$  (central values in Table 4.1).

For each parameter, we set a range around its reference value to describe the interval in which the parameter will be varied during the sensitivity analysis. We inferred the parameters ranges mainly from two studies: from Lombaert et al [17], who used DTI to measure fiber fields in 10 ex-vivo healthy human hearts; and from Geerts et al [11], who used DTI to measure fiber orientation in a population of 5 ex-vivo healthy goat hearts. We interpreted the mode of the standard deviation of the helix angle reported in Lombaert et al [17] ( $11.5^\circ$ ) as the maximum helix angle variation achievable by any combination of  $h_v^0$  and  $h_v^1$ . Therefore, we allowed variation of about  $8^\circ$  on  $h_v^0$ . Since  $h_v^1$  represents half of the range of the transmural distribution of  $\alpha_h$ , we set its variation to  $4^\circ$ . The parameter  $h_u^1$  represents longitudinal variation in the helix angle. We vary this parameter by  $\pm 0.25$  to represent the standard deviation of about  $20^\circ$

$\alpha_h$			$\alpha_t$	
$h_v^0$	$h_v^1$	$h_u^1$	$t_u^0$	$t_u^1$
$20.43^\circ \pm 8^\circ$	$60^\circ \pm 4^\circ$	$0 \pm 0.25$	$0^\circ \pm 6^\circ$	$9.96^\circ \pm 8.67^\circ$

**Table 4.1:** Central parameter combination  $\pm$  parameter ranges. The central parameter combination is obtained as the least square projection of the helix angle from Bovendeerd et al [6] and the transverse angle from Geerts et al [11] onto our five parameters model (4.2.8) (4.2.9).

found in the mean fiber configuration in Lombaert et al [17]. The variation in  $t_u^0$  was set to  $\pm 6^\circ$ , based on the longitudinal distribution of the transverse angle presented by Geerts et al [11]. The range for  $t_u^1$  was set using the mode of the standard deviation of the transverse angle reported in Lombaert et al [17] ( $13^\circ$ ). This value was re-scaled using the range of the longitudinal parameter  $u$ , thus leading to  $8.67^\circ$ . The reference parameters and their variations are shown in Table 4.1.

#### 4.2.4 Computation of left ventricular wall mechanics

Left ventricular wall mechanics was computed by solving for equilibrium between forces related to active stress, passive stress and cavity pressure, as explained in detail in 2.2.1. In short,

$$\left\{ \begin{array}{ll} \text{Div}(\mathbf{P}(\mathbf{F})) = \vec{0} & \text{in } \Omega_0, \\ \mathbf{P}\vec{n}_0 = -p\mathbf{J}\mathbf{F}^{-T}\vec{n}_0 & \text{on } \Gamma_{0,Endo}, \\ \mathbf{P}\vec{n}_0 = \vec{0} & \text{on } \Gamma_{0,Epi}, \end{array} \right. \quad (4.2.10)$$

where  $\mathbf{P}$  is the first Piola-Kirchhoff stress tensor;  $\mathbf{F}$  is the deformation gradient; and  $\partial\Omega_0 = \Gamma_{0,Base} \cup \Gamma_{0,Endo} \cup \Gamma_{0,Epi}$  represents the decomposition of the unloaded boundary in basal, endocardial and epicardial surfaces, respectively; and  $\vec{n}_0$  is the normal vector defined over those surfaces. To prevent rigid body motion we suppressed displacement normal to the basal plane and circumferential displacement of the basal endocardium. We did not couple our LV model to the closed circulation model described in [6]. Instead, we let the heart fill until a fixed preload of 1.5 kPa was reached. From this end-diastolic state, we then simulated the isovolumic contraction phase by initiating active stress development and computing the increase of cavity pressure while keeping cavity volume constant. As soon as cavity pressure reached a preset afterload pressure of 12 kPa, we let the heart eject against this constant pressure until it reached the end-systolic state, defined as the state of minimum cavity volume. From the simulations, end-systolic strains with respect

to the end-diastolic configuration were computed using the Green-Lagrange strain tensor along the wall-bound basis vectors in circumferential ( $\vec{e}_c$ ), longitudinal ( $\vec{e}_l$ ), and transmural ( $\vec{e}_t$ ) directions.

### 4.2.5 Computation of the unloaded configuration

To perform a finite element simulation of LV mechanics we need to recover a virtually unloaded configuration from the loaded end-diastolic configuration, provided in the atlas. In order to estimate this unloaded configuration, we followed the same procedure as the one in 3.2.4. We deflated the end-diastolic configuration, obtained from the atlas of the MESA study [20], using a standard approach based on the concept of Inverse Design [3]. This method relies on the solution of the momentum balance equation in the deformed configuration  $\Omega$  as follows

$$\begin{cases} \operatorname{div}(\boldsymbol{\sigma}(\mathbf{F})) = \vec{0} & \text{in } \Omega, \\ \boldsymbol{\sigma}\vec{n} \cdot \vec{n} = -p & \text{on } \Gamma_{Endo}, \\ \boldsymbol{\sigma}\vec{n} = \vec{0} & \text{on } \Gamma_{Epi}, \end{cases} \quad (4.2.11)$$

and the same kinematic boundary conditions of (3.2.8). The sought solution is the displacement from  $\Omega$  to the virtually stress free configuration  $\Omega_0$

$$\vec{x}_0(\vec{x}) = \vec{x} - \vec{u}(\vec{x}), \quad (4.2.12)$$

$$\mathbf{F}(\vec{x}_0) = \frac{\partial \vec{x}}{\partial \vec{x}_0}(\vec{x}_0). \quad (4.2.13)$$

Since  $\Omega_0$  and its metric are unknown, the derivatives involved in the definition of  $\mathbf{F}$  cannot be computed. However, the problem can be circumvented by using the spatial deformation gradient  $\mathbf{f}$ , defined as

$$\begin{aligned} \mathbf{f}(\vec{x}) &= \left( \mathbf{I} - \frac{\partial \vec{u}(\vec{x})}{\partial \vec{x}} \right) \\ &= \left( \mathbf{I} + \frac{\partial \vec{u}(\vec{x}_0)}{\partial \vec{x}_0} \right)^{-1} \Bigg|_{\vec{x}_0 = \vec{x} - \vec{u}} = \mathbf{F}^{-1}(\vec{x}). \end{aligned} \quad (4.2.14)$$

Consequently the Cauchy stress tensor reads

$$\begin{aligned} \boldsymbol{\sigma}(\mathbf{F}) &= \boldsymbol{\sigma}(\mathbf{f}^{-1}) \\ &= \frac{\mathbf{f}^{-1}}{\det(\mathbf{f}^{-1})} \frac{\partial \mathcal{W}}{\partial \mathbf{E}} \Bigg|_{\mathbf{F} = \mathbf{f}^{-1}} \mathbf{f}^{-T}, \end{aligned} \quad (4.2.15)$$

where we assumed that no residual active stress  $\sigma_a$  is present during diastole. To solve (4.2.11), an end-diastolic pressure load  $p$  is needed. Since the pressure is unknown, we increment the pressure load until the unloaded configuration reaches an estimated unstressed cavity volume. We assumed that under normal circumstances this volume  $V_{c,0}$  would be equal to  $V_{c,ES}$ , the volume at end ejection. In turn, this volume was estimated from the end-diastolic cavity volume by assuming a physiological ejection fraction (EF) of 60%

$$V_{c,0} \approx V_{c,ES} = (100 - EF) V_{c,ED}. \quad (4.2.16)$$

Note that the solution of (4.2.11) modifies the domain on which the fibers are defined and affects their orientation. Therefore, fiber orientation in the unloaded state  $\vec{e}_{f,0}$  is defined as a function of  $\mathbf{f}$  and  $\vec{e}_{f,ED}$  as follows

$$\vec{e}_{f,0} = \frac{\mathbf{f}\vec{e}_{f,ED}}{\|\mathbf{f}\vec{e}_{f,ED}\|_2}. \quad (4.2.17)$$

#### 4.2.6 Finite element implementation

We use the same Finite Element model described in 3.2.5. The spatial discretization of the problem was studied in order to achieve an accurate prediction of strains at an affordable computational cost. In this respect, we use a sub-parametric finite element approach where the geometry is discretized using linear tetrahedra and the solution is discretized using quadratic Lagrangian polynomials. The spatial discretization resulted in 5760 elements and 24519 degrees of freedom. The nonlinear problem was solved using the Newton-Raphson algorithm and the resulting linear systems were solved using the LU decomposition implemented in the MUMPS library [?].

#### 4.2.7 Sensitivity analysis approach

As in 3.2.6, we use the Elementary Effects method [?]. It is a global sensitivity analysis method that was first presented by Morris [?] as a screening method and later improved by Campolongo et al [7]. It is a non-intrusive method that has been applied in the cardiovascular field [? ?]. It allows to compute sensitivity indices of the strain distributions without requiring the use of meta-modeling techniques.

To explain the sensitivity analysis we first consider a general case with  $n_p$  parameters. We built a structured grid with a  $n_n$  nodes resolution along each parameter direction in the parameter space yielding  $n_n^{n_p}$  parameter combinations. Using an optimized sampling strategy we generated  $n_t$  trajectories

with a maximum spread [7], visiting a total of  $M$  different parameter combinations. Each trajectory visits a set of  $n_p + 1$  nodes in the parameter grid  $(\vec{s}^{j_1}, \vec{s}^{j_2}, \dots, \vec{s}^{j_{n_p}}, \vec{s}^{j_{n_p+1}})$  that allows the computation of an elementary effect along every parameter direction  $i$  ( $\vec{s}^{j_{i+1}} = \vec{s}^{j_i} + \Delta_i \vec{e}_i$ , for  $i = 1, \dots, n_p$ ). As output we considered all six end-systolic Green-Lagrange strain components  $E_{\alpha\beta}$ , referred to the state at end diastole, where  $\alpha$  and  $\beta$  are in  $\{c, l, t\}$ .

As in 3.2.6, per strain component  $E_{\alpha\beta}$  and per node  $\vec{x}_k$  in the FE model, we computed the coefficient of variation (CV), defined as the standard deviation of the strain component computed over all the  $M$  simulated fiber configurations normalized with respect of the norm of the average respective strain.

$$E_{\alpha\beta}^{avg}(\vec{x}_k) = \frac{1}{M} \sum_{j=1}^M E_{\alpha\beta}(\vec{x}_k, \vec{s}^j), \quad (4.2.18)$$

$$CV_{E_{\alpha\beta}}^{avg}(\vec{x}_k) = \frac{\sqrt{\frac{1}{M-1} \sum_{j=1}^M \left( E_{\alpha\beta}(\vec{x}_k, \vec{s}^j) - E_{\alpha\beta}^{avg}(\vec{x}_k) \right)^2}}{\|E_{\alpha\beta}^{avg}(x)\|_{\infty}}, \quad (4.2.19)$$

where  $k = 1, \dots, N_{LV}$ ,  $N_{LV}$  is the number of nodes used in the discretization of the finite element LV model, and  $\|E_{\alpha\beta}^{avg}(x)\|_{\infty}$  is the  $\ell^{\infty}$  norm over all the LV nodes  $\vec{x}_k$ . To analyze the contribution of each parameter to the CV, we first assessed the elementary effects  $EE_i$ . For a specific point in the parameter space  $\vec{s} = (s_1, \dots, s_{n_p})$ ,  $EE_{i,\alpha\beta}$  gives an estimation of the effect that a perturbation in parameter  $s_i$  by an amount  $\Delta_i$  has on a strain component  $E_{\alpha\beta}$ :

$$EE_{i,\alpha\beta}(\vec{x}_k, \vec{s}) = \frac{E_{\alpha\beta}(\vec{x}_k, \vec{s} + \Delta_i \vec{e}_i) - E_{\alpha\beta}(\vec{x}_k, \vec{s})}{\Delta^*}, \quad (4.2.20)$$

$$\Delta^* = \frac{n_n}{2(n_n - 1)}, \quad (4.2.21)$$

$$\Delta_i = 2\Delta^* \text{range}_i, \quad (4.2.22)$$

where  $k = 1, \dots, N_{LV}$ ,  $\vec{e}_i$  is the  $i$ -th vector of the standard orthogonal basis of the  $n_p$ -dimensional parameter space,  $n_n$  is the grid resolution of the parameter space, and  $\text{range}_i$  is the actual range considered for the  $i$ -th parameter.

Elementary effects  $EE_{i,\alpha\beta}$  were computed for all six end-systolic strain components. By collecting all the elementary effects over the  $n_t$  trajectories, three

sensitivity indices were computed as follows:

$$\mu_{i,\alpha\beta}(\vec{x}_k) = \frac{1}{n_t} \sum_{j=1}^{n_t} EE_{i,\alpha\beta}^j(\vec{x}_k, \vec{s}^{j_i}), \quad (4.2.23)$$

$$\mu_{i,\alpha\beta}^*(\vec{x}_k) = \frac{1}{n_t} \sum_{j=1}^{n_t} |EE_{i,\alpha\beta}^j(\vec{x}_k, \vec{s}^{j_i})|, \quad (4.2.24)$$

$$\sigma_{i,\alpha\beta}(\vec{x}_k) = \sqrt{\frac{1}{n_t - 1} \sum_{j=1}^{n_t} \left( EE_{i,\alpha\beta}^j(\vec{x}_k, \vec{s}^{j_i}) - \mu_{i,\alpha\beta}(\vec{x}_k) \right)^2}, \quad (4.2.25)$$

where  $k = 1, \dots, N_{LV}$ ,  $n_t$  is the number of trajectories,  $\mu_i$  gives an overall estimation of the effect of a variation on parameter  $s_i$ ,  $\mu_i^*$  is used to detect whether variations on  $s_i$  are non influential, and  $\sigma_i$  gives information about how much the effect of a perturbation on  $s_i$  depends on the sampling point in the parameter space, giving an estimation of the ensemble of the parameter's effects due to interactions and nonlinear behaviors. Note that these quantities are statistics of the elementary effects and therefore are summed over the number of trajectories.

To obtain the average strain variation within the parameter space, we multiplied the indices  $\mu_{i,\alpha\beta}(\vec{x})$  and  $\mu_{i,\alpha\beta}^*(\vec{x})$  by the variation step  $\Delta^*$ . We then normalized the variation with the infinity norm of the respective strain computed using the reference fiber configuration as follows:

$$\hat{\mu}_{i,\alpha\beta} = \frac{\mu_{i,\alpha\beta} \Delta^*}{\|E_{\alpha\beta}^{ref}\|_{\infty}}, \quad \hat{\mu}_{i,\alpha\beta}^* = \frac{\mu_{i,\alpha\beta}^* \Delta^*}{\|E_{\alpha\beta}^{ref}\|_{\infty}}, \quad \hat{\sigma}_{i,\alpha\beta} = \frac{\sigma_{i,\alpha\beta} \Delta^*}{\|E_{\alpha\beta}^{ref}\|_{\infty}} \quad (4.2.26)$$

where  $i$  varies between 1 and  $n_p$  as the parameters.

To summarize the detailed node-wise information in  $\hat{\mu}_{i,\alpha\beta}(\vec{x})$  and  $\hat{\mu}_{i,\alpha\beta}^*(\vec{x})$  we compute the average 1-norm which is the 1-norm re-scaled using the number of nodes involved in the finite element LV discretization  $N_{LV}$

$$\hat{\mu}_{i,\alpha\beta}^{avg} = \frac{1}{N_{LV}} \|\hat{\mu}_{i,\alpha\beta}(\vec{x})\|_1 = \frac{1}{N_{LV}} \sum_{k=1}^{N_{LV}} |\hat{\mu}_{i,\alpha\beta}(x_k)|, \quad (4.2.27)$$

$$\hat{\mu}_{i,\alpha\beta}^{*,avg} = \frac{1}{N_{LV}} \|\hat{\mu}_{i,\alpha\beta}^*(\vec{x})\|_1 = \frac{1}{N_{LV}} \sum_{k=1}^{N_{LV}} |\hat{\mu}_{i,\alpha\beta}^*(x_k)|, \quad (4.2.28)$$

$$\hat{\sigma}_{i,\alpha\beta}^{avg} = \frac{1}{N_{LV}} \|\hat{\sigma}_{i,\alpha\beta}(\vec{x})\|_1 = \frac{1}{N_{LV}} \sum_{k=1}^{N_{LV}} |\hat{\sigma}_{i,\alpha\beta}(x_k)|. \quad (4.2.29)$$



We use  $\hat{\sigma}_{i,\alpha\beta}^{avg}$  to estimate the interactions between the parameters. Differently from 3.2.6, to fully investigate the sensitivity of LV wall strains to settings of the fiber parameters, we performed three types of analysis: the complete analysis, the single-parameter analysis, and the double-parameter analysis. In the complete analysis ( $n_p = 5$ ,  $n_n = 4$ ,  $n_t = 500$ ), we varied all the 5 parameters altogether around the reference configuration reported in Table 4.1. We performed also 5 single-parameter analyses ( $n_p = 1$ ,  $n_n = 128$ ,  $n_t = 64$ ) in which we varied one single parameter at a time. The considered parameter was varied according to the range reported in Table 4.1 while the other parameters were kept at their reference values. Lastly, we performed 10 double-parameter analyses ( $n_p = 2$ ,  $n_n = 16$ ,  $n_t = 128$ ) varying a pair of parameters per time. The two considered parameters were varied according to the range reported in Table 4.1 while the other parameters were kept at their reference values.

We used the results from the complete analysis to compute the CV and the sensitivity indices  $\hat{\mu}_{i,\alpha\beta}$ ,  $\hat{\mu}_{i,\alpha\beta}^*$ , and  $\hat{\sigma}_{i,\alpha\beta}$ . The  $\hat{\sigma}_{i,\alpha\beta}$  computed in this analysis includes both the possible nonlinear behavior of the considered parameter and all the interactions with the other parameters until the fifth order. It is therefore hard to assess the contribution of each individual parameter to the interactions using only results coming from this analysis. To this end, we used results from the single-parameter analyses to estimate the nonlinear behavior of each parameter and those from the double-parameter analyses to estimate the magnitude of second order interactions. When no superscript is indicated on  $\hat{\mu}_{i,\alpha\beta}$ ,  $\hat{\mu}_{i,\alpha\beta}^*$ , and  $\hat{\sigma}_{i,\alpha\beta}$  we refer to results coming from the complete analysis varying all the five parameters altogether. In the investigation of interactions we indicated as  $\hat{\sigma}_{i,\alpha\beta}^{avg}$  the index coming from the complete analysis, as  $\hat{\sigma}_{i,\alpha\beta}^{avg,1}$  the index coming from the single-parameter analysis, and as  $\hat{\sigma}_{i,\alpha\beta}^{avg,2}$  the index coming from the double-parameter analysis. We indicated with  $\hat{\sigma}_{i,\alpha\beta}^{avg,int}$  the component of  $\hat{\sigma}_{i,\alpha\beta}^{avg,2}$  that account for the second order interactions only. It is defined as follows

$$\hat{\sigma}_{i,\alpha\beta}^{avg,int}(j) = \sigma_{i,\alpha\beta}^{avg,2}(i,j) - \sigma_{i,\alpha\beta}^{avg,1}(i), \quad \text{if } i \neq j, \quad (4.2.30)$$

where  $i$  is the parameter along which the elementary effects are computed, and  $j$  is the parameter for which the interaction with  $i$  is assessed. The purpose is that of investigating and distinguishing the nonlinear behavior (given by  $\hat{\sigma}_{i,\alpha\beta}^{avg,1}$ ) from the second order interactions (in  $\hat{\sigma}_{i,\alpha\beta}^{avg,2}$  together with the nonlinear part).

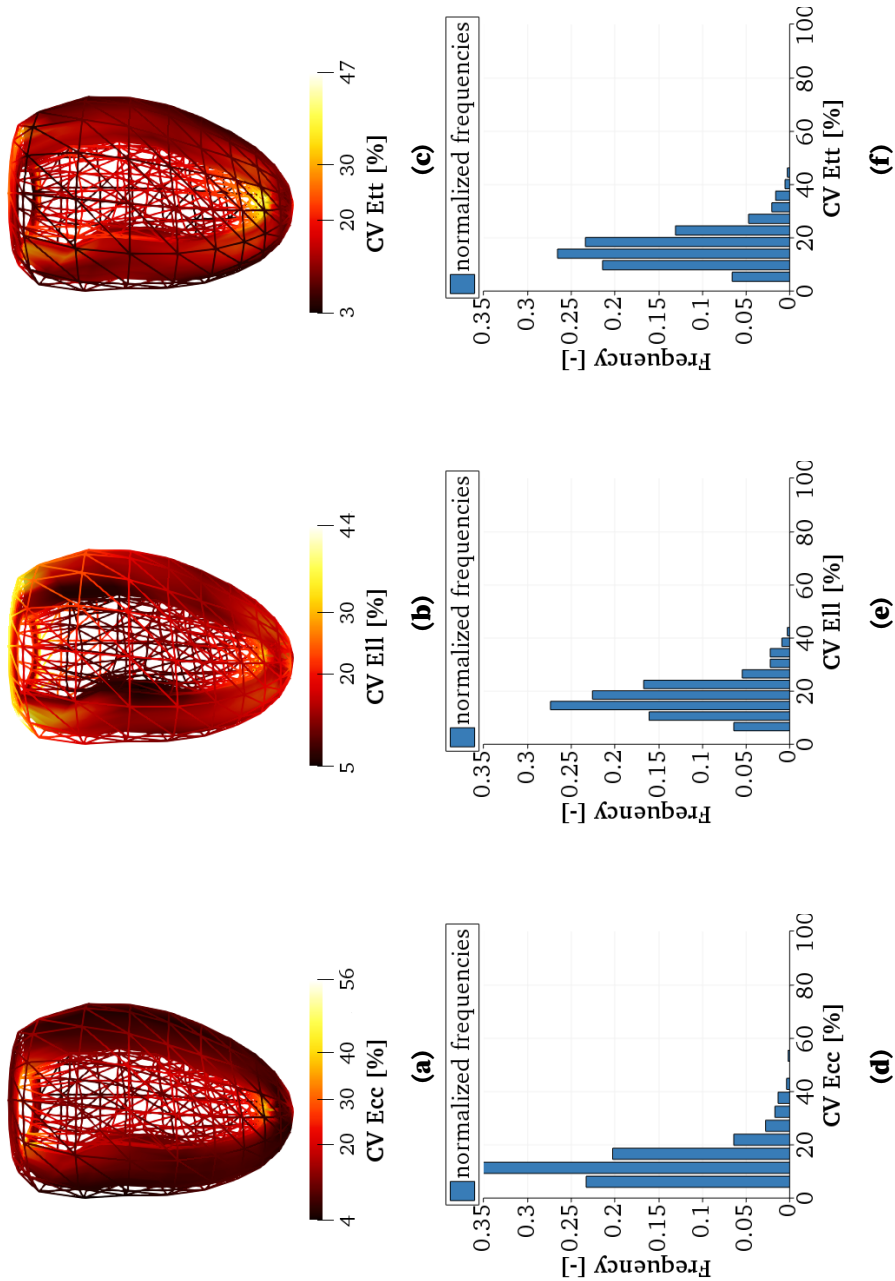


**Figure 4.3:** Coefficient of variation of normal strains. From left to right the coefficient of variation of circumferential, longitudinal, and transmural strains. The top row shows the spatial distribution, the bottom row shows histograms indicating the frequency within the geometry.

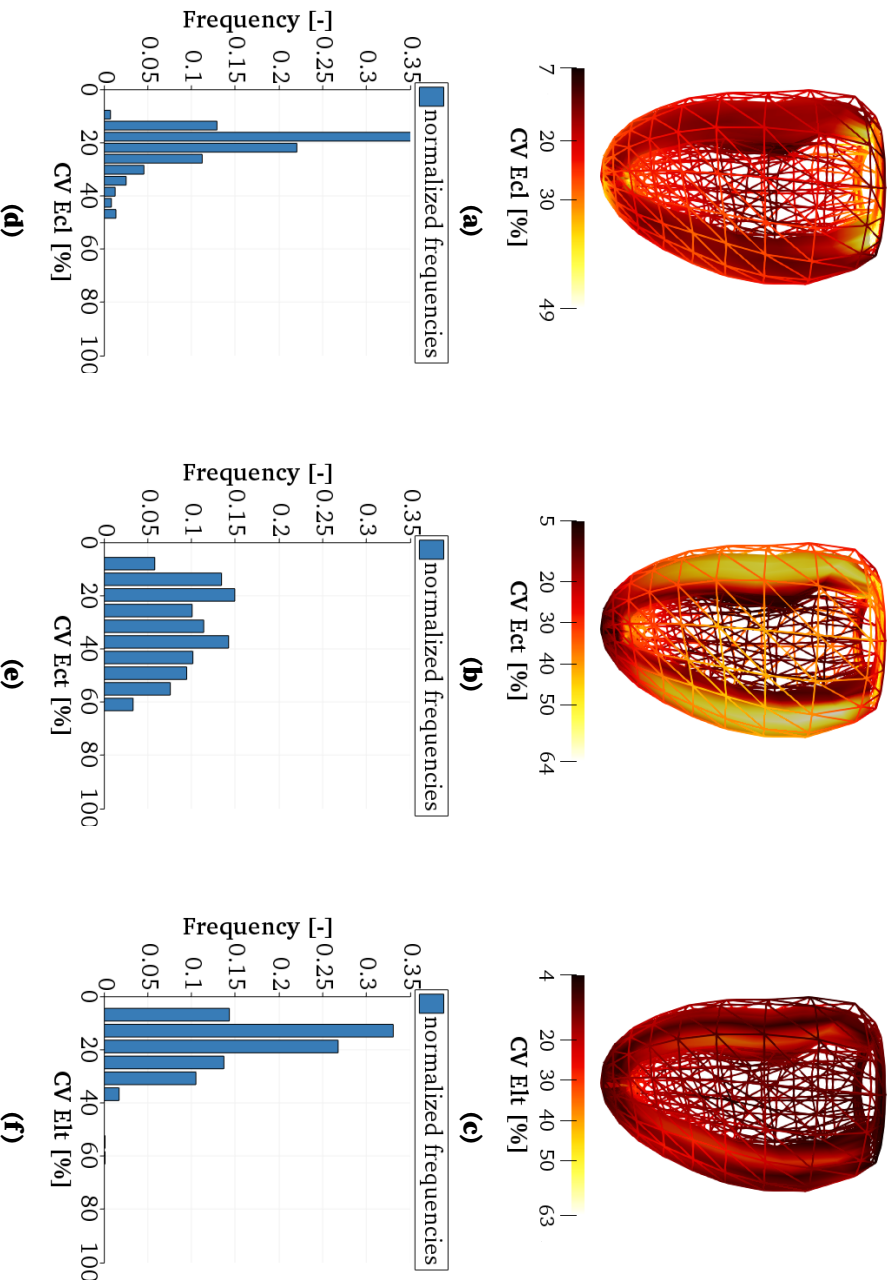


**Figure 4.4:** Coefficient of variation of shear strains. From left to right the coefficient of variation of circumferential-longitudinal, circumferential-transmural, and longitudinal-transmural shear strains. The top row shows the spatial distribution, the bottom row shows histograms indicating the frequency within the geometry.

## 4.3 Results

### 4.3.1 Complete analysis

In the complete analysis, we computed the sensitivity indices for the end-systolic strains by performing constant preload-constant afterload experiments for the selected combinations of fiber parameters. The five parameters of the 5-parameter fiber model were within the ranges presented in Table 4.1. Each constant preload-constant afterload experiment was preceded by an unloading stage in which the average end-diastolic configuration was deflated using the selected fiber field. The unloading procedure from the average MESA geometry ( $V_{c,ED} = 106.41\text{mL}$ ) resulted in an average unloaded cavity volume  $V_{c,0}$  of about  $42.44 \pm 0.06\text{mL}$  and an average cavity pressure of  $1.483 \pm 0.012\text{kPa}$ . Inflation of the unloaded geometry until an end-diastolic pressure of  $1.5\text{kPa}$  yielded an end-diastolic volume of  $107.57 \pm 0.32\text{mL}$ . Ejection against the afterload pressure of  $12\text{kPa}$  resulted in a stroke volume of  $49 \pm 7\text{mL}$  and an ejection fraction of  $46 \pm 6\%$ . Thus, the effect of fiber orientation during passive filling is minor as compared to the effect during active ejection. The ejection fraction of the central parameter combination is  $53\%$ . About  $67\%$  of the standard deviation is due to  $t_u^0$  and  $h_v^0$  only.

Figure 4.3 shows the spatial distribution and the histogram of the coefficient of variation (CV) of normal strains: the circumferential strain  $E_{cc}$ , the longitudinal strain  $E_{ll}$  the transmural strain  $E_{tt}$ . The norms used in the definition of CV in (4.2.19) were  $\|E_{cc}^{avg}\|_{\infty} = 0.28$ ,  $\|E_{ll}^{avg}\|_{\infty} = 0.26$ , and  $\|E_{tt}^{avg}\|_{\infty} = 1.32$ . The maximum values of the CV occur in both the basal and the apical regions for  $E_{cc}$ ,  $E_{ll}$ , and  $E_{tt}$ . The minimum values for  $E_{cc}$  and  $E_{tt}$  are mostly in the sub-epicardium, and for  $E_{ll}$  the minimum values occur in the sub-endocardium in the equatorial region. For the circumferential, the longitudinal and the transmural strains the coefficient of variation ranges from about  $4\% - 56\%$ ,  $5\% - 44\%$ , and  $3\% - 47\%$ , respectively. From the spatial distributions of CV in Figures (4.3a, 4.3b, 4.3c), we derived the histograms shown in Figures (4.3d, 4.3e, 4.3f). From the histograms the average and the standard deviation are about  $15\% \pm 7\%$  for  $E_{cc}$ ,  $22\% \pm 8\%$  for  $E_{ll}$ , and  $17\% \pm 7\%$  for  $E_{tt}$ .

Figure 4.4 shows the spatial distribution and the histogram of the coefficient of variation (CV) of shear strains: the circumferential-longitudinal shear strain  $E_{cl}$ , the circumferential-transmural shear strain  $E_{ct}$ , and the longitudinal-transmural shear strain  $E_{lt}$ . The norms used in the definition of CV were  $\|E_{cl}^{avg}\|_{\infty} = 0.19$ ,  $\|E_{ct}^{avg}\|_{\infty} = 0.60$ , and  $\|E_{lt}^{avg}\|_{\infty} = 0.54$ . The maximum values for the CV occur in both the basal and the apical regions for  $E_{cl}$ , at mid-wall in both basal and equatorial regions for  $E_{ct}$ , and at the apex for  $E_{lt}$ . The min-

imum values occur on the endocardial side at equator for  $E_{cl}$ , in most of the sub-endocardial region and at the apex for  $E_{ct}$ , and mostly between mid-wall and the sub-epicardial region for  $E_{lt}$ . For the circumferential-longitudinal, the circumferential-transmural and the longitudinal-transmural shear strains the coefficient of variation ranges in about 7%–49%, 5%–64%, and 4%–63%, respectively. The bottom row of Figure 4.4 shows the frequency of CV for normal strains. From the histograms the average and the standard deviation are  $25\% \pm 8\%$  for  $E_{cl}$ ,  $38\% \pm 18\%$  for  $E_{ct}$ , and  $21\% \pm 9\%$  for  $E_{lt}$ .

To explain how the different parameters contribute to the  $CV$  of the strains, in Table 4.2 we report the sensitivity index  $\hat{\mu}_{i,\alpha\beta}^{*,avg}$  for the six considered strains and the five parameters. This index is an upper bound on the sensitivity to a parameter and it is a good proxy for the Sobol total effect index  $S_T$  [7], thus  $\hat{\mu}_{i,\alpha\beta}^*$  can be used to detect non influential parameters. In Table 4.2 we highlighted values above 10% in pink and those larger than 20% in red. In this respect, varying the transmural range of the helix angle  $\alpha_h$  through  $h_v^1$  affects all the strain components by less than 10%. Variation of  $h_u^1$ , determining the longitudinal variation of the helix angle, and  $t_u^1$ , determining the base-to-apex range of the transverse angle at midwall, affects only one strain component above 10% ( $E_{ll}$  and  $E_{ct}$ , respectively). Instead, variation of  $h_v^0$ , determining helix angle at midwall at the equator, affects 4 out of 6 strain components beyond 10%. Finally, variation of  $t_u^0$ , determining the longitudinal position at which the transverse angle is zero, affects 6 out 6 strain components beyond 10% of which  $E_{ct}$  and  $E_{lt}$  beyond 20%.

	$h_v^0$	$h_v^1$	$h_u^1$	$t_u^0$	$t_u^1$
$E_{cc}$	9.91	2.76	3.64	13.98	9.24
$E_{ll}$	10.46	8.71	13.35	13.44	8.72
$E_{tt}$	8.17	3.21	4.49	15.67	7.90
$E_{cl}$	19.44	7.56	8.18	12.29	7.23
$E_{ct}$	10.92	3.85	5.99	35.96	14.27
$E_{lt}$	13.45	4.68	6.46	21.01	9.81

**Table 4.2:** Spatially averaged relative sensitivity of strains  $E_{\alpha\beta}$  (rows) to variations in the  $i$ -th parameter (columns), expressed in parameter  $\hat{\mu}_{i,\alpha\beta}^{*,avg}$  [%]. Values above 10% are highlighted in pink. Those above 20% are highlighted in red.

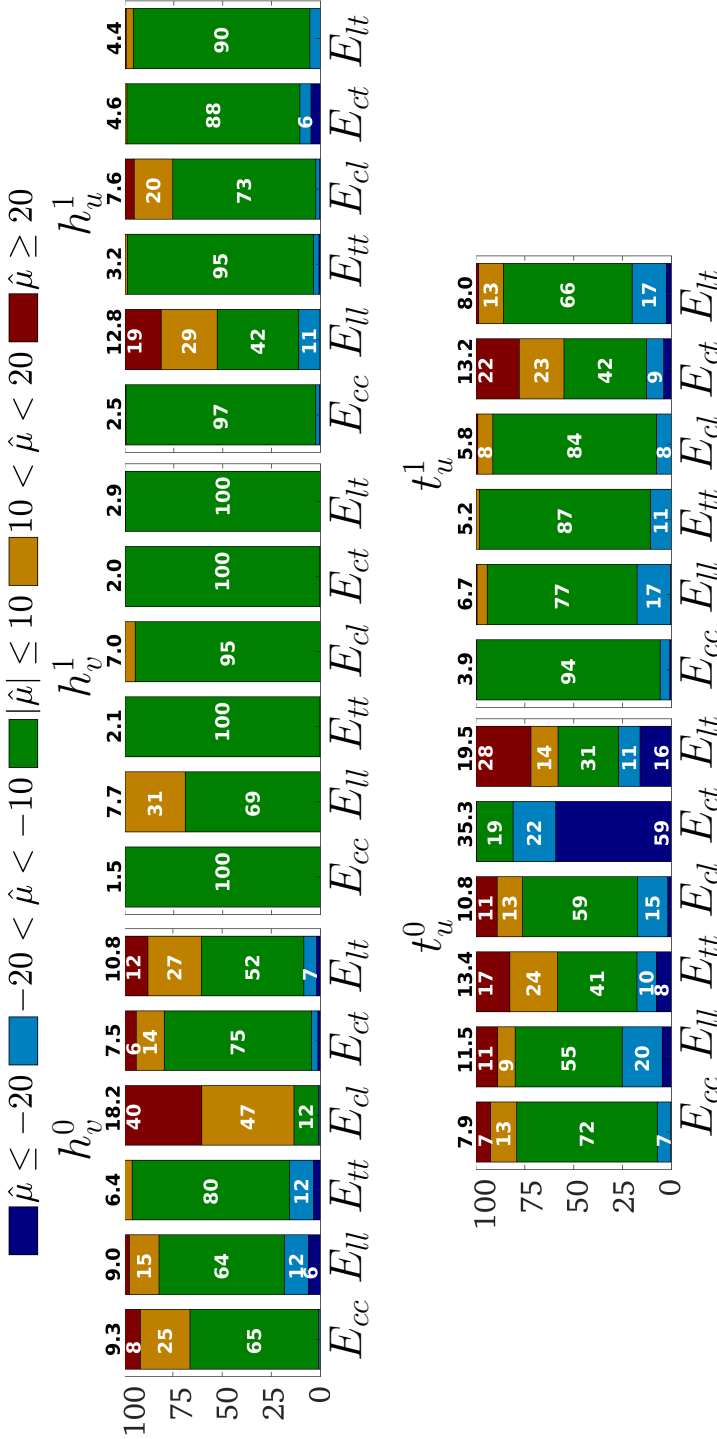


**Figure 4.5:** Bar plots of the spatial distribution of  $\hat{\mu}_{i,\alpha\beta}(\vec{x})$  for the six end-systolic strains. Each bar is divided in five. The blue bar represents the fraction of the geometry with  $\hat{\mu}_{i,\alpha\beta}(\vec{x}) < -20\%$ , the light blue the one with  $-20\% < \hat{\mu}_{i,\alpha\beta}(\vec{x}) < -10\%$ , the green bar the portion where  $|\hat{\mu}_{i,\alpha\beta}(\vec{x})| < 5\%$ , the yellow bar represents the fraction of the geometry with  $5\% < \hat{\mu}_{i,\alpha\beta}(\vec{x}) < 10\%$ , and the red one the region with  $\hat{\mu}_{i,\alpha\beta}(\vec{x}) > 20\%$ . On top of each bar it is written in black the value of  $\hat{\mu}_{i,\alpha\beta}^{avg}$  for the respective mode and strain. The five values written in white on the bars indicates the frequency of  $\hat{\mu}_{i,\alpha\beta}(\vec{x})$  in the respective sub-regions. For the sake of readability we did not indicate the number for bars smaller than 5%.

Figure 4.5 shows the spatial distribution of  $\hat{\mu}_{i,\alpha\beta}(\vec{x})$  for each strain component categorized in five regions: below  $-20\%$ , between  $-20\%$  and  $-10\%$ , between  $-10\%$  and  $10\%$ , between  $10\%$  and  $20\%$ , and above  $20\%$ . On top of each bar the value  $\hat{\mu}_{i,\alpha\beta}^{avg}$  is indicated. To explain the presentation, we first focus on the effect of parameter  $h_v^0$  on the normal strain  $E_{cc}$ , presented in the upper left bar. The green region indicates that in 65% of the LV nodes the effect of a variation of  $h_v^0$  on  $E_{cc}$  was below 10% of the value of  $E_{cc}$  obtained with the central parameter settings. The orange region indicates that  $E_{cc}$  was increased in between 10% and 20% of the average value in 25% of the nodes. The red region indicates that  $E_{cc}$  was increased by more than 20% of the average value in 8% of the nodes. Apparently,  $E_{cc}$  is reduced by more than 10% in only 2% of the nodes. Figure 4.6 shows how these changes in  $E_{cc}$  are distributed over the LV wall, represented by a 17 segment AHA distribution. The increase in  $E_{cc}$  occurs mainly in the sub-endocardial, sub-basal region.

Overall,  $h_v^0$  affects 2 out of 6 strain components with a  $\hat{\mu}_{h_v^0,\alpha\beta}^{avg}$  beyond 10%:  $E_{cl}$  (18.2%), and  $E_{lt}$  (10.8%).  $E_{cl}$  tends to increase due to variation in  $h_v^0$  by more than 10% in 87% of the geometry and by more than 20% in 40% of the geometry. Those variations occur almost everywhere in the myocardium with a larger magnitude in the sub-epicardium, as shown by Figure 4.6.  $E_{lt}$  tends to increase due to variation in  $h_v^0$  by more than 10% in 39% of the geometry and by more than 20% in 12% (dark red bar), mostly in the apical regions (except the septum, see Figure 4.6), while  $E_{lt}$  tends to decrease by more than 10% in 9% of the geometry.

Variation of  $h_v^1$  does not affect any strain component on average beyond 10%. There is a slight tendency for an increase of  $E_{ll}$  in the equatorial sub-epicardial region, see Figure 4.6.

Variation of  $h_u^1$  affects mainly  $E_{ll}$  with a  $\hat{\mu}_{h_u^1, ll}^{avg} = 12.8\%$ .  $E_{ll}$  tends to increase due to variation in  $h_u^1$  by more than 10% in 48% of the geometry and by more than 20% in 19% of the geometry, mostly in the sub-epicardial equatorial regions (Figure 4.6).

Variation of  $t_u^0$  affects 5 out of 6 strain components with a  $\hat{\mu}_{t_u^0,\alpha\beta}^{avg}$  beyond 10%:  $E_{ct}$  (35.3%),  $E_{lt}$  (19.5%),  $E_{tt}$  (13.4%),  $E_{ll}$  (11.5%), and  $E_{cl}$  (10.8%). In particular, variation of  $t_u^0$  affects  $E_{ll}$  and  $E_{cl}$  similarly (11.5% and 10.8%, respectively) with a similar distribution of positive and negative contributions. Variation in  $t_u^0$  increases  $E_{ll}$  in 20% of the geometry and increase  $E_{cl}$  23% of the geometry, both at the base, while variations in  $t_u^0$  decrease  $E_{ll}$  in 25% of the geometry in the apical sub-epicardial regions and decrease  $E_{cl}$  in 17% of the geometry. The average influence of  $t_u^0$  on  $E_{tt}$  is 13.4%.  $E_{tt}$  increases due to variation in  $t_u^0$  by more than 10% in 41% of the geometry and by more than 20% in 17% (dark

red bar), mostly in sub-equatorial regions, while  $E_{tt}$  decreases more than 10% in 18% of the geometry and by more than 20% in 8% (dark blue bar), mostly in at the base Figure 4.6. Variations in the value of  $t_u^0$  greatly affect  $E_{ct}$  (35.3%) asymmetrically with the tendency to reduce its value by more than 10% in 71% of the geometry and by more than 20% in 59% (dark blue bar). Figure 4.6 shows how these changes occur almost everywhere in the myocardium with the exception of the apex. Variations in the value of  $t_u^0$  largely affect also  $E_{lt}$  (19.5%) although in a more symmetric manner.  $E_{lt}$  tends to increase due to variation in  $t_u^0$  by more than 10% in 42% of the geometry and by more than 20% in 28% of the geometry (dark red bar), mostly in the sub-endocardial region (Figure 4.6), while  $E_{lt}$  tends to decrease more than 10% in 27% of the geometry and by more than 20% in 16% of the geometry (dark blue bar), mostly in the sub-epicardium.

Variation in  $t_u^1$  affects mainly  $E_{ct}$  with a  $\hat{\mu}_{t_u^1, ct}^{avg} = 13.2\%$ .  $E_{ct}$  tends to increase by more than 10% in 45% of the geometry and by more than 20% in 22% of the geometry. Those increases happen in the apical regions with larger magnitude in the sub-epicardium, as shown by Figure 4.6.



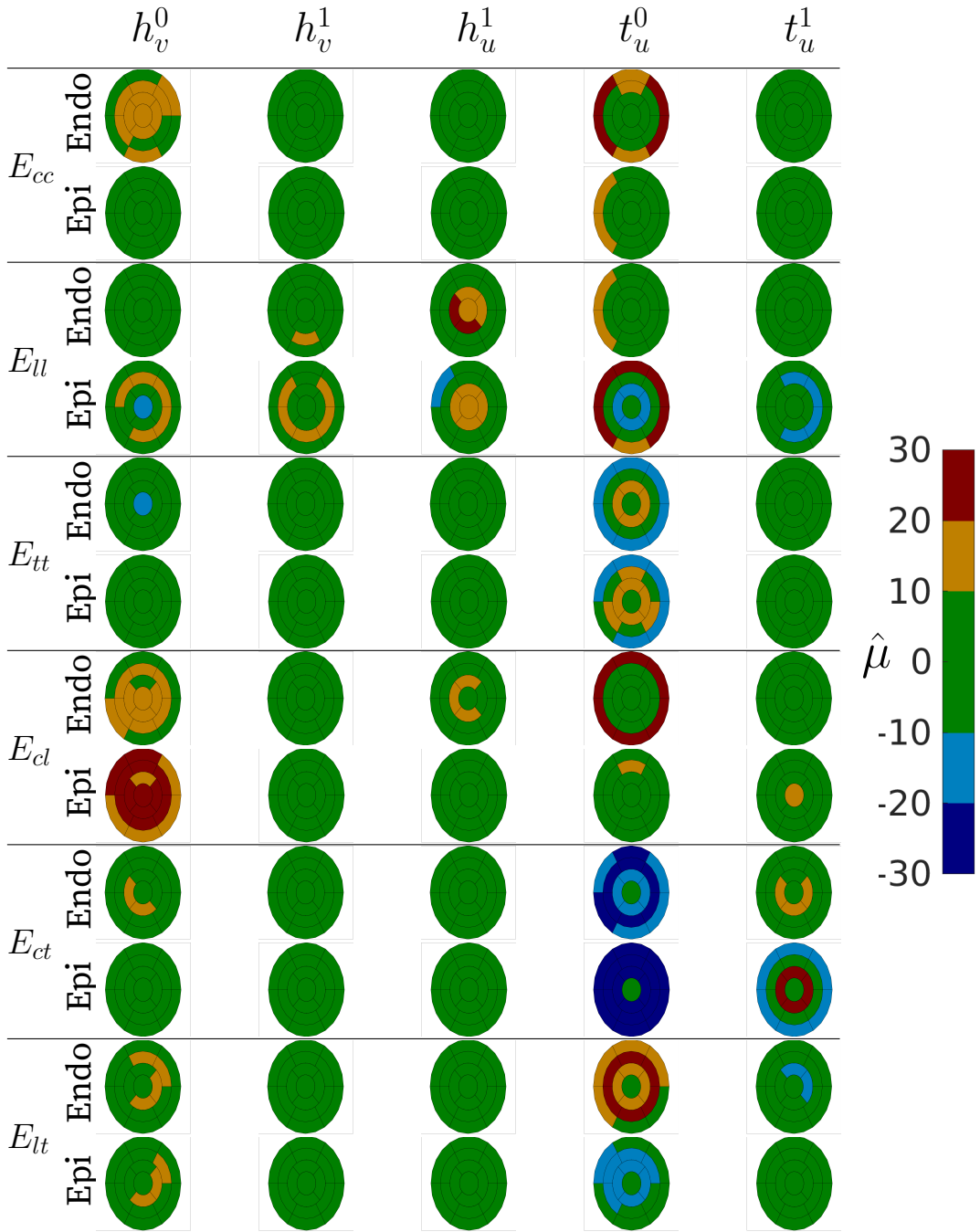


**Figure 4.6:** AHA 17 segments representation of  $\hat{\mu}_{i, \alpha \beta}$  averaged over each segment. The myocardium has been split in two regions: the sub-epicardium, from endocardium to mid-wall; and sub-endocardium, from mid-wall to epicardium.

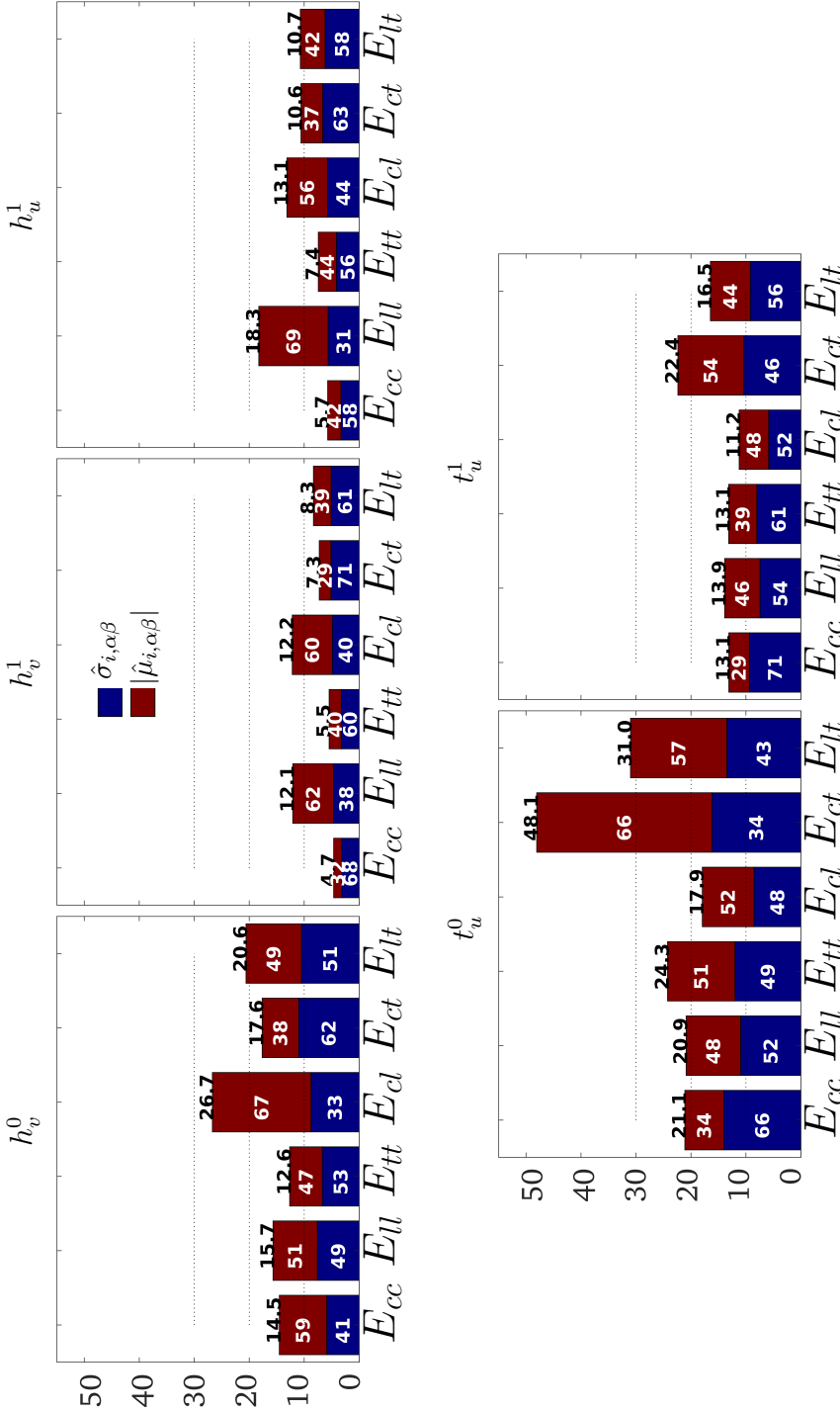


**Figure 4.7:** Bar plot representing  $|\hat{\mu}_{i,\alpha\beta}^{avg}|$  (red) and  $\hat{\sigma}_{i,\alpha\beta}$  (blue). Numbers on top of each bar indicate the average 1-norm of the sum of  $\hat{\sigma}_{i,\alpha\beta}$  and  $|\hat{\mu}_{i,\alpha\beta}|$ . The white numbers indicate the percentage contributions to the overall influence of the direct effect of the considered parameter (values on the red bars) and of nonlinear behavior and interactions with other parameters (values on the blue bars).

To evaluate the interactions between the setting of parameters, we evaluate  $\hat{\sigma}_{i,\alpha\beta}$  together with  $\hat{\mu}_{i,\alpha\beta}$ . Figure 4.7 shows the cumulative effect of the direct influence ( $\hat{\mu}_{i,\alpha\beta}$ ) and the ensemble of nonlinear effect and interactions ( $\hat{\sigma}_{i,\alpha\beta}$ ) for all the combinations of strain components and parameters. The total height of the bars (black values on the top) indicates the overall influence of a parameter on a strain component due to its direct effect (red bar, representing  $\hat{\mu}_{i,\alpha\beta}^{avg}$ ) and due to nonlinear effects and interactions with other parameters (blue bar, representing  $\hat{\sigma}_{i,\alpha\beta}$ ). The percentage contributions to the overall influence due to  $\hat{\mu}_{i,\alpha\beta}$  and  $\hat{\sigma}_{i,\alpha\beta}$  are indicated in white on the respective bars. We applied the k-means algorithm to create two groups out of the 30 combinations, representing strain-parameter combinations with high and low total overall influence. The group of high overall influence includes all the parameter-strain combinations that exceed the threshold value of about 20%. No combinations of  $h_v^1$  and  $h_u^1$  with any strain components are present in the high overall influence group. The eight combinations in this group, sorted in descending order, are:  $E_{ct}$ ,  $E_{lt}$ ,  $E_{tt}$ ,  $E_{cc}$ ,  $E_{ll}$ , due to  $t_u^0$ ;  $E_{cl}$ , and  $E_{lt}$  due to  $h_v^0$ ; and  $E_{ct}$  due to  $t_u^1$ . The percentage contribution of  $\hat{\sigma}_{i,\alpha\beta}^{avg}$  to the overall influence for these bars ranges between 34% and 66%. For these elements, the overall influence on the respective strain component can be lowered by studying the composition of  $\hat{\sigma}_{i,\alpha\beta}$  using single and double-parameter analyses.

### 4.3.2 Single-parameter and double-parameter analyses

To investigate deeper the interactions between parameters, we compare the value of  $\hat{\sigma}_{i,\alpha\beta}^{avg}$  coming from the complete analysis with the ones obtained from the single-parameter and the double-parameter analyses. We recall that the complete analysis was obtained analyzing the sensitivity of all parameters together, the single-parameter analysis was obtained varying only one single parameter and keeping the rest at their reference values, and the double-parameter analysis was obtained varying all the possible pairs of parameters and keeping the other parameters at their reference values. The  $\hat{\sigma}_{i,\alpha\beta}$  computed in the single-parameter analysis represents the nonlinear effect of the considered parameter. The  $\hat{\sigma}_{i,\alpha\beta}$  computed in the double-parameter analysis represents the nonlinear effect of the considered parameter and its interaction with the other parameter included in the analysis. The  $\hat{\sigma}_{i,\alpha\beta}$  computed in the complete analysis represents the nonlinear effect of the considered parameter and its interaction with the other parameter included in the analysis. The use of the three  $\hat{\sigma}_{i,\alpha\beta}$  computed in the three analyses allows to evaluate the nonlinear effect of a parameter, the second order interactions, and the remaining higher order interactions. The results are shown in Figure 4.8. We fo-

cus on the 8 strain-parameter combinations with high total overall influence, as identified in the complete analysis. For each strain-parameter combination we show three bars: the black one represents  $\hat{\sigma}_{i,\alpha\beta}^{avg}$ , the interactions of any order up to the fifth between the 5 parameters and nonlinear effects from the complete analysis; the second bar represents  $\hat{\sigma}_{i,\alpha\beta}^{avg,int}$ , the second order interaction between the considered parameter and the one indicated by the bar color; the third bar represents  $\hat{\sigma}_{i,\alpha\beta}^{avg,1}$ , the nonlinear behavior of the considered parameter. 5 figures out of the 8 in Figure 4.8 refer to  $t_u^0$ , meaning that this parameter not only is influential for most of the strain components but also presents interactions more than the other parameters. In those 5 figures, the nonlinear behavior of  $t_u^0$  is always larger than the sum of all the second order interactions. The parameter showing the largest interaction with  $t_u^0$  is  $t_u^1$ , as shown by the red bars representing  $\hat{\sigma}_{t_u^0,\alpha\beta}^{avg,int}$ . The interactions between  $h_v^0$  and  $t_u^0$  are comparable to those between  $t_u^0$  and  $t_u^1$  for  $E_{ct}$  and  $E_{lt}$ , as shown by the light blue bars. 2 figures out of the 8 in Figure 4.8 refer to  $h_v^0$  and concern  $E_{cl}$  and  $E_{lt}$ . All the parameters interact with  $h_v^0$  similarly and there is not a dominant parameter in the interactions. The last figure refers to  $t_u^1$ .  $E_{ct}$  is affected by the interactions of  $t_u^1$  with the other parameters. The interaction between  $t_u^1$  and  $t_u^0$  is dominant while the nonlinear behavior of  $t_u^1$  equals the effect of the remaining interactions.

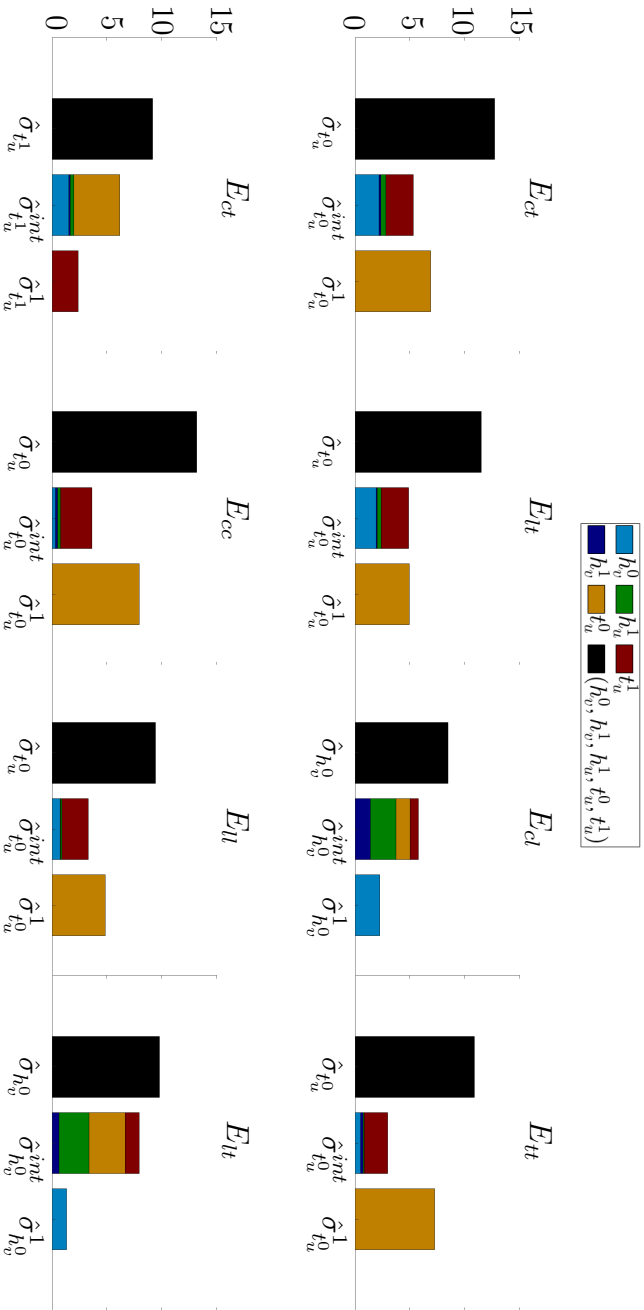


**Figure 4.8:** Bar plot comparing nonlinear effects, second order interactions, and complete interactions (nonlinear effects and all the interactions until the fifth order). The black bar accounts for the effects that interactions of the considered parameter (subscript of  $\hat{\sigma}$ ) with all the other parameters (and itself) have on the considered strain component. The second bar shows the nonlinear effect of the considered parameter. Each parameter is indicated in a different color: light blue for  $h_u^0$ , dark blue for  $h_u^1$ , green for  $h_u^1$ , yellow for  $t_u^0$ , and red for  $t_u^1$ .

## 4.4 Discussion

### 4.4.1 Methods

We performed an unloading phase in order to get a virtually unloaded geometry starting from the average end-diastolic MESA configuration. The unloading procedure led to physiological values for both cavity volume and cavity pressure. The average ratio between the computed unloaded cavity volume and wall volume  $V_{c,0}/V_w = 0.34$  agrees with the values measured by Nikolić et al [23] and McCulloch et al [19]. The low standard deviation found on estimated end-diastolic pressure shows that the influence of fiber orientation during the LV passive filling is low. This is not surprising, since the level of anisotropy of the myocardium in the passive phase is low (the ratio between fiber and cross-fiber stiffness being about 2).

We did not couple our LV model to a closed circulation model because then ventricular preload and afterload would become dependent on LV pump function itself: a lower pump function would lead to a lower arterial pressure and volume, and consequently a higher preload pressure and vice versa. In our constant preload-constant afterload experiment, we avoid that the feedback from the circulation model could confound our results and ensure that we purely test the effects that fiber orientation has on the contractile function of the LV.

We used the elementary effects method to compute the sensitivity indices  $\mu$ ,  $\mu^*$ , and  $\sigma$ , and to compute the CV of strains. In all the three sensitivity analyses we adopted a number of trajectories large enough to achieve a high coverage of the parameter space and to allow the sensitivity indices to converge. However, because of the computational effort required by the analysis, the more parameters we included in the sensitivity analyses, the lesser was the resolution of the parameter space. For this reason, in the complete analysis, the number of nodes along each direction was set to 4. The choice of the parameter space grid resolution affects directly the computation of elementary effects via  $\Delta^*$ . However,  $\Delta^*$  converges to 0.5 as  $n_n$  approach infinity, according to (4.2.21). This means that increasing the resolution of the parameter space may lead to changes in the elementary effects, but this increase should reflect the convergence of  $\Delta^*$ . Instead, the enrichment of the parameter space would probably allow to highlight even more the nonlinear behavior of parameters and their interactions, since variations in the parameter would induce complex nonlinear variations in the spatial strain distribution. To investigate in more detail the nonlinear behavior and the second order interaction of parameters, we applied the elementary effect method using increasing number

of parameters ( $n_p = \{1, 2, 5\}$ ) and decreasing number of nodes per parameter ( $n_n = \{128, 16, 4\}$ ). From this analysis, it emerged that higher order interactions were much smaller than second order interactions and non-linearities. To understand whether this is due to the limited resolution of the complete analysis or it is actually a property of the considered model, the same analysis must be performed with a much finer parameter space grid. However, due to the high computational cost, the coverage of the total parameter combinations must be lowered to make this analysis feasible.

## 4.4.2 Results

### Effects of fiber orientation on hemodynamics

We achieved the end-diastolic configuration by setting a fixed preload pressure of 1.5 kPa for all the fiber configurations considered. The end-diastolic cavity volume shows very little variation, meaning that fiber orientation does not affect the filling phase much. This can be explained by the low anisotropy of the myocardium during filling. Conversely in the active phase, where fibers contract and tissue anisotropy is much higher, the change in volume is much more affected by the orientation of fibers. Similarly, ejection fraction is also largely affected by fiber orientation ( $46 \pm 6\%$ ). This variation is way larger than that found in our sensitivity analysis to geometry [2], where it was about 2% ( $53 \pm 1\%$ ). Most of this variability is due to  $h_v^0$  and  $t_u^0$ . The average ejection fraction obtained in this analysis is a bit lower than normal physiological values; however, we consider it to be good enough to obtain meaningful end-systolic strains for our sensitivity analysis.

### Effects of fiber orientation on end-systolic strains

Our results shows that end-systolic shear strains are in general more sensitive to fiber orientation as compared to normal strains. Among the shear strains,  $E_{ct}$  and  $E_{cl}$  are the most affected. From a mechanical point of view,  $E_{cl}$  is related to shortening of the oblique fibers in the sub-endocardial and sub-epicardial layers. Contraction of sub-endocardial myofibers ( $\alpha_h \sim 60^\circ$ ) would cause a clockwise apical rotation, when viewing the apex in apex-to-base direction. Contraction of sub-epicardial myofibers ( $\alpha_h \sim -60^\circ$ ) would cause the opposite effect. The balance between these effects will result in a net rotation and a net torsional deformation and will create a transmural shear load that leads to circumferential-radial shear. This shear load is counteracted by the passive myocardial tissue and by the myofibers transmural component introduced by the transverse angle  $\alpha_t$ . Among the normal strains,  $E_{cc}$  is related to

the overall circumferential component of fibers and  $E_{ll}$  is related to the overall longitudinal component of fibers. Both the circumferential and the longitudinal components of fiber orientation are mainly determined by the helix angle  $\alpha_h$ . Instead,  $E_{tt}$  is related to both the helix and the transverse angle. On the one hand, to a first approximation,  $E_{tt}$  is strongly coupled to  $E_{cc}$  and  $E_{ll}$  by incompressibility and is related to  $\alpha_h$ . On the other hand, the transmural fiber component introduced by  $\alpha_t$  increases the transmural stiffness, which in turn affects  $E_{tt}$ . Following this interpretation, we expect that parameters describing  $\alpha_t$  would affect  $E_{ct}$ . In fact, among the parameters describing this angle,  $t_u^0$  (the mid-wall value assumed by  $\alpha_t$  at equator) is the most influential parameter, since it affects 5 out of 6 strain components beyond 10%. It affects the most  $E_{ct}$  with the tendency to decrease it. Parameter  $t_u^1$  affects  $E_{ct}$  to a lesser amount than  $t_u^0$ . Conversely from  $t_u^0$ ,  $t_u^1$  increases  $E_{ct}$ .  $t_u^0$  affects the ratio of the size of the two regions having positive  $\alpha_t$  (base) and negative  $\alpha_t$  (apex). Instead,  $t_u^1$  affects the magnitude of  $\alpha_t$  in those regions. This difference might explain the different effect on  $E_{ct}$ . This also explains the large second order interaction found between the two parameters. In fact, our analysis of interactions between parameters for the most affected strains shows that  $t_u^1$  is always the parameter interacting the most with  $t_u^0$  and vice-versa. In this analysis, the nonlinear effect of a parameter is discerned from the interaction with other parameters. The second most influential parameter,  $h_v^0$  (the mid-wall value of assumed by  $\alpha_h$  at equator), largely affects 2 out of 6 strain components. It mostly affects  $E_{cl}$  with the tendency to increase its value. This can be motivated by the fact that  $h_v^0$  introduces transmural asymmetry in the helix angle, thus shifting the balance in torque, created by the oblique fibers in the sunendocardial and subepicardial layers. This interpretation explains also the small increase of  $E_{ct}$  induced by  $h_v^0$ . Surprisingly, other parameters describing the helix angle,  $h_v^1$  (the transmural slope of  $\alpha_h$ ) and  $h_u^1$  (the longitudinal slope of  $\alpha_h$ ) resulted to be quite non-influential. Their main contribution is in the slight increase of  $E_{ll}$  that can be explained by an overall increased longitudinal component of the fibers.

Besides being the most influential parameter,  $t_u^0$  shows also the largest nonlinear behavior, which at least equals the sum of all the second order interactions. For this reason, among all the parameters,  $t_u^0$  should be included in the description of fibers and should be carefully personalized. Also  $h_v^0$  must be included in  $\alpha_h$  and, given its influence, also its value should be personalized. Among the least influential parameters, we found  $h_v^1$ ,  $h_u^1$ , and  $t_u^1$ . However, two considerations must be made. First, we found a large interaction between  $t_u^1$  and  $t_u^0$  (Figure 4.8). This interaction creates an indirect influence of  $t_u^1$  on the strain components affected by  $t_u^0$  and the other way round (Figure 4.7 and



Figure 4.8). It is therefore convenient to include also  $t_u^1$  among the influential parameters. Second, both  $h_v^1$  and  $h_u^1$  modify the transmural slope of the helix angle. Consequently, we may have over-represented variations in the transmural slope of  $\alpha_h$  (see Figure 4.2c). Nonetheless, even when over-estimated the transmural slope of the helix angle does not affect end-systolic strains as much as  $t_u^0$  and  $h_v^0$ . For this reason, we consider these two parameters non influential and we suggest to set them to generic values that represent the average values found in the human population.

Although we were conservative in the setting of the parameter ranges of  $\alpha_t$ , the transverse angle resulted to be the most influential angle in the description of fibers. In fact, we included data from Geerts et al [11], whose measured values for the transverse angle comply well with the small transverse angle measured by Streeter et al [32]. The resulting values of the transverse angle are in line with those presented by Toussaint et al [34] for in-vivo measured DTI fibers. However, DTI measurements of other studies (e.g. Lombaert et al [17]) present larger values for the transverse angle, especially at the endocardial side. This might be due to difficulties of the reconstruction algorithms in identifying the surfaces, especially at endocardium where the presence of papillary muscles and of trabeculation make the determination of a surface very difficult. The irregular trabeculated surface might affect the computation of the basis vectors used for the computation of angles, while the presence of papillary muscles may bias the diffusion tensor acquisition. This might explain the large values measured for the transverse angle, since non nil  $\alpha_t$  at the endocardium means fibers sticking out from the surface.

Other studies have investigated the sensitivity to fiber orientation in the context of cardiac mechanics. In particular, sensitivity of the passive mechanics of the left ventricle to fiber orientation has been addressed by Wang et al [35], Hassaballah et al [13], Nikou et al [24], and Rodriguez-Cantano et al [29]. Hassaballah et al [13] studied the effects that fiber orientation have on the cavity volume during the diastole and compared their results with experimental measurements. No quantitative assessment was performed, but among the most physiological fiber fields considered ( $\alpha_{h,epi}, \alpha_{h,endo} = -60^\circ, 60^\circ, -30^\circ, 60^\circ$ , and  $-60^\circ, 30^\circ$ ), basically a null coefficient of variation of the cavity volume is observed throughout the filling phase. This is in line with the low variability in end-diastolic cavity volume found in our results. Wang et al [35] and Nikou et al [24] tested the effects that variations in the transmural range of the helix angle have on end-diastolic stress along fibers. Both the analyses concluded that end-diastolic fiber stress is affected by the helix angle. However, both studies lack a proper quantification of the sensitivity. From the circumferential distribution of fiber stress at mid-ventricle presented by Nikou et al [24]

an average coefficient of variation of about 13 % is to be expected. Rodriguez-Cantano et al [29] assessed the sensitivity of 4 end-diastolic quantities of interest to both model based variations to fiber orientation and to fiber orientation seen as a random vector field. They employed the Polynomial Chaos Expansion together with Quasi-Monte Carlo simulations to quantify the sensitivity using the Sobol sensitivity indices [31] and coefficient of variations. They concluded that the 4 end-diastolic quantities of interest (end-diastolic cavity volume, apex lengthening, wall thickening, and wall volume) are rather insensitive to endocardial and epicardial values of the helix angle (affecting only 2 % of the output variance), while are more sensitive to local variations and noise in the fiber orientation (about 4 % coefficient of variation). In our study, we did not focus on end-diastolic stresses and strains. But we found that end-diastolic filling volume is hardly affected by fiber orientation and attributed this to the low anisotropy of the passive tissue. The same motivation probably explains the low sensitivity of end-diastolic stresses and strains to fiber orientation.

Concerning the sensitivity of the mechanics of the left ventricle to fiber orientation during the active phase, Geerts et al [12] compared the sensitivity of average fiber strain and stress during the ejection phase to variations in geometry definition spanning the whole human population with sensitivity to variations in the helix angle in the range of ex-vivo measurement error. They concluded that the coefficient of variation of fiber strain for the considered variations in geometry is about 10 %, which is comparable with the same coefficient of variation computed for variation of  $8^\circ$  in fiber orientation. Considering the wide range of geometries included in their analysis as compared with the limited variation included in fiber orientation, their results highlight the stronger influence of fiber orientation in computation of fiber strain. Pluijmert et al [28] quantified that a perturbation of about  $8^\circ$  in the fiber orientation led to a variations in pump work in the range of 11 – 19%, which was at least double the one obtained applying variations to the description of geometry (5%). Although it is not a global sensitivity analysis on local strain distributions, this analysis gives results qualitatively in agreement with ours with fiber influencing end-systolic strains by two times more than geometry [2] (see Figure 4.9). In fact, compared with our previous sensitivity analysis of end-systolic strains to real human geometries [2], we found that the uncertainty propagated from fiber orientation to the strain components is at least twofold that propagated from the geometry. Most of this uncertainty is due to the transverse angle. Current models tend to focus on patient-specific geometry and often use generic rule based fiber field, typically modeled using  $h_v^1$  only and neglecting the transverse angle. Our results suggest that a precise

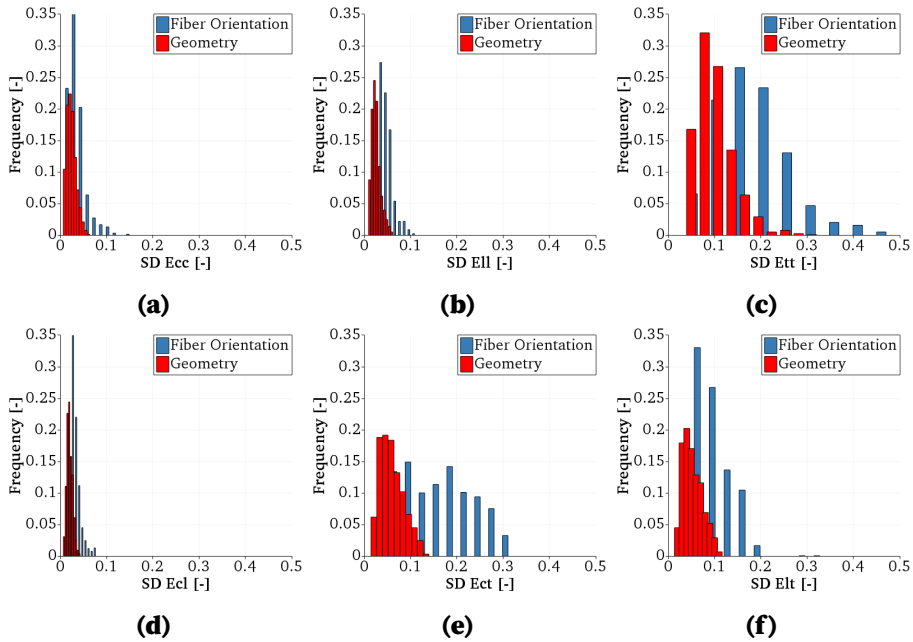


**Figure 4.9:** Comparison between the spatial distribution of SD due to variation of fiber orientation computed in this study (light blue) and the spatial distribution of SD due to variation of geometry description (red) from **chapter 3**.

prediction of end-systolic strains may be hindered by the lack of information concerning fiber orientation, even when using a personalized geometry. To our knowledge, no other global sensitivity study that addressed the sensitivity of end-systolic strains to fiber orientation has been published in literature. In this sense, this is the first attempt to quantify variations in end-systolic strain distributions induced by variation in myofiber orientation representing the variability within the human population.

#### 4.4.3 Limitations

Limitations of this study are related to the choice of the mathematical model, the availability of data, and the computational cost. Regarding the mathematical model, we assumed the onset of active stress development to be simultaneous throughout the geometry. Even though it has been suggested that pattern of mechanical activation is less inhomogeneous than pattern of electrical depolarization [14], the effect of asynchronous mechanical activation might be investigated.

Another limitation shared with other similar studies [12, 13, 35, 24, 29, 25] is

the geometry, which is an isolated LV. We generated the geometry from the MESA dataset which includes the LV only. It is not clear how the difference in wall thickness of the RV may impact on the sensitivity indices. In general, we expect that, due to the mechanical coupling between the two ventricle, the strain distribution patterns would be affected in a bi-ventricular geometry. However, in terms of sensitivity, Pluijmert et al [28] used a bi-ventricular geometry and obtained results similar to ours.

We opted to model fiber orientation using a rule-based approach and to interpret measurements found in literature in terms of parameters of our model. Even though we use a simplified 5-parameter model, the fiber orientation included in our analysis (see Figure 4.2) complies with both physiology and other studies of this kind (Geerts et al [12] and Pluijmert et al [28], for instance). All the fiber fields were generated using an axisymmetric model. We partly compensated for the lack of circumferential variability in our rule-based model by reorienting the fiber according to the geometrical mapping between the template axisymmetric geometry and the average geometry of the MESA population [20].

Another source of uncertainty concerns the boundary conditions. The uniform pressure boundary condition at the endocardial surface and the stress free conditions at the epicardial surface are commonly used in other models in literature and considered appropriate. Applying realistic boundary conditions at the base, to represent the interactions with the atria and the large arteries is less obvious. At the base we avoided rigid body motions trying not to constrain the basal deformations too much. In fact, we adopted the same boundary conditions applied in [6], that are in line with other models in literature and comply with the findings of a recent study comparing different choices of boundary conditions [26].

Due to the high computational cost related to the complete sensitivity analysis and the analyses performed to investigate the low order interactions, we did not refine further the grid for the discretization of the parameter space. This would have required further compromises in the discretization of the finite element solution or the use of meta-modeling techniques (see for instance [5, 4, 3]). In this respect, our results must be seen as lower bound estimations. We cannot exclude that increasing the parameter space grid resolution  $n_n$  and studying the second order interactions further from the reference parameter combination might increase the role of nonlinear behaviors and interactions.

## 4.5 Conclusions

In this work we assessed the sensitivity of LV end-systolic wall strains to LV fiber orientation, varied according to ranges inferred from data found in literature. We quantified how the uncertainty propagated from parameters describing fiber orientation affects the spatial distribution of end-systolic Green-Lagrange strains. To the best of our knowledge this is the first attempt to apply global sensitivity techniques to quantify the effects that fiber orientation have on 3D end-systolic strain fields.

We concluded that the strain components most affected by fiber orientation are two shear-strains: the circumferential-transmural shear strain  $E_{ct}$ , with a coefficient of variation of  $38 \pm 18\%$ ; and the circumferential-longitudinal shear strain  $E_{cl}$ , with a coefficient of variation of  $25 \pm 8\%$ . Most of the variability of  $E_{ct}$  is due to  $t_u^0$ , describing the longitudinal offset of the transverse angle, while most of the variability of  $E_{cl}$  is due to  $h_v^0$ , describing the transmural offset of the helix angle. The two parameters  $t_u^0$  and  $h_v^0$  were found to be the most influential among all those considered. Parameter  $t_u^1$ , describing the longitudinal slope of the transverse angle was less influential, and parameters  $h_v^1$ , describing the transmural slope of the helix angle, and  $h_u^1$ , describing the longitudinal slope of the helix angle, resulted to be the least influential.

These conclusions imply that the transverse angle should be included in the description of fiber orientation to correctly predict the end-systolic strain distribution. Moreover, in the context of model personalization, the personalization of the helix angle should focus on the transmural offset rather than the most commonly modeled transmural range.

## Acknowledgement

This work was supported by the European Commission within the Horizon 2020 Framework through the MSCA-ITN-ETN European Training Networks (project number 642458)

---

## Bibliography

- [1] G. Balaban, H. Finsberg, S. Funke, T. F. Håland, E. Hopp, J. Sundnes, S. T. Wall, and M. E. Rognes. In vivo estimation of elastic heterogeneity in an infarcted human heart. *Biomechanics and Modeling in Mechanobiology*, 17(5):1317–1329, 2018.
- [2] L. Barbarotta and P. Bovendeerd. A computational approach on sensitivity of left ventricular wall strains to geometry. In *International Conference on Functional Imaging and Modeling of the Heart*, pages 240–248. Springer, 2019.
- [3] G. Blatman and B. Sudret. Sparse polynomial chaos expansions and adaptive stochastic finite elements using a regression approach. *Comptes Rendus Mécanique*, 336(6):518–523, 2008.
- [4] G. Blatman and B. Sudret. An adaptive algorithm to build up sparse polynomial chaos expansions for stochastic finite element analysis. *Probabilistic Engineering Mechanics*, 25(2):183–197, 2010.
- [5] D. Bonomi, A. Manzoni, and A. Quarteroni. A matrix deim technique for model reduction of nonlinear parametrized problems in cardiac mechanics. *Computer Methods in Applied Mechanics and Engineering*, 324:300–326, 2017.
- [6] P. H. M. Bovendeerd, W. Kroon, and T. Delhaas. Determinants of left ventricular shear strain. *American Journal of Physiology-Heart and Circulatory Physiology*, 297(3):H1058–H1068, 2009.
- [7] F. Campolongo, J. Cariboni, and A. Saltelli. An effective screening design for sensitivity analysis of large models. *Environmental modelling & software*, 22(10):1509–1518, 2007.
- [8] R. Chabiniok, P. Moireau, P. F. Lesault, A. Rahmouni, J. F. Deux, and D. Chapelle. Estimation of tissue contractility from cardiac cine-mri using a biomechanical heart model. *Biomechanics and modeling in mechanobiology*, 11(5):609–630, 2012.
- [9] H. Finsberg, G. Balaban, S. Ross, T. F. Håland, H. H. Odland, J. Sundnes, and S. T. Wall. Estimating cardiac contraction through high resolution data assimilation of a personalized mechanical model. *Journal of Computational Science*, 24:85 – 90, 2018.

- [10] H. Gao, H. Wang, C. Berry, X. Luo, and B. E. Griffith. Quasi-static image-based immersed boundary-finite element model of left ventricle under diastolic loading. *International Journal for Numerical Methods in Biomedical Engineering*, 30(11):1199–1222, 2014.
- [11] L. Geerts, P. H. M. Bovendeerd, K. Nicolay, and T. Arts. Characterization of the normal cardiac myofiber field in goat measured with mr-diffusion tensor imaging. *American Journal of Physiology-Heart and Circulatory Physiology*, 283(1):H139–H145, 2002.
- [12] L. Geerts, R. Kerckhoffs, P. Bovendeerd, and T. Arts. Towards patient specific models of cardiac mechanics: a sensitivity study. In *International Workshop on Functional Imaging and Modeling of the Heart*, pages 81–90. Springer, 2003.
- [13] A. Hassaballah, M. Hassan, A. Mardi, and M. Hamdi. Modeling the effects of myocardial fiber architecture and material properties on the left ventricle mechanics during rapid filling phase. *Applied Mathematics & Information Sciences*, 9(1):161, 2015.
- [14] R. Kerckhoffs, P. Bovendeerd, J. Kotte, F. Prinzen, K. Smits, and T. Arts. Homogeneity of cardiac contraction despite physiological asynchrony of depolarization: a model study. *Annals of biomedical engineering*, 31(5):536–547, 2003.
- [15] W. Kroon, T. Delhaas, P. Bovendeerd, and T. Arts. Computational analysis of the myocardial structure: Adaptation of cardiac myofiber orientations through deformation. *Medical image analysis*, 13(2):346–353, 2009.
- [16] S. Land, S. A. Niederer, and N. P. Smith. Efficient computational methods for strongly coupled cardiac electromechanics. *IEEE Transactions on Biomedical Engineering*, 59(5):1219–1228, May 2012.
- [17] H. Lombaert, J.-M. Peyrat, P. Croisille, S. Rapacchi, L. Fanton, F. Chieriet, P. Clarysse, I. Magnin, H. Delingette, and N. Ayache. Human atlas of the cardiac fiber architecture: study on a healthy population. *IEEE transactions on medical imaging*, 31(7):1436–1447, 2012.
- [18] S. Marchesseau, H. Delingette, M. Sermesant, R. Cabrera-Lozoya, C. Tobon-Gomez, P. Moireau, R. M. Figueras i Ventura, K. Lekadir, A. Hernandez, M. Garreau, et al. Personalization of a cardiac electromechanical model using reduced order unscented kalman filtering from regional volumes. *Medical image analysis*, 17(7):816–829, 2013.

- 
- [19] A. D. McCulloch, B. Smaill, and P. Hunter. Regional left ventricular epicardial deformation in the passive dog heart. *Circulation research*, 64(4):721–733, 1989.
- [20] P. Medrano-Gracia, B. R. Cowan, B. Ambale-Venkatesh, D. A. Bluemke, J. Eng, J. P. Finn, C. G. Fonseca, J. A. C. Lima, A. Suinesiaputra, and A. A. Young. Left ventricular shape variation in asymptomatic populations: the multi-ethnic study of atherosclerosis. *Journal of Cardiovascular Magnetic Resonance*, 16(1):56, Jul 2014.
- [21] A. Nagler, C. Bertoglio, M. Gee, and W. Wall. Personalization of cardiac fiber orientations from image data using the unscented kalman filter. In *International Conference on Functional Imaging and Modeling of the Heart*, pages 132–140. Springer, 2013.
- [22] A. Nagler, C. Bertoglio, C. T. Stoeck, S. Kozerke, and W. A. Wall. Maximum likelihood estimation of cardiac fiber bundle orientation from arbitrarily spaced diffusion weighted images. *Medical image analysis*, 39:56–77, 2017.
- [23] S. Nikolić, E. L. Yellin, K. Tamura, H. Vetter, T. Tamura, J. S. Meisner, and R. Frater. Passive properties of canine left ventricle: diastolic stiffness and restoring forces. *Circulation Research*, 62(6):1210–1222, 1988.
- [24] A. Nikou, R. C. Gorman, and J. F. Wenk. Sensitivity of left ventricular mechanics to myofiber architecture: A finite element study. *Proceedings of the Institution of Mechanical Engineers, Part H: Journal of Engineering in Medicine*, 230(6):594–598, 2016.
- [25] H. Osnes and J. Sundnes. Uncertainty analysis of ventricular mechanics using the probabilistic collocation method. *IEEE Transactions on Biomedical Engineering*, 59(8):2171–2179, 2012.
- [26] M. Peirlinck, K. L. Sack, P. De Backer, P. Morais, P. Segers, T. Franz, and M. De Beule. Kinematic boundary conditions substantially impact in silico ventricular function. *International journal for numerical methods in biomedical engineering*, 35(1):e3151, 2019.
- [27] S. Pezzuto, D. Ambrosi, and A. Quarteroni. An orthotropic active-strain model for the myocardium mechanics and its numerical approximation. *European Journal of Mechanics - A/Solids*, 48:83 – 96, 2014. *Frontiers in Finite-Deformation Electromechanics*.



- [28] M. Pluijmert, T. Delhaas, A. F. de la Parra, W. Kroon, F. W. Prinzen, and P. H. Bovendeerd. Determinants of biventricular cardiac function: a mathematical model study on geometry and myofiber orientation. *Biomechanics and modeling in mechanobiology*, 16(2):721–729, 2017.
- [29] R. Rodríguez-Cantano, J. Sundnes, and M. E. Rognes. Uncertainty in cardiac myofiber orientation and stiffnesses dominate the variability of left ventricle deformation response. *International journal for numerical methods in biomedical engineering*, 35(5):e3178, 2019.
- [30] S. Rossi, T. Lassila, R. Ruiz-Baier, A. Sequeira, and A. Quarteroni. Thermodynamically consistent orthotropic activation model capturing ventricular systolic wall thickening in cardiac electromechanics. *European Journal of Mechanics - A/Solids*, 48:129 – 142, 2014. *Frontiers in Finite-Deformation Electromechanics*.
- [31] I. M. Sobol'. Global sensitivity indices for the investigation of nonlinear mathematical models. *Matematicheskoe modelirovanie*, 17(9):43–52, 2005.
- [32] D. D. Streeter Jr. Gross morphology and fiber geometry of the heart. In B. R. M, editor, *Handbook of Physiology - The Cardiovascular System I*, chapter 10, pages 61–112. American Physiological Society Bethesda, MD, 1979.
- [33] D. D. Streeter Jr, H. M. Spotnitz, D. P. Patel, J. Ross Jr, and E. H. Sonnenblick. Fiber orientation in the canine left ventricle during diastole and systole. *Circulation research*, 24(3):339–347, 1969.
- [34] N. Toussaint, C. T. Stoeck, T. Schaeffter, S. Kozerke, M. Sermesant, and P. G. Batchelor. In vivo human cardiac fibre architecture estimation using shape-based diffusion tensor processing. *Medical image analysis*, 17(8):1243–1255, 2013.
- [35] H. Wang, H. Gao, X. Luo, C. Berry, B. Griffith, R. Ogden, and T. Wang. Structure-based finite strain modelling of the human left ventricle in diastole. *International journal for numerical methods in biomedical engineering*, 29(1):83–103, 2013.
- [36] V. Y. Wang, H. I. Lam, D. B. Ennis, B. R. Cowan, A. A. Young, and M. P. Nash. Modelling passive diastolic mechanics with quantitative mri of cardiac structure and function. *Medical image analysis*, 13(5):773–784, 2009.

- [37] J. Xi, P. Lamata, J. Lee, P. Moireau, D. Chapelle, and N. Smith. Myocardial transversely isotropic material parameter estimation from in-silico measurements based on a reduced-order unscented kalman filter. *Journal of the mechanical behavior of biomedical materials*, 4(7):1090–1102, 2011.
- [38] J. Xi, P. Lamata, S. Niederer, S. Land, W. Shi, X. Zhuang, S. Ourselin, S. G. Duckett, A. K. Shetty, C. A. Rinaldi, et al. The estimation of patient-specific cardiac diastolic functions from clinical measurements. *Medical image analysis*, 17(2):133–146, 2013.







## **Chapter 5**

# **Parameter Estimation in a Rule-Based Fiber Orientation model from End Systolic Strains Using the Reduced Order Unscented Kalman Filter**

**Abstract**

In **chapter 4** we showed that fiber orientation is a major factor in the determination of end systolic strains within finite element models of cardiac mechanics. Its precise modeling might improve the fidelity of models and might lead to better estimations when these models are used to inversely analyse patient data. Unfortunately, patient-specific fiber orientation measurements via DT-MRI are not viable nowadays in clinical practice. Therefore, alternative methods are required to assess patient-specific fiber orientation based on viable data. In this respect, we investigated the application of the Reduced Order Unscented Kalman Filter to estimate rule-based fiber orientation parameters from end systolic wall strains of the patient, as could be observed using imaging techniques commonly included in clinical practice. We address the estimation of fiber orientation in the physiological left ventricle. End systolic strain observations were generated in-silico using two different rule-based fiber models. The estimation process focused on the determination of the three most influential parameters emerged from our sensitivity study: two model parameters for the transverse angle (describing the endocardium-to-epicardium component of the fiber vector) and one model parameter for the helix angle (describing the base-to-apex component). Results show that the strain component  $E_{ct}$  alone carries enough information to achieve the estimation of the three parameters  $h_0^v$  (the transmural offset of the helix angle),  $t_0^u$  (the longitudinal offset of the transverse angle), and  $t_1^u$  (longitudinal slope of the transverse angle) within the measurement error of DT-MRI.

## 5.1 Introduction

Patient-specific models of cardiac electromechanics might constitute a precious tool for assisting cardiologists during decision making. Patient-specific models are obtained by tailoring a generic model including patient data. Patient data come typically from imaging techniques currently adopted in the clinic, such as MRI and Ultrasound. Using such methodologies, patient-specific geometries can be derived and myocardial strains can be computed non-invasively [14, 3, 17, 22]. Non-invasive in-vivo strain measurements are often included in data assimilation procedures in order to achieve a patient-specific model that allows a physics-based interpretation of patient data [5, 18, 27, 11, 12, 30]. Data assimilation is typically used to inversely estimate regional quantities such as contractility and moment of activation. These quantities might be helpful for clinicians during diagnosis and decision making as this information is more directly related to the pathology than information on abnormalities in the spatial distribution of strains and displacement.

In models of cardiac mechanics, the orientation of fibers in the myocardium plays an important role in determining cardiac function [25, 13]. Myofibers follow a complex path and constitute a major direction of anisotropy during the myocardial contraction. In the free wall of the left ventricle, they largely vary their orientation transmurally in the circumferential-longitudinal plane from  $-60^\circ$  at epicardium, to approximately  $0^\circ$  (circumferential) at mid-wall, to  $60^\circ$  at endocardium. Myofiber orientation can be measured using Diffusion Tensor MRI (DT-MRI). Peyrat et al [23], proposed a methodology to build atlases out of ex-vivo DT-MRI measurements and applied this methodology to measurements obtained from nine ex-vivo canine hearts. A 3D fiber atlas from ten ex-vivo healthy human hearts has been created by Lombaert et al [16] using DT-MRI. Typically, such ex-vivo DT-MRI data are often used to define fiber fields in models of cardiac mechanics [15], although they cannot be considered patient-specific. Patient-specific information might be obtained using in-vivo DT-MRI, but this is more complicated due to the bulk motion of the heart. In this regard, Toussaint et al [28] developed a technique to reconstruct the 3D fiber field from several 2D slice acquisitions. However, the acquisition of each single slice took between 10 min to 15 min. Despite optimizations, the current long acquisition time of in-vivo DT-MRI acquisition does not allow its use in clinical practice.

Most often in data assimilation procedures applied to models of electromechanics, fiber orientation is chosen according to generic ex-vivo Diffusion Tensor MRI measurements [27] or generic rule-based fiber models [5, 12, 30]. Given the important role of fiber orientation within those models, the long



acquisition time required by DT-MRI, and the measurement error of such procedure, alternative solutions are required arrive at a patient-specific fiber field and hence to improve the predictive capabilities of such methodology. A possible solution might come from the application of data assimilation techniques to estimate patient specific fiber orientation without requiring DT-MRI measurements. One of the first attempts to use data assimilation techniques to estimate fiber orientation was proposed by Nagler et al [20], who applied the Reduced Order Unscented Kalman Filter (ROUKF) to estimate the parameters of a rule-based fiber model from noisy DT-MRI measurements. This method, however, still relies on the availability of a DT-MRI measurement of the patient, which is difficult to achieve. The same author in [21] applied a maximum likelihood estimator to reconstruct fiber orientation from arbitrarily spaced DT-MRI acquisition. Despite still relying on DT-MRI measurement, the method constitutes a possible acceleration factor for DT-MRI acquisitions for fiber orientation reconstruction. Alternatively, to overcome the difficulty in obtaining patient-specific DT-MRI measurements, the application of data assimilation methodologies to estimate parameters of rule-based fiber models based on available patient measurements should be investigated. In this chapter, we investigate the use of strain data to inversely estimate parameters of a rule-based fiber model using the ROUKF [19]. As a first step, we use strain data obtained in-silico rather than in-vivo.

We perform three experiments of parameter estimation for a model describing the spatial distribution of fiber orientation. The estimation is based on the observation of a subset of Green-Lagrange end-systolic strain components in ellipsoidal coordinates using the end-diastolic configuration as reference. In the first experiment, observations are generated in-silico using our model of mechanics of the LV with a simplified fiber orientation model including five parameters. The fiber parameters are then estimated using the same fiber model starting from the ground truth values. This experiment is used to determine which combination of strain components best allows to estimate parameters. In the second experiment, the estimation procedure involves the same model of mechanics and the same fiber model of the previous experiment, but the fiber parameters are initialized at one SD-distance from their ground truth values. This experiment is used to determine whether the parameter estimation converges also when introducing a perturbation in the initial guess proportional to the uncertainty typically encountered in fiber orientation measurements. In the last experiment, observations are generated using a twelve parameter fiber orientation model presented by Bovendeerd et al [7] and then fiber parameters are estimated using the simplified five parameter fiber model. This experiment allows to understand whether the presence

of incomplete information concerning the fiber model would still allow to extract meaningful information.

## 5.2 Methods

### 5.2.1 Reduced order unscented Kalman filter

Kalman filtering can be used to estimate the state of a dynamic system affected by model and observation errors. It is a convenient approach that allows the sequential estimation of a process state by minimizing the variance of the estimation error. Sequential means that, as soon as new information is available, the estimation is updated without the need of recomputing everything, but only updating the posterior probability density function (PDF) including the new observation [4]. Assuming a linear process and a linear observation operator, if both the model error and the observation error are Gaussian white noise, then the posterior PDF is Gaussian and the estimation obtained using a Kalman Filter (KF) is optimal. Two issues prevent the straightforward application of the KF for the problem of cardiac mechanics: the non-linearity and the dimension of the problem. A solution to the first issue, comes from the Unscented Transform [29], which allows at least a second order approximation of the PDF after the nonlinear transformation by using sigma-points. Sigma-points are a set of  $n + 1$  points in  $n$ -dimension that allows to define a discrete distribution having a certain given mean and covariance. A solution to the second issue, comes from the reduction of covariance matrices [9, 6]. However, in general further modifications must be introduced in the filter algorithm as in [24].

In this work, we implemented a Reduced Order Unscented Kalman Filter presented by Moireau et al [19] to estimate parameters in a fiber orientation model included in the model of LV mechanics (2.2.43). The ROUKF algorithm requires three stages: a sampling stage, a prediction stage, and a correction stage. In the sampling stage, the sigma-points are generated according to the updated average and covariance of the parameters involved in the estimation. In the prediction stage, the predictive model predicts the states corresponding to the sigma-points sampled at the previous stage. In this work, the state is the deformed configuration of the LV and the sigma-points are a subset of the fiber parameters. At the correction stage, the average and the covariance of state and parameters are corrected using the difference between the measurements and the observations derived from the prediction stage.

The prediction stage relies on the simulation of a cardiac cycle until the end-systolic configuration. Given  $\vec{\theta}_n$ , a vector of parameters of the LV mechan-

ics model to be estimated, the end-systolic configuration  $\vec{x}_{n+1}$  is achieved by means of the following nonlinear operator

$$\vec{x}_{n+1} = \mathcal{A}_{n+1|n}(\vec{x}_0, \vec{\theta}_n), \quad (5.2.1)$$

where  $\vec{x}_0$  is the unloaded configuration and  $\mathcal{A}_{n+1|n}$  is nonlinear operator that solves the circulation-mechanics coupled problem until the end-systolic configuration at time  $n + 1$  given the parameters  $\vec{\theta}_n$ , defined as follows

$$\mathcal{A}_{n+1|n}(\vec{x}_0, \vec{\theta}_n) = \begin{cases} \begin{cases} \text{(solve until end systole)} \\ \mathcal{C}(p_{lv}) \rightarrow V_{lv}, & \text{circulation} \\ \mathcal{M}(\vec{u}; p_{lv}, \vec{\theta}_n) = 0 \rightarrow V_c, & \text{wall mechanics} \\ \text{until } V_c = V_{lv}, \end{cases} \\ \vec{x}_{n+1} = \vec{x}_0 + \vec{u}(\vec{x}_0; \vec{\theta}_n), \end{cases} \quad (5.2.2)$$

where  $\mathcal{C}$ , defined in (2.2.34), is the nonlinear operator that represents the circulation problem,  $\mathcal{M}$ , defined in (2.2.43), is the nonlinear operator that represents the mechanics, and  $V_c$  and  $V_{lv}$  are the two cavity volumes computed within the fixed-point iteration scheme in (2.2.61). The state  $\vec{x}$  is observed at the end of systole using the nonlinear observation operator  $\mathcal{H}$  that computes end-systolic Green-Lagrange strains with respect to the end-diastolic configuration from the displacement. Given a set of pairs of normal vectors  $(\vec{e}_{i_1}, \vec{e}_{j_1}) \dots (\vec{e}_{i_n}, \vec{e}_{j_n})$ , with  $i_1, \dots, i_n$  and  $j_1, \dots, j_n$  in  $\{c, l, t\}$  (c circumferential, l longitudinal, and t transmural), it reads

$$\vec{z}_{n+1} = \mathcal{H}(\vec{x}_{n+1}) + \vec{v}, \quad \text{with:} \quad (5.2.3)$$

$$\mathcal{H}(\vec{x}_{n+1}) = [\mathbf{E}^{ED \rightarrow ES}(\vec{x}_{n+1}) \vec{e}_{i_1} \cdot \vec{e}_{j_1}, \dots, \mathbf{E}^{ED \rightarrow ES}(\vec{x}_{n+1}) \vec{e}_{i_n} \cdot \vec{e}_{j_n}]^T, \quad (5.2.4)$$

$$\mathbf{E}^{ED \rightarrow ES}(\vec{x}_{n+1}) = \frac{1}{2} \left[ \nabla_0 \vec{x}_{ED, n+1}^{-T} \nabla_0 \vec{x}_{n+1}^T \nabla_0 \vec{x}_{n+1} \nabla_0 \vec{x}_{ED, n+1}^{-1} - \mathbf{I} \right], \quad (5.2.5)$$

where  $\vec{x}_{ED, n+1}$  is the end-diastolic configuration,  $\vec{v}$  is a Gaussian random variable with covariance matrix  $\mathbf{W}$  that describes the measurements and the discretization errors. Note that the nonlinear operator  $\mathcal{A}_{n+1|n}$  is static and its application on  $\vec{x}_0$  using parameters  $\vec{\theta}_n$  leads directly to the estimation of the end-systolic configuration and, consequently, to the observation of the end-systolic strain components via  $\mathcal{H}$ . Therefore, the parameter estimation is ac-

complished by solving a sequence of application of  $\mathcal{A}_{n+1|n}$  without including information from the intermediate states achieved during the cardiac cycle. To achieve the parameter estimation, first an ensemble of points, called sigma-points, is drawn during the sampling stage. Then, these sigma-points are simulated using operator  $\mathcal{A}_{n+1|n}$  during the prediction stage. Eventually during the correction stage, the posterior distribution is updated and the solution is corrected accordingly. These three stages are repeated sequentially until the satisfaction of a stopping criterion.

The algorithm initialization starts with the definition of a centered (zero-mean) sigma-points matrix  $\mathbf{V}^* \in \mathbb{R}^{p \times r}$ , where  $p$  is the number of parameters to be estimated and  $r$  the number of sigma-points. According to Moireau et al [19] for the simplex case, which requires a minimum amount of sigma-points ( $r = p + 1$ ) and requires no re-sampling, a possible choice for  $\mathbf{V}^*$  is

$$\mathbf{V}^* = \begin{bmatrix} 1 & & 0 & -1 \\ & \ddots & & \\ 0 & & 1 & -1 \end{bmatrix}, \quad (5.2.6)$$

from which sigma-points with unitary variance ( $\mathbf{I}^* \in \mathbb{R}^{p \times r}$ ) can be derived using the following formula

$$\mathbf{I}^* = (\mathbf{V}^* \mathbf{D}_\alpha \mathbf{V}^{*T})^{-\frac{1}{2}} \mathbf{V}^{*T}, \quad \text{where,} \quad (5.2.7)$$

$$\mathbf{D}_\alpha = \frac{1}{r} \begin{bmatrix} 1 & & 0 \\ & \ddots & \\ 0 & & 1 \end{bmatrix}, \quad (5.2.8)$$

where  $\mathbf{D}_\alpha \in \mathbb{R}^{r \times r}$ . Exploiting the definitions of  $\mathbf{V}^*$  and  $\mathbf{D}_\alpha$  the a-priori covariance can be defined as

$$\mathbf{P}_\alpha^V = \mathbf{V}^* \mathbf{D}_\alpha \mathbf{V}^{*T}. \quad (5.2.9)$$

The last step of the initialization requires the definition of  $\mathbf{L}_0^\theta \in \mathbb{R}^{p \times p}$ , and  $\mathbf{L}_0^x \in \mathbb{R}^{s \times p}$  (with  $s$  being the size of  $\vec{x}$ ), the operators that transform the sigma-points into parameter and state vectors, respectively.  $\mathbf{L}_0^\theta$  is initialized as the identity matrix and  $\mathbf{L}_0^x$  is initialized as the null matrix. Finally,  $\mathbf{U}_0 = \text{Cov}(\delta\vec{\theta})^{-1} \in \mathbb{R}^{p \times p}$  representing the inverse of the covariance matrix of the parameters will be defined in the results section depending on the involved parameters.

The sampling stage requires the definition of  $\sqrt{\mathbf{U}_n^{-1}}$ , achieved using the Cholesky decomposition, and exploits this matrix to convert sigma-points into

new state and parameter vectors

**(sampling)**

$$\begin{cases} \mathbf{C}_n = \sqrt{\mathbf{U}_n^{-1}}, & (\text{Cholesky decomposition on } \mathbf{U}_n^{-1}), \\ \vec{x}_n^{(i)+} = \vec{x}_n^+ + \mathbf{L}_n^x \mathbf{C}_n^T \vec{I}^{(i)}, \\ \vec{\theta}_n^{(i)+} = \vec{\theta}_n^+ + \mathbf{L}_n^\theta \mathbf{C}_n^T \vec{I}^{(i)}, \end{cases} \quad (5.2.10)$$

where  $i = 1, \dots, r$ ,  $\vec{I}^{(i)}$  is the  $i$ -th column of  $\mathbf{I}^*$ , and the superscript  $+$  means that the quantities have been corrected (in the previous iteration).

The prediction stage requires the simulation of the  $r$  sigma-points and a correction using the Kalman gain matrix

**(prediction)**

$$\begin{cases} \mathbf{K}_{n+1|n} = \mathbf{L}_n^x (\mathbf{P}_\alpha^V)^{-1} \mathbf{H}_{L,n}^{xT} \mathbf{W}_n^{-1}, \\ \vec{x}_{n+1}^{(i)-} = \mathcal{A}_{n+1|n} \left( \vec{x}_0, \vec{\theta}_n^{(i)+} \right) + \mathbf{K}_{n+1|n} \left( \vec{Z}_n - \mathcal{H} \left( \vec{x}_n^{(i)+} \right) \right), \\ \vec{x}_{n+1}^- = E_\alpha \left( \vec{x}^{*-} \right) = \frac{1}{r} \sum_{i=1}^r \vec{x}_{n+1}^{(i)}, \\ \vec{\theta}_{n+1}^{(i)-} = \vec{\theta}_n^+, \end{cases} \quad (5.2.11)$$

where the superscript  $-$  means that the quantities are predicted but not yet corrected,  $\mathbf{W}_n$  is the covariance matrix of the observation error,  $\vec{x}^{*-} \in \mathbb{R}^{s \times r}$  is the matrix made by collecting all the column vectors  $\vec{x}_{n+1}^{(i)-}$ , and  $\mathbf{H}_{L,n}^x \in \mathbb{R}^{q \times p}$  (with  $q$  the size of the observation vector and  $\mathbf{H}_{L,0}^x$  initialized to the null matrix) is defined during the correction stage of the previous iteration.

Finally, the correction stage allows to update the factorized posterior covariance matrix by means of  $\mathbf{L}_{n+1}^x$ ,  $\mathbf{L}_{n+1}^\theta$ ,  $\mathbf{U}_{n+1}$ , and  $\mathbf{H}_{L,n+1}^x$

**(correction)**

$$\begin{cases} \mathbf{L}_{n+1}^x = \mathbf{x}^{*-} \mathbf{D}_\alpha \mathbf{V}^{*T}, \\ \mathbf{L}_{n+1}^\theta = \mathbf{\theta}^{*-} \mathbf{D}_\alpha \mathbf{V}^{*T}, \\ \vec{z}_{n+1}^{(i)} = \mathcal{H} \left( \vec{x}_{n+1}^{(i)-} \right), \\ \mathbf{H}_{L,n+1}^x = \mathbf{z}_{n+1}^* \mathbf{D}_\alpha \mathbf{V}^{*T}, \\ \mathbf{U}_{n+1} = \mathbf{P}_\alpha^V + \mathbf{H}_{L,n+1}^{xT} \mathbf{W}_{n+1}^{-1} \mathbf{H}_{L,n+1}^x, \\ \vec{x}_{n+1}^+ = \vec{x}_{n+1}^- + \mathbf{L}_{n+1}^x \mathbf{U}_{n+1}^{-1} \mathbf{H}_{L,n+1}^{xT} \mathbf{W}_{n+1}^{-1} \left( \vec{z}_{n+1} - E_\alpha \left( \mathbf{z}_{n+1}^* \right) \right), \\ \vec{\theta}_{n+1}^+ = \vec{\theta}_{n+1}^- + \mathbf{L}_{n+1}^\theta \mathbf{U}_{n+1}^{-1} \mathbf{H}_{L,n+1}^{\theta T} \mathbf{W}_{n+1}^{-1} \left( \vec{z}_{n+1} - E_\alpha \left( \mathbf{z}_{n+1}^* \right) \right), \end{cases} \quad (5.2.12)$$

where  $\mathbf{z}_{n+1}^* \in \mathbb{R}^{q \times r}$  is made by collecting all the observation vectors  $z_{n+1}^{(i)}$ ,  $\theta^{*-} \in \mathbb{R}^{p \times r}$  is made by collecting the parameter vectors  $\vec{\theta}_{n+1}^{(i)-}$ , and  $\vec{z}_{n+1}$  is the measurement vector. Note that the use of factorization for the covariance matrices prevented the creation of a square dense covariance matrix of the same size of the state variable. For a more in depth description of the algorithm, refer to Moireau et al [19].

### 5.2.2 Simulation settings

At each iteration of the ROUKF algorithm,  $r$  sigma-points, corresponding to  $r$  sets of fiber parameters, are sampled. For each sigma-point, a cardiac cycle simulation is performed until the end-systolic configuration using the corresponding fiber parameters. The remaining parameters are kept to their default values, which are reported in Table 2.2, Table 2.3, Table 2.4. For the sake of computational time, the discretization of the problem relies on linear continuous Lagrangian piece-wise polynomials ( $r = 1$  in (2.2.37)). Briefly, an ellipsoidal geometry with cavity volume 44 mL and wall volume of 136 mL is used to generate an anisotropic mesh using 16 circumferential elements, 10 longitudinal elements, and 6 transmural elements. The geometry is characterized by a  $\xi_{endo} = 0.371$  and  $\xi_{epi} = 0.678$  and a planar base at  $z = 24$  mm.

We perform three estimation procedures. In all three estimation procedures the fiber orientation is modeled using the simplified 5-parameters model in (4.2.8) and (4.2.9). Within this model, the helix and the transverse angles are defined using 5 parameters and the normalized longitudinal and transmural coordinates ( $u$ , and  $v$ ).

$$\begin{aligned}\alpha_h(u, v) &= (h_0^v + h_1^v v) (1 + h_1^u), \\ \alpha_t(u, v) &= (1 - v^2) (t_0^u + t_1^u u).\end{aligned}\tag{5.2.13}$$

Among the 5 parameters, we include in the estimation process only the three most influential parameters emerged from our previous sensitivity analysis in **chapter 4**, which are  $h_0^v$ ,  $t_0^u$ ,  $t_1^u$ . In each of the three estimation procedures, we considered seven parameter combinations: three single parameter estimations ( $h_0^v$ ,  $t_0^u$ ,  $t_1^u$ ), where only one parameter is estimated per procedure; three double parameter estimations ( $(h_0^v, t_0^u)$ ,  $(h_0^v, t_1^u)$ ,  $(t_0^u, t_1^u)$ ), where two parameters are estimated per procedure; and a three-parameter experiments, where all the three parameters are estimated in the same estimation procedure. For all the parameter combinations, six combinations of the three observed end-systolic strains are considered that were found to be most sensitive to variations in the fiber field in **chapter 4**. These combinations are based on

observations of  $E_{ct}$ , the strain component most affected by  $t_0^u$  and  $t_1^u$ ,  $E_{cl}$ , the strain most affected by  $h_0^v$ , and  $E_{cc}$ , the strain affected in a similar fashion by  $h_0^v$  and  $t_0^u$ . The six considered combinations are:  $z = [E_{ct}]^T$ ,  $z = [E_{cl}]^T$ ,  $z = [E_{cc}]^T$ ,  $z = [E_{ct}, E_{cl}]^T$ ,  $z = [E_{ct}, E_{cc}]^T$ ,  $z = [E_{ct}, E_{cl}, E_{cc}]^T$ . We left out the combination  $z = [E_{cl}, E_{cc}]^T$  as, after simulating the first three combinations, it was clear that  $E_{ct}$  played the main role in the estimation.

In a real application, the covariance matrix of the observation error should represent the many sources of error affecting the strain measurement in patients. Among these errors, for instance, the error affecting the image acquisition depends on the measurement methodology, might not be uniform in time and space, and it might affect strain components differently. We are unable to quantify this error. Instead, since in our previous analysis (**chapter 4**) we estimated the variation of end-systolic strains induced by perturbation of fiber orientation. We make use of this piece of information to model the covariance matrix of the observation error  $\mathbf{W}_n$ . This covariance matrix is assumed to be diagonal (spatially independent noise) with diagonal values being equal to the mean coefficient of variation computed from the sensitivity analysis multiplied by the infinity-norm of the measured strain component. These mean coefficients of variation for the three strains considered are:  $E_{cc} = 0.15$ ,  $E_{cl} = 0.25$ , and  $E_{ct} = 0.38$ . Since the observation vector is generated by in-silico experiments, the infinity-norm of the measured components depends on the ground truth values of the fiber model.

The difference between the three estimation procedures relies in the fiber model used to generate in-silico the observations and the initialization of fiber parameters. For the first two estimation procedures, observations are generated using the same 5-parameters model. Instead, in the third estimation procedure, observations are generated using the fiber model proposed by Bovendeerd et al [7].

In the first procedure, experiment 1, fiber parameters are initialized to their ground truth values. Instead, in the second procedure, experiment 2, fiber parameters are initialized at one SD-distance from the ground truth values. In these first two experiments, the ground truth parameter values for the 5-parameters model are:  $h_0^v = 0.3565$  rad,  $h_1^v = -1.0471$  rad,  $h_1^u = 0$  rad,  $t_0^u = 0$  rad, and  $t_1^u = 0.1738$  rad. Observations generated using these values result in end-systolic strains with the following infinity-norm (the maximum absolute value within the geometry)

$$\|E_{cc}\|_\infty = 0.2774, \quad \|E_{cl}\|_\infty = 0.1731, \quad \|E_{ct}\|_\infty = 0.2875. \quad (5.2.14)$$

For the third estimation procedure, experiment 3, observations are generated using the fiber model proposed by Bovendeerd et al [7]. The model has

been rewritten here without using Legendre polynomials in order to have a clearer correspondence between the parameters of the two considered models. This procedure led to the following definition, that we address as the 14-parameters model

$$\begin{aligned}\alpha_h(u, v) &= \left( \sum_{i=0}^4 a_i v^i \right) \left( \sum_{i=0}^4 b_i u^i \right), \\ \alpha_t(u, v) &= \left( \sum_{i=0}^2 c_i v^i \right) (1 - v^2) \left( \sum_{i=0}^5 d_i u^i \right),\end{aligned}\tag{5.2.15}$$

where the parameter values are shown in Table 5.1.

$a_0$	$a_1$	$a_2$	$a_3$	$a_4$
0.4010	-1.3535	0.0442	0.3225	0.2686
$b_0$	$b_1$	$b_2$	$b_3$	$b_4$
0.9245	0	0.4105	0	-0.3067

$c_0$	$c_1$	$c_2$	$d_0$	$d_1$	$d_2$	$d_3$	$d_4$	$d_5$
0.749	-0.626	0.753	0	0.3807	0	0.1950	0	0.2993

**Table 5.1:** Parameter values for the 14-parameters model corresponding to the same fiber model proposed by Bovendeerd et al [7]. All values are expressed in radian.

In experiment 3, since we use two different fiber models for generating the observations and for the estimation process, the definition of ground truth values is not straightforward. We projected the 14-parameters model onto the 5-parameters model using the  $L^2([-1, 1] \times [-1, 0.5])$  integral scalar product, leading to  $h_0^v = 0.3565$  rad,  $h_1^v = -1.0471$  rad,  $h_1^u = 0$  rad,  $t_0^u = 0$  rad, and  $t_1^u = 0.5164$  rad. These values will be considered as the ground truth in the third estimation procedure. Observations generated using the 14-parameters model result in end-systolic strains with the following infinity-norm

$$\|E_{cc}\|_\infty = 0.2771, \quad \|E_{cl}\|_\infty = 0.0540, \quad \|E_{ct}\|_\infty = 0.1684.\tag{5.2.16}$$

## 5.3 Results

### 5.3.1 Experiment 1: estimation without model error from ground truth

In this first estimation experiment, the observations are generated using the 5-parameters fiber model (5.2.13). The same 5-parameters fiber model is used



in the estimation procedure. The estimation algorithm starts from fiber parameter values set equal to the ground truth. Figure 5.1 shows the evolution of parameter errors in estimation experiments where different strain component combinations were considered. Each panel of the figure represents the absolute error of a parameter from its ground truth value. The line color identifies the parameter:  $h_v^0$  in green,  $t_u^0$  in blue, and  $t_u^1$  in red. The line style classifies the combination of parameters estimated in the experiment. The estimation algorithm starts from fiber parameter values set equal to the ground truth and the parameters not included in the estimation are not perturbed from the ground truth. Note that this information is not included in the figures as it refers to the state at iteration zero. At the very first iteration, the estimated parameters are already perturbed using the initial guess of the inverse covariance matrix of the parameters  $\mathbf{U}_0$  during the sampling stage. All the estimation experiments were stopped once the absolute incremental variation of all the parameters involved in the estimation was below a threshold value of  $5 \times 10^{-4}$  rad. For this reason, not all the experiments needed the same number of iterations. A gray region is represented in the plot to indicate the DTI measurement error ( $\sim 10^\circ$  [26]).

Figure 5.1a, Figure 5.1b, Figure 5.1c, show the results when the observed strain is  $E_{cc}$ ,  $E_{cl}$ , and  $E_{ct}$ , respectively. For the sake of readability only a narrow range close to the zero-error level is shown. In this range for every panel four lines should be visible. Otherwise, the missing lines indicate diverged parameter estimations or estimations that converged to values that differ from the ground truth by more than 0.3 rad. In this sense, only  $E_{ct}$  allows the estimation of the three parameters to converge with an error below 0.05 rad for  $h_v^0$  and  $t_u^0$  and an error of about 0.1 rad for  $t_u^1$  (Figure 5.1c). Instead, observing only  $E_{cc}$  or  $E_{cl}$  does not allow to estimate  $h_v^0$  and  $t_u^1$  within the measurement error in two out of four experiments. In particular for  $t_u^1$ , the estimation failed (error beyond 0.3 rad) when all the parameters were involved in the estimation. Results similar to those obtained observing  $E_{ct}$  exclusively were obtained when observing  $[E_{ct}, E_{cl}]^T$  (Figure 5.1d) and  $[E_{ct}, E_{cl}, E_{cc}]^T$  (Figure 5.1f). In these three cases, similar results are achieved for all the parameter combinations, with the estimation error of  $t_u^1$  in the three-parameter estimations always being the largest. These estimated parameters lead to an average difference between the ground truth and the estimated fiber vectors of  $1.4^\circ$  (maximum  $5.6^\circ$ ) when observing  $E_{ct}$ ,  $1.2^\circ$  (maximum  $5.3^\circ$ ) when observing  $[E_{ct}, E_{cl}]^T$ , and  $1.4^\circ$  (maximum  $5.3^\circ$ ) when observing  $[E_{ct}, E_{cl}, E_{cc}]^T$ . Concerning convergence, when estimating the three considered parameters altogether (dashed lines in Figure 5.1), there is only a slight decrease in the number of iterations required when observing  $[E_{ct}, E_{cl}]^T$  (Figure 5.1d), 12 iterations compared to 15

requested by  $E_{ct}$  (Figure 5.1c) and  $[E_{ct}, E_{cl}, E_{cc}]^T$  (Figure 5.1f). Among the estimations of the three parameters altogether that included the observation of  $E_{ct}$ , only the observation of  $[E_{ct}, E_{cc}]^T$  led to a converged value for  $t_u^1$  further than one measurement error distance from the ground truth (Figure 5.1e).

The error between the ground truth strains and the strains predicted using the estimated parameters can be seen in Figure 5.4. The error is expressed in terms of average 1-norm, which is the average over the discretization nodes of the absolute value of the node-wise difference between ground truth and predicted strains. The average 1-norm of the error is shown in Figure 5.4a for the observation of  $E_{ct}$ , in Figure 5.4b for the observation of  $[E_{ct}, E_{cl}]^T$ , and in Figure 5.4c for the observation of  $[E_{ct}, E_{cl}, E_{cc}]^T$ . For these three strain combinations, a steady observation error is achieved after 8 iterations. These error equal about 0.023 (68 % error drop from iteration 1), about 0.014 (73 % error drop), and about 0.013 (79 % error drop) for observation of  $E_{ct}$ ,  $[E_{ct}, E_{cl}]^T$ , and  $[E_{ct}, E_{cl}, E_{cc}]^T$ , respectively.

### 5.3.2 Experiment 2: estimation without model error

We repeated the previous experiment setting the initial guess for the parameters at about measurement error-distance from the ground truth. This resulted in initial values of 0.175 rad (ground truth 0.3565 rad) for  $h_v^0$ ,  $-0.175$  rad (ground truth 0 rad) for  $t_u^0$ , and 0 rad (ground truth 0.1738 rad) for  $t_u^1$ .

Figure 5.2 shows the evolution of parameter errors in estimation experiments for the three end-systolic strain combinations that led to best estimations in experiment 1:  $z = [E_{ct}]^T$ ,  $z = [E_{ct}, E_{cl}]^T$ , and  $z = [E_{ct}, E_{cl}, E_{cc}]^T$ . All the estimation experiments were stopped once the absolute variation of all the parameters involved in the estimation was below a threshold value of  $5 \times 10^{-4}$  rad. Figure 5.2 shows that results obtained with the three different strain combinations are similar. Only the joint estimation of  $h_v^0$  and  $t_u^1$  failed to converge within 0.20 rad error for all the observed combination of strains. In all other experiments, the parameters were estimated within the measurement error. Figure 5.2a and Figure 5.2c show a small difference in number of iterations. In fact, when jointly estimating the three parameters, 19 iterations are required when observing  $E_{ct}$  and 15 iterations are required when observing  $[E_{ct}, E_{cl}, E_{cc}]^T$ . The observation of  $[E_{ct}, E_{cl}]^T$  required many more iterations for the parameters to converge (48 iterations). However, the estimation of  $t_u^1$  was twice as accurate ( $t_u^1 = 0.12$  rad) whereas the accuracy of  $h_v^0$  and  $t_u^0$  remained unchanged. The joint estimations of the three parameters lead to an average difference between the ground truth and the estimated fiber vectors of  $1.3^\circ$  (maximum  $5.5^\circ$ ) when observing  $E_{ct}$ ,  $0.8^\circ$  (maximum  $2.4^\circ$ ) when ob-

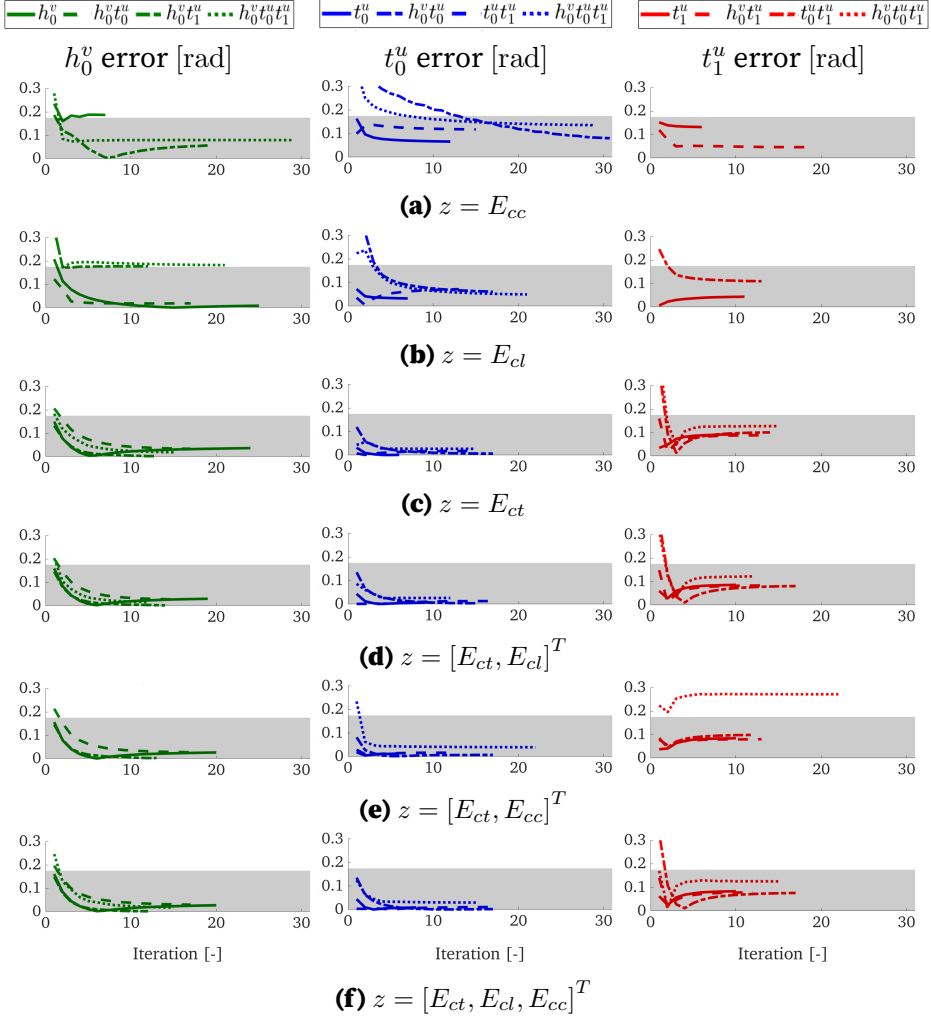


**Figure 5.1:** Experiment 1: evolution of parameter errors when observation and estimation are performed using the same fiber model. Each estimation started from the ground truth values of the parameters. Three columns, one per parameter, and six rows, one per observed strain combination, are shown. Three colors are used to indicate different parameters errors: green for  $h_v^0$ , blue for  $t_u^0$ , and red for  $t_u^1$ . The line type determines the parameters included in the estimations: solid lines refer to estimations with a single parameter, dotted lines refer to the joint estimation of all the three parameters, and dashed and dash-dotted lines refer to the joint estimation of a pair out of the three parameters. The gray area represents the DT-MRI measurement error reported in [26].

serving  $[E_{ct}, E_{cl}]^T$ , and  $1.4^\circ$  (maximum  $5.3^\circ$ ) when observing  $[E_{ct}, E_{cl}, E_{cc}]^T$ . The error between the ground truth strains and the strains from the estima-

## Parameter Estimation in a Rule-Based Fiber Orientation model from End Systolic Strains Using the Reduced Order Unscented Kalman Filter

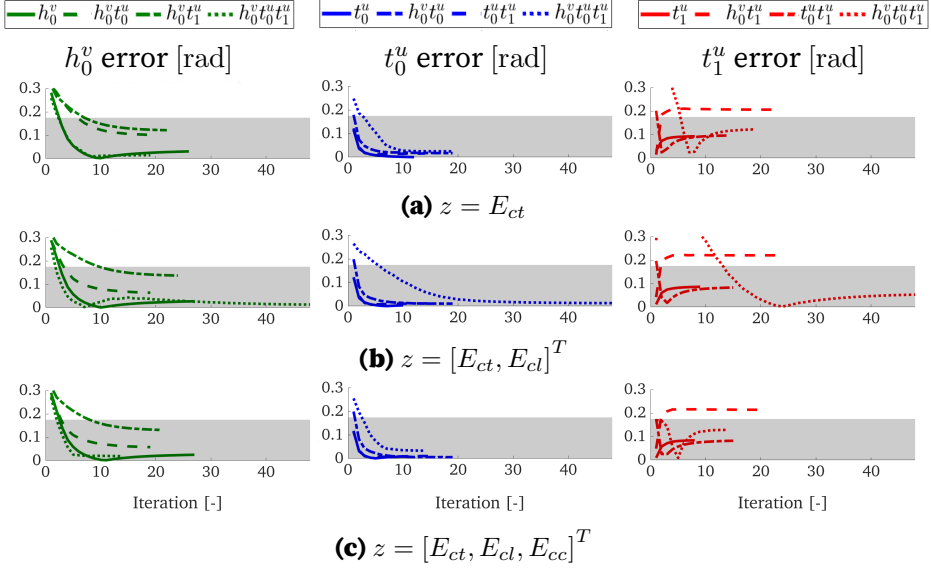


**Figure 5.2:** Experiment 2: evolution of parameter errors when observation and estimation are performed using the same fiber model. The initial guess for the parameters was set at one measurement error-distance from the ground truth values. Three columns, one per parameter, and three rows, one per observed strain combination, are shown. As in Figure 5.1, colors and line types refer to different parameter errors and to different set of estimated parameters, respectively.

tion can be seen in Figure 5.4. For all the three strain combinations, a steady error very close to that of experiment 1 is achieved: 0.022 after 20 iterations for the observation of  $E_{ct}$  (Figure 5.4a), 0.016 after 40 iterations for the observation of  $[E_{ct}, E_{cl}]^T$  (Figure 5.4b), and 0.012 after 15 iterations for the observation of  $[E_{ct}, E_{cl}, E_{cc}]^T$  (Figure 5.4c).

### 5.3.3 Experiment 3: estimation with model error

The estimation is performed using the 5-parameter fiber model whereas the observed strains were generated using the 14-parameter fiber model. The initial values for the parameters are set to the values obtained from the  $L^2$  projection of the 14-parameters model from Bovendeerd et al [7] onto the 5-parameters model.

Figure 5.3 shows the evolution of parameter errors in estimation experiments for three combinations of end-systolic strains:  $E_{ct}$ ,  $[E_{ct}, E_{cl}]^T$ , and  $[E_{ct}, E_{cl}, E_{cc}]$ . All the estimation experiments were stopped once the absolute variation of all the parameters involved in the estimation was below a threshold value of

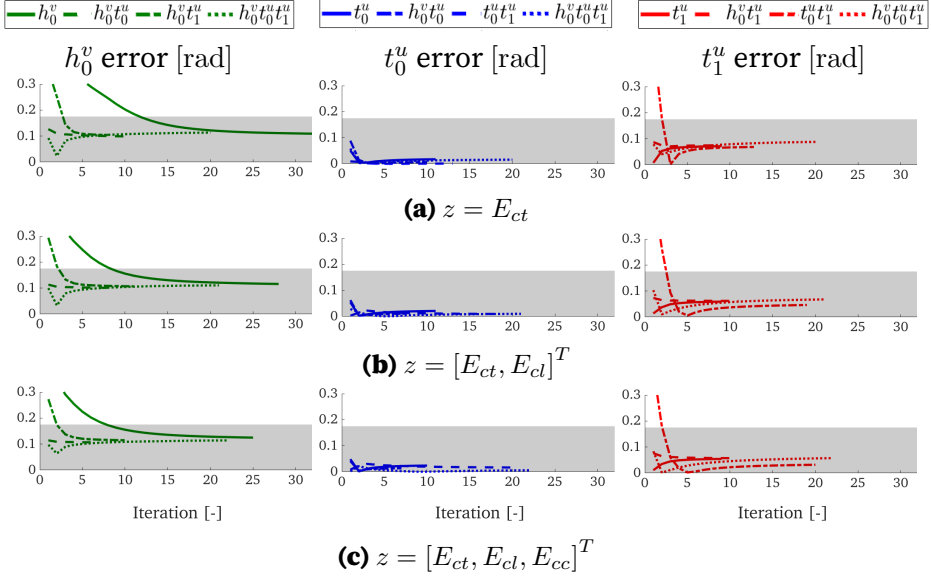


**Figure 5.3:** Experiment 3: evolution of parameter errors when observation and estimation are performed using different fiber models. Three columns, one per parameter, and three rows, one per observed strain combination, are shown. As in Figure 5.1, colors and line types refer to different parameter errors and to different set of estimated parameters, respectively.

$1 \times 10^{-5}$  rad. All the parameter estimations converged within a maximum deviation of 0.11 rad ( $6^\circ$ ). In the three cases, similar converged values for the parameters are achieved and a similar number of iterations is required. For the joint estimation of the three parameters, there is a decrease of parameter errors when increasing the number of the observed strain components. For  $t_u^0$  it decreases from 0.016 rad for  $E_{ct}$  to 0.006 rad for  $[E_{ct}, E_{cl}, E_{cc}]^T$  and for  $t_u^1$  it decreases from 0.088 rad for  $E_{ct}$  to 0.057 rad for  $[E_{ct}, E_{cl}, E_{cc}]^T$ . For  $h_v^0$ , it remains unaffected at about 0.11 rad. Also, the number of iterations required shows a limited increase when increasing the number of observed strain components (20 for  $E_{ct}$ , 21 for  $[E_{ct}, E_{cl}]^T$ , and 22 for  $[E_{ct}, E_{cl}, E_{cc}]^T$ ). In general, the number of iterations required is in line with those required by the previous experiments. The joint estimations of the three parameters lead to an average difference between the ground truth and the estimated fiber vectors of  $6.5^\circ$  (maximum  $7.1^\circ$ ) when observing  $E_{ct}$ ,  $6.3^\circ$  (maximum  $6.6^\circ$ ) when observing  $[E_{ct}, E_{cl}]^T$ , and  $6.5^\circ$  (maximum  $6.7^\circ$ ) when observing  $[E_{ct}, E_{cl}, E_{cc}]^T$ . The error between the observation and the estimation can be seen in Figure 5.4. For all the three strain combinations, a slightly increased steady error with respect of that of experiment 1 is achieved: 0.027 after 20 iterations

## Parameter Estimation in a Rule-Based Fiber Orientation model from End Systolic Strains Using the Reduced Order Unscented Kalman Filter

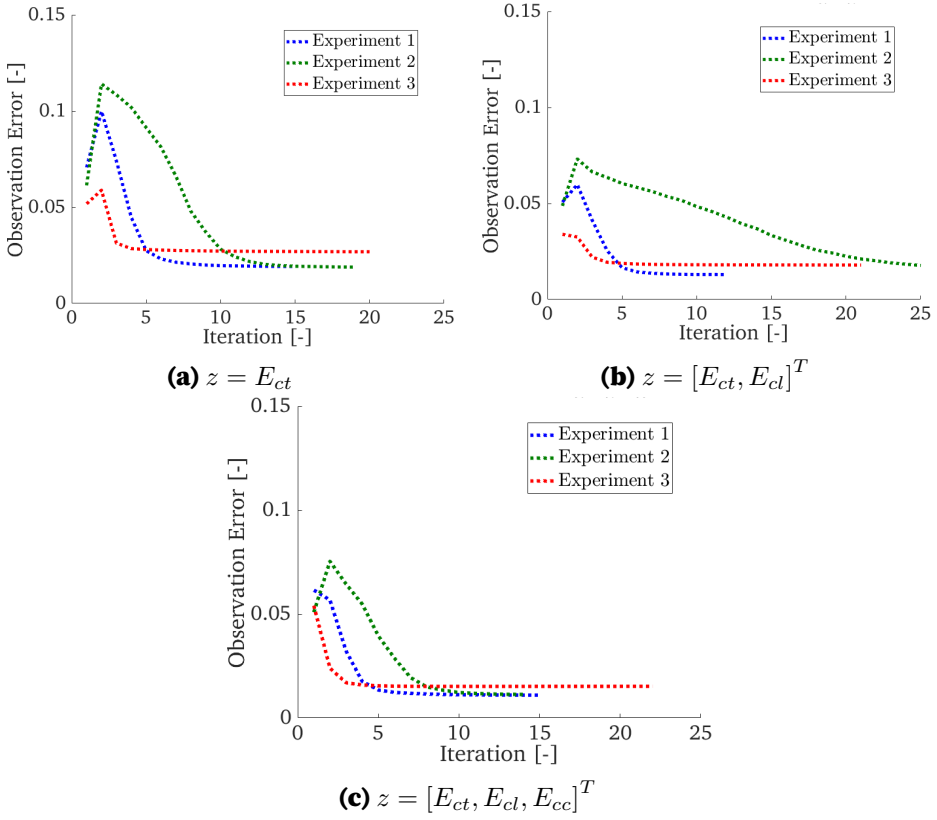


**Figure 5.4:** Average 1-norm error of the observed strains, collected in the quantity  $z$ . The errors refer to the joint estimation of  $h_v^0$ ,  $t_u^0$ , and  $t_u^1$  in the three experiments. Results were obtained observing  $E_{ct}$  (top left panel), observing  $[E_{ct}, E_{cl}]^T$  (top right panel), and observing  $[E_{ct}, E_{cc}, E_{cc}]^T$  (bottom panel).

for the observation of  $E_{ct}$  only, 0.018 after 21 iterations for the observation of  $[E_{ct}, E_{cl}]^T$ , and 0.015 after 22 iterations for the observation of  $[E_{ct}, E_{cl}, E_{cc}]^T$ . All the three strain combinations present a sharp decrease of the observation error within the first 5 iterations.

### 5.4 Discussion

A description of cardiac fiber orientation is an important ingredient of patient-specific models of cardiac electro-mechanics. Since direct experimental assessment of fiber orientation is currently not feasible in clinical practice, the goal of this chapter is to study a methodology that allows to obtain patient-

specific fiber orientation using strain measurements that can be derived using common imaging methodologies employed in clinics, such as Ultrasound and MRI.

### 5.4.1 Choices

We employed the Reduced Order Unscented Kalman Filter (ROUKF). Within the context of ROUKF, information about the initial covariance matrices of the parameters and observation noise is required. For the former, we assumed independence and we set a  $10^\circ$  initial standard deviation (compliant with findings from Scollan et al [26]) for all the parameters. This value is overestimated, since Scollan et al [26] measured about  $10^\circ$  difference for the whole fiber vector, not for the parameters describing its distribution. However, this overestimation affects only the first iteration of the algorithm, since the covariance matrix of the parameters  $\mathbf{U}_{n+1}$  is updated in the correction step according to (5.2.12), coherently with the choice of the sigma-points and the covariance of the observation error. Still, a large deviation at the first iteration might induce a different dynamics in the evolution of the estimated parameters. In this sense, further analyses are required. For the covariance of the strain observation error, we included information about the standard deviation computed in our previous sensitivity analysis on fiber orientation. This choice allowed to include information about the variability within our computer model of the measured strain and also allowed to set different observation errors for different strain components (coherently with our previous analysis). We assumed spatial independence and independence between strain components. In this context, we neglected the spatial variability of the strains and we set the same measurement error covariance for every node, again resulting in an overestimation of the measurement error. We also did not vary those values. For this reason, further analyses are required to assess the robustness of the prediction with respect to different measurement error levels.

Following our previous sensitivity analysis of end-systolic strains to fiber orientation, a simplified rule-based fiber orientation model has been used in order to limit the number of parameters. In particular, the same fiber model was used in a sensitivity analysis research involving five parameters for the definition of fiber orientation (**chapter 4**). Of those five parameters, two parameters, the least influencing ones according to our previous analysis, were fixed to generic values representing commonly measured fiber fields. Our model is less detailed than the fiber model used in [7], which uses 12 parameters to characterize the fiber orientation. Still, it captures most of the features of the extended one having both helix and transverse angles with transmural

and longitudinal variability.

In our experiments we focused on the observation of combinations of the strain components  $E_{ct}$ ,  $E_{cl}$ , and  $E_{cc}$ . These components emerged from our sensitivity analysis in **chapter 4**.  $E_{ct}$  was included because it resulted to be the strain component with the largest sensitivity to the three considered parameters.  $E_{cl}$  was included because, conversely from  $E_{ct}$ , it is more sensitive to  $h_v^0$  than to  $t_u^0$ .  $E_{cc}$  was included to try decoupling the estimation of  $h_v^0$  from that of  $t_u^0$ .

In the assessment of the converged estimated parameter values we used the fiber orientation measurement error reported in [26]. This threshold value of  $10^\circ$  represents the average measurement error of the whole fiber vector throughout the rather than the error affecting the parameters defining fiber orientation. We use this reference value only to improve the readability of the figures and the understanding of the results, as the upper bound set by this choice is not tight. In fact, if the estimation error of all the parameters approached this reference value, the overall difference in the angle between the ground truth and the estimated fiber vectors would exceed the  $10^\circ$  threshold. For this reason, when a parameter converged beyond this reference value we did not consider the estimation satisfactory. When all the parameters converged within this reference value, we quantified the error in terms of difference between fiber vectors and we verified that this difference was within the  $10^\circ$  threshold.

### 5.4.2 Results

We performed three main estimation experiments: in the first two experiments, we assumed perfect knowledge of the fiber model, which was assumed to coincide with the 5-parameters model; in the latter, we generated the observation using the 14-parameters model and we performed the estimation using the 5-parameters model (5.2.13). In the first experiment, we initiated the algorithm from the ground truth parameter set and we found that three strain combinations,  $E_{ct}$ ,  $[E_{ct}, E_{cl}]$ , and  $[E_{ct}, E_{cl}, E_{cc}]$  allowed for stable estimates of all the considered parameter combinations (see Figure 5.1) within an error margin based on the accuracy of ex vivo DTI measurements. In the second experiment (Figure 5.2), we focused on these three strain combinations and we set the initial parameters at one measurement error-distance from the ground truth. Again stable estimates of the three fiber parameters were obtained with in general an error similar to that obtained in the first experiment. The initialization of the algorithm at one measurement error distance from the ground truth mostly affected the number of iterations required to achieved a converged solution, when jointly estimating all the three param-



eters. Instead, when a subset of the three parameters were estimated, the estimation error was in general larger for  $h_v^0$  and  $t_u^1$ . In the last experiment, we estimated  $h_v^0$ ,  $t_u^0$ , and  $t_u^1$  of the 5-parameters fiber model from observations of strains generated by the 14-parameters fiber model. The estimation achieved a converged state within the chosen margin from the ground truth values, for all the considered parameter combinations and for the three strain combinations. Although this is a simple experiment, where we initiated the algorithm from the ground truth values, it proves that in the considered strain combinations there is enough information for the estimation of parameters of the fiber model, even in presence of model error. The comparison with the second experiment seems to indicate that the initialization of the algorithm may impact parameter estimation more than the inexact modeling of fiber orientation. However, further analyses are required to ascertain this. A minimum number of 20 iterations was required for the joint estimation of the three considered fiber parameters. In a perfect parallel implementation of the ROUKF, the algorithm would take the same time required by 20 executions of the predictive model. This computational time can be lowered by changing the stopping criterion of the algorithm, since after about 5 iterations both the observation error and the parameter increments stabilize. The current methodology might be used as a calibration stage before applying data assimilation techniques to extract information about patient pathology from images and measurements. It only requires one measurement of  $E_{ct}$  at end systole, leaving other available information for the estimation of the pathology.

At this stage of the research, it is not clear whether the presented methodology can be combined with pathology estimation algorithms. The inclusion of the personalization of the fiber field in such algorithms may improve the estimation of pathology related quantities, given the strong impact that fiber orientation has on the local mechanics. However, we expect that the advantage of this inclusion depends on how the addressed pathology affects the strain distributions. In particular, we would expect a large improvement from this inclusion if the magnitude of the impact of a pathology on strain distributions is comparable or smaller than that induced by uncertainty on fiber orientation. Concerning the performance of the estimation algorithm, two factors may be affected: the number of iterations required by the algorithm to converge, and the achieved converged state. The former, is due to the fact that more parameters are included in the estimation algorithm, thus requiring more prediction steps. Moreover, this inclusion may also affect the evolution of the estimated parameters, resulting in a faster or slower convergence. Regarding the latter, we addressed only the physiological LV for the personalization of fiber

parameters. The presence of a pathology in the LV may affect locally the spatial distribution of strains and may prevent the convergence of the estimation when using circumferentially symmetric fiber models.

The ROUKF methodology for the estimation of fiber orientation has been already used by Nagler et al [20] for the estimation of parameters of a rule-based fiber model. Their goal was to extract the parameters of a rule-based fiber model from a noisy measurement of patient-specific fibers, most likely to obtain a more regular representation of the fiber field. Compared to their approach, ours does not require difficult patient-specific fiber measurements and improves the rule-based fiber model by including a longitudinally varying transverse angle.

Concluding, the preliminary results presented in this work show that obtaining personalized fibers observing only the end-systolic strain component  $E_{ct}$  is feasible and, if the ROUKF is implemented in parallel, the computational time required is about that of five complete cardiac cycle simulations.

## 5.5 Limitations

Our results can be further tested and improved by addressing some limitations of the current work.

First, we employed an idealized isolated left ventricular geometry for our simulations on which we defined a rule-based fiber model relying on the normalized coordinates derived from the coordinate vector basis. The considered rule-based fiber model includes transmural and longitudinal variability of both helix and transverse angles, but neglects the circumferential variability. Introducing further parameters in the rule-based fiber orientation model describing circumferential variability or using a surface-patches approach [21] to introduce patch-specific parameters, would allow for the estimation of non axisymmetric fiber fields.

The presented approach suffers from the typical high computational cost of parameter estimation techniques, which require several evaluations of the underlying predictive model. At every iteration, a number of simulations approximately equal to the number of parameters to be estimated are required. In a parallel implementation of the ROUKF, these independent simulations can be computed simultaneously by different computational nodes. However, also in this case several iterations of the algorithm are required to obtain a converged solution. Given the large numbers of estimation tests performed in this research, for the sake of time, we adopted a linear finite element discretization of the problem. This choice results in smaller algebraic nonlinear

systems that can be solved faster. This choice allows to achieve a complete cardiac cycle in less than 5 min, but affects the accuracy of strain predictions (**chapter 2**). If instead we had used a quadratic finite element approximation, each prediction step would have taken approximately 50 min. Further analyses are required to confirm the effectiveness of the approach using a more appropriate discretization. The use of a more adequate numerical discretization would increase the problem size and the size of the observation vector and its covariance matrix. It is not clear yet whether the same observation operator would be feasible under those circumstances.

In fact, another limitation of this research is the choice of the observation operator. In our analysis, we had a one-to-one correspondence between the nodal values of the observed and predicted strains. This corresponds to using an identity operator on the strain itself. This results in an ideal situation, since it prevents the use of interpolation operators that might constitute a further source of error. Moreover, in real applications, strain measurements may not be available throughout the whole myocardium. For this reason, the role of the observation operator  $\mathcal{H}$  should be addressed in future extensions of this research. These extensions might improve both the robustness of the presented estimation methodology and its feasibility. In fact, decreasing the size of the observation array directly affects the size of the covariance matrix  $\mathbf{W}$ , which is the most demanding matrix of the ROUKF in terms of memory allocation. In this regard, an alternative option would be the inclusion of a subset of the strains (corresponding to a measured sub-region) or the use of local averages in sub-regions such as those defined by the AHA17 segment model [8].

A good practice in the testing of parameter estimation algorithms is to check the robustness with respect to noise and the initialization point. Due to time constraints, we could not perform more analyses to prove the effectiveness of the proposed methodology when the algorithm is initiated far from the ground truth in experiment 3. We modeled observation noise by means of the dedicated covariance matrix, but we did not perturb the observation with different level of noise. Instead, we directly addressed the case where the observations and the estimations were performed by different models.

## 5.6 Conclusion

In this work we propose a methodology based on the Reduced Order Unscented Kalman Filter for the patient-specific estimation of rule-based fiber model parameters. The algorithm is based on the observation of end-systolic strains

and it does not require complex DT-MRI measurement of the patient, which are unavailable in clinical practice. Instead, it relies on strains that can be obtained in the clinic using common imaging techniques such as Ultrasound [3, 10] and MRI [14, 2, 1, 31].

We focused on the parameters that were identified to be the most influential parameters by our former sensitivity analysis of end-systolic strains to fiber orientation. Our results suggest that the estimation of  $h_v^0$ , the transmural offset of the helix angle,  $t_u^0$ , the longitudinal offset of the transverse angle, and  $t_u^1$ , the longitudinal slope of the transverse angle, can be achieved based on the estimation of the end-systolic Green-Lagrange circumferential-transmural shear strain  $E_{ct}$  in the physiological LV.

## Bibliography

- [1] A. H. Aletras, R. S. Balaban, and H. Wen. High-resolution strain analysis of the human heart with fast-dense. *Journal of Magnetic Resonance*, 140(1):41–57, 1999.
- [2] A. H. Aletras, S. Ding, R. S. Balaban, and H. Wen. Dense: displacement encoding with stimulated echoes in cardiac functional mri. *Journal of magnetic resonance (San Diego, Calif.: 1997)*, 137(1):247, 1999.
- [3] B. H. Amundsen, T. Helle-Valle, T. Edvardsen, H. Torp, J. Crosby, E. Lyseggen, A. Støylen, H. Ihlen, J. A. Lima, O. A. Smiseth, and S. A. Slørdahl. Noninvasive myocardial strain measurement by speckle tracking echocardiography. *Journal of the American College of Cardiology*, 47(4):789–793, 2006.
- [4] M. Asch, M. Bocquet, and M. Nodet. *Data assimilation: methods, algorithms, and applications*, volume 11. SIAM, 2016.
- [5] G. Balaban, H. Finsberg, H. H. Odland, M. E. Rognes, S. Ross, J. Sundnes, and S. Wall. High-resolution data assimilation of cardiac mechanics applied to a dyssynchronous ventricle. *International journal for numerical methods in biomedical engineering*, 33(11):e2863, 2017.
- [6] R. N. Bannister. A review of forecast error covariance statistics in atmospheric variational data assimilation. i: Characteristics and measurements of forecast error covariances. *Quarterly Journal of the Royal Meteorological Society: A journal of the atmospheric sciences, applied meteorology and physical oceanography*, 134(637):1951–1970, 2008.
- [7] P. Bovendeerd, W. Kroon, and T. Delhaas. Determinants of left ventricular shear strain. *American Journal of Physiology. Heart and Circulatory Physiology*, 297(3):H1058–68, 2009.
- [8] M. D. Cerqueira, N. J. Weissman, V. Dilsizian, A. K. Jacobs, S. Kaul, W. K. Laskey, D. J. Pennell, J. A. Rumberger, T. Ryan, et al. Standardized myocardial segmentation and nomenclature for tomographic imaging of the heart: a statement for healthcare professionals from the cardiac imaging committee of the council on clinical cardiology of the american heart association. *Circulation*, 105(4):539–542, 2002.
- [9] S. E. Cohn and R. Todling. Approximate data assimilation schemes for stable and unstable dynamics. *Journal of the Meteorological Society of Japan. Ser. II*, 74(1):63–75, 1996.

- 
- [10] M. De Craene, G. Piella, O. Camara, N. Duchateau, E. Silva, A. Doltra, J. D'hooge, J. Brugada, M. Sitges, and A. F. Frangi. Temporal diffeomorphic free-form deformation: Application to motion and strain estimation from 3d echocardiography. *Medical image analysis*, 16(2):427–450, 2012.
- [11] H. Delingette, F. Billet, K. C. Wong, M. Sermesant, K. Rhode, M. Ginks, C. A. Rinaldi, R. Razavi, and N. Ayache. Personalization of cardiac motion and contractility from images using variational data assimilation. *IEEE transactions on biomedical engineering*, 59(1):20–24, 2011.
- [12] H. Finsberg, G. Balaban, S. Ross, T. F. Håland, H. H. Odland, J. Sundnes, and S. Wall. Estimating cardiac contraction through high resolution data assimilation of a personalized mechanical model. *Journal of computational science*, 24:85–90, 2018.
- [13] L. Geerts, R. Kerckhoffs, P. Bovendeerd, and T. Arts. Towards patient specific models of cardiac mechanics: a sensitivity study. In *International Workshop on Functional Imaging and Modeling of the Heart*, pages 81–90. Springer, 2003.
- [14] A. T. Hess, X. Zhong, B. S. Spottiswoode, F. H. Epstein, and E. M. Meintjes. Myocardial 3d strain calculation by combining cine displacement encoding with stimulated echoes (dense) and cine strain encoding (senc) imaging. *Magnetic Resonance in Medicine*, 62(1):77–84, 2009.
- [15] A. Krishnamurthy, C. T. Villongco, J. Chuang, L. R. Frank, V. Nigam, E. Belezouli, P. Stark, D. E. Krummen, S. Narayan, J. H. Omens, et al. Patient-specific models of cardiac biomechanics. *Journal of computational physics*, 244:4–21, 2013.
- [16] H. Lombaert, J.-M. Peyrat, P. Croisille, S. Rapacchi, L. Fanton, F. Cheriet, P. Clarysse, I. Magnin, H. Delingette, and N. Ayache. Human atlas of the cardiac fiber architecture: study on a healthy population. *IEEE transactions on medical imaging*, 31(7):1436–1447, 2012.
- [17] R. G. Lopata, M. M. Nillesen, J. M. Thijssen, L. Kapusta, and C. L. de Korte. Three-dimensional cardiac strain imaging in healthy children using rf-data. *Ultrasound in Medicine & Biology*, 37(9):1399 – 1408, 2011.
- [18] S. Marchesseau, H. Delingette, M. Sermesant, R. Cabrera-Lozoya, C. Tobon-Gomez, P. Moireau, R. F. i Ventura, K. Lekadir, A. Hernandez, M. Garreau, et al. Personalization of a cardiac electromechanical model

using reduced order unscented kalman filtering from regional volumes. *Medical image analysis*, 17(7):816–829, 2013.

- [19] P. Moireau and D. Chapelle. Reduced-order unscented kalman filtering with application to parameter identification in large-dimensional systems. *ESAIM: Control, Optimisation and Calculus of Variations*, 17(2):380–405, 2011.
- [20] A. Nagler, C. Bertoglio, M. Gee, and W. Wall. Personalization of cardiac fiber orientations from image data using the unscented kalman filter. In *International Conference on Functional Imaging and Modeling of the Heart*, pages 132–140. Springer, 2013.
- [21] A. Nagler, C. Bertoglio, C. T. Stoeck, S. Kozerke, and W. A. Wall. Maximum likelihood estimation of cardiac fiber bundle orientation from arbitrarily spaced diffusion weighted images. *Medical image analysis*, 39:56–77, 2017.
- [22] N. J. Petterson, L. S. Fixsen, M. C. M. Rutten, N. H. J. Pijls, F. N. van de Vosse, and R. G. P. Lopata. Ultrasound functional imaging in an ex vivo beating porcine heart platform. *Physics in Medicine & Biology*, 62(23):9112–9126, nov 2017.
- [23] J.-M. Peyrat, M. Sermesant, X. Pennec, H. Delingette, C. Xu, E. R. McVeigh, and N. Ayache. A computational framework for the statistical analysis of cardiac diffusion tensors: application to a small database of canine hearts. *IEEE Transactions on Medical Imaging*, 26(11):1500–1514, 2007.
- [24] D. T. Pham. Stochastic methods for sequential data assimilation in strongly nonlinear systems. *Monthly weather review*, 129(5):1194–1207, 2001.
- [25] M. Pluijmert, T. Delhaas, A. F. de la Parra, W. Kroon, F. W. Prinzen, and P. H. Bovendeerd. Determinants of biventricular cardiac function: a mathematical model study on geometry and myofiber orientation. *Biomechanics and modeling in mechanobiology*, 16(2):721–729, 2017.
- [26] D. F. Scollan, A. Holmes, R. Winslow, and J. Forder. Histological validation of myocardial microstructure obtained from diffusion tensor magnetic resonance imaging. *American Journal of Physiology-Heart and Circulatory Physiology*, 275(6):H2308–H2318, 1998.

- [27] M. Sermesant, R. Chabiniok, P. Chinchapatnam, T. Mansi, F. Billet, P. Moireau, J.-M. Peyrat, K. Wong, J. Relan, K. Rhode, et al. Patient-specific electromechanical models of the heart for the prediction of pacing acute effects in crt: a preliminary clinical validation. *Medical image analysis*, 16(1):201–215, 2012.
- [28] N. Toussaint, C. T. Stoeck, T. Schaeffter, S. Kozerke, M. Sermesant, and P. G. Batchelor. In vivo human cardiac fibre architecture estimation using shape-based diffusion tensor processing. *Medical image analysis*, 17(8):1243–1255, 2013.
- [29] E. A. Wan, R. Van Der Merwe, and S. Haykin. The unscented kalman filter. *Kalman filtering and neural networks*, 5(2007):221–280, 2001.
- [30] J. Xi, P. Lamata, S. Niederer, S. Land, W. Shi, X. Zhuang, S. Ourselin, S. G. Duckett, A. K. Shetty, C. A. Rinaldi, et al. The estimation of patient-specific cardiac diastolic functions from clinical measurements. *Medical image analysis*, 17(2):133–146, 2013.
- [31] S. B. Yeon, N. Reichek, B. A. Tallant, J. A. Lima, L. P. Calhoun, N. R. Clark, E. A. Hoffman, K. K. Ho, and L. Axel. Validation of in vivo myocardial strain measurement by magnetic resonance tagging with sonomicrometry. *Journal of the American College of Cardiology*, 38(2):555–561, 2001.





## **Chapter 6**

# **General Discussion**

## 6.1 Summary of contributions

The driving idea of our research is that by observing regional strains non-invasively measured from the patient it is possible to estimate parameters that could increase the understanding of the patient pathology. Typically, such parameters would include regional contractility, regional tissue stiffness, and activation pattern. In a data assimilation approach, such parameters would be the unknowns and strains the data. Consequently, to be able to estimate those parameters in the pathological case, the effect of pathology on regional strains must exceed that of the underlying model uncertainty. In this thesis, we addressed part of that uncertainty. In particular, we investigated how the description of the geometry and fiber orientation of the LV myocardium affects the prediction of end-systolic strains. We present in the following paragraphs the main contributions of this thesis.

In **chapter 2** we presented a new implementation of the model of the mechanics of the LV published by Bovendeerd et al [?] based on the FEniCS library [?]. In that chapter, we showed the consistency of our implementation with the previous one and we performed a numerical verification of the implementation. In this verification, we studied how the numerical discretization of the problem affected the distribution of end-systolic strains and we proposed an optimal discretization that allows containing the average transmural error of all the strain components below a 10% threshold, yet keeping computational time for a cardiac cycle below 1 h.

In **chapter 3** and **chapter 4**, we proposed a methodology to apply the elementary effects method to estimate the sensitivity of end-systolic strains to physiological variations in the description of the geometry and fiber orientation, both accounting for the variability within the human population. In particular, in **chapter 3**, we included information about the anatomy of 300 healthy volunteers in the form of six shape modes identified by Medrano-Gracia et al [?] and Zhang et al [?]. The six shape modes were used to represent a multitude of geometries in the neighborhood of one standard deviation around the average patient anatomy. This analysis allowed to estimate the influence of geometry on the determination of end-systolic strain distributions and to quantify each shape mode contribution. Similarly, in **chapter 4**, we extracted parameter ranges describing fiber orientation from DT-MRI measurements of different studies [?] trying to represent variability within the human population. From this analysis, we quantified the overall effect that fiber orientation has on end-systolic strain distributions and we quantified the contribution of every single parameter.

Our findings show that fiber orientation affects end-systolic strain distribu-

tions at least twice as much as geometry. In particular, the main contribution to this influence is given by the transverse angle, being described by two of the most influential parameters identified by the analysis: the parameter describing its longitudinal offset,  $t_0^u$ , and the parameter describing its longitudinal slope,  $t_1^u$ . Another important contribution comes from the parameter describing the transmural offset of the helix angle,  $h_0^v$ . This parameter, together with the whole transverse angle, is often neglected when describing fiber orientation with a rule-based model, where the helix angle at mid-wall is assumed to be zero. Instead, in our analysis, the transmural slope of the helix angle presented the least influence among the considered parameters. Concerning geometry, only the first shape mode, related to the variability in the size of the LV within the human population, has an impact somewhat comparable to that of the most influential parameters describing fiber orientation.

These results are in line with previous studies [1, 8]; nonetheless, in this thesis, we properly quantified the effects induced by considering physiological variations of the parameters within the human population, instead of local variations of parameters around a central setting. Moreover, we addressed the spatial variability of end-systolic strains and provided regional estimations based on the 17 regions of the AHA segmentation. This information is valuable in model personalization since it highlights the importance of proper modeling of fiber orientation to improve the predictive power of a computational model of cardiac mechanics. In particular, it supports the inclusion of the transverse angle. It also suggests that the advantages of creating a patient-specific geometry might be lost whenever a generic model for fiber orientation is employed.

Following our two sensitivity analyses, in **chapter 5** we presented a technique based on the ROUKF that aims at estimating patient-specific parameters of a rule-based fiber model using a single observation of the end-systolic circumferential-transmural shear strain  $E_{ct}$ . Our preliminary results show that the estimation of  $h_0^v$ , describing the transmural offset of the helix angle,  $t_0^u$ , describing the longitudinal offset of the transverse angle, and  $t_1^u$ , describing the longitudinal slope of the transverse angle, can be achieved within the mean DT-MRI measurement error of  $10^\circ$  in the physiological left ventricle. Similarly, a relation between shear strains and fiber orientation was used by Kroon et al [?] to build an adaptation model for fiber reorientation, postulating that shear strains contributed to damage and regeneration of the extracellular matrix. The advantage of their approach is that it does not require an underlying model for the description of fiber orientation and potentially asymmetric fiber orientations can be obtained. However, despite a physiological explanation of the adaptive process, their approach does not aim to reproduce strain

measured in patients nor can provide a steady solution. Our approach, instead, relies on a single observation of patient data, shows convergence in our experiments, and differently from [? ], it does not require long and complex DT-MRI acquisitions. Still, further investigations are needed to confirm the robustness of the proposed method to different initialization points, different levels of noise and different models of the mechanics and fiber orientation. Nonetheless, the proposed method might constitute a precious calibration technique to improve prediction and outcome of the inverse analysis.

## 6.2 Study limitations

The work presented in this thesis investigates the role of geometry and fiber orientation within computational models of the mechanics of the LV. The results provide valuable information about the quantification of the effects that geometry and fiber orientation have on end-systolic strains. These results can potentially improve the understanding and the effectiveness of strain-based inverse analysis approaches aiming to estimate pathological deviations of tissue properties from normal physiological values. However, this work presents three major limitations.

The first limitation concerns the models employed in our study. The main modeling limitations concern the geometry, the rule-based fiber orientation, the homogeneous mechanical activation of the myocardium, and the boundary conditions. We addressed the mechanics of an isolated LV with synchronous mechanical activation and axisymmetric rule-based fiber orientation. Considering the results of our SA on the LV, where the size is more important than other shape factors, we expect that a similar consideration would also hold when substituting the LV geometry with a biventricular one. We do expect differences in spatial strain distributions, but the magnitude of strain variations resulting from a SA should be in line with those of the LV.

Despite the large number of parameters of the fiber model that carefully describe the longitudinal and transmural variability of myofibers, our model lacks circumferential variability. Introducing such variability may even increase the sensitivity of strains to fiber orientation.

In our model, the inclusion of a physiological activation pattern of the myocardium led to the prediction of unphysiological strain distributions [2]. For this reason, the mechanical activation was modeled to occur simultaneously in the physiological case while in other studies, where our model was used to simulate the dyssynchronous heart, the activation pattern was derived from the Eikonal model [7].

The inclusion of an asynchronous activation pattern would have surely affected the strain distributions resulting from our model. Interpreting how this change in the spatial distribution of the moment of activation would have affected the computation of the strain sensitivity indices is not straightforward. We expect that the sensitivity of end-systolic strains to variations of geometry and fiber orientation, which do not affect greatly the spatial distribution of the moment of activation, would not change largely with asynchronous activation patterns. Most of the shape modes included in our SA introduced small shape variations; therefore, the difference in distances traveled by the activation waves in different geometries could be considered negligible. The effect of variations of the LV size on the moment of activation is more difficult to predict, as a change in size increases the distance traveled by the activation wave both transmurally and longitudinally. In this sense, there might be a slightly delayed activation in basal end epicardial regions in larger ventricles and a slightly accelerated activation in smaller ventricles. We expect the effect of variations in fiber orientation to be much smaller on the moment of activation than on the mechanics. This is because the anisotropy level in the wave propagation is much lower than that in tissue stiffness.

Concerning the choice of boundary conditions, we adopted commonly used boundary conditions and this choice complies with recommendations of a recent study addressing the topic [6]. Nonetheless, the resulting boundary conditions are a simplification and the effect of more realistic conditions should be addressed. It would be interesting comparing the uncertainty propagated from this choice with results of sensitivity presented in this thesis.

The last modeling issue regards the sensitivity technique adopted in this research. The elementary effects method was originally proposed for parameter screening. It is less quantitative than gold-standard variance-based techniques. Still, it allowed quantifying variations of the spatial distribution of strains without the need for surrogate models. Nonetheless, a comparison using a variance-based method would enhance the strength of our results.

The second limitation of our study is that we did not address pathological cases. We estimated the sensitivity of the mechanics to geometry and fiber orientation on strain distributions in physiological conditions. Similarly, the fiber personalization method here proposed has been studied under physiological conditions. It is not clear whether the method works also in pathological conditions nor whether it might improve pathology estimation if included in a broader data assimilation context.

The last limitation concerns computational time. Our model of the LV takes approximately 50 min for simulating a cardiac cycle on a modern workstation. Inverse analysis and SA studies require several evaluations of the model.

While SA and UQ can be performed for validating a methodology before applying it in the clinics, the goal of the inverse analysis is to improve understanding of patient data measured in clinics. Currently, the computational cost of data assimilation requires the use of sub-optimal discretizations as in **chapter 5**. At this level of computational cost, data assimilation could be applied only in very specific case studies.

### **6.3 Future perspectives**

This thesis provided precious insights about the role of geometry and fiber in model personalization. The results achieved can be extended by addressing the model limitations, by addressing other sources of uncertainty, and by addressing how pathologies affect the prediction of the model.

#### **6.3.1 Model extension**

The Cardiac Atlas Project published a new dataset containing four biventricular shape modes extracted from MRI of the UK Biobank [4]. After extending the implementation of the mechanics to include biventricular geometries, our sensitivity study on geometry can be repeated including such dataset.

Another simple extension of the implementation would be the inclusion of an Eikonal solver to compute the activation pattern of the myocardium. It would be interesting to compare the sensitivity to different commonly adopted choices of initiation of the depolarization wave to the sensitivity to geometry and fiber orientation, as presented in this thesis.

Another source of uncertainty in models of cardiac mechanics regards boundary conditions. Addressing the role of different choices of boundary conditions commonly adopted in literature will allow comparing their influence with that of other parameters more easily measurable.

The elementary effects method can be extended to work with groups of parameters [9]. A complete sensitivity analysis including groups of parameters describing the geometry, fiber orientation, initiation of depolarization wave, and boundary conditions would provide a quantification of major sources of uncertainty of the model and would allow to prioritize between parameters and groups of parameters.

#### **6.3.2 Prioritize model parameters in pathological cases**

We investigated the importance of parameters describing geometry and fiber orientation in determining end-systolic strains in the physiological LV. Our

goal was to quantify the uncertainty concerning those parameters propagated to the observation of strains in order to make choices in the personalization of the model in view of the inverse estimation of pathologies. Before reaching that point, we need to address the uncertainty in the pathological case. In fact, strain distributions might be completely altered by pathology and the role of pathology related parameters might exceed that of inexact modeling of geometry and fiber orientation. Several questions remain still unanswered: how much do pathologies affect strain patterns? Can the uncertainty in geometry and fiber orientation be neglected compared to the magnitude of strain variations induced by pathologies? If not, do we have to include the most important parameters describing the geometry and fiber orientation in the inverse parameter estimation algorithm? Do pathologies also alter geometry and fiber orientation? A first step towards the answers to those questions requires us to investigate how strain patterns are affected by different pathologies. This could be achieved by simulating in-silico a pathology and studying the sensitivity of strains to pathology-specific parameters. From this study, a relation between pathology-related parameters and strain patterns should emerge. The analysis of the relations between strains and pathologies would clarify whether different pathologies could be distinguished one from the other. This investigation will allow to better select what observation to include in an inverse analysis and whether the choice of parameters involved in the estimation should be set a priori.

### **6.3.3 Combining data assimilation and meta-modeling for (almost) real time computations**

Data assimilation is most likely the way by which computational models will enter clinical practice. However, given the current computational requirements of models and the available resources, the application of data assimilation in clinical practice is unfeasible. A possibility would be to use such a technique only on few specific cases, where a quantitative assessment would help the clinician to better understand a case. Still, before reaching that level of confidence inside the clinic, a computational model must undergo extensive verification, validation, and uncertainty quantification (VVUQ) [5]. Both data assimilation and VVUQ require several model runs and their combination is prohibitive because of the computational cost of the underlying models. A potential solution might come from model order reduction [3] or the use of surrogate models [10] such as polynomial models, neural networks, Kriging, that run much faster than the original ones.



## **6.4 General conclusions**

In this thesis, we developed a computational framework to assess the sensitivity of end-systolic strains to physiological variations in the geometry and fiber orientation descriptions. The analysis allowed to quantify the effect of geometry and fiber orientation on the spatial distribution of end-systolic strains and highlighted important relations between strain components and relevant parameters. These relations have been exploited to create a methodology to personalize a rule-based model for fiber orientation.

---

## Bibliography

- [1] L. Geerts, R. Kerckhoffs, P. Bovendeerd, and T. Arts. Towards patient specific models of cardiac mechanics: a sensitivity study. In *International Workshop on Functional Imaging and Modeling of the Heart*, pages 81–90. Springer, 2003.
- [2] R. Kerckhoffs, P. Bovendeerd, J. Kotte, F. Prinzen, K. Smits, and T. Arts. Homogeneity of cardiac contraction despite physiological asynchrony of depolarization: a model study. *Annals of biomedical engineering*, 31(5):536–547, 2003.
- [3] T. Lassila, A. Manzoni, A. Quarteroni, and G. Rozza. Model order reduction in fluid dynamics: challenges and perspectives. In *Reduced Order Methods for modeling and computational reduction*, pages 235–273. Springer, 2014.
- [4] C. Mauger, K. Gilbert, A. M. Lee, M. M. Sanghvi, N. Aung, K. Fung, V. Carapella, S. K. Piechnik, S. Neubauer, S. E. Petersen, et al. Right ventricular shape and function: cardiovascular magnetic resonance reference morphology and biventricular risk factor morphometrics in uk biobank. *Journal of Cardiovascular Magnetic Resonance*, 21(1):41, 2019.
- [5] P. Pathmanathan and R. A. Gray. Ensuring reliability of safety-critical clinical applications of computational cardiac models. *Frontiers in physiology*, 4:358, 2013.
- [6] M. Peirlinck, K. L. Sack, P. De Backer, P. Morais, P. Segers, T. Franz, and M. De Beule. Kinematic boundary conditions substantially impact in silico ventricular function. *International journal for numerical methods in biomedical engineering*, 35(1):e3151, 2019.
- [7] M. Pluijmert, P. Bovendeerd, J. Lumens, K. Vernooy, F. W. Prinzen, and T. Delhaas. New insights from a computational model on the relation between pacing site and crt response. *EP Europace*, 18(suppl\_4):iv94–iv103, 12 2016.
- [8] M. Pluijmert, T. Delhaas, A. F. de la Parra, W. Kroon, F. W. Prinzen, and P. H. Bovendeerd. Determinants of biventricular cardiac function: a mathematical model study on geometry and myofiber orientation. *Biomechanics and modeling in mechanobiology*, 16(2):721–729, 2017.

- [9] A. Saltelli, M. Ratto, T. Andres, F. Campolongo, J. Cariboni, D. Gatelli, M. Saisana, and S. Tarantola. *Global sensitivity analysis: the primer*. John Wiley & Sons, 2008.
- [10] B. Sudret, S. Marelli, and J. Wiart. Surrogate models for uncertainty quantification: An overview. In *2017 11th European conference on antennas and propagation (EUCAP)*, pages 793–797. IEEE, 2017.





# Summary

Computational models of the heart might constitute a precious tool for cardiologists during diagnosis and decision making. In this context, a computational model of the mechanics of the heart can be used to achieve a better interpretation of the patient clinical measurements or to simulate different intervention scenarios. Typically, for those applications the model requires a personalization stage. Personalization of geometry may be based on information acquired from imaging. Personalization of additional model parameters requires the use of data assimilation techniques fed by patient data measured in the clinic. For computational models of the mechanics of the heart, such data typically include deformations or strains derived from non invasive imaging methodologies. In this process, very often great attention is put on personalization of the geometry whereas fiber orientation is modeled using generic rule-based models. This is due mostly to the fact that geometry can be measured in-vivo more easily than fiber orientation. However, the personalized descriptions for geometry and fiber orientation both suffer from presence of measurement noise and reconstruction errors. In this research, we quantify the impact that different choices for the modeling of geometry and fiber orientation have on strain predicted by a model of the mechanics of the left ventricle. Next, we make a first step towards data assimilation by estimating patient-specific fiber orientation from end-systolic strain.

In **chapter 2**, we present and verify a new numerical implementation of a model of left ventricular mechanics, and we propose an optimal choice for spatial and temporal discretization.

In **chapter 3** and **chapter 4**, we apply the elementary effects method to estimate the sensitivity of end-systolic strains to physiological variations in the description of the geometry and fiber orientation. Six shape modes describing the anatomy of 300 healthy hearts were used to represent a multitude of geometries in the neighborhood of one standard deviation around the average patient geometry. Information from two atlases of fiber orientation, obtained from ex-vivo Diffusion Tensor Imaging, was used to represent variations of

one standard deviation around an average configuration. Our findings show that fiber orientation affects end-systolic strain distributions at least twice as much as geometry. The main contribution of this influence is given by the transverse angle, that describes the transmural component of the fiber vector, and the transmural offset of the helix angle, that describes the longitudinal component of the fiber vector. Concerning geometry, only the first shape mode, related to the variability in the size of the left ventricle within the human population, has an impact somewhat comparable to that of fiber orientation.

In **chapter 5**, we apply a reduced-order unscented Kalman filter to estimate parameters in the description of fiber orientation that are most influential for end-systolic strain. The difference between the estimated and ground truth fiber orientation was found to be within the mean DT-MRI measurement error of 10 degrees.

In conclusion, in this thesis we show that fiber orientation affects the distribution of end-systolic strains twice as much as geometry and we propose a methodology to estimate patient-specific fiber orientation from data that can be measured in the clinic.

# Publications

## Journal

Barbarotta, L., Rossi, S., Dedè, L., Quarteroni, A. (2018). A transmurally heterogeneous orthotropic activation model for ventricular contraction and its numerical validation. *International journal for numerical methods in biomedical engineering*, 34(12), e3137.

Barbarotta, L., Bovendeerd, P. (2019). A computational approach on sensitivity of left ventricular wall strains to geometry. In *International Conference on Functional Imaging and Modeling of the Heart* (pp. 240-248). Springer, Cham.

Barbarotta, L., Bovendeerd, P. (Submitted - February 2020). Estimation of uncertainty in left ventricular systolic wall strains induced by population based variations in geometry. *Journal of Biomechanical Engineering*.

## Congress Contributions

Barbarotta, L., Bovendeerd, P. A computational approach on sensitivity of left ventricular wall strains to fiber orientation and geometry. In *International Conference on Functional Imaging and Modeling of the Heart*, September 2019. New York City, United States of America. Oral presentation

Barbarotta, L., Bovendeerd, P. A computational approach on sensitivity of left ventricular wall strains to geometry. In *International Conference on Functional Imaging and Modeling of the Heart*, June 2019. Bordeaux, France. Poster presentation

Barbarotta, L., Bovendeerd, P. Towards model assisted analysis of the patient heart: does geometry matter? *Advanced Techniques and Therapies in Cardiovascular Care*, September 2018. Venice, Italy. Oral presentation





# Acknowledgements

Here we are. If I am writing these pages, it means that I am very close to defend my PhD. Still, things can go terribly wrong until the very last moment, but, at the time of this writing, I am strongly hoping for the best. When I started my PhD, I had a clue that I could manage to get through it. However, besides my background and passion in computational predictive models, I could not have predicted all the struggles I have faced to get to this point. If I made it this far, though, I feel there is a long list of people that I need and wish to thank.

First, I would like to thank my promotor Frans. Thank you for trusting me and for giving me the opportunity to pursue a PhD in your group. Doing research in your group was a very inspiring and enriching experience.

Peter, your guidance has always put me on the right track whenever I thought I was lost. You always found a kind way to spot an issue without pointing the finger. Your contribution was crucial to make me become a better engineer and a better researcher. I enjoyed working with you and I especially enjoyed our meetings. We always started with a challenging discussion and eventually ended up talking about our lives and the most disparate topics. Thank you for your support and your friendship. In the next few years, I will tell you if you successfully taught me how not to sabotage myself.

I would like to thank the members of the committee for reviewing my thesis and for giving their availability to take part in my defense ceremony. Thank you, Maxime, Leif Rune, Lukas, Natal, and Wouter. Thank you, Maarten Merckx for chairing my defense committee.

I would like to acknowledge the European research and training consortium Marie Skłodowska-Curie Innovative Training Networks (ITN-ETN) for funding my research. Thank you to the many people that made this project possible.

## Acknowledgements

---

In particular, I would like to mention Alberto Redaelli and Marco Rasponi. In this wonderful experience, I had the chance to meet a very clever and pleasant company of fellow researchers: Daniela, Dario, Fabrice, Federico, Giorgia, Guru, Joao, Luca, Michał, Noemi, Patricio, Sebastião, Selene and Yağmur. It would be really great if we could arrange another MUSICARE meeting after the pandemic will be over. Federico, as discussed in New York City, Arezzo is the best place for the meeting. Let's make it happen!

Ema, we started our PhD on the same day of that December of five years ago. Back then, I didn't know we would have become best friends. I didn't know either how important your support would have been throughout my PhD. At the beginning of our path, your help was fundamental to build up some confidence with the English language and to feel at home in a foreign country. Throughout the PhD, you have been a great colleague and you always found the time to listen to me while I was (often rambling) thinking aloud. At the end of the PhD, when things seemed to be too complicated to be sorted out, you always reassured and supported me. Thank you. I wouldn't have been able to come this far without your help. I agree with you that our next meeting should be in Codroipo. I don't see a better place to exorcise the Covid-19 pandemic that so badly affected our PhD celebrations.

Thank you to the two madams Daniela and Teresa, who introduced me to the cult of Bin 343 (aka Ladone) and to the fine art of party crashing. After a whole life without cycling, you taught me once again how to ride a bike and how to fall off of it in the same night. The first night with you was the perfect induction to Eindhoven. I am glad I had met you.

Teresa, thank you also for arranging my social life while living together in the old times at zio Henk's. If I have friends in Eindhoven is also because you forced me not to work too much and to enjoy life here and there. Thank you also for being the mastermind behind the ambitious Aushita plan that successfully allowed Morena to relocate to Eindhoven.

Friends of many parties and many BBQs (more or less in the order in which I first met you): Zandra, Szilardo, Bibi, Carmine, Humberto, Alok, Fernando, Pasquale, Gianremo (aka Gianluca, l'uomo che non regge l'alcool), Marta, Cristian, Federica, Valeria, Nrupa, Giorgio, Alessia, Raj, Gianmarco, and Tommaso. I have many memories with you between parties, Carnivals, trip to the sea, bachelor parties, exclusive birthday parties, and wonderful BBQs in the Eindhovense summer. Thank for delighting my four years in the Netherlands.

You have been a second family to me.

Marta and Cristian, I always enjoyed our dinners together, particularly when followed by an intense session of Road Redemption. You also have always been in the forefront when it came to helping me and Morena to move. We especially appreciated your hospitality during our final days in Eindhoven. We had not expected those days to be so tough. Your emotional support greatly improved that experience. Thank you.

Emanuele (Ema la tecnica scolastica) and Alberto (Bibi il sarto dall'anomalo estroso), I had a great time playing tennis with you guys. Unfortunately, I am still the worst player among us, but I still put lots of grit into it. One day we shall arrange a trip to Helmod to collect all my tennis balls. There must be a field full of them. Also, there are people in Busto Arsizio that wishes to play rough street-tennis with you in the (in)famous Open di Büsti. Will you ever have the guts to join this prestigious tournament?

I would like to give special thanks to the members of Ndujah (the best metal band in Eindhoven/Netherlands/World): Demetrio, Carmine, and Simone. I had much fun playing the bass guitar for the Ndujah. Without you, I definitely would have never visited Asten (but probably not even Valencia). Despite my unbounded talent, my solo career isn't proceeding as expected in Cambridge. I hope we will be able to play again together in the future (yes, I am begging a reunion!).

Thanks also to Ndujah's first and best supporter Elaine, who followed us in our single-dated world tour in Valencia. Thanks for supporting us and for sharing the flat in Valencia with four wild beasts without complaints.

Thanks to the Wasaboys: Omar, Zio Marco, Giacomo, Tommy, and Riccardo. Besides the infinite time spent together in Italy and the uncountable memories I have with you, I would like to thank you for coming to Eindhoven in a few occasions to keep up the good name of Busto Arsizio in the world. Among the memorable events occurred during our crusades in Eindhoven:

- An incredible exhibition at the Ameezing Karaoke of Eindhoven that originated the legend.
- A Guinness world record plunge that saved the honor of a young damsel.
- An unforgettable train trip on a crazy nightrain Amsterdam-Busto Arsizio in which we were ready to crash and burn together.

## Acknowledgements

---

I am glad I had lived these moments with you guys. Despite the distance, we are still able to live new valuable experiences together.

Thanks also to the Wasagirls: Erica, Simona, Marina, Nicole, Emma. It still surprises me how well you managed to get along and become actual friends by simply joining the Wasaboys meetings. You created a very special bond that makes every moment that we spend together a special one.

Simona is not only a proud founding member of Wasagirls. She is also my sister in law and has become a cornerstone of our family. Thank you for hosting me endless times and for treating me like a brother.

Stella, Raffaele, e Simona. Grazie per il vostro supporto ed il vostro affetto. Ma soprattutto, grazie per volermi ancora bene nonostante vi abbia portato via Morena.

Morena. You deserve the biggest gratitude. You turned down your career and decided to completely change your life for following your heart. You have spent lots of energies to keep our relationship alive no matter all my crazy plans to travel the world. Thank you for living all these adventures together with me. It is also your merit if my real and my virtual hearts beat.

Mamma e Papà, se sono riuscito a raggiungere gli obiettivi che mi sono posto lo devo in gran parte a voi. Voi mi avete concesso tutte le possibilità che voi non avete avuto. Questo mio piccolo successo è frutto di tanti vostri sacrifici, passati inosservati ai più. Grazie per avermi insegnato l'importanza e l'efficacia del duro lavoro.

Finally, Giacomo and Riccardo, whenever I look back to the best moments I had in my life, you two were present. Leaving you to follow my dreams was one of the hardest things I had to do. You have always been my best friends before being my brothers and you are always there to cheer me up and motivate me during my struggles. I can't wait to be able to spend time more regularly with you.

Cambridge (UK), 15<sup>th</sup> November 2020  
Luca Barbarotta

# Curriculum Vitae



Luca Barbarotta was born on the 23<sup>rd</sup> of April, 1987 in Busto Arsizio, Italy. He received his Bachelor's degree in Mathematical Engineering in July 2010 from the Polytechnic University of Milan in Italy. He then studied Computational Science and Engineering at the Polytechnic University of Milan in Italy. In 2014 he graduated with the thesis 'A mathematical and numerical study of the left ventricular contraction based on the reconstruction of a patient specific geometry', in which he studied active strain activation models using a patient-specific left ventricular geometry. After obtaining his master degree, he continued his research at the Swiss Federal Institute of Technology of Lausanne within his master thesis supervisor's group CMCS - Chair of Modelling and Scientific Computing. In December 2015, he was awarded a Marie-Skłodowska-Curie Innovative Training Networks grant as early researcher in the CardioVascular BioMechanics (CVBM) group at the Eindhoven University of Technology within the MUSICARE (MUltiSectorial Integrative approaches to CARDiac caRE) project. Within this project, he pursued Ph.D. studies under the supervision of prof.dr.ir. F.N. van de Vosse and dr.ir. P.H.M. Bovendeerd. In his research, he addressed the patient specific modeling of the left ventricular mechanics for clinical applications. The driving idea of his research was that a computational model of the left ventricle could predict outputs that can be measured in the clinic and that this predicted outputs could be used to obtain a physics-based interpretation of the patient's pathology by means of inverse analysis. In particular, he focused on the quantification of the uncertainty propagated from the model input to the predicted output with the goal to gain new insights for the selection of the observed quantities of interests within inverse analysis approaches. Since May 2020, he is working as a software engineer at The MathWorks.